INFLUENCE OF ZR SOLUTE ON THE STRUCTURAL, MECHANICAL, AND THERMAL PROPERTIES OF NANOTWINNED AL ALLOYS

by

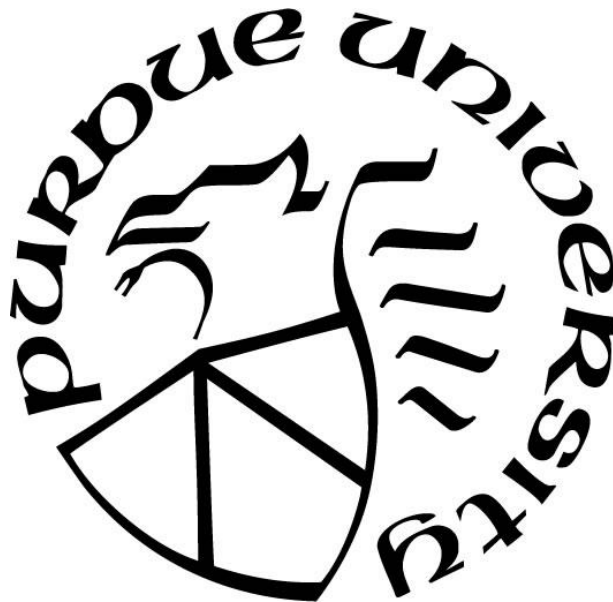**Nicholas A. Richter**

A Dissertation

Submitted to the Faculty of Purdue University

In Partial Fulfillment of the Requirements for the degree of

Doctor of Philosophy

School of Materials Engineering

West Lafayette, Indiana

May 2023

THE PURDUE UNIVERSITY GRADUATE SCHOOL
STATEMENT OF COMMITTEE APPROVAL

Dr. Xinghang Zhang, Chair

School of Materials Engineering

Dr. David F. Bahr

School of Materials Engineering

Dr. David Johnson

School of Materials Engineering

Dr. Haiyan Wang

School of Materials Engineering

Approved by:

Dr. Nikhilesh Chawla

Brave faces, everyone

This thesis is dedicated to:
My wife Alayna,
My parents Bryan & Lisa
My sister Taryn
My grandparents, Tom & Gail and Dennis & Janice
and my friends

ACKNOWLEDGMENTS

TABLE OF CONTENTS

LIST OF TABLES

LIST OF FIGURES

13

18

LIST OF ABBREVIATIONS AND SYMBOLS

Ag	Silver
Al	Aluminum
AlF_3	Aluminum Fluoride
$Al(OH)_3$	Aluminum Hydroxide
Al_2O_3	Bauxite
APT	Atom probe tomography
Ar	Argon
As	Arsenic
b	Burgers vector
B	Boron
BCC	Body centered cubic
BF	Bright field
CG	Coarse grained
Co	Cobalt
Cr	Chromium
CSL	Coincident site lattice
CTB	Coherent twin boundary
Cu	Copper
d	Grain size
D	Diffusion coefficient
DBTT	Ductile-to-brittle transition temperature
DC	Direct current
DF	Dark field
DFT	Density functional theory
EBSD	Electron backscatter diffraction
ECAE	Equal channel angular extrusion
ECAP	Equal channel angular pressing
EDS	Energy dispersive spectroscopy
E_r	Reduced modulus

FCC	Face centered cubic
Fe	Iron
FEM	Finite element modeling
FIB	Focused ion beam
G	Shear modulus
Ga	Gallium
GB	Grain boundary
GBE	Grain boundary engineering
GND	Geometrically necessary dislocation
GPFE	Generalized planar fault energy curve
H	Hardness
H_2O	Water
HCP	Hexagonal close packed
HEA	High entropy alloy
Hf	Hafnium
HRTEM	Hi-resolution transmission electron microscopy
In	Indium
ISE	Indentation size effect
ISFE	Intrinsic stacking fault energy
ITB	Incoherent twin boundary
k	Boltzmann's constant
k_y	Hall-Petch coefficient
m	Strain rate sensitivity exponent
MD	Molecular Dynamics
Mg	Magnesium
Mo	Molybdenum
n	Strain hardening exponent
Na_3AlF_6	Cryolite
$NaAlO_2$	Sodium Aluminate
NaOH	Sodium Hydroxide
Nb	Niobium

Ni	Nickel
NT	Nanotwinned
ODS	Oxide disperse strengthened
PVD	Physical vapor deposition
RF	Radio frequency
S	Stiffness
Sc	Scandium
SEM	Scanning electron microscopy
SF	Stacking fault
SFE	Stacking fault energy
Si	Silicon
Sn	Tn
SPD	Severe plastic deformation
SRS	Strain rate sensitivity
STEM	Scanning transmission electron microscopy
Ta	Tantalum
TB	Twin boundary
Ti	Titanium
TiB_2	Titanium diboride
TEM	Transmission electron microscopy
T_m	Melting temperature
TWIP	Twinning induced plasticity
UFG	Ultra-fine grained
USFE	Unstable stacking fault energy
V	Vanadium
W	Tungsten
XRD	X-ray diffraction
YSZ	Yttria stabilized zirconia
Zn	Zinc
Zr	Zirconium
$\dot{\varepsilon}$	Strain rate

μ	Shear modulus
ρ_{dis}	Dislocation density
σ_0	Friction stress
σ_y	Yield strength
τ_b	Bowing shear stress
τ_c	Cutting shear stress
τ_{CRSS}	Critically resolved shear stress
Ω	Atomic volume

ABSTRACT

Aluminum (Al) possesses a plenitude of remarkable properties, such as strong corrosion resistance, high thermal and electrical conductivity, and high specific strength. However, Al and its alloys are still remarkably weaker than most high strength steels and susceptible to drastic softening at high temperatures, preventing many applications where its low density would be beneficial. Severe plastic deformation can yield ultra-fine grained Al alloys with similar strengths as steels, although they are highly unstable even at room temperature. Nanotwinned (NT) metals have demonstrated concomitant strength and ductility, enabled by twin boundaries which simultaneously act to inhibit dislocation motion and generate partial dislocations that aid in plasticity. In spite of having a high stacking fault energy, nanotwins have been introduced into Al alloys using transition metal solutes during magnetron sputtering. This thesis aims to explore the impact Zr has on the microstructure, deformation, and thermal stability of nanotwins in NT Al.

Our studies identify how Zirconium (Zr) aids in the formation of a significant volume fraction of 9R phase and an abundance of finely spaced incoherent twin boundaries, leading to a maximum hardness of 4.2GPa. They further uncover through *in-situ* micropillar compression that NT Al-Zr alloys are highly deformable and reach a flow stress of ~1.1GPa. Constant strain rate nanoindentation tests demonstrate the enhanced strain rate sensitivity in NT Al-Zr alloys. Zr is also identified to be a remarkable thermal stabilizer when incorporated into NT Al-Co alloys, with no apparent softening up to 450 °C (0.78 T_m). The influence of substrate texture on nanotwinned Al-Zr alloys microstructure was also thoroughly explored.

1. INTRODUCTION

1.1 Historical perspective of metallic materials and Aluminum alloys

Time periods throughout human history are often delineated by specific technological innovations in materials processing. Humanity's progression out of the Stone Age manifested significant agricultural, engineering, and economic evolutions that forever altered society [1–3]. The smelting of copper (Cu) ores initiated the Bronze Age and led to the production of copper alloyed with arsenic and tin, typically referred to as bronze, and can be traced back to the Iranian plateau in the 5th millennium BC [2]. The Bronze Age saw the forging of bronze coins that shifted economic transactions from bartering goods to exchanging these same goods for valuable coins [4]. Progressing into the 1st millennium BC saw a transition into the Iron Age as more complex furnaces enabled the combination of iron (Fe) ore with charcoal to produce Fe and steel. These steel tools quickly replaced bronze due to their remarkable strength and toughness [5,6]. Further furnace developments in the 18th and 19th centuries led to the explosion of the steel industry and ultimately the recent industrial revolutions that have shaped our modern age [7]. Interestingly, these early historical periods were dominated by discoveries related to metallurgy that became associated with massive societal development.

The ability to extract the most abundant metallic element from earth's crust (Aluminum, Al) was not possible until thousands of years after the first bronze tools were forged, which led to initial considerations of Al being a precious metal [7]. The invention of the Bayer and Hall-Héroult Processes in the 1880's facilitated the production of Al alloys on an industrial scale. The Bayer process reacts bauxite ore (Al_2O_3) with sodium hydroxide (NaOH) to produce sodium aluminate ($NaAlO_2$), which is then slowly cooled to produce aluminum hydroxide $Al(OH)_3$ [8]. The final step takes the produced $Al(OH)_3$, which is calcined at elevated temperatures to produce refined alumina (Al_2O_3). The reactions driving the Bayer process are given as Equations 1-1 and 1-2 as follows:

$$Al_2O_3 + 2NaOH \rightarrow 2NaAlO_2 + H_2O \quad (160 - 170\,°C) \tag{1-1}$$

$$NaAlO_2 + 2H_2O \rightarrow Al(OH)_3 + NaOH \tag{1-2}$$
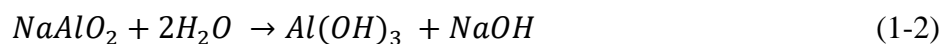
The Hall-Héroult process utilizes molten cryolite (Na_3AlF_6) to dissolve the resulting Al_2O_3, lowering its melting point enabling electrolysis that extracts pure Al. Aluminum fluoride (AlF_3) is

typically added to the electrolyte to further lower its melting point [9]. Coke provides a carbon source that reduces the molten Al_2O_3 into Al. Figure 1-1(a) shows a schematic depicting the Hall-Héroult electrolytic cell setup implemented to produce Al [7]. The molten Al sinks to the bottom of the steel shell due to its higher density than the electrolyte bath. Further refinement steps remove excess impurities, such as oxides, and subsequent processing is then conducted to produce various Al alloys. The basic reaction governing the Hall-Héroult process is provided below:

$$2Al_2O_3 + 3C \rightarrow 2Al + 3\,CO_2 \tag{1-3}$$
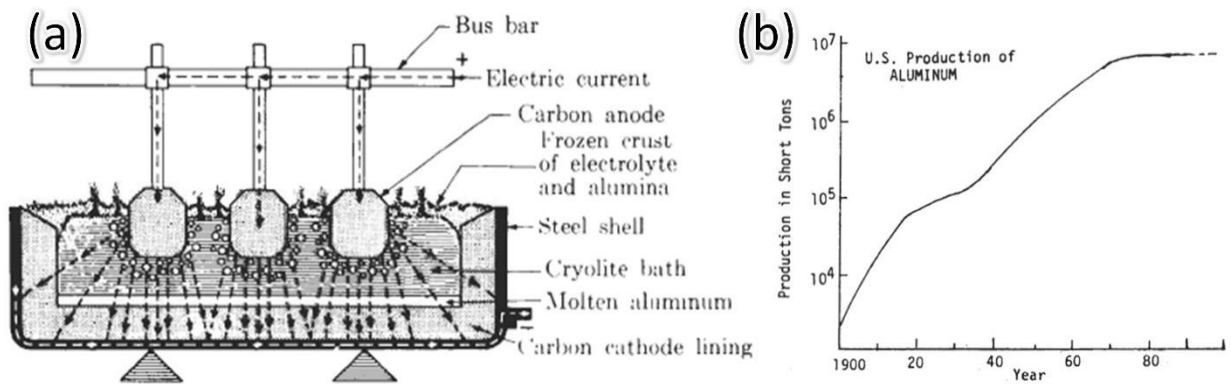
Figure 1-1. (a) Schematic illustrating the electrolytic cell used in the Hall-Héroult process to reduce bauxite ore into pure Aluminum. (b) Progression of Aluminum production in short tons over the course of the 1900's . [7]

The 20th century witnessed the explosion of the automobile and aerospace industries that both hinged on the ability to produce Al alloys on the industrial scale enabled by the Hall-Héroult process. Figure 1-1(b) captures this massive shift in Al production over the course of the 20th century [7]. The light weight and corrosion resistance of Al alloys provided significant benefits that were constantly employed in automobiles and aircraft as well as in storage applications, such as the Al can [10–12]. Additionally, Al alloys possess high electrical and thermal conductivities, making them attractive for power transmission lines and heat sinks in electronics, respectively. The fabrication of Al alloys also benefits from the recyclability of the material, with remelted Al retaining its original properties [13].

Al alloys can be grouped together into different 4 digit classifications based on processing conditions and chemistry. The refined Al output from the Hall-Héroult process is remelt and cast

with various alloying additions to meet the industrial specifications. In wrought Al alloys, the first digit signifies the alloy group and the second modifies the original chemistry. The last two digits identify the alloy or the Al purity. In cast alloys, the final digit clarifies the cast form, typically either casting or ingot. The resulting alloys are organized further based on their subsequent processing. Heat treatments and tempers are further designated using a hyphen to indicate the necessary processing steps to reach the desired properties, and Table 1 details the various chemistry classifications and indicate the primary alloying element in each class [7]. Table 2 provides an overview of Al alloy temper and heat treatments [7].

Table 1-1. Various Al alloy classifications indicating the primary alloying elements for both wrought and cast Al alloys

Wrought Al alloy groups		Cast Al alloy groups	
1xxx	Min. 99.00% Al	1xx.x	min. 99% Al
Grouped by major alloying elements			
2xxx	Copper	2xx.x	Copper
3xxx	Manganese	3xx.x	Silicon with Copper or Magnesium
4xxx	Silicon	4xx.x	Silicon
5xxx	Magnesium	5xx.x	Magnesium
6xxx	Magnesium and Silicon	7xx.x	Zinc
7xxx	Zinc	8xx.x	Tin
8xxx	Other elements	9xx.x	Other elements

Table 1-2. List of temper and hardening designations for Al alloys

Basic Temper Designations	
F	As fabricated
O	Annealed and recrystallized
H	Strain hardened
T	Heat treated
Strain Hardened Subdivision (second digit indicates degree of strain hardening)	
H1x	Strain hardened only
H2x	Strain hardened and partially annealed
H3x	Strain hardened and stabilized
Heat Treated Subdivisions	
W	Solution treated
T	Age hardened
T1	Cooled from fabrication temperature and naturally aged
T2	Cooled from fabrication temperature, cold worked and naturally aged
T3	Solution treated, cold worked and naturally aged
T4	Solution treated and naturally aged
T5	Cooled from fabrication temperature and artificially aged
T6	Solution treated and artificially aged
T7	Solution treated and stabilized by over-aging
T8	Solution treated, cold worked and artificially aged
T9	Solution treated, artificially aged and cold worked
T10	Cooled from fabrication temperature, cold worked and artificially aged

One persistent issue with casting and welding Al alloys is hot cracking. This phenomenon is driven by solidification shrinkage and a narrow freezing range often leads large degrees of chemical segregation and ultimately cracking that undermine the integrity of the alloy. This issue can be either mitigated or exacerbated through alloying element selecting, with Figure 2(a) showing microstructures of alloys that typically experience hot cracking [14]. Figure 2(b) contains a micrograph of brittle intermetallic formation in Al-Fe alloys that severely degrades the toughness and strengths of the alloy [15]. Figures 2(c) and 2(d) contain phase diagrams for Al alloys susceptible to hot cracking and immune to hot cracking, respectively [16,17]. Hot cracks, or solidification cracks, are highly relevant to the future of Al alloy fabrication as additive manufacturing ushers in a new era of metallurgy. Developing high strength, crack free Al alloys is a vital goal for the future of additive manufacturing.
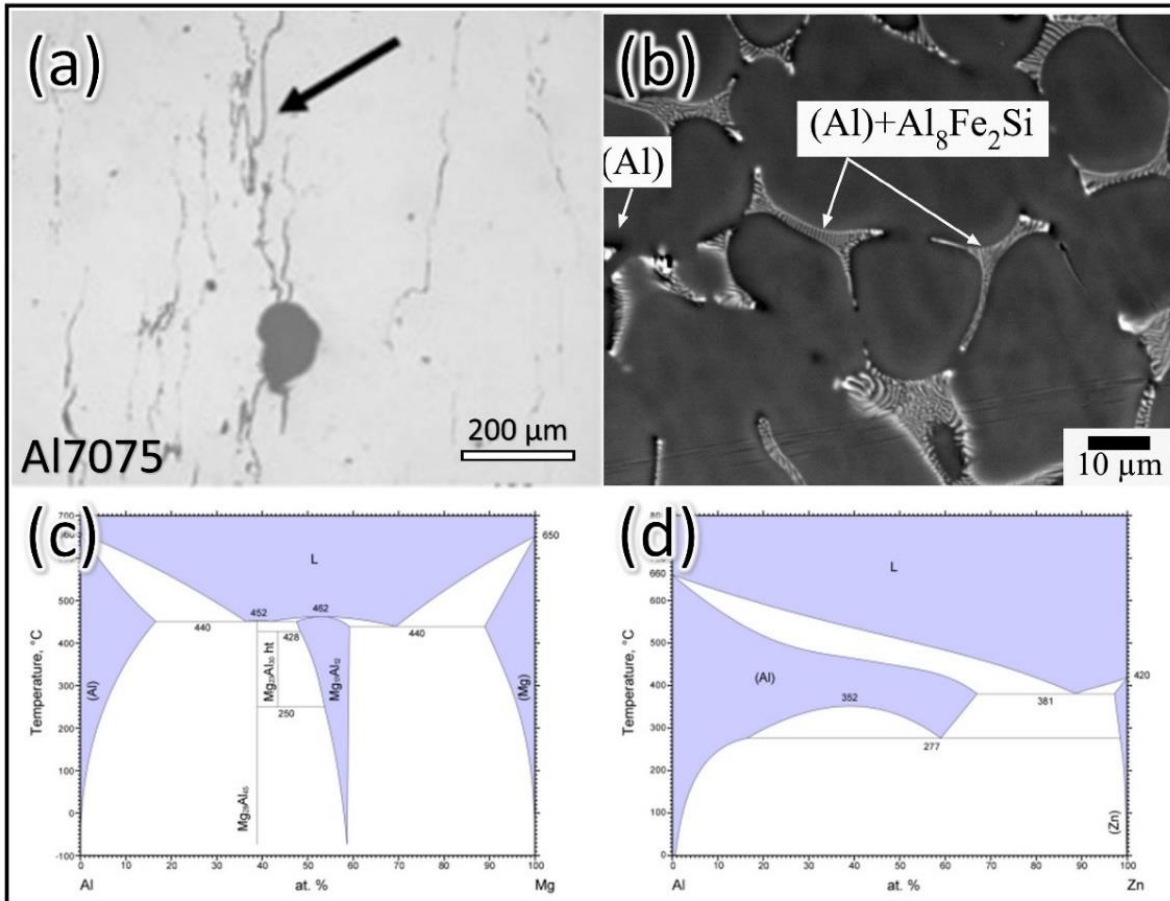
Figure 1-2. (a) Hot cracking in an Al-7075 alloy processed using laser powder bed fusion (b) Intermetallics identified in as-cast Al-Fe alloys (c) Phase diagram for Al-Mg alloys that have a narrow freezing range and are less suseptible to hot cracking(d) Phase diagram for Al-Zn alloys that have a large freezing range and are prone to hot cracking. [14–17]

The attractiveness of Al alloys due to their low density is often hindered due to their lower strengths compared with steel and titanium counterparts. Extensive efforts have been undertaken over the past century to further enhance the strength of Al alloys, however pushing the boundaries of alloy strength is often detrimental to ductility which limits its toughness and processability. Developing alloys that simultaneously boost strength and maintain ductility are highly sought after, identified as pushing into the upper right quadrant of the classical "banana curve" used to describe the strength ductility tradeoff. An example of this curve can be found in Figure 1 of [18] and this phenomenon is discussed at length in this thesis.

1.2   Strengthening mechanisms of metallic materials

The industrial revolutions of the 19th and 20th centuries provided a plethora of opportunities for materials to be at the forefront of technological and scientific advances. With the development of the steel and Al alloy industries came the need to understand where they derived their impressive strengths and properties. The flow strength of crystalline materials is increased through the restriction of dislocation motion. Providing obstacles to moving dislocations necessitates a higher stress to continue plastic flow, thereby increasing the strength of a material. This section provides a brief review of the major strengthening mechanisms governing deformation in metal systems and provides background for the analysis performed in this thesis.

1.2.1   Strain hardening

Dislocations (distinct line defects within crystals) can serve as barriers to other dislocation motion as their surrounding stress fields interact. Continuous plastic deformation of metallic materials increases the dislocation density (ρ_{dis}) providing more obstacles to a moving dislocation [19,20]. This dislocation multiplication process induces "strain hardening" and the plot in Figure 1-3(a) depicts the 3 stages of strain hardening, which will be described here [21,22]. First, a crystal begins with a low ρ_{dis} and very few slip systems operating, leading to the plateau in Stage I, which ends with the activation of more slip systems. This is referred to as "easy glide" as dislocations are able to freely traverse the crystal. Stage II is characterized by "linear hardening" and a rapid increase in ρ_{dis} leads to a jump in critically resolved shear stress (τ_{CRSS}). This ρ_{dis} change is depicted in Figures 1-3(b-e) in experiments from single crystal Cu [23,24]. Ultimately, Stage III, which is referred to as "dynamic recovery", is initiated due to extensive dislocation climb leading to dislocation annihilation and recovery. Stage III is highly dependent on loading rate and temperature, as well as the materials stacking fault energy (SFE). The mechanisms governing these stages all interact simultaneously, however different mechanisms are more dominant corresponding to different stages (i.e., athermal hardening, dynamic recovery).
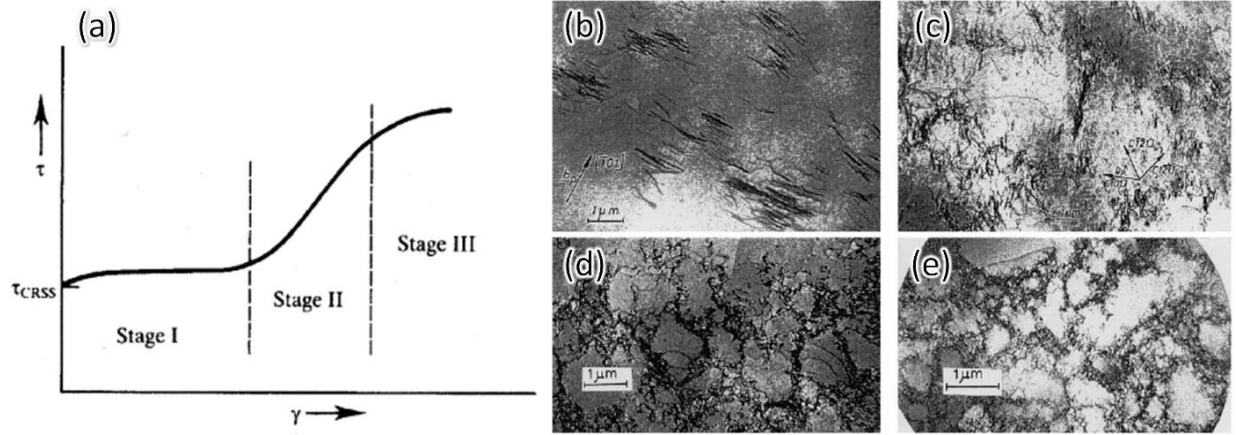
Figure 1-3. (a) This plot depicts the evolution of critically resolved shear stress (τ_{CRSS}) with strain (γ) when loading a single crystal with the 3 stages of work hardening labeled. (b-e) show evolving Cu single crystals deformed at various stress levels, (b) 1.1 MPa, (c) 14 MPa, (d) 28 MPa and (e) 69 MPa. [21,23,24]

The origins of work hardening have long been debated and the dislocation mechanisms governing the phenomenon have slowly been uncovered since the 1950's [19,20,25]. The details of these interactions will not be discussed at length here and are reviewed in [22]. Essentially, the intersection of dislocations produces pinned immobile segments. These pinned regions produce Frank-Read sources that lead to dislocation multiplication. Figure 1-4 shows the results from molecular dynamics (MD) simulations and microscopy experiments of dislocation interactions in Molybdenum (Mo) revealing dislocation interaction and multiplication [25]. These types of multiplication reactions drive stage II of strain hardening and lead to microstructures shown in Figures 1-3(b-e). The accumulation of dislocations increases the stress barrier for dislocation motion requiring a larger stress to continue plastic deformation, and the relationship between dislocation density and flow stress can be described by:

$$\tau = \alpha\mu b\sqrt{\rho_{dis}} \tag{1-4},$$

where τ is the flow stress, μ is the shear modulus and b is the burgers vector [22]. The strain hardening exponent (*n*) is a parameter that describes the ability of a material to accumulate dislocations. A larger *n* indicates more rapid strain hardening. It has been identified that a metal's strain hardening response is dependent on intrinsic factors such as the grain size (d) [26–28], SFE [22,29], and texture [30–32], as well as extrinsic properties like the loading conditions [33], temperature [34–36], and strain rate [37,38]. Ultimately, theories that describe strain hardening provide significant insight into the stress strain curve.
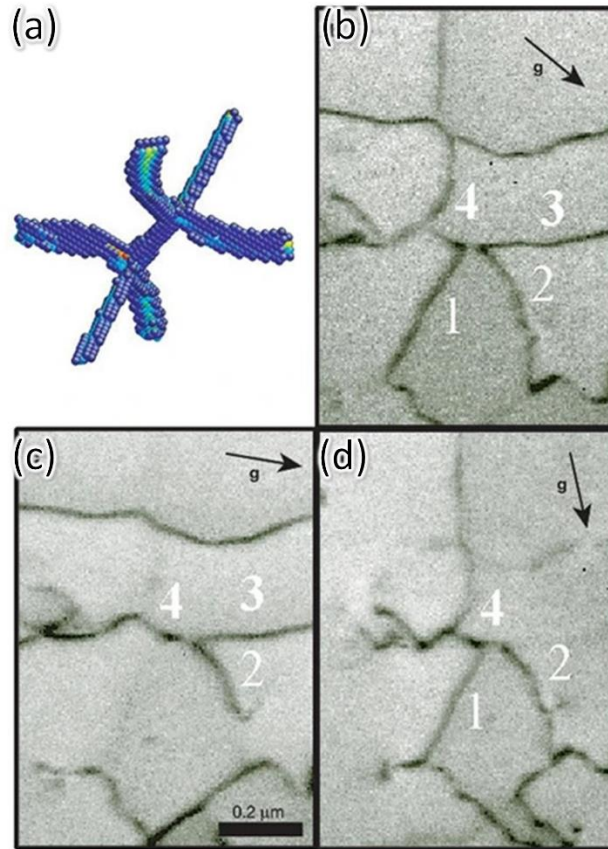
Figure 1-4. (a) Results from molecular dynamics (MD) simulations in a Molybdenum (Mo) single crystal showing a multi-junction forming from the interaction between dislocations (b-d) Transmission electron microscopy (TEM) micrographs of deformed Mo single crystals confirming similar multi-junctions found in MD. [25]

Strain hardening is highly relevant to a multitude of machining and forming processes related to metallic materials. Commonly referred to as "cold working", a metal workpiece is plastically deformed with the goal of permanently changing the shape of the alloy. Permanent shape changes through various forming processes (cold rolling, drawing, forging etc.) lead to a corresponding increase in ρ_{dis}, and coupled with corresponding heat treatments, the final properties can be highly tuned. Additionally, combining high temperatures with forming processes such as rolling allow for significant thickness reduction to metal sheets while accelerating stage III recovery mechanisms. "Hot working" is frequently used to change the shape of a metal workpiece without the adverse strengthening effects of strain hardening. In contrast to these processes, undesirable work hardening can occur during machining process that leads to cracking and brittle failure of a component.

1.2.2   Hall-Petch strengthening

Planar defects within crystals (grain boundaries) also obstruct dislocation motion and their spacing directly impacts a materials strength. The 1950s provided the first documentation by both E.O. Hall [39] and N.J. Petch [40] of the inverse square root relationship between low carbon steels yield strength (σ_y) and its grain size (d), and has properly been named the Hall-Petch relation:

$$\sigma_y = \sigma_0 + k_y d^{-1/2} \qquad (1\text{-}5),$$

where σ_0 is the friction stress and the Hall-Petch coefficient is given by k_y. The degree of strengthening imparted by restricting grain size is described by k_y, which describes the effectiveness of strengthening by grain boundaries. Grain boundaries disrupt slip plane continuity due to crystallographic misorientation, which impedes a gliding dislocations motion and requires a significantly high stress for dislocation transmission and continued deformation. Figure 1-5 illustrates the Hall-Petch strength dependence on grain size for multiple crystal structures [41]. These plots (and the review by Cordero et al. [41]) expand upon the initial findings for low carbon steel by Hall and Petch, and identify the exact same inverse square root dependence across a range of systems and crystal structures. This universal applicability makes tailoring grain size a popular choice for controlling a materials strength.
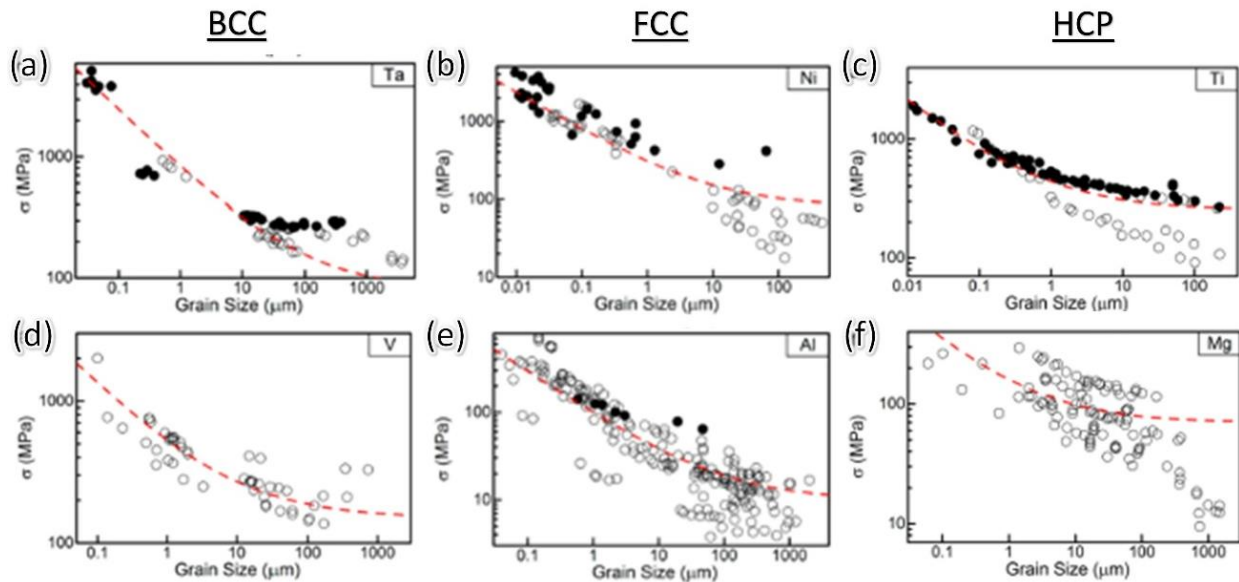
Figure 1-5. Plots of yield strength vs grain size identifying the classical Hall-Petch relationship for BCC (a) Ta and (d) V, FCC (b) Ni and (e) Al, and HCP (c) Ti and (f) Mg. [41]

The mechanisms governing Hall-Petch strengthening have been developed over the past half century and are briefly discussed here [21,41]. Microscopic slip begins the deformation process as certain favorably oriented grains yield and facilitate dislocation motion. Ultimately, multiple dislocations "pileup" against a grain boundary separating the favorably oriented grain from a non-yielded grain. This dislocation pileup produces macroscopic yielding by either (1) transmitting dislocations across the grain boundary into the adjacent grain, or by (2) generating a stress concentration significant enough to initiate yielding in adjacent grains. The physics governing the stress concentration at the head of the pileup dictate that stress concentrations produced from pileups is larger with a larger d, which indicates lower applied stresses are needed to plastically deform a material with large d. Debate between mechanism (1) and (2) has been extensive as the theory of dislocation pileups fits the results from experiments, however, there have been few instances of dislocation pileup being identified [41]. Additionally, the pileup model is insufficient in describing the influence of different types of boundaries, discussed more at length in the following subsection. The Li model expands upon (1) and proposes Hall-Petch strengthening is governed by dislocation emission from grain boundaries. Unfortunately, there is also limited evidence supporting this theory as well. Ashby provided an additional model based on geometrically necessary dislocations (GNDs) and many subsequent models have been based on his idea. Basically, deformation initiates similar to the pileup model in isolated, favorably oriented grains, however neighboring grains with different crystal orientations become geometrically incompatible. To reconcile this, GNDs are generated to accommodate plastic strain and reconcile the geometric incompatibility. Ashby arrived at the original inverse square root relationship by relating boundary hardening through Taylor hardening induced by these GNDs. The review conducted by Cordero et al. succinctly discusses the debate between these models and relates the scatter in data seen in Figure 1-5 back to other strengthening mechanism unaccounted for in the Hall-Petch model [41]. Figure 1-6 presents microstructure and corresponding Hall-Petch plot for pure Cu [42].
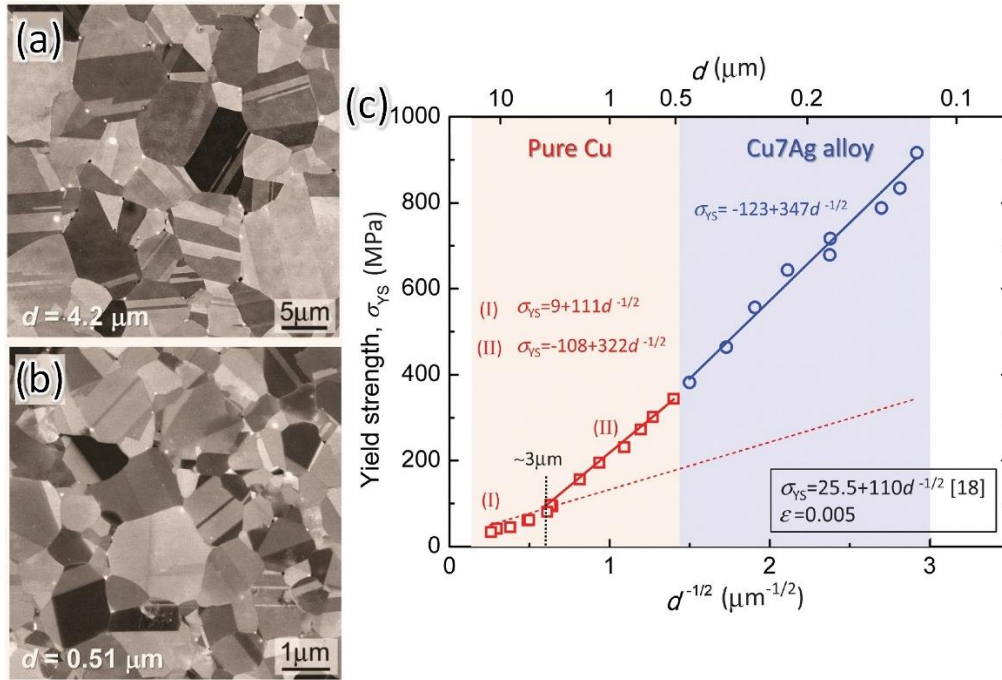
Figure 1-6. (a-b) SEM micrographs revealing microstructure of Pure Cu specimens after different annealing treatments (c) Hall-Petch plot revealing the dependence of yield strengths on grain size (*d*) for pure Cu from (a-b) and a Cu-7Ag alloy [42]

Continued grain refinement into the nanoscale in theory should continue to restrict dislocation motion and produce materials pushing the strengthening limits, however recent studies have found a critical grain size upon which softening actually begins. This phenomenon has been termed the "Inverse Hall Petch" effect and has been theorized to correspond with the activation of grain boundary mediated deformation mechanisms [43–45]. Chokshi et al. were the first to identify this phenomenon in 1989 and their results are presented in Figure 1-7 [43].
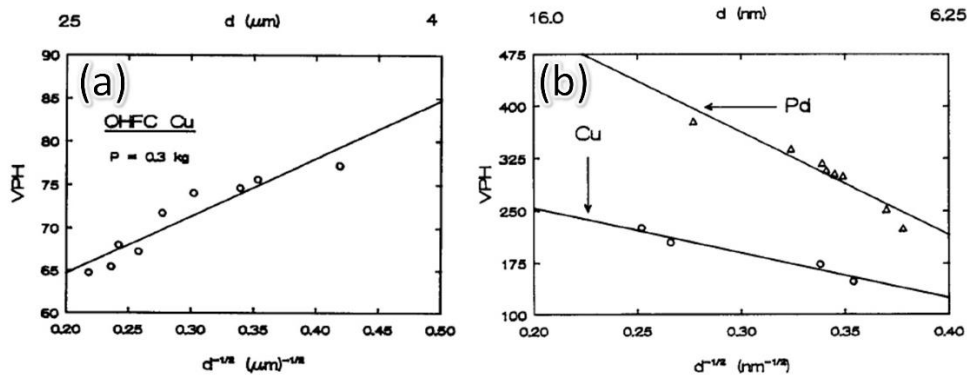
Figure 1-7. Results from Chokshi et al. revealing (a) conventional Hall-Petch relationship in coarse grained Cu and (b) an inverse Hall-Petch relationship in nanocrystalline Cu and Pd [43]

These diffusion-based mechanisms are activated since d is physically too small to accommodate dislocation activity. Additionally, a significant fraction of a materials atoms are residing within grain boundaries, leading to an alteration in strengthening mechanisms. Coble creep was activated in the now large volume fraction of amorphous grain boundaries and required a lower stress to become active than dislocation transmission from grain boundaries. Mohamed et. al provided an example model where dislocation-accommodated boundary sliding was used to carry plasticity in nanocrystalline metals and established this based on the activation energy and volumes as well as the sliding rate [46]. This work also was able to predict the critical grain size for Ni and Cu to be 13 and 25nm, respectively. There is still significant debate on the topic of this deviation from the linear Hall-Petch trend, and continued work must be done through experiments and simulations to fully understand the phenomenon [43–45,47–52].

1.2.3   Grain boundary engineering

Section 1.2.2 demonstrates the efficacy of introducing more grain boundaries as a strategy to impart high strengths into materials. The inherent structure and character of the boundaries themselves also impacts mechanical response and mechanical and thermal stability. Being able to tailor different misorientation angles is referred to as "grain boundary engineering" (GBE) and has been a hot topic of research since the 1980s [53]. This strategy hinges on the concept of introducing a larger volume fraction of coincident site lattice (CSL) boundaries within the material [53–56]. As a result, grain boundaries would have fewer locations where embrittlement, cracking or undesirable segregation could degrade the mechanical properties of a material. These boundaries are characterized by having specific degrees of misorientation leading to a corresponding fraction of lattice sites "coinciding" at the same location. These boundaries also possess different levels of inherent grain boundary energy, leading to certain CSL boundaries being more stable and resistant to deformation than others. Figure 1-8(a) plots the relationship between misorientation angle and boundary energy [54].
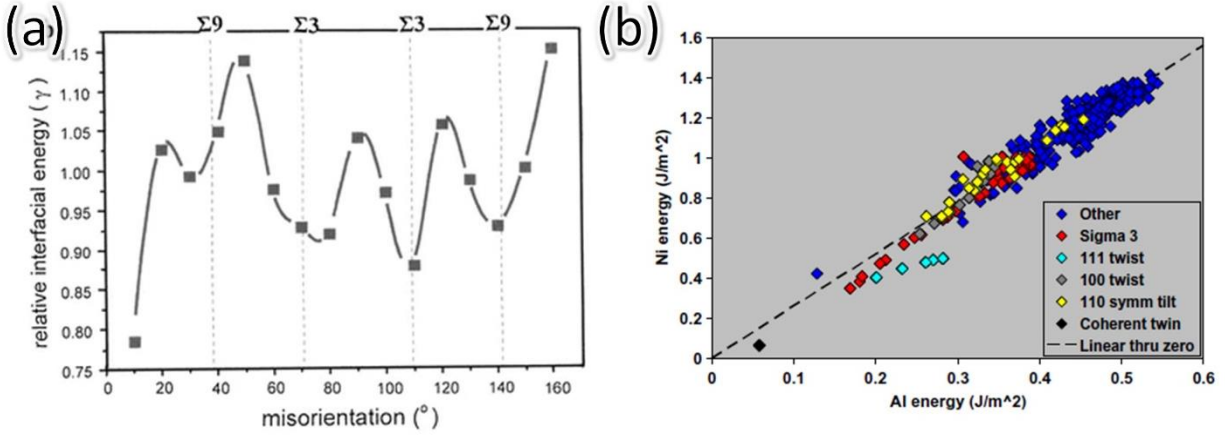
Figure 1-8. (a) Relative interfacial energy as a function of misorientation angle with corresponding CSL Σ value labeled for reference. (b) Evolution of Ni boundary energy vs Al boundary energy showing a similar linear trend and energy progression for similar types of boundaires. [54,55]

The most widely studied of these types of boundaries is the $\Sigma3$ twin boundary, which will be discussed at length in Section 1-5. Figure 1-8(b) depicts the energy level of various types of CSL boundaries in Ni and Al, with the lowest being the coherent twin boundary as well as other $\Sigma3$ type boundaries [55]. Typically, these types of CSL boundaries are introduced into materials through thermomechanical treatments, however the relevance to this thesis is the synthesis of highly twinned Al alloys via one step (magnetron sputtering).
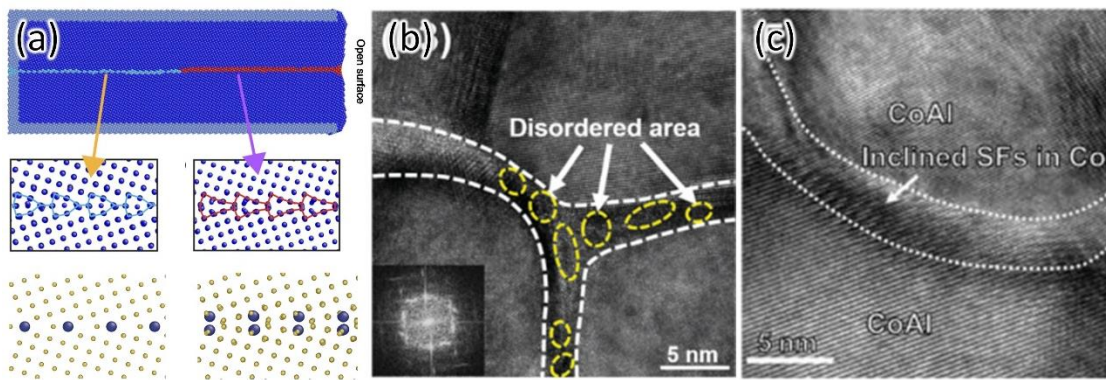
Figure 1-9. (a) Grain boundary complexions simulated for grain boundaries in Cu. (b) Thick grain boundaries generated in annealed Ni-Mo alloys. (c) Stacking fault (SF) induced plasticity from Co-rich grain boundaries surrounding a brittle CoAl core. [57–60]

In addition to controlling the character of specific boundaries within materials, the internal structure of grain boundaries can also be tailored. Grain boundary complexions are an example of this, and one instance is shown in Figure 1-9(a) in Cu using MD [57]. Complexions are typically seen as an intermediate step on the transformation into different CSL boundaries and is highly relevant to their development after high levels of plastic deformation. Additionally, examples of unique "thick" grain boundaries that impart high strength and thermal stability into Ni-Mo alloys are presented in Figure 1-9(b) [58,59]. Intermetallic compounds also can benefit from a unique "core-shell" structure where crystalline Co-rich grain boundaries surround brittle CoAl intermetallics, imparting significant strength and plasticity [60].

1.2.4   Solid solution strengthening

Solute elements can be added into a pure metal to produce various alloys, such as adding carbon (C) into Fe to produce steel, or many of the examples of Al alloys from Table 1-1 [7]. Before casting these alloys, minor solute additions (often only a fraction of a percent) are added into the melt to impart various properties, including higher strength via solid solution strengthening or to promote precipitate formation (discussed in the following sub-section). A wide range of alloys are used across many industries, including steels, Al alloys, Ni-based super alloys, Ti alloys and Zircaloy, and understanding the interactions between solute additions and resulting properties is crucial to their implementation, and to the work in this thesis. It is understood solute atoms interact with mobile dislocations through multiple factors: elastic interactions, chemical interactions and electronic interactions [21]. These factors all contribute to interactions with the long range stress fields of dislocations gliding along slip planes and act as obstacles to their motion.

First, the elastic interactions encompass the size difference between the added solute atom and the solvent lattice atom, and the differences in modulus between the solute and the solvent [61]. When a solute atom resides on a lattice site, it is termed a substitutional point defect and generates spherical distortions to the surrounding lattice due to the size difference. Additionally, point defects residing at interstitial sites (between lattice sites) generate shear components to the strain filed surrounding the lattice site. The corresponding stress fields of edge dislocations (hydrostatic) and screw dislocations (shear) interact heavily with substitutional and interstitial solute atoms, respectively. Modulus mismatch also factors into the elastic contributions to solid solution strengthening [21,61]. As a dislocation's line energy is dependent on the materials modulus,

37

adding solute with different moduli either "attracts" or "repels" dislocations. Solute atoms with lower moduli inherently have lower energy and the dislocation prefers to reside at these sites, leading to an "attraction". In contrast, a larger modulus "repels" the dislocation because of the unfavorable energetic conditions. Ironically, a "softer" solute atom actually strengthens a crystal more than a "hard" one [21]. For most metallic alloys, these elastic contributions dominate solid solution strengthening. This elastic contribution has become significantly more relevant as the development of high entropy alloys has produced multi-principal elements and significant levels of lattice distortion due to size mismatch [62–68]. Figure 1-10 highlights this phenomenon in refractory high entropy alloys (HEAs) and presents an extreme case of solid solution strengthening being enhanced with larger lattice strains [69].
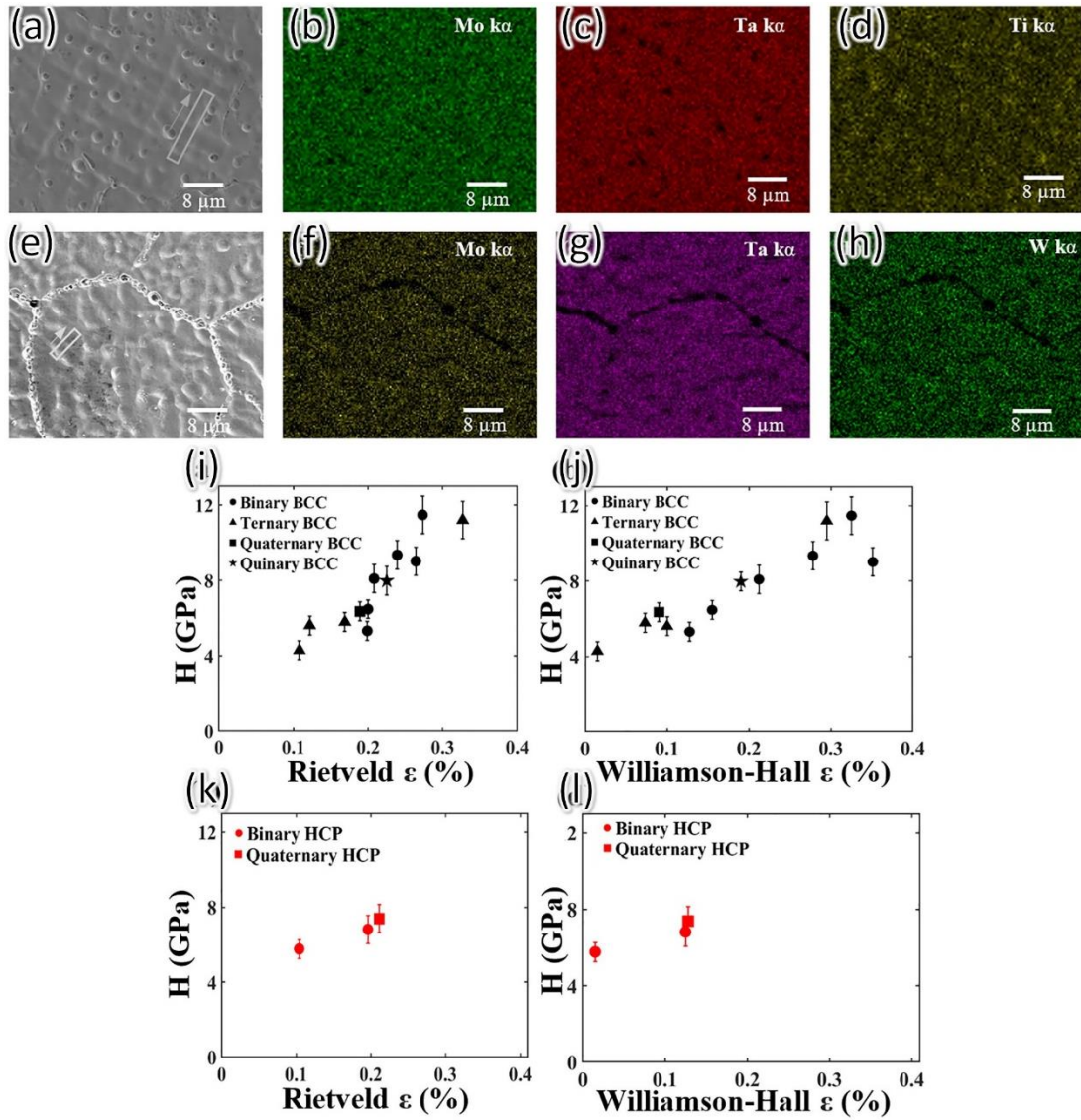
Figure 1-10. (a) STEM image of MoTaTi medium entropy BCC alloy. (b-d) EDS maps revealing majority solid solution within the MoTaTi alloy. (e) STEM image of MoTaW medium entropy BCC alloy. (f-h) EDS maps revealing majority solid solution within the MoTaW alloy. (i-l) Hardness evolution as a function of strain measured using (i,k) Rietveld analysis and (j-l) the Williamson-Hall method. [69]

Additionally, albeit less significantly, the chemical and electronic interactions contribute to solid solution strengthening. Chemical interactions between solute atoms hinge on the impact solute has on the local SFE surrounding a dislocation [21]. The core width of a dislocation directly influences its mobility, ability to cross slip and its propensity for being obstructed by obstacles. Dislocations in close packed metals (such as FCC) typically have wider cores than metals composed of BCC microstructures. The core width is inversely proportional to the SFE, and wider cores have more limited cross slip and easier glide along slip planes as a result. The electronic contributions are extremely minor in metallic alloys but play a larger role in ionic crystalline solids. Basically, this effect is related to the valence differences caused by how solute atoms locally alter the electronic charge distribution.

Multiple models have attempted to fully capture the impact of solid solution strengthening, and the two most famous models are the Fleischer [70–73] and Labusch [74] models. The former builds upon the aforementioned ideas of elastic interactions to predict τ_{CRSS}. Fleischer described the increment to τ_{CRSS} using:

$$\Delta\tau = \alpha \cdot G \cdot \varepsilon^{3/2} \cdot c^{1/2} \tag{1-6},$$

where α is a factor dependent on material, G is the shear modulus and c is the solute concentration. ε_s is the interaction factor that relates the change in lattice parameter with G, and is given by:

$$\varepsilon_s = \left| \frac{\frac{1}{G}\frac{dG}{dc}}{1+\frac{1}{2}\left|\frac{1}{G}\frac{dG}{dc}\right|} - 3 \cdot \frac{1}{a} \cdot \frac{da}{dc} \right| \tag{1-7}.$$

Here, *a* represents the lattice parameter. In this thesis, an α of 0.0235 was used based on experimental data for nanocrystalline Ni-W. The Fleischer model has its limitations (neglecting chemical and electronic contributions); however, it is highly reliable for predicting the solid solution strengthening of many alloys. Additionally, the Labusch model is similar to the Fleischer model in predicting the increment in τ_{CRSS} by incorporating solute atoms and focusing on the elastic interactions, although it more reliably accounts for different types of obstacles:

$$\Delta\tau = \beta \cdot G \cdot \left[\left(\frac{1}{G} \cdot \frac{dG}{dc}\right)^2 + 15\left(\frac{1}{a_{Al}} \cdot \frac{da}{dc}\right)^2\right]^2 \cdot c^{3/2} \tag{1-8}$$
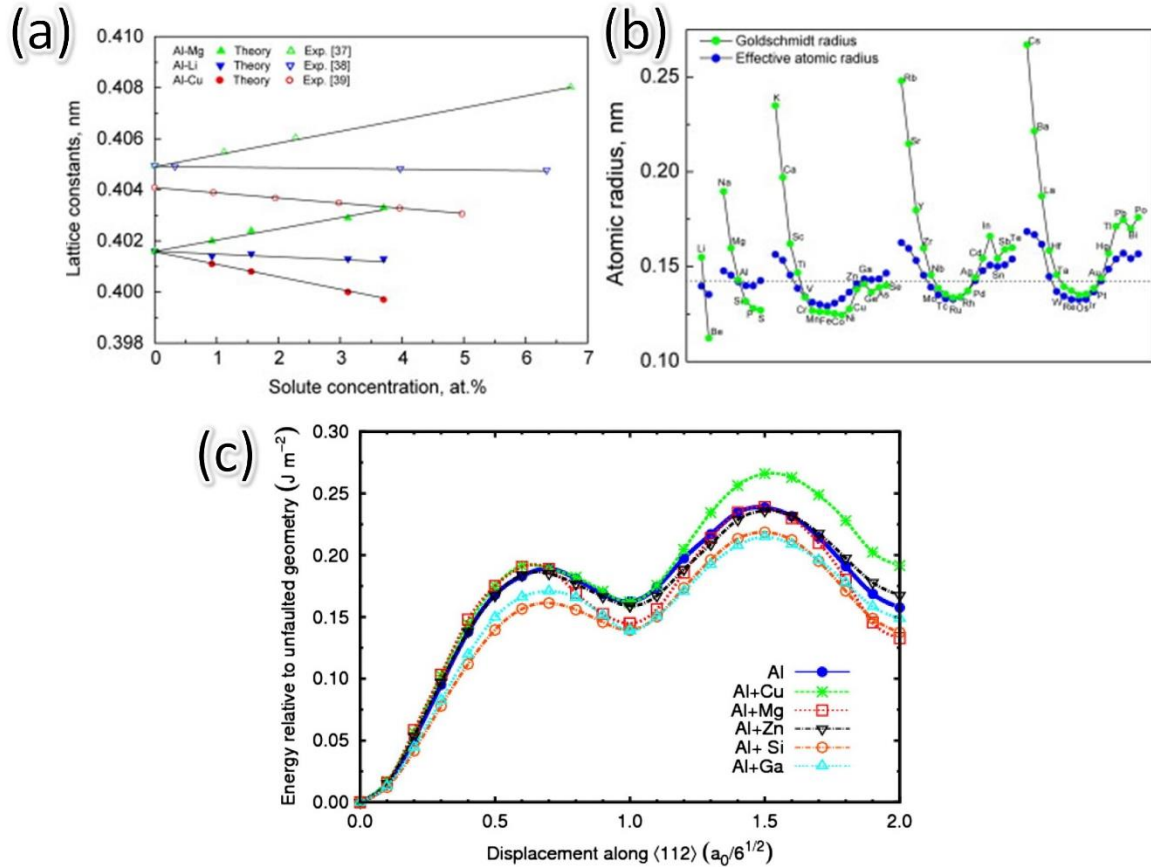
Figure 1-11. (a) Lattice constant evolution as a function of solute concentration for various binary Al alloys. (b) Effective atomic radius change of Al-X binary alloys organized by period. (c) Generalized planar fault energy (GPFE) curve detailing the energy change corresponding to various solute additions to pure Al. Shifting the curve up provides a larger energy barrier to dislocation motion. [75–77]

Solid solution strengthening is a crucial factor of producing multiple Al alloys. Figure 1-11(a-b) are plots detailing the evolution of the lattice parameter and atomic radius in Al depending on added solute [75]. More recent efforts have focused on various simulation techniques to provide a more detailed description of solid solution strengthening. Figure 1-11(c) provides an example of a generalized planar fault energy curve [61,76–78] (GPFE) for various binary Al-X alloys [77]. Ultimately, this provides deeper insight into the elastic, chemical and electronic contributions to solid solution alloys and better predictions for future alloy developments.

1.2.5 Precipitation strengthening

Incorporating solute into an alloy can also generate precipitates, or second phase particles, depending on the thermodynamic interactions between solute atoms and the principal solvent element. Precipitates are even bigger obstacles for dislocation motion than isolated solute atoms and can also help stabilize microstructures and provide creep resistance. Figure 1-12(a-c) shows an example of $L1_2$ precipitation forming in Al-Zr-Sc alloys after an isothermal aging for 24 hours at 400 °C [79]. As is clear in Figure 1-12(c), the introduction of these precipitates leads to a corresponding jump in hardness. The hardness evolution in Figure 1-12(c) is representative of precipitate aging, with over aging occurring after either (1) too long of a heat treatment or (2) aging at too high of a temperature. The kinetics of precipitate formation governs the shape of this curve and more can be learned here [80,81]. One of the most famous examples of precipitation hardening is 2xxx series Al alloys where Cu precipitates impart high strengths. This was advantageous in the early stages of developing aircraft engines as the Wright Brothers cast Al-8%Cu age hardened alloys [80]. Figure 1-13(a) displays the progression of work hardening rate of Al-Cu alloys against aging time, with the rest of Figure 1-13 providing examples of the θ and θ' precipitate evolution in Al-Cu alloys during deformation [82].
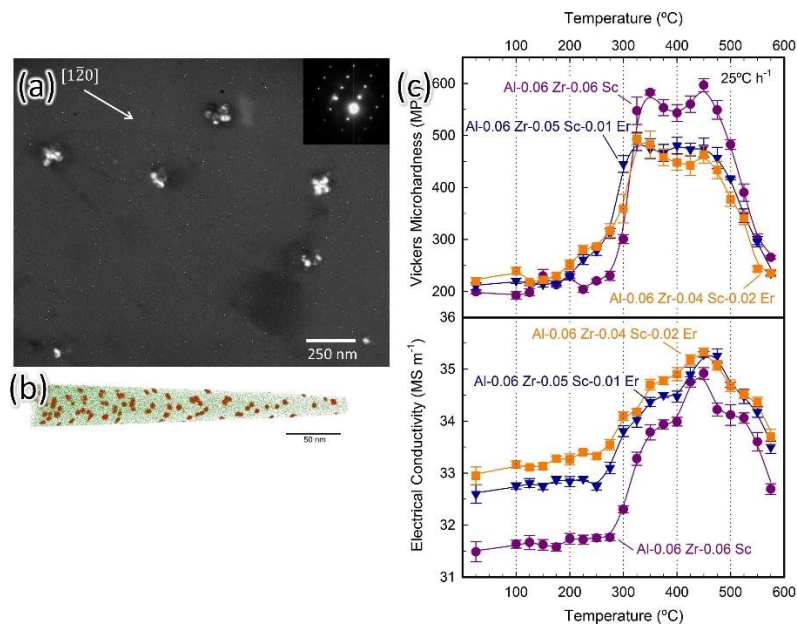
Figure 1-12. (a) Bright field (BF) TEM micrograph identifying the uniform distribution of $Al_3(Sc, Zr)$ ($L1_2$) precipitates after aging at 400 °C for 24 hours. (b) Corresponding atom probe tomography (APT) collected for the aged alloy in (a). (c) Evolution of Vickers microhardness and electrical conductivity with aging temperature for 3 different alloy compositions. [79]
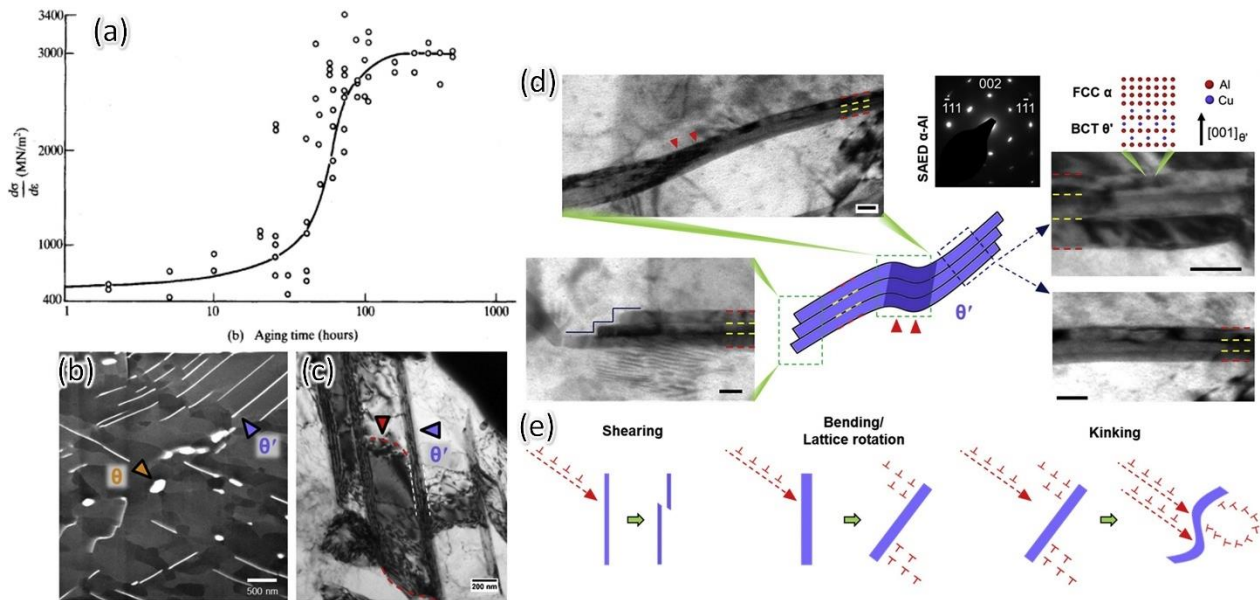
Figure 1-13. (a) Work hardening rate evolution with aging time highlighting the increase in precipitate density until reaching a plateau upon over aging. (b-c) Examples of θ and θ' precipitates in an Al-4Cu alloy from TEM micrographs. (d) Post-deformation TEM micrographs revealing various kinking deformation mechanisms with corresponding schematics provided in (e). [21,82]

Dislocations interact with precipitates through two main mechanisms, either (1) precipitate cutting/shearing or (2) dislocation bowing, and multiple factors dictate which mechanism operates [21]. The nature of the interface between precipitate and matrix is often the key factor in determining whether a precipitate will shear, or dislocations will bow around it. Coherent interfaces are most common from small precipitates characteristic of the early stages of aging. Due to differences in interatomic spacings, lattice distortion occurs in the matrix to maintain this coherent interface, leading to stress fields that behave similar to the aforementioned solid solution strengthening. As aging continues, precipitates grow in size and coherency is often lost, removing the source of lattice strain [80,83,84]. Ultimately, the strain energy necessary to maintain an ordered interface becomes thermodynamically unfavorable. Figure 1-14 depicts these types of interphase boundaries schematically [21]. Interface nature directly influence the operating deformation mechanism, as smaller coherent precipitates (Figure 1-14(a)) typically result in dislocations "cutting" through the precipitate, while larger precipitates with disordered interfaces (Figure 1-14(b)) forces dislocations to bow between precipitates.
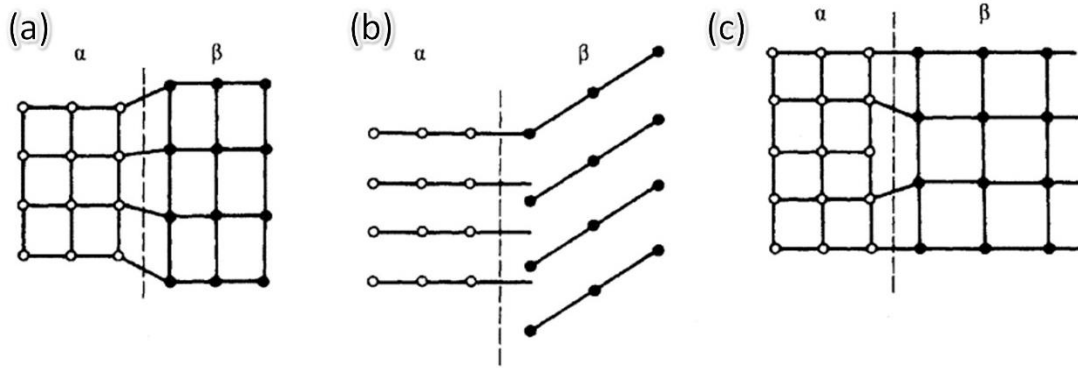
Figure 1-14. Schematics depicting (a) ordered (coherent) interface structure, (b) disordered (incoherent) interface structure and (c) semi-ordered interface structure between 2 different phases, α & β. [21]

Additionally, the cutting and bowing shear stresses can be calculated in order to predict dislocation/precipitate interaction mechanism [21]. If the cutting shear stress (τ_c) is lower than the bowing shear stress (τ_b) the dislocation will cut through the precipitate:

$$\tau_b = \frac{G}{(L-2r)}$$ (1-9),

where G is the shear modulus of the matrix, L is the dislocation separation distance and *r* is the precipitate diameter. Precipitate strengthening reaches a maximum (peak of the hardness vs aging temperature plot in Figure 1-12(c)) when $\tau_c = \tau_b$. Precipitate cutting imparts significant levels of strengthening through multiple factors, including stress fields generated from maintaining a coherent interface, variations in shear modulus across precipitate/matrix interface leading to a dislocation line energy change, and more minor contributions from stacking fault energy difference and maintenance of an ordered structure in precipitate compounds [80,81]. In contrast, bowing dominates in overaged, disordered large precipitates leading to larger levels of dislocation multiplication and work hardening than direct strengthening. Industries are often able to tailor precipitate size and distribution through varying heat treatments [80,83–85]. This provides a powerful tool to control a metal's mechanical properties.

1.3   Strain rate sensitivity

Understanding plastic flow at different strain rates is pertinent to various forming, machining and safety applications. As there are a multitude of deformation processes exhibiting different loading conditions and differing levels of strain rate, it is necessary to assess a materials sensitivity to changing strain rate $(\dot{\varepsilon})$. From a more fundamental perspective, mechanisms controlling plasticity are known to change at low strain rates (dislocation creep) versus high strain rate (dislocation glide). The competing rate controlling mechanisms governing plasticity are considered to be thermally activated, and strain rate sensitivity (SRS) is intimately linked with the activation volume of these mechanisms. This also accounts for the temperature dependence of metallic mechanical behavior, such as the ductile-to-brittle transition temperature (DBTT) seen in ferritic steels. Certain materials can also exhibit superplasticity (100-1000% plastic strain) when subjected to elevated temperatures and strain rates. Additionally, fracture mechanics is strain-rate dependent, with high rates initiating brittle fracture in ductile materials. Table 1-3 provides an overview of different mechanical tests and the corresponding $\dot{\varepsilon}$, with the work from this thesis falling under the static tension / compression regime [86].

Table 1-3. Strain rate ranges corresponding to different types of mechanical testing, with the shaded row corresponding to the tests conducted within this thesis. [86]

Strain rate (s^{-1})	Test type
$10^{-8} – 10^{-5}$	Creep test
$10^{-5} – 10^{-1}$	Static tension / compression
$10^{-1} – 10^{2}$	Dynamic tension / compression
$10^{2} – 10^{4}$	High speed with impact bars
$10^{4} - 10^{8}$	Hyper velocity using projectiles

SRS describes a change in a materials mechanical response with changing strain rates, and is characterized by the SRS exponent, *m*. Conventionally, static tension tests conducted at various strain rates with a constant temperature are used to measure SRS and *m* can then be determined:

$$m = \left(\frac{\partial \ln \sigma}{\partial \ln \dot{\varepsilon}}\right) = \frac{\log(\sigma_2/\sigma_1)}{\log(\dot{\varepsilon}_2/\dot{\varepsilon}_1)} \qquad (1\text{-}10).$$

The *m* value for most metallic materials ranges from 0.02-0.3, and this value is highly dependent on temperature. It is well established that increasing the strain rate induces an increase in flow stress and a corresponding drop in ductility. Figure 1-15(a) captures this trend as increasing

the shear strain rate ($\dot{\gamma}$) from 5×10^{-5} to 8.5×10^{-2} sees a jump in shear stress in commercially pure Al 1100 [87]. The linear portion of the plot in Figure 1-15(b) demonstrates a similar increase in shear stress with increasing strain rate. Both plots in Figure 1-15 demonstrate the significant deviation in commercially pure Al 1100 when the strain rate is above ~10^4 where significant increases in shear stress are identified from Kolsky bar shock tests. Clifton associated this sharp change in hardening rate with an increased rate of formation of dislocation tangles due to the dramatic change in kinetics governing plasticity at such high strain rates [87].
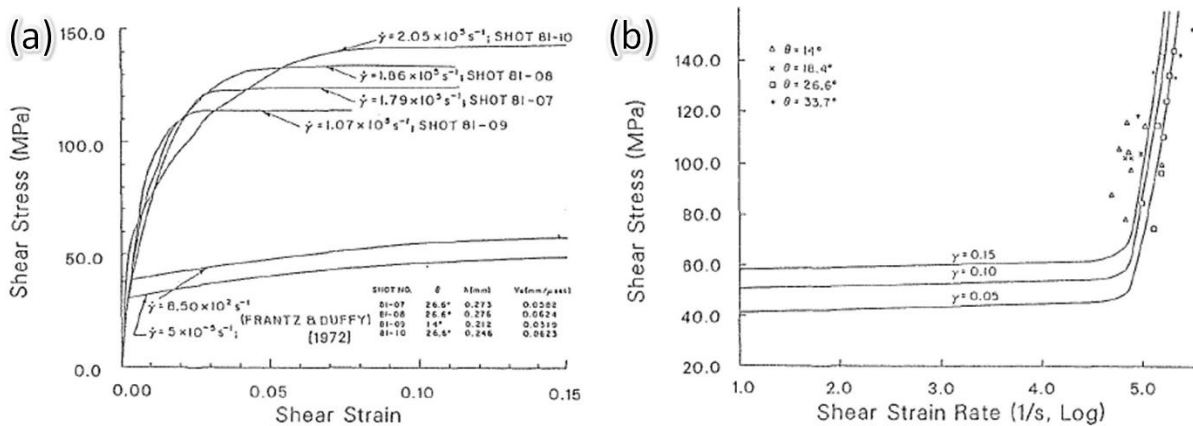
Figure 1-15. (a) Dynamic stress-strain curves for 1100 commercially pure Al revealing changes in hardening rate and yield stress with varied strain rates. (b) Shear stress as a function of shear strain rate for 1100 commercially pure Al tested at constant strain rates. [87]

Figure 1-16(a) provides an additional example of the SRS probed by tension tests exhibited by nanocrystalline Ni with a jump in flow stress realized at higher strain rates [88]. Static tension tests are the most conventional method for systematically assessing the SRS of a bulk material, however many nanocrystalline materials often have sample dimension limitations preventing such tests. The advent of nanoindentation enabled measurements of loads and displacements on the micro and nanoscale, respectively. This technique provided a convenient and reliable tool to measure hardness and modulus of thin films that was previously impossible [89,90]. The precise control of the loading conditions of the indenter tip into the material spawned constant strain rate tests, facilitating the measurement of creep and SRS. Simply holding the indenter tip at a reduced applied load allows for reliable measurements of a materials creep resistance [91,92]. Lucas and Oliver demonstrated constant strain rate nanoindentation for the first time to probe the SRS of In

single crystals [93]. This technique provided consistent results with literature at moderate and higher strain rates, however exhibited significant deviations in *m* when tested at low strain rates [94,95]. This inconsistency was attributed to thermal drift significantly impacting low strain rates due to the extended duration of the experiments. Strain rate jump tests were also adapted from tensile strain rate jump tests providing a different means to quickly measure a range of strain rates. One limitation of this methodology is indentation depths can approach ~500nm, which is often too deep for 1-2 μm thin films. Figure 1-16(b) compares *m* from conventional constant strain rate nanoindentation and strain rate jump tests for nanocrystalline Ni, highlighting the boost in reliability from strain rate jump nanoindentation tests [88,96]. Since nanoindentation hardness and modulus measurements hinge on reliable determination of the contact depth and area, a novel method was developed by Liu et al that combines the moderate strain rate measurement with low strain rate to remove thermal drift and not require the indentation depth of jump tests [95]. This methodology is implemented in Chapter 4 of this thesis where the details are discussed at length. Finally, another strain rate jump technique has been adapted since the development of micropillar compression in the mid-2000s. Figure 1-16(c) provides an example of these tests for yttria-stabilized zirconia (YSZ) performed at different temperatures to probe the underlying deformation mechanisms [97]. Cho et al. attributed the improvement of plasticity to the accommodation of dislocation climb by oxygen vacancy migration at elevated strain rates and temperatures.
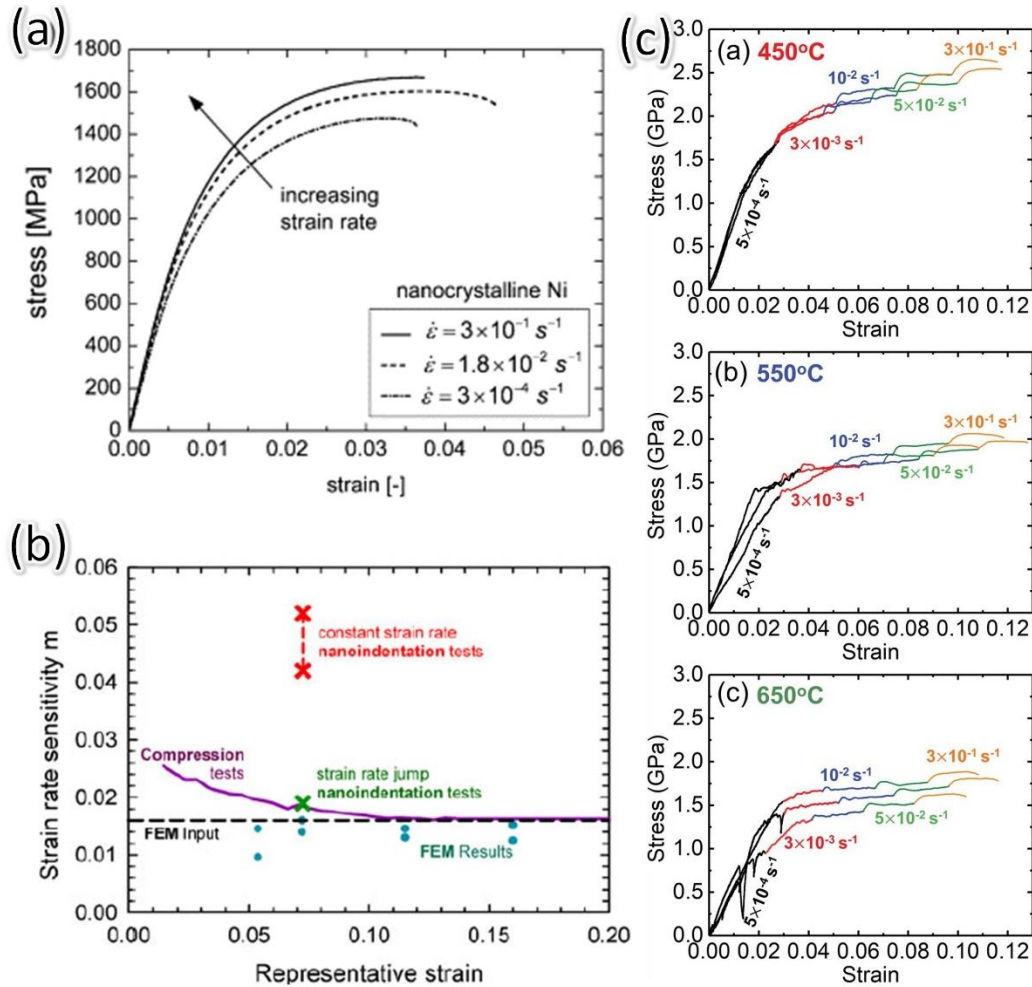
Figure 1-16. Results from strain rate sensitivity experiments revealing higher flow stresses at higher strain rates in (a) conventional tension testing of nanocrystalline Ni, (b) strain rate jump tests of nanocrystalline Ni performed using nanoindentation and (c) strain rate jump tests performed using *in-situ* micropillar compression tests of flash sintered yttria-stabilized zirconia. [88,96,97]

Improving *m* for metals is a major goal in metallurgy as it heightens the metals resistance to necking, improving its ductility. Strategies focused on enhancing dislocation activity promote higher SRS, such as precipitates in a 5A06 Al alloy promoting cross slip and the formation of dislocation forests. This enhanced strain hardening combats strain softening, which in turn suppresses necking and produces a larger *m* value [98]. Another thrust focuses on restricting grain size into the ultra-fine grained and nanocrystalline regimes, and severe plastic deformation (SPD) is a popular methodology to achieve these unique microstructures [99–101]. Smaller grains prevent full dislocation activities from operating, leading to the activation of grain boundary and diffusion

based mechanisms as the strain rate is increased. Wei et al. developed a descriptive model that describes the influence of grain size on the SRS exponent for FCC metals:

$$m = \frac{kT}{\xi b} \cdot \frac{1}{\chi(\alpha\mu b\sqrt{\rho}d)+\beta\sqrt{d}},$$ (1-11),

where k is Boltzmann's constant, b is the Burgers vector, μ is shear modulus, ξ is distance swept by a glide dislocation, and α, β, and χ are proportional factors [102,103]. This model clearly captures the expected trends seen in Figure 1-17 for both ultra-fine grained (UFG) and NT materials. Figure 1-17(a) demonstrates the efficacy of twin boundaries for improving both the strength and ductility of Cu [104].The generation and mobility of partial dislocations from kinks in coherent twin boundaries carries additional plasticity, preventing necking and improving *m*. Additionally, the reduction in activation volume (ξ) also increases *m*. Figure 1-17(b) is a micrograph depicting the high levels of dislocation activity surrounding the nanotwinned Cu microstructure [104]. UFG Al exhibits a similar trend as its SRS far outperforms the coarse grained (CG) counterpart, with Figure 1-17(c) demonstrating this trend, and Figure 1-17(d) contains a TEM micrograph showing the equiaxed, UFG microstructure [105]. Tailoring microstructure and defect structure within nanocrystalline materials provides an avenue for fabricating high strength materials with improved resistance to necking and fracture.
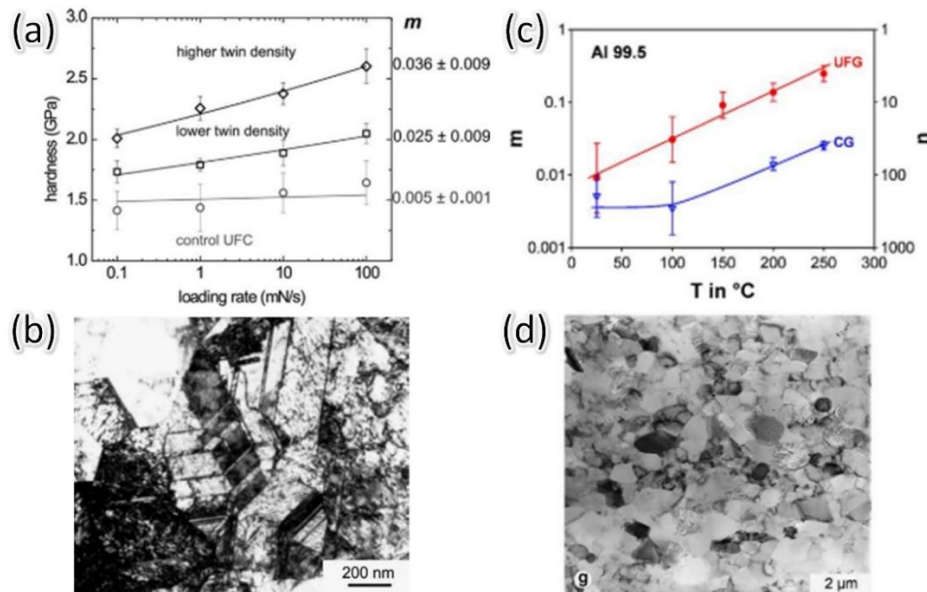
Figure 1-17. (a) Change in hardness as a function of loading rate with the corresponding strain rate sensitivity (*m*) for nanotwinned and ultra-fine grained Cu. (b) Micrograph of post deformed nanotwinned Cu with extensive dislocation activity leading to improved *m*. (c) Progression of *m* with increasing temperature for ultra-fine grained and coarse grained pure Al. (d) As heat treated microstructure of severely deformed pure Al revealing ultra-fine grains (below 1μm) [104,105]
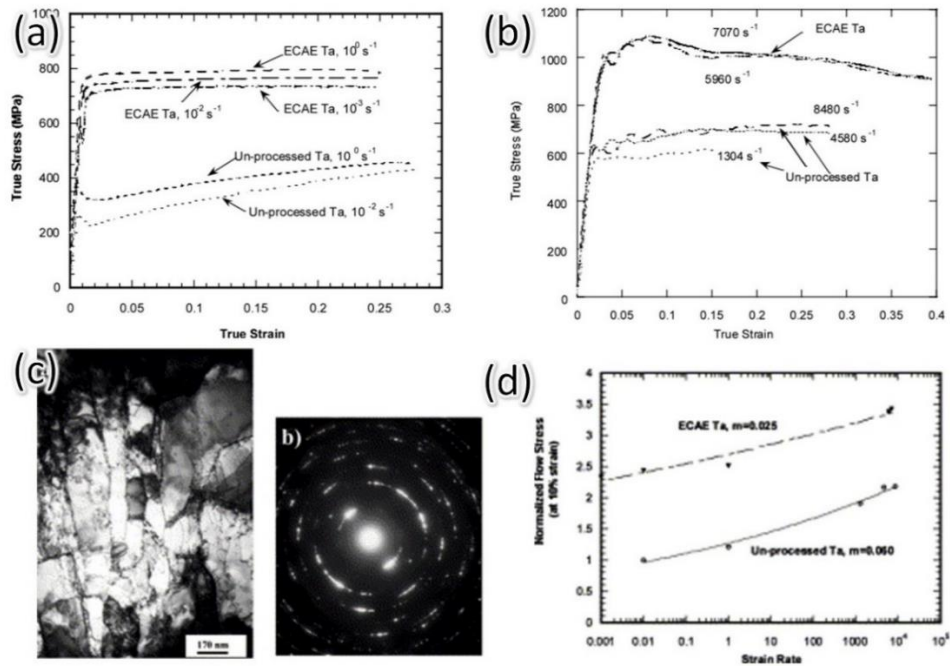
Figure 1-18. (a) True stress – true strain (b) True stress – true strain curves from kolsky bar tests at high strain rates revealing higher strain rates and ductility at extremely high strain rates. (c) Microstructure of Ta processed by Equal Channel Angular Extrusion (ECAE) revealing a microstructure of elongated ultra-fine grained. (d) Comparison of the flow stress evolution with strain rate between unprocessed and ECAE processed Ta [106]

Extremely high strain rates ($10^2 – 10^4$ s^{-1}) have generated interest in applications requiring high strength materials subjected to rapid strain (i.e., armor, high speed machining), and Kolsky bars enable dynamic tension tests at these strain rates. Deforming a metal this rapidly alters the plasticity mechanisms from conventional thermally activated mechanisms to thermal-phonon resisted motion of dislocations [87]. Materials often see simultaneous boosts in flow strength and ductility in this strain rate regime. Wei et al. compared static tension tests of Ta, presented in Figure 1-18(a) to dynamic Kolsky bar tension test in Figure 1-18(b) and identified a notable difference in the stress-strain curves [106]. The UFG Ta was produced using ECAE and is composed of elongated grains (~200 nm) and the microstructure is presented in Figure 1-18(c). This material presents a traditional response to increased strain rate in static tension tests (Figure 1-18(a)) with minor increments in flow stress with increasing strain rate. The flow stress continues to increase with increasing strain rate in the Kolsky bar tests, however interestingly the elongation to failure also increases. This presents another example of the importance of understanding the response of materials to different strain rates and the significant differences in mechanisms operating in different strain rate regimes.

1.4   Thermal stability of metallic materials

The ability of a material to maintain its structural integrity and properties during operation at elevated temperatures is especially relevant to metals with low melting temperatures (T_m), such as Al (T_m ~660 °C), with well documented poor thermal stabilities [91,107–109]. Since recrystallization occurs at temperatures at ~0.3-0.5 T_m, the operation range for Al alloys is severely limited above ~200 °C. Heating above this range leads to solute redistribution and segregation as well as the coarsening of both grains and precipitates, compromising strength. Figure 1-19(a) shows the progression of ultimate tensile strength for a precipitation strengthened Al6061-T6 alloy when tested at temperatures ranging from cryogenic to 400 °C [110]. This highlights the poor thermal stability exhibited by a majority of Al alloys as softening is induced even after annealing at 200 °C for 0.5h, and drastic softening occurs after annealing at 150 °C for any extended period of time. Figures 1-19(b-d) details the microstructural evolution of an ultra-fine grained (UFG) Al2024 alloy prepared by equal-channel angular pressing (ECAP), with significant recrystallization identified after annealing at 200 °C for 1h [109]. In comparison, oxide disperse strengthened (ODS) steels can often operate above 700 °C with minimal recrystallization or microstructural change, which is depicted in Figure 1-20 [111].
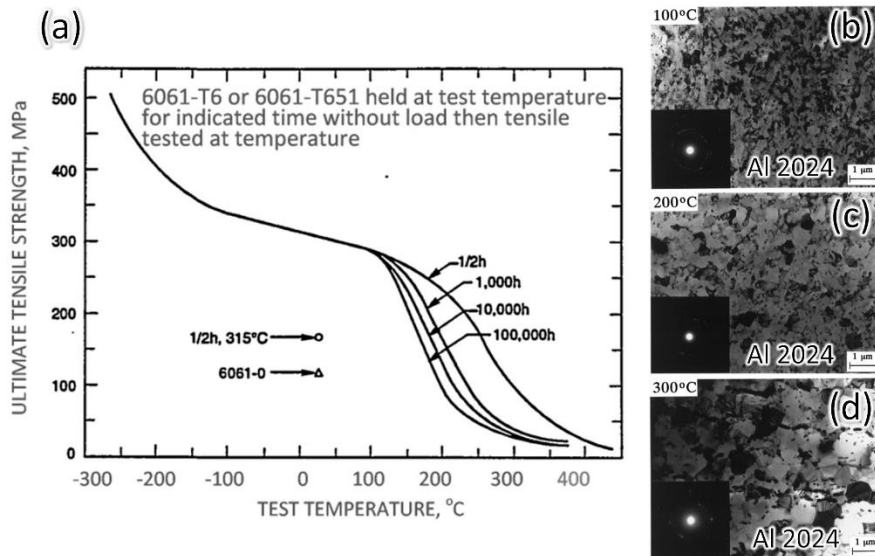
Figure 1-19. (a) Progression of Al6061-T6 ultimate tensile strength (σ_{UTS}) when tested at increasing temperatures. (b-d) Significant recrystallization and grain coarsening in an ultra-fine grained Al 2024 alloy prepared using Equal-channel angular pressing (ECAP). Micrographs taken after annealing at (b) 100 °C, (c) 200 °C and (d) 300 °C for 1 hour. [109,110]
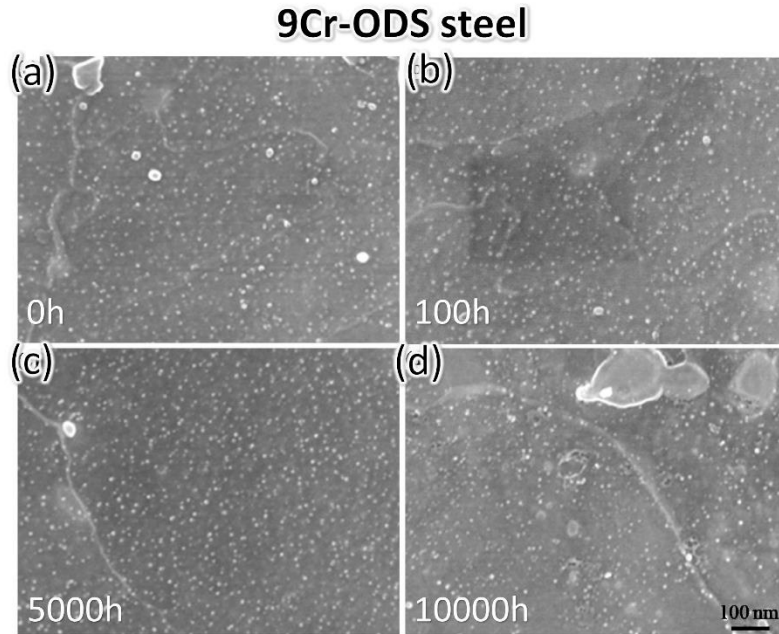
Figure 1-20. Microstructural evolution depicted using scanning transmission electron microscopy (STEM) of a 9Cr-ODS steel revealing relatively no change in precipitate/oxide size or distribution after annealing at 700 °C for (a) 0h, (b) 100h, (c) 5,000h and (d) 10,000h. [111]

The continued development of nanocrystalline materials is impeded by one significant deficiency in spite of their impressive as-processed properties: structural stability. Far-from-equilibrium processing, such as severe plastic deformation (SPD) [112,113], magnetron sputtering [114] and high energy ball milling [115–117], is often needed to trap high energy nanostructures. Multiple studies have documented grain coarsening occurring in nanocrystalline metals at ambient temperatures and when exposed to low external stresses [107,118,119]. This mechanical and thermal instability is more sensitive for nanocrystalline Al alloys with already poor inherent thermal stability. Developing materials composed of thermally stable nanograins is a mammoth task due to large inherent grain boundary energies promoting significant instability. Multiple approaches have emerged that successfully stabilize these nanostructures and overcome the massive driving force for grain coarsening. These can be categorized by either (1) classical approaches to kinetically pin grain boundaries using small particles as obstacles to boundary migration (Zener pinning), or (2) thermodynamically stabilizing the boundaries themselves through solute segregation or grain boundary engineering.

First, Zener pinning is a long used strategy utilizing both solute atoms and second phase particles to kinetically obstruct the motion of grain boundaries. Titanium diboride (TiB_2) has been

extensively used in as an inoculant in a variety of Al alloys [120,121]. These particles introduce a "drag force" to grain boundary motion during solidification that slows down their motion and prevents grain coarsening. Figure 1-21(a-e) contain micrographs and resulting grain size measurements demonstrating the potent grain refining effect of TiB_2 on an Al-Zn-Mg-Cu alloy as even a fraction of a percent drastically changes the grain size [122]. This idea can easily be extrapolated to stabilizing nanocrystalline metals as both solute and nanoprecipitates can prevent grain growth. Figure 1-21(f-i) provides an example of a ball-milled nanocrystalline Fe-Cr alloy that is stabilized by Hf solute additions [123]. Precipitation and solute segregation kinetically pin the nanograins up to 1000 °C, which is remarkable in an alloy with such fine grains (~50nm).
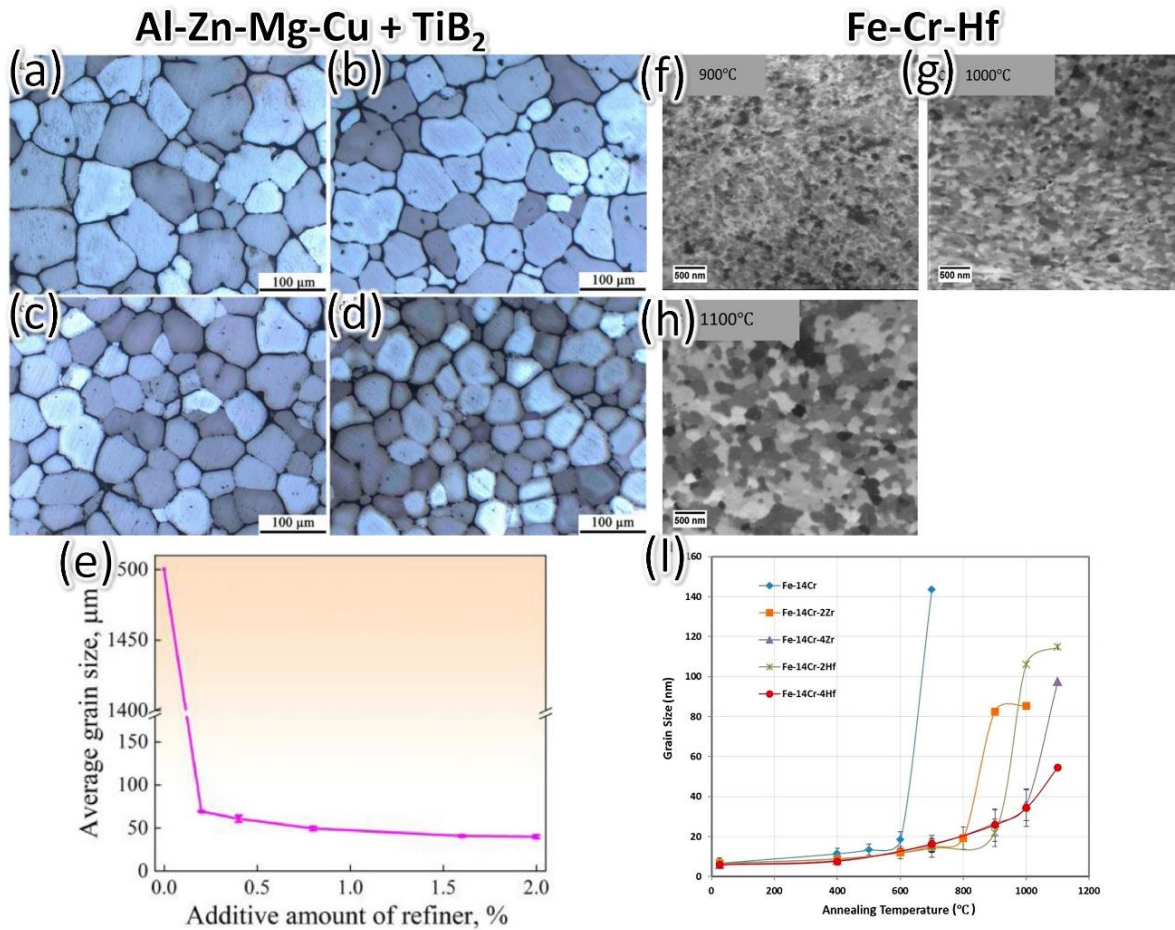
Figure 1-21. (a-d) Optical micrographs of an etched, cast Al-Zn-Mg-Cu alloy revealing the grain morphologies with additions of (a) 0.2%, (b) 0.4%, (c) 0.8% and (d) 1.2% Al-5Ti-1B. (e) Plot of the resulting grain sizes from (a-e) as a function of amount of Al-5Ti-1B refiner. (f-h) FIB channeling contrast images revealing the microstructure of ball-milled Fe-14Cr-4Hf alloys after 1 hour annealing at (f) 900 °C, (g) 1000 °C and (h) 1100 °C. (i) Grain size evolution as a function of annealing temperature for various Fe-14Cr-xHf alloys. [122,123]

Second, more recent attempts have focused on tailoring the inherent grain boundary energy through solute segregation and grain boundary engineering. These strategies focus on minimizing the inherent driving force for grain coarsening instead of simply blocking grain boundary motion. Weissmüller presented a thermodynamic concept that alloys with large heat of segregations would exhibit solute segregation with the potential of reducing grain boundary energy [124]. Further research built upon it with multiple thermodynamic models, simulations, and experiments underscoring the effectiveness of this strategy [125–132]. Essentially, solute decorates grain boundaries within nanocrystalline materials and lowers the excess energy, producing a more stable nanostructure. Figure 1-22(a) provides a "stability map" to solute selection in tungsten-based binary alloys where solutes with high enthalpy of segregation and low enthalpy of mixing promote stable nanocrystalline alloys [133]. This map is based on thermodynamic criterion and specific solutes are able to reduce the system energy enough to produce thermally stable nanocrystalline materials, specifically W-Ti alloys [133]. Additional examples are presented in Figures 1-22(b-d) where specific solute selection significantly enhances thermal stability [126,131]. Similarly, engineering grain boundaries with lower inherent energies can also provide similar levels of thermal stability in nanocrystalline alloys [134–136].
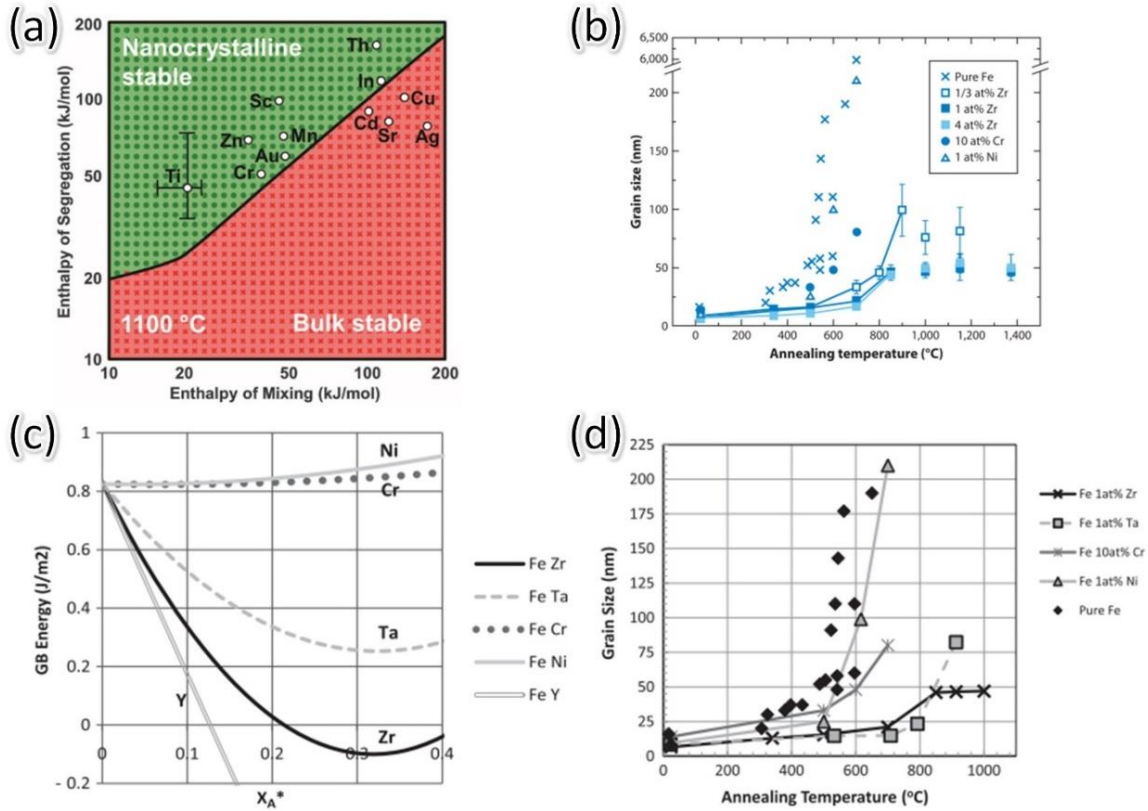
Figure 1-22. (a) Nanostructure stability map for binary W-based alloys determined on the basis of varied enthalpy parameters. (b) Grain size measurements for various Fe based binary alloys as a function of annealing temperatures identifying which systems are the most thermally stable. (c) Calculated GB energies for Fe based alloys with Ni, Cr, Ta, Zr and Y solute additions revealing which minimize boundary energy. (d) Corresponding grain size map for (c) identitifying Ta and Zr solute provides the most significant microstructure stabilization. [126,131,133]

Since recrystallization and grain coarsening (Ostwald ripening) are both diffusion-based processes, an in depth assessment of elemental diffusivities in Al provides a strong launching off point for predicting thermal stability of Al alloys. This also provides a direction for improving the thermal stability of the nanotwinned Al alloys studied in this thesis as well as a roadmap for future exploration. The data organized in the review by Czerwinski aided in the development of this collection and provides more in depth analysis of the thermal stability of various Al alloy systems [110]. Diffusion is accommodated through the thermally activated movement of atoms and vacancies throughout the lattice, and as a result solute atoms with different atomic radii and activation energies will diffuse at different rates. Typically, atoms with lower solubilities in Al will have lower diffusivities in Al leading to the formation of undesirable second phases and segregation [137]. However, a tradeoff exists as these elements also promote improved thermal stabilities because of their low diffusivities and strategies to incorporate them in future Al alloys

55

(such as the super saturated solid solutions presented in this thesis) are desirable. Figures 1-22(a-b) present the compiled diffusion data organized in the review by Czerwinski, with the Table 1-4 presenting the data plotted in Figure 1-23 and adapted from [110]. Notably, transition metal solutes such as Mo, Nb, V, Ti and Zr have significantly reduced diffusivities in Al compared with other solutes (such as Si and Mg which have higher diffusivities in Al than Al self-diffusion). This aligns well with previous studies on nanotwinned Al ternary alloys as both report significant boosts in thermal stability with the incorporation of Ti (Al-Fe-Ti and Al-Ni-Ti) [138,139]. These findings raise questions on other solutes similar to Ti: will they facilitate the formation of twins while also improving thermal stability? This provides the motivation for the exploration of Zr solute in nanotwinned Al alloys and is addressed at length in this thesis.
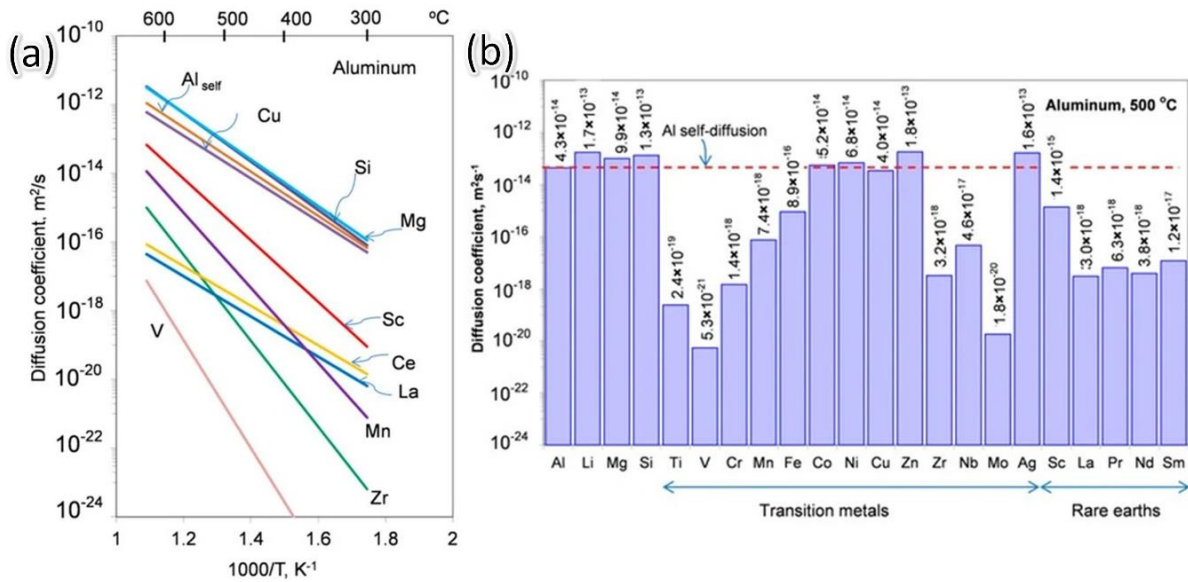
Figure 1-23. (a) Diffusion coefficient (D) data for a range of solute elements within Al as a function of temperature. (b) D plotted for various solute elements all compared for diffusion in Al at 500 °C. [110]

56

Table 1-4. Collection of diffusion coefficient data for various solute elements in Al

Element	Diffusion coefficient (at 500 °C)	Activation energy (kJ/mol)	Temperature range (°C)	References
Al (self-diffusion)	5.7×10^{-14}	124	227-527	[140]
Li	1.11×10^{-13}	126.1	150-240	[141]
Si	1.3×10^{-13}	136	480-620	[142]
Mg	1.05×10^{-13}	115	-	[143]
Transition metals				
Ti	2.38×10^{-19}	261.5	-	[144]
Zr	3.2×10^{-18}	242	531-640	[110]
V	5.18×10^{-21}	241	Calculated	[144]
Nb	4.61×10^{-17}	82.22	350-480	[145]
Cr	2.24×10^{-18}	199.7	Calculated	[146]
Mo	1.79×10^{-20}	250	-	[110]
Mn	5.73×10^{-17}	211	460-660	[147]
Fe	8.95×10^{-16}	190	-	[148]
Co	8.57×10^{-14}	168	-	[110]
Ni	6.83×10^{-14}	144.7	-	[148]
Cu	9.06×10^{-13}	113.8	Calculated	[144]
Ag	1.61×10^{-13}	116.4	Calculated	[149]
Zn	1.80×10^{-13}	120.7	-	[150]
Rare earth metals				
Sc	9.2×10^{-16}	176	400-450	[151]
La	3×10^{-18}	113	-	[152]
Ce	5.69×10^{-18}	111.3	450-630	[152]
Pr	6.35×10^{-18}	99.9	520-630	[152]
Nd	3.85×10^{-18}	105	450-630	[152]
Sm	1.18×10^{-17}	95.7	-	[152]

1.5 Twin boundaries in metals

Twin boundaries are a specific type of ordered grain boundary characterized by its mirror symmetry. These boundaries are highly coherent as there is little to no atomic misfit, and as a result possess the lowest inherent grain boundary energy among various CSL boundaries. Twins are highly sought after due to both their strengthening benefits and the lack of tradeoff between strength and ductility, conductivity and thermal stability. As a result, significant attention has been given to twin boundaries, especially nanostructures composed of twins (nanotwinned materials), over the past few decades.

1.5.1   Types of twins

Twin boundaries (TBs) are often categorized by their formation mechanism: (1) Annealing twins, (2) Deformation twins, and (3) Growth twins. Although formed through different methods, the atomic structure is consistent across all three mechanisms. In terms of crystallography, there are two further designations that can be made depending on the specific crystallographic plane the twin is aligned with. TBs with a {111} habit plane are considered $\Sigma 3$ coherent twin boundaries (CTBs) and they separate two perfect crystals with mirror symmetry. Figure 1-24(a) provides an example of a CTB and 1-24(b) depicts the atomistic coherency of this structure in an electrodeposited nanotwinned (NT) Cu sample using HRTEM [153]. In comparison, TBs that form along a habit plane of {112} are considered $\Sigma 3$ incoherent twin boundaries (ITBs) and Figure 1-24(c) contains an example of an ITB replicating from a low SFE Ag layer into a high SFE Al layer enabled by epitaxial growth in Ag/Al multilayers [154]. ITBs are fundamentally different than CTBs in that they are composed of an array of partial dislocations instead of a coherent, perfect lattice with mirror symmetry. Figure 1-24(d) presents this stacking fault array schematically based on simulations and HRTEM evidence [155]. Each example from Figure 1-24 represents types of growth twins. The atomic structure of the ITB has been debated and the accepted model is that ITBs are composed of a periodic array of 3 Shockley partial dislocations with a $b_2:b_1:b_3$ arrangement involving 3 adjacent {111} planes [155–159]. The b_2 and b_3 Shockley partials are relatively immobile mixed dislocations with 1/6 $[\overline{2}11]$ and $1/6[1\overline{2}1]$ Burgers vectors, respectively. The b_1 Shockley partial is a pure edge dislocation with a Burgers vector of $1/6[11\overline{2}]$. b_1 is able to glide due to a smaller Peierls barrier, leading to diffuse ITBs, or 9R phase [155].
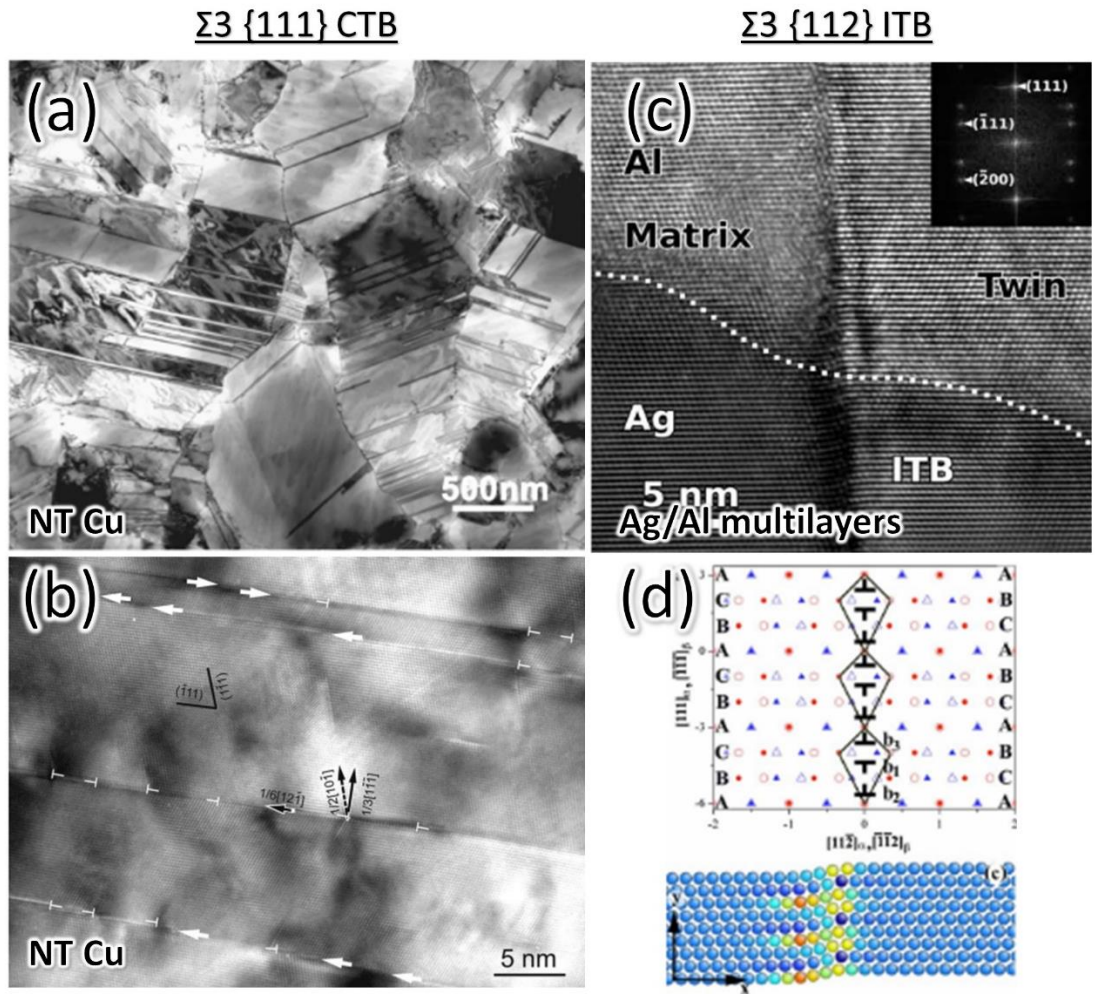
Figure 1-24. (a) BF-TEM micrograph of NT Cu revealing an abundance of finely spaced CTBs within randomly oriented polycrystalline grains, with (b) providing an atomistic view through HRTEM analysis of CTBs. (c) HRTEM image of an ITB replicating from a low SFE Ag layer into a high SFE Al layer. (d) Atomistic simulations and dichromatic pattern identifying the partial dislocation array composing ITBs. [153–155]

59

Annealing twins are the result of recrystallization processes occurring in metals with a low SFE. These defects were first identified in sluiced gold as early as 1897 and have since been identified in multiple FCC metals [160]. The density of annealing twins is related to the metals stacking fault energy, grain size, plastic strain and annealing temperature and has a direct impact on mechanical properties. When metals are plastically deformed, they accumulate strain energy, and annealing at elevated temperatures provides the energy to drive recrystallization and facilitate energy minimization. This has been widely accepted as the driving force behind the formation of annealing twins as they inherently have lower boundary energy than conventional high angle grain boundaries. The formation mechanism however is still debated, with three main competing theories. The first theory can be described as the "Grain Encounter" model as it suggests grain boundary migration leads to the intersection of two grains that happen to have twin orientation. The boundary then reorients itself, becoming a CTB. The second theory hinges on the formation of stacking fault packets during grain boundary migration, leading to their propagation and formation of CTBs within grain interiors. Although these theories can explain portions of the annealing twin phenomenon, they both lack significant experimental evidence to support the claims. The third theory proposes grain boundary ledges form as a result of "growth accidents" which provides sites for the generation and propagation of partial dislocations/stacking faults [161]. This model does not require the need for grain boundary migration similar to the first two theories and has plenty of supporting evidence [161–165]. Mahajan et al. provided support for this by demonstrating annealing twins can be introduced through the nucleation of partial dislocations on adjacent {111} planes through growth accidents [163]. Figure 1-25(a) provides an example of annealing twins forming in a deformed and annealed CrCoNi [166]. Figure 1-25(b) demonstrates the grain size dependence of annealing twin density with more annealing twins forming in finer grained materials, which supports the theory of "growth accidents" facilitating twin formation [167]. Figure 1-25(c) demonstrates a similar grain size trend in addition to increasing annealing twin density at higher levels of cold work [167].

60
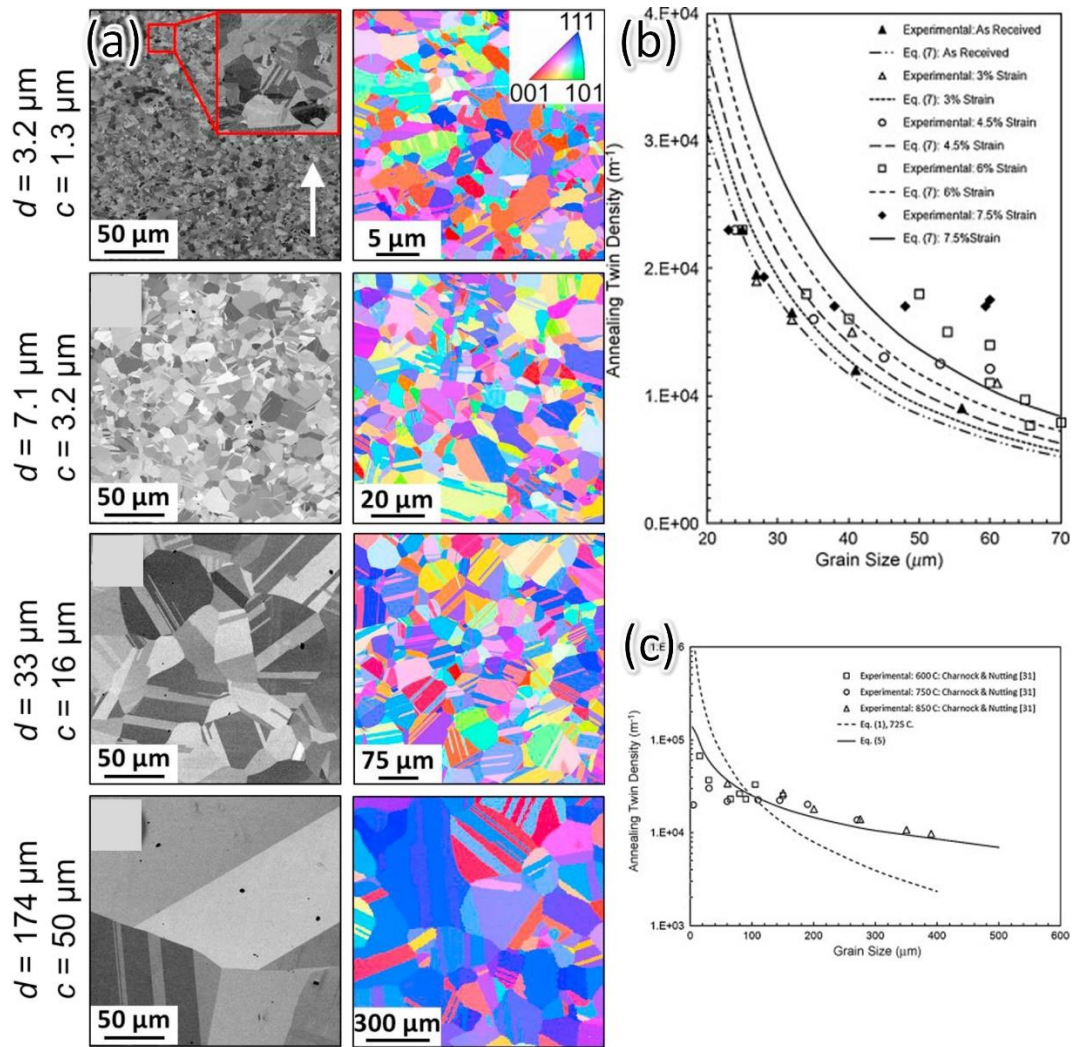
Figure 1-25. (a) Annealing twins identified using EBSD in a CrCoNi high entropy alloy as a function of starting grain size. Annealing twin density as a function of (b) grain size and (c) percent cold work in Cu and Ni, respectively. [166,167]

Deformation twinning is a mode of plastic deformation that accommodates additional plasticity when dislocation slip is insufficient, such as when few slip systems are active, when deformed at high strain rates, or when tested at low temperatures. As a result, deformation twins are heterogeneously distributed throughout the material and often nucleate from locations of high stress, such as crack tips, dislocation pileups, or grain boundaries. Deformation twins are more common in body centered cubic (BCC) metals, hexagonal close packed (HCP) metals, and various ordered compounds, but have also been identified in FCC metals albeit with lower frequency. HCP metals and ordered compounds exhibit twinning as a major carrier of plasticity and their complex crystallography facilitates more modes of twinning, however this will not be discussed at length here. Twinning induced plasticity (TWIP) steels are a famous example of deformation twins enabling simultaneous high strengths and plasticity in low SFE FCC metals. This brief overview focuses on FCC deformation twinning due to the relevance to this thesis. Deformation twinning is less well understood than conventional dislocation slip, and different twinning modes are still being investigated. Twinning follows a multi-step procedure including twin nucleation, propagation and thickening. In FCC metals, full dislocation glide is carried through the emission and propagation of Shockley partial dislocation pairs, and the spacing between these partials (w) influences their deformation mode. Reducing w leads to full dislocation slip instead of twinning. A key parameter governing this spacing is the intrinsic SFE, depicted as γ_1 in the generalized planar fault energy (GPFE) curve in Figure 1-26(a). Metals with lower γ_1 are more likely to deform through twinning as less work is needed to separate the leading and trailing partial dislocations. Metals with a low ratio of γ_1/γ_U are expected to have a higher ability to deform by twinning. Deformation twin nucleation is initiated from dislocation dissociation reactions that form twin dislocations, which are also Shockley partial dislocation on {111} twin planes (Burger's vector of $\frac{a}{6}\langle 112 \rangle$). These dislocations can initiate from various defects but are most commonly seen from slip dislocations or grain boundaries. Deformation twins then grow from the collective shear of twin dislocations through the parent lattice and are typically quite thin. Figures 1-26(b-d) highlight the benefit of deformation twinning in TWIP steels.
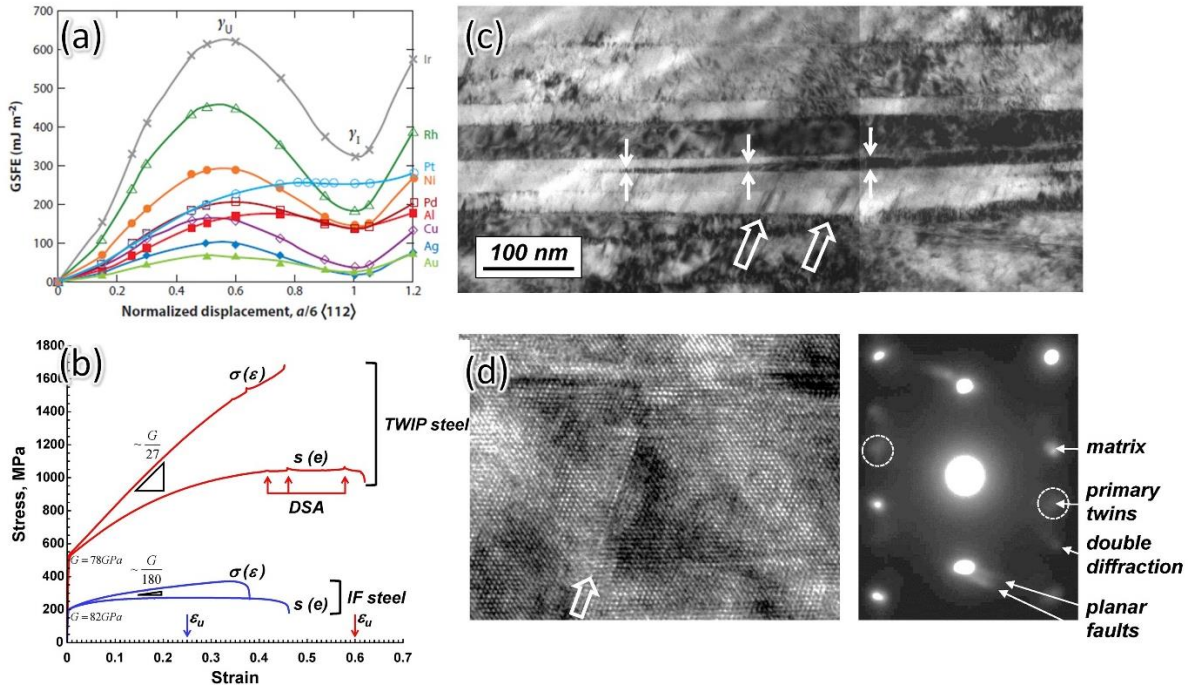
Figure 1-26. (a) Generalized planar fault energy (GPFE) curve for the {111} surface with the unstable stacking fault energy (γ_u) and intrinsic stacking fault energy (γ_1) labeled. This plot illustrates the energy barrier for Shockley partial motion along {111} planes. (b) Stress-strain curve comparing TWIP and interstitial free steels identifying the significant boost in strength and plasticity in TWIP steels. (c) TEM micrograph revealing multiple deformation twins in a TWIP steel after tension testing, with (d) corresponding HR-TEM imaging of the twin atomic structure. [168]
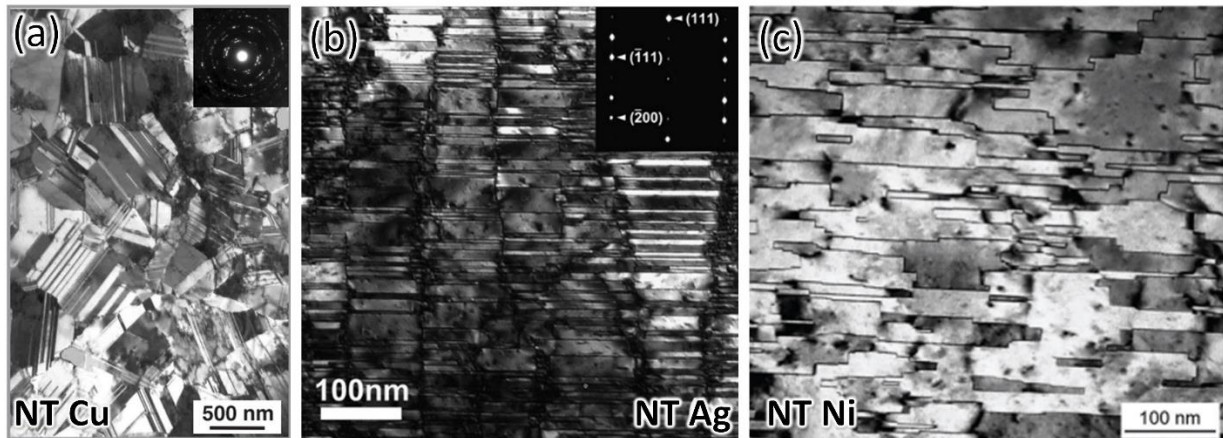
Figure 1-27. (a) TEM micrograph of finely spaced nanotwins dispersed among randomly oriented polycrystalline grains in electrodeposited Cu. (b) Finely spaced parallel CTBs in sputtered Ag. (c) Unique twin structure composed of both CTBs and ITBs in electrodeposited Ni. [169–171]

Growth twins are the result of far-from-equilibrium processes that thermodynamically trap a larger density of typically unstable TBs. Electrodeposition and magnetron sputtering are the

major workhorses of fabricating materials with a large density of growth twins. Similar to deformation twinning, the motion of Shockley partial dislocations during film growth leads to the formation of faults in the FCC stacking sequence, leading to twin formation. Increasing deposition rate leads to a corresponding jump in twin density as the frequency of {111} fault formation increases. This trend is exhibited in both electrodeposited (Figure 1-27(a, c)) and sputtered (Figure 1-27(c)) coatings with unique microstructures capable of forming TBs [169–171]. The large increase in twin density facilitates boosts in strength and thermal stability, which are typically mutually exclusive. Growth twin formation in sputtered coatings has been modeled thermodynamically and twin propensity is dependent on critical radius nucleation energy. Perfect ($r^*_{perfect}$) and twin (r^*_{twin}) nucleus radii can be calculated with the following:

$$r^*_{perfect} = \frac{\gamma}{\left(\frac{kT}{\Omega} \ln\left[\frac{J\sqrt{2\pi mkT}}{P_S}\right]\right)} \tag{1-12}$$

$$r^*_{twin} = \frac{\gamma}{\left(\frac{kT}{\Omega} \ln\left[\frac{J\sqrt{2\pi mkT}}{P_S}\right] - \frac{\gamma_t}{h}\right)} \tag{1-13}$$

where γ is the surface energy, k is Boltzmann's constant, T is temperature during deposition, Ω is the atomic volume, J is deposition flux, m is the atomic mass of the deposited element, P_s is the vapor pressure at the film surface, γ_t is the twin boundary energy, and h is the twin nucleus height. These equations illustrate the dependence of propensity for twin formation on deposition rate (J) and the substrate temperature (T). Additionally, the SFE (γ_t) is an important parameter dictating twin formation. Equation 1-13 clearly demonstrates how a higher SFE leads to larger critical nuclei, meaning twinned nuclei are less likely to form.

1.5.2 Nanotwinned metals: high strength and ductility

Regardless of formation mechanism, TBs can obstruct the motion of slip dislocations leading to increased hardening. Similar to Hall-Petch strengthening, refining twin spacing is a simple method to further enhance mechanical properties. This section will focus on understanding the mechanical response of growth twins in FCC metals as they are the most relevant to the work conducted in this thesis. As mentioned previously, electrodeposition and magnetron sputtering are highly efficient at introducing an abundance of nanotwins into metals with low SFE. Anderoglu et al. demonstrate extremely fine CTBs oriented perpendicular to the growth direction, surrounded by high angle columnar grain boundaries (Figure 1-28(b)) [172]. The twin spacing averages ~10

nm and leads to high hardness as dislocation motion is extremely limited, depicted in the Hall-Petch plot in Figure 1-28(a) [172]. This study also identified improved electrical resistivity and thermal stability due the coherency of CTBs, far outperforming NC Cu counterparts. Additionally, twin spacing (d_{twin}) in electrodeposited Cu can be tailored by controlling the deposition rate. Figure 1-28(d) shows the microstructure NT electrodeposited Cu with a d_{twin} of ~100nm [173]. A network of finely CTBs dispersed among randomly oriented polycrystalline grains induces hardening with decreasing d_{twin} until a critical d_{twin} is reached, upon which high levels of plasticity and softening are observed. This softening can be clearly seen in the true stress – true strain curves in Figure 1-28(c) and is attributed to an increase in partial dislocation density in coatings with finer d_{twin}. These partial dislocations originate from steps formed during deposition along CTBs, and finer twin spacing produces a larger fraction of partials that carry high levels of plasticity and induce softening. The resulting stacking faults are shown in the HRTEM image in Figure 1-28(e) [173].
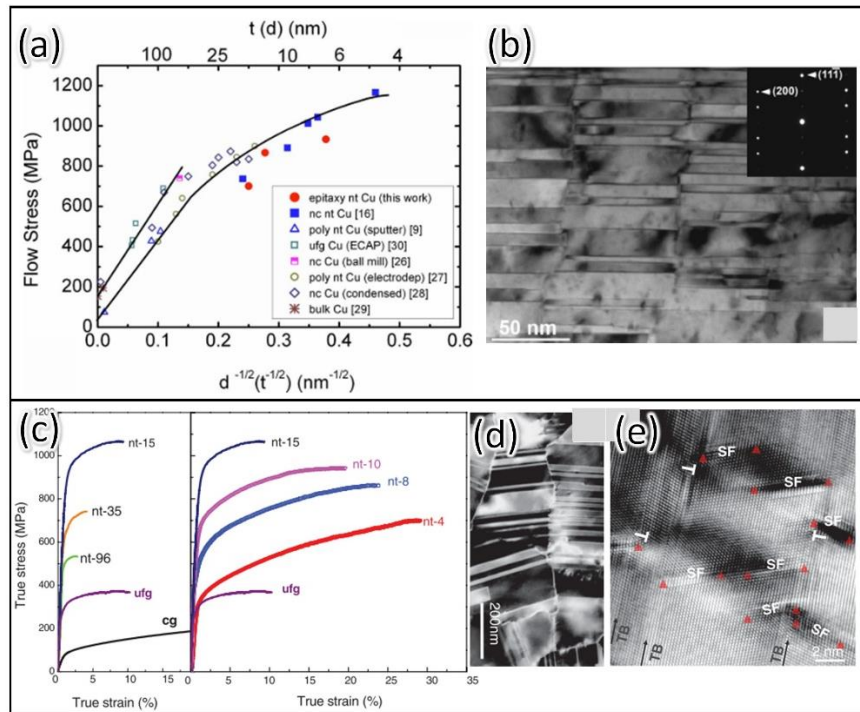
Figure 1-28. (a) Hall-Petch plot demonstrating the improvement of NT Cu deposited using magnetron sputtering over electrodeposition and other NC Cu materials. (b) BF-TEM micrograph revealing the fine, parallel NT microstructure in sputtered Cu. (c) True stress – true strain curves for NT Cu fabricated by electrodeposition. Samples are classified by their twin spacing, X (nt-X) and demonstrate the improved strength and ductility until the critical twin thickness at X=15nm, upon which softening and significant plasticity are initiated. (d) As-deposited microstructure of electrodeposited NT-Cu with finely spaced CTBs dispersed among randomly oriented polycrystalline grains. (e) Post-deformed microstructure revealing extensive partial dislocation activity and stacking faults in the nt-15 sample from (d). [173–175]

The mechanisms governing hardening in NT metals have been probed using *in-situ* TEM nanoindentation experiments [156,157,174–177] as well as MD simulations [159,178–180]. Twin boundaries behave similar to grain boundaries at obstructing dislocation motion; however, twins are more effective at preventing dislocation transmission into neighboring grains. Additionally, dislocation–CTB interactions have been modeled and uncover the role CTBs play in hardening and plasticity. Figure 1-29(a-b) contain snapshots from MD simulations of a screw dislocation interacting with a CTB in (a) pure Al and (b) pure Cu [179,180]. In the Al case, an applied shear stress constricts and recombines the leading and trailing partial at the CTB interface (t = 0.5ps), and then the screw dislocation dissociates along the CTB plane (t = 1.3ps). A resolved shear stress of ~100MPa is needed in order to recombine the partials. In comparison, Figure 1-29(b) depicts the screw dislocation cutting through the CTB in Cu and propagating into the twinned lattice. The difference in behavior can be attributed to the materials SFEs, specifically the aforementioned γ_1 and γ_{twin} from Figure 1-26(a) [181]. In Al, $\gamma_{twin} > \gamma_1$, meaning the screw dislocation will spontaneously dissociate at the CTB, as demonstrated in the MD simulations in Figure 1-29(a) [179]. This is not the case in Cu or Ni, enabling the screw dislocation to dissociate into partials after cutting through the CTB. These phenomena all operate at relatively high critically resolved shear stresses (100-400MPa) underscoring the efficacy of CTBs for obstructing dislocation motion [179]. These mechanisms also demonstrate the ability of CTBs to facilitate plasticity in addition to imparting high strengths. Zhang et al demonstrated similar behavior using MD in stainless steel with a resolved shear stress of 1.77GPa required for dislocation transmission, shown in Figure 1-29(c) [178]. These simulations were performed at 0K, which leads to an inflated resolved shear stress, however the behavior still indicates CTBs are highly effective boundaries for strengthening. Further simulations have characterized the interaction of non-screw dislocations with CTBs, and the complexity expands due to the possibility of cross slip onto more paths [180].
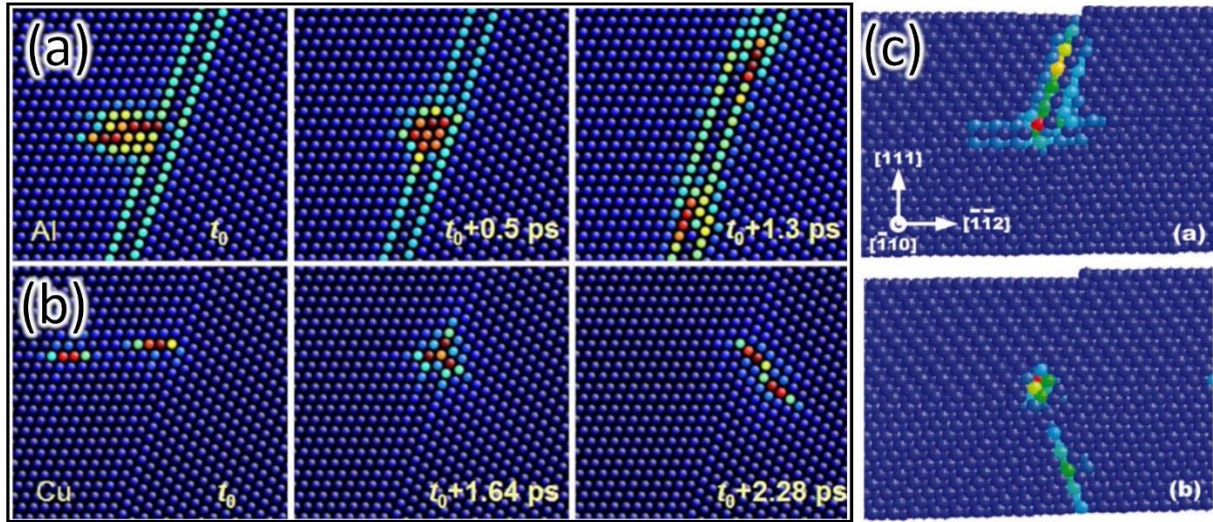
Figure 1-29. Molecular dynamics (MD) simulation snapshots identifying the interaction mechanisms between screw dislocations and CTBs in (a) Al and (b) Cu. MD simulation snapshots revealing the impressive barrier strength of perpendicularly oriented CTBs to dislocation propagation in stainless steel. [179,180]

Twin orientation is another factor influencing resulting mechanical properties as nanotwinned metals behave anisotropically. The electrodeposited NT Cu and Ni presented in Figures 1-27 and 1-28 are randomly oriented and do not exhibit anisotropic mechanical response as a result. Figure 1-30(a) contains schematics detailing CTB and grain boundary orientations in Cu simulated using MD, with the 90° case resembling sputtered NT Cu (Figure 1-28(b)) [80,182]. Depending on the orientation of the CTBs (0°, 90°, or 45°), plasticity is carried from different types of dislocations. All angles are given in relationship to the vertical axis (growth direction). For example, Figure 1-30(b-c) reveal the 90° case operates in the "hard" mode for dislocation motion since the slip planes are inclined to the horizontal CTBs. The CTBs completely obstruct dislocations from transmitting across the boundary except under large-applied stresses. This leads to the high strengths captured from finite element modeling (FEM) and MD. The 0° case leads to hairpin dislocations bowing out between the vertically oriented CTBs. The "soft" mode occurs in the 45° case as junctions between the inclined CTBs and the GBs act as nucleation sites for dislocations. The slip planes are now oriented parallel to the CTBs, so they are free to glide throughout the lattice, resulting in the low stresses seen in Figure 1-30(b-c) [182]. One characteristic of MD is the extremely high strain rates due to the short simulation times, which could influence the plasticity mechanisms seen in this study [182]. Li et al were able to experimentally probe the anisotropic behavior using micromechanical testing of NT Al-Fe alloys

with a thin spacing of 22nm [183]. Figure 1-30(d) contains SEM images and schematics detailing the test directions and micromechanical setup [183]. The difference in flow/fracture stress is obvious from Figure 1-30(e) as when tested in the out-of-plane orientation (parallel to the ITBs), higher strengths are achieved than the in-plane orientation (orthogonal to the ITBs). Additionally, expanded levels of plasticity are identified in the out-of-plane samples as dislocations and Shockley partials are able to carry plasticity. Shear banding is identified in the in-plane compression sample, with the in-plane tension sample failing catastrophically. The capability of fabricating ductile NT Al is still under question as neither tension test demonstrated the same levels of plasticity as the compression samples, and future work is needed to achieve this goal.
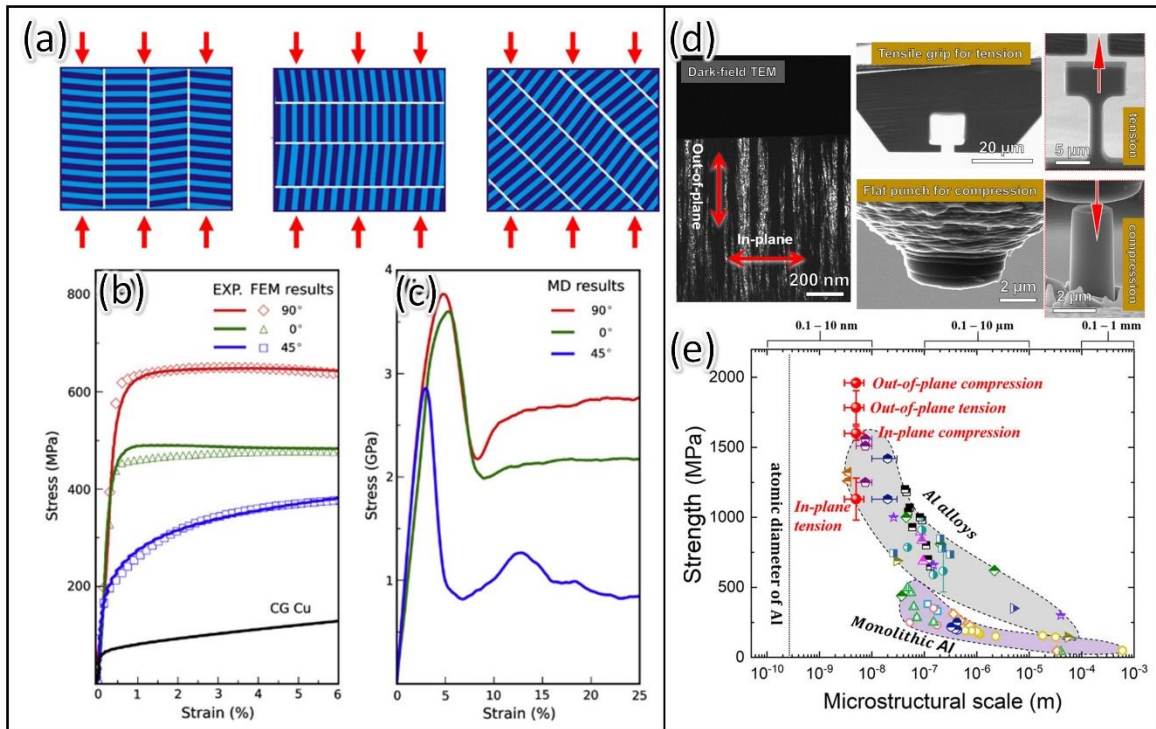
Figure 1-30. (a) Schematics detailing the corresponding twin orientations for 0°, 90° and 45° orientations. (b-c) Stress strain curves revealing the mechanical response of the differently oriented twin microstructures in (a) simulated using (b) finite element modeling (FEM) and (c) MD. (d) Schematic and DF-TEM micrograph detailing the columnar nanotwinned microstructure in NT Al-Fe and the corresponding micromechanical test setups for in-plane and out-of-plane tension/compression. (e) Plot comparing the strengths from the micromechanical tests in (d) with various literature Al alloys as a function of microstructural scale. [183,184]

1.5.3 Twins in Al: A rare phenomenon

A metal's stacking fault energy (SFE) represents the energy barrier for twin formation and metals with a lower SFE have a higher propensity for twin formation. TBs are incredibly rare in Al under equilibrium conditions mainly due to its relatively high SFE ($\sim$160 mJ/m^2). There are additional factors that influence the stabilization of TBs in Al, and a key factor is depicted in the generalized planar fault energy (GPFE) curve in Figure 1-31(a) [78]. This curve represents the energy penalty required to shift a (111) plane along the <112> direction, and γ_{USFE} in Figure 1-31(a) represents the energy required to produce a leading partial dislocation. The second hump represents the energy penalty required to form a twin boundary and this large energy penalty effectively blocks twin formation under equilibrium conditions [78]. Although incorporating a large % of solute into solution can lower these energy penalties, equilibrium processing only supports a fraction of a % meaning Al alloys also behave in this manner. Extreme conditions, such as in nanocrystalline Al (Figure 1-31(b)), at large stress regions ahead of crack tips (Figure 1-31(c)), or under shock loading (Figures 1-31(d-g)) are typically needed to stabilize even small twins in Al [185–187]. The MD simulations in Figure 1-31(f-g) confirm the stabilization of stacking faults in Al exposed to a shock wave, confirming the finding from high velocity projectile impact experiments [187]. Figure 1-31(e) shows a high density of localized stacking faults in Al after these impact experiments [187].
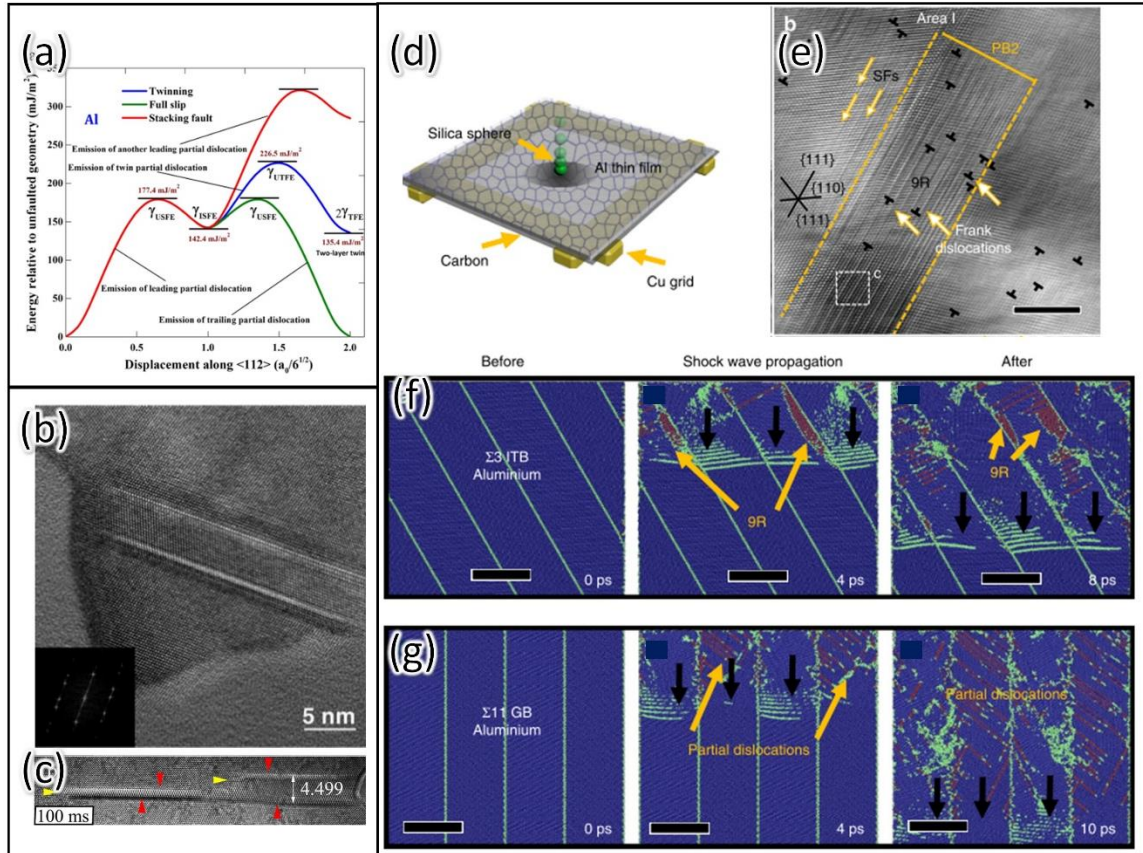
Figure 1-31. (a) Generalized planar fault energy (GPFE) curves for pure Al identifying the barriers to stacking fault and twin formation and stabilization. (b-c) HRTEM micrographs revealing deformation twins forming under extreme conditions in Al, including (b) nanocrystalline Al and (c) at a crack tip in Al. (d) Schematic detailing the high-velocity projectile impact experiments with silica microspheres impacting nanocrystalline Al. (e) HRTEM micrograph revealing the formation of a high density of stacking faults, Frank partial dislocations and 9R phase in Al after exposure to high velocity projectile impact testing. (f-g) MD simulations identifying the difference in 9R phase stability after the exposure of (f) $\Sigma 3$ ITBs and (g) $\Sigma 11$ GBs to a shock wave in Al. [78,187,188]

Recently, magnetron sputtering has provided another far-from-equilibrium processing method for stabilizing twin boundaries in Al. Early strategies revolved around replicating twin structures from a low SFE seed layer into a high SFE coating. A low SFE seed layer and minimal lattice mismatch was needed between the seed layer and the deposited coating, and Ag met both criteria for Al. As demonstrated in Figures 1-32(a-f), multiple mechanisms were identified where Ag acted as a template layer for twin replication into high SFE Al [154]. Figure 1-32(a, d) demonstrate an ITB being replicated in the Al layer due to the coherency of the Ag and Al layers. Minimizing lattice mismatch enables epitaxial growth and the continuation of the ITB. Figure 1-32(b, e) identifies a second mechanism for lateral replication of a CTB into an Al layer due to the waviness of the layer interface [154]. CTB replication is more energetically favorable than

terminating the defect with an ITB, enabling the CTB to continue into the Al layer. Mechanism 3 is shown in Figure 1-32(c, f) and reveals the formation of stacking faults in Ag can lead to the nucleation of ITBs in Al [154]. Mechanisms 1 and 3 lead to the formation of a large density of ITBs in Al grown on Ag, with a low density of CTBs documented [154]. Xue et al. demonstrated the stabilization of twins in thin Al coatings without the assistance of a template layer. The thermodynamic model discussed previously with Eqs. (1-12,1-13) provided the basis for the formation mechanism presented in Figure 1-32(g) [189]. During the nucleation phase of film deposition, twinned nuclei can form based on the aforementioned thermodynamic model and continue to grow. Additionally, competition between different oriented nuclei occurs during film growth and two nuclei that are oriented with a twin relationship can impinge and share a twin boundary. Xue et al. identified a maximum twin density at a critical film thickness of 80nm and attributed this to the energy penalty becoming too large as the twin grows longer into the film. Eventually, terminating CTBs becomes energetically favorable, leading to a drop in twin density above 80nm [189]. Xue et al. also probed twin formation in different textured Al coatings and identified the following: (1) Al(110) formed a relatively low twin density; (2) Al(111) formed a high density of ITBs and no CTBs; and (3) Al(112) formed the highest twin density and formed a mixture of ITBs and CTBs. The grain boundary misorientation distributions are presented in Figure 1-33(d), and the specific twin formation mechanisms are shown schematically in Figures 1-33(a-c) [190]. Further, the incorporation of various coherent interfaces into Al nanolayer films lead to additional formation mechanisms of twins in Al as nucleation and growth kinetics are altered [158,191–194]. Examples of these mechanisms are presented in Figure 1-34 as coherent Mg interfaces facilitate ITB and 9R phase formation.
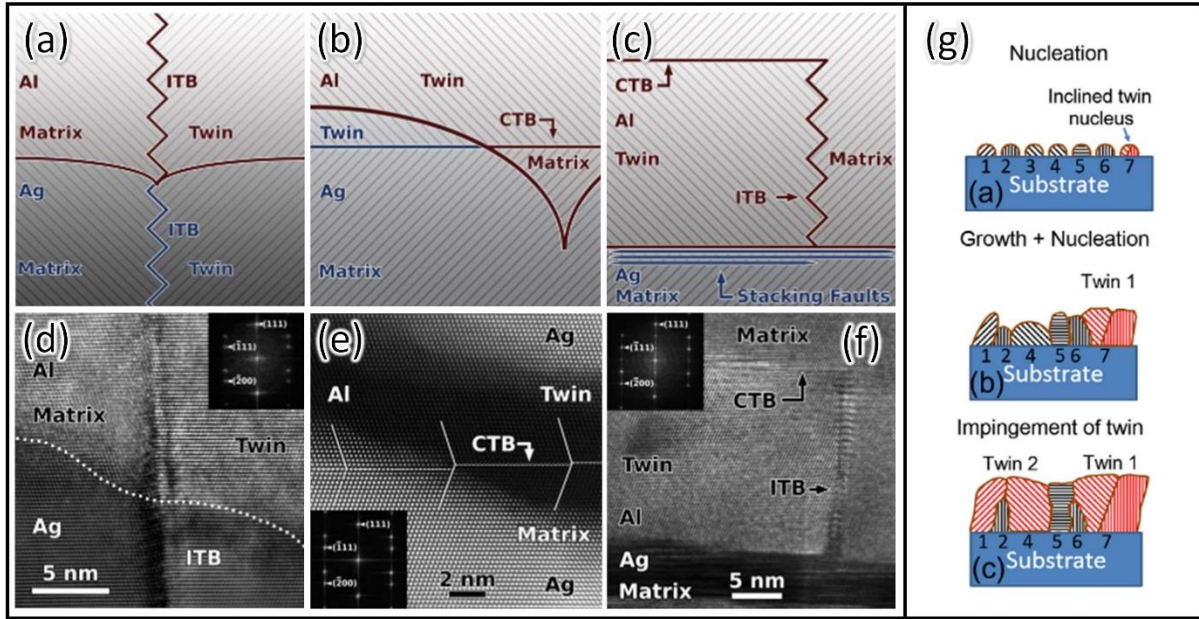
Figure 1-32. (a-c) Schematics and (d-f) HRTEM images identifying 3 different mechanisms for the replication of twin boundaries from low SFE Ag template layer into a high SFE Al coating. (g) Schematics detailing the formation mechanism of twins in Pure Al coatings spanning from nucleation through film growth [154,189]
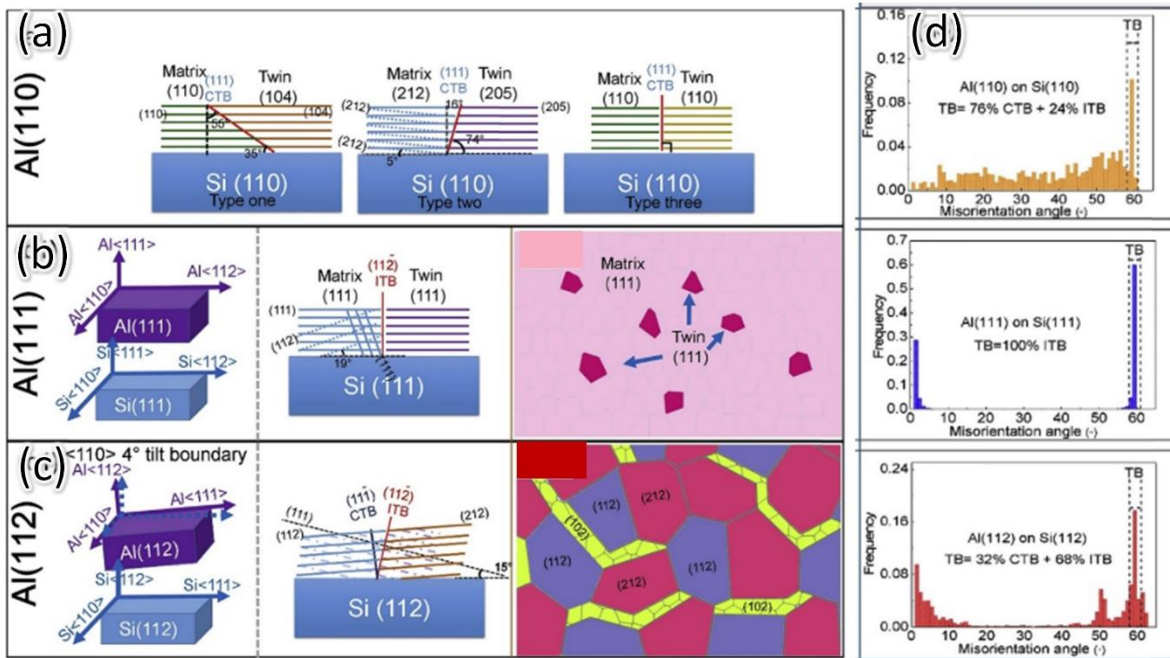
Figure 1-33. Schematics illustrating the orientation relationships leading to twin formation for (a) Al(110), (b) Al(111) and (c) Al(112) oriented films. (d) Histograms detailing the distribution of misorientation angles in grain boundaries for Al(110), Al(111) and Al(112) films. Al(112) coatings possessed the highest density of twin boundaries. [190]
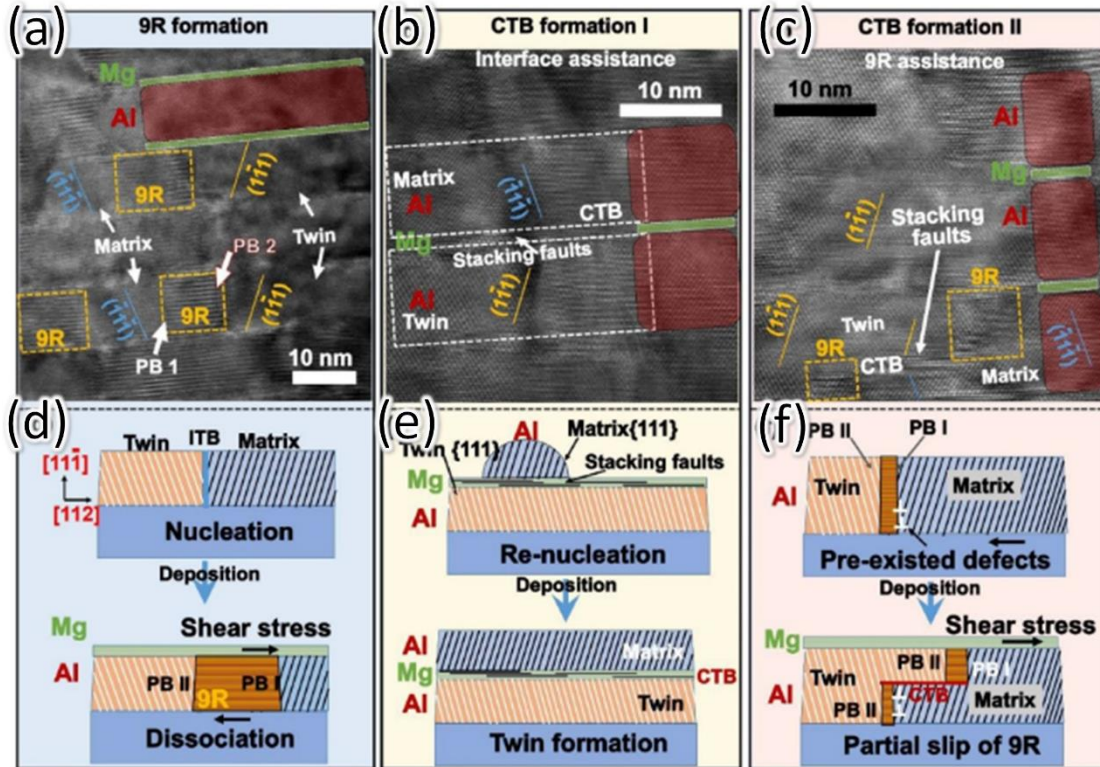
Figure 1-34. (a) HRTEM image detailing the mechanisms for 9R phase formation in Al layers separated by epitaxial thin Mg layers with corresponding schematic shown in (d). (b) HRTEM image depicting the role of the coherent Mg layer in forming CTBs in Al through stacking fault formation in Mg, with the corresponding schematic in (e). (c) HRTEM image depicting a second mechanisms for CTB formation where the coherent Mg layer applies a shear stress leading to the migration of Shockley partials within 9R phase. Corresponding schematic in (f). [191]

Building upon these previous findings, co-sputtering Al with various transition metal solutes enabled the stabilization of an abundance of vertically oriented ITBs in thicker coatings [138,139,159,195–199]. Solute additions combined with strong (111) texture increase the twin propensity in binary and ternary Al sputtered films. Al deposited with 10at% Mg solute stabilized a large fraction of nanotwins, shown in Figure 1-35(b) [198], and 5.9at% Fe solute induces a flow stress of ~1.5GPa (Figure 1-35(f)) [159]. The influence of specific solutes on binding energies and SFEs was probed by Gong et al. using density functional theory (DFT) providing insight into solute selection for promoting NT microstructures [200]. In good agreement with previous studies, Fe, Co and Ni solute were found to significantly increase the binding energy corresponding with potent grain refiners [159,196,197,200]. Similarly, Zr was identified as an element expected to promote nanotwin and 9R phase formation, and the role of Zr on twin formation and the mechanical response of twinned Al-Zr alloys is discussed at length in this thesis.
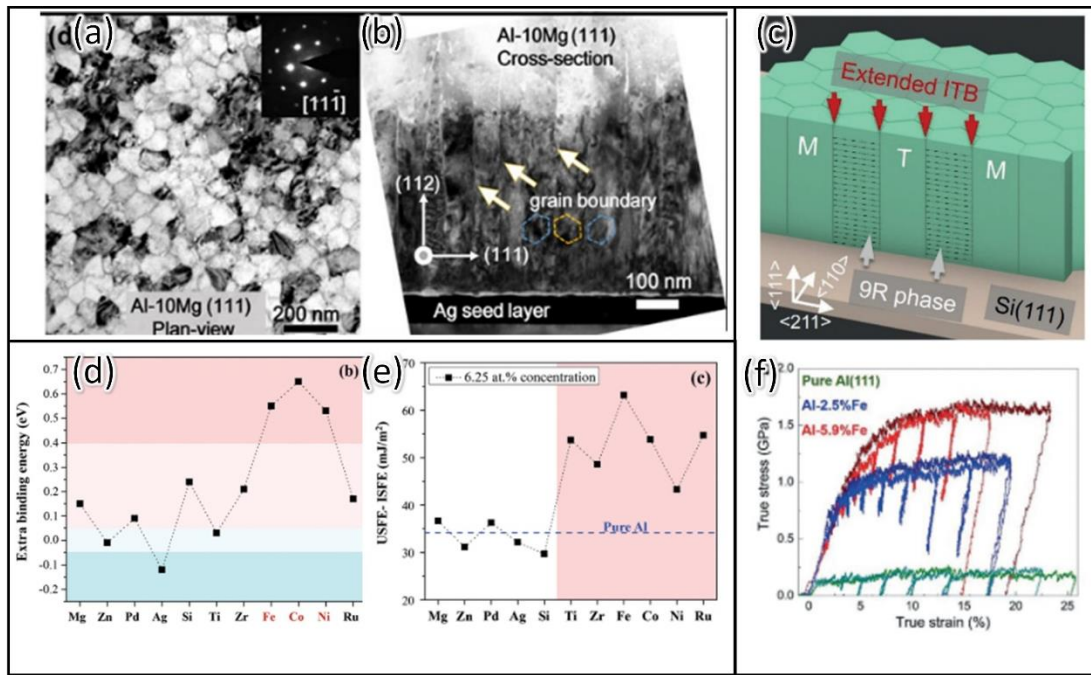
Figure 1-35. (a-b) BF-TEM images identifying the highly textured (111) oriented Al-Mg films forming an abundance of vertically oriented ITBs. (c) Schematic depicting the columnar NT microstructure characteristic of NT Al alloys, similar to the microstructure shown in Al-Mg in (b). (d) Extra binding energy calculated using density functional theory (DFT) calculations identifying Fe, Co and Ni to be highly effective grain refiners. (e) Unstable stacking fault energy (USFE) – intrinsic stacking fault energy (ISFE) for various solutes in Al calculated using DFT, identifying Ti, Zr, Fe, Co, Ni and Ru as effective solutes for forming NT microstructures. (f) Stress strain curves identifying high strength (~1.5GPa) and maintained deformability in NT Al-Fe alloys. [159,198,200]

1.6   Research scope and goals

The scope of this thesis encompasses the synthesis of nanotwinned Al-Zr alloys through the use of magnetron sputtering and the subsequent analysis of their microstructure and mechanical properties. Extensive analysis using transmission electron microscopy enabled the detailed study of these alloys' twin structure and chemical distribution, as well as their post-deformed microstructure. *In-situ* micropillar compression combined with nanoindentation provide the means for a detailed analysis of NT Al-Zr mechanical properties and deformation mechanisms. The work in this thesis was conducted with the following goals: (1) probe the influence of specific solutes (Zr) on the formation of incoherent twin boundaries (ITBs) and 9R phase; (2) explore the deformation mechanisms of nanotwinned Al alloys; and (3) study the thermal stability of this unique nanotwinned microstructure.

First, a simple exploration of the as-deposited microstructure of NT Al-Zr alloys was conducted revealing a super-saturated solution of Zr solute within Al. This enhanced solid solution coupled with strong texture promoted high flow strengths (above 1GPa) due to the abundance of nanotwins and 9R phase. This study was followed up with an analysis of the strain rate sensitivity of NT Al-Zr alloys. Nanoindentation enabled the probing of the mechanical response at a range of strain rates and demonstrated an enhanced strain rate sensitivity in Al-Zr alloys composed of a large volume fraction of 9R phase and ITBs. The following study probed a similar microstructure in NT Al-Co alloys with minor Zr additions which provided a means to isolate and study the role of Zr solute on thermal stability of these NT alloys. This yielded notable results as the combination of Co-Zr solute pairs with more stable twin boundaries yielded a nanostructured alloy that was thermally stable up to $0.78T_m$! Next, the texture dependence was studied by growing epitaxially textured Al-Zr alloys on varied textured silicon substrates, which provided insight on both the texture and the role of Zr solute on twin formation.

Overall, this thesis contains systematic analysis of the NT Al-Zr alloy system and provides multiple relevant findings to the nanotwinned and Al alloy communities. This thesis accomplished each of the 3 goals outlined at the outset of the project and sets up the possibility of future work digging deeper into the deformation mechanisms of these NT Al alloys.

2. EXPERIMENTAL

2.1 Magnetron sputtering

Magnetron sputtering is a physical vapor deposition (PVD) process that is popular for the deposition of high quality thin films and coatings for a range of applications. Most notably, magnetron sputtering is used by the semiconductor industry to deposit various materials to fabricate integrated circuits and computer chips. Sputtering involves the ejection of atoms from a source material (referred to as the target) onto a substrate to grow a resulting film. Achieving ultra-high vacuum in the deposition chamber is a necessary precursor to ensure high film quality and an efficient deposition process. This is accomplished through a combination of mechanical roughing pumps, turbomolecular pumps and cryogenic pumps. In a diode magnetron sputtering system, the target is referred to as the cathode, and the substrate the anode. After flooding the deposition chamber with a process gas (typically Ar), a large voltage is applied to the cathode using either a direct current (DC), radio frequency (RF) or pulsed DC power supply. Free electrons ionize the process gas (Ar) generating a plasma, and the Ar ions are then pulled towards the target surface which "sputters" the target atoms onto the substrate. The substrate is attached to a rotary stage in order to ensure film uniformity. Stochiometric compounds can also be deposited by further introducing a reactive gas into the chamber during deposition (i.e., nitrogen or oxygen). The color associated with sputter plasmas (depicted in Figure 2-1) occurs due to the recombination of free electrons in the plasma with sputtered ions. Magnets behind the target material enhance the Ar ionization near the target surface and aid in maintaining a stable plasma in addition to bolstering the deposition rate. Targets must be produced to be flat and significant levels of cooling are necessary due to excessive heating induced by the large voltage applied to the cathode during deposition. Each of these factors are crucial to maintaining a stable deposition process. Figure 2-1 contains a schematic depicting the magnetron sputtering process [201].
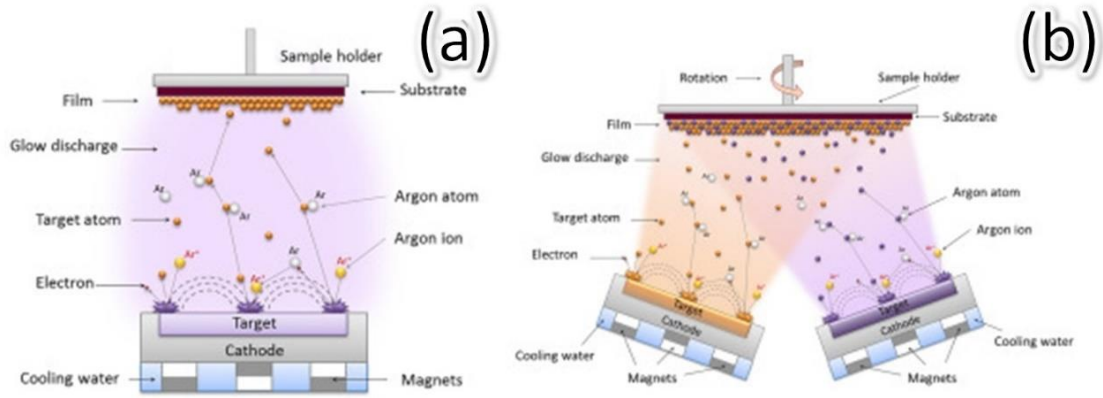
Figure 2-1. Schematic depicting the basic principles of magnetron sputtering with (a) a single target and (b) co-sputtering multiple targets [201]

The Al-Zr alloy films studied in this thesis were deposited using DC magnetron sputtering. The chamber was evacuated to pressures ranging from 6 x 10^{-9} – 4 x 10^{-8} and an Ar gas pressure of 3.5 mTorr was used across all depositions. Al (99.999%) and Zr (99.95%) targets were used during sputtering. Samples were deposited onto single crystal silicon (Si) substrates with (100), (110), (111) and (112) crystallographic orientations, as well as amorphous silicon dioxide (SiO_2). Textured Si substates were etched for 30 seconds using hydrofluoric acid (HF) to remove any formed surface oxides. No substrate bias or substrate heating was applied during deposition. A quartz crystal monitor was used *in-situ* in order to determine deposition rates to ensure reliable film chemistries. Chemistries were then tuned by varying the DC power applied to each target materials cathode. The two magnetron sputtering systems used for these studies are shown in Figure 2-2. A mixture of both systems was used throughout these studies and care was used to maintain constant film chemistry.
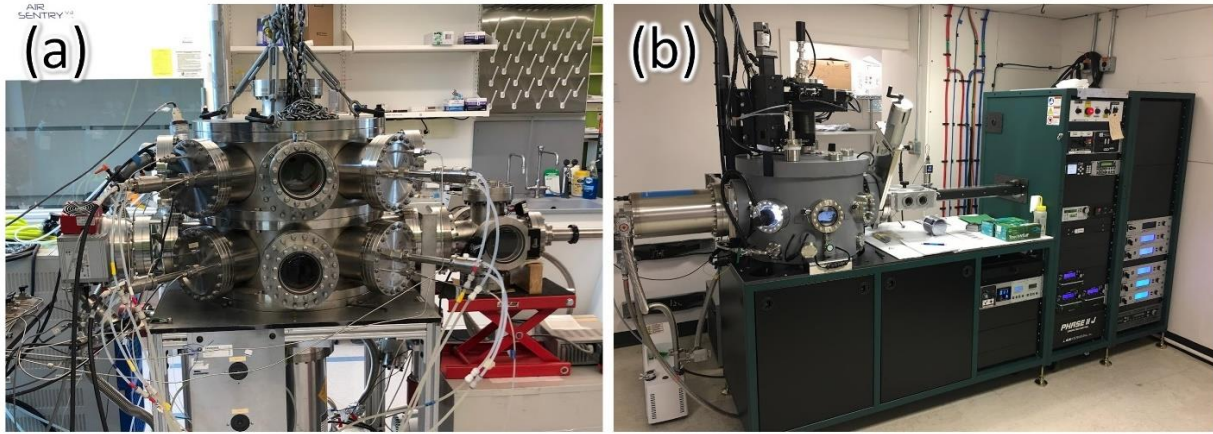
Figure 2-2. (a) Magnetron sputtering system with 4 sputter guns and 2 DC power supplies. (b) AJA ATC-2200-UHV magnetron sputtering system with 8 sputter guns, 5 DC power supplies, and 2 RF spupplies. This system also possesses a quartz crystal deposition rate monitor and substrate heating and biasing capabilites.

2.2 X-ray diffraction

The fundamental structural information of a crystalline material can be determined using x-ray diffraction (XRD). A significant understanding of the molecular arrangement of solids has come from XRD experiments. It can also provide information related to a sample's grain/crystal size, residual stress, overall texture and the atomic scale differences between materials [202]. Diffraction is a wave phenomenon that results from the interaction between an incoming wave (x-rays) and periodically spaced objects that can scatter a wave (atoms composing a crystalline solid). The atomic spacing between atoms is on the order of the wavelength of x-rays. This is why x-ray diffraction has been so influential in fields like materials science where crystallography is highly relevant to a myriad of properties. A schematic illustrating an XRD is provided in Figure 2-3 depicting an incoming x-ray diffracting through a crystalline lattice [203].
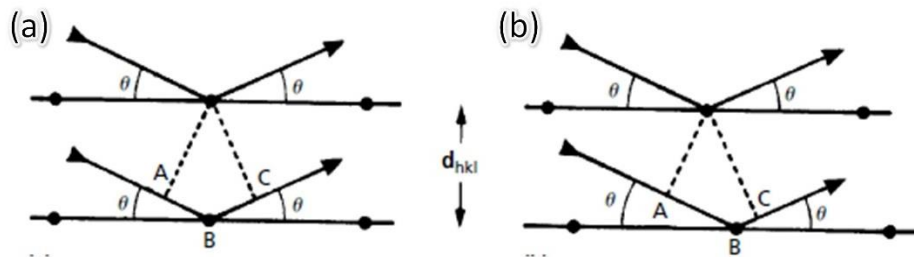
Figure 2-3. Vector schematic depicting x-rays diffracting through lattices where (a) A = B and (b) A ≠ B [203]

Bragg's law describes the relationship depicted in Figure 2-3 between the wavelength of the incoming x-ray (λ), the interplanar spacing of the crystalline solid (d_{hkl}) and the angle at which diffraction occurs. This relationship is given in Equation 2-1. Constructive phase interference is also needed to observe a diffracted wave, which is why only specific angles/crystallographic orientations produce diffraction with specific crystal structures [203]. The geometry behind this constructive interference is calculated through a relationship between atomic scattering factors (f) and structure factors (F_{hkl}), and this is given in Equation 2-2:

$$n\lambda = 2d_{hkl} \sin\theta \tag{2-1}$$

$$F_{hkl} = \sum_{n=0}^{n=N} f_n exp2\pi i(hx_n + ky_n + lz_n) \tag{2-2},$$

where h, k, and l are the miller indices corresponding to specific crystallographic planes.
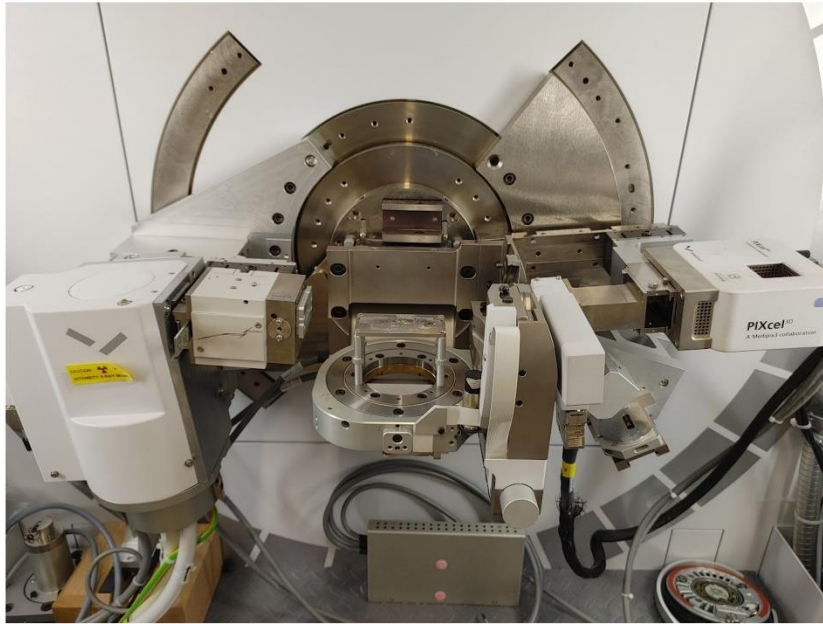
Figure 2-4. The Panalytical Empyrean X'Pert PRO MRD used in this thesis with the Cu source on the left and the detector on the right.

The diffractometer used for the out-of-plane θ-2θ, and pole figure experiments performed in this thesis was a Panalytical Empyrean X'Pert PRO MRD and is shown in Figure 2-4. All experiments were operated using a Cu Kα1 with a wavelength of 0.154nm with the source operated at 40kV. A tube-in-line focus, a capillary X-ray lens and a parallel plate collimator were all used in order to perform the pole figure experiments.

2.3 Nanoindentation

The development of integrated circuits provided a challenge related to assessing the mechanical properties of thin films and coatings that conventional, destructive mechanical testing could not address. Additionally, indentation hardness techniques often provided too large of loads and relied on imaging of the residual indent surface to determine the hardness. With thin coatings, indentation depths necessary to prevent incorporating the influence of the substrate leads to indents too small to image for subsequent hardness calculations. The development of nanoindentation provided a means of non-destructive mechanical testing for thin films that hinged on the ability to reliably monitor the indentation depth [89,90,204]. Hardness and modulus can be calculated based on the data from one loading and unloading cycle from nanoindentation. As the films deposited in this study are all 2μm or thinner, nanoindentation was crucial to analyzing the mechanical response of varying solute and twin density. Every hardness test performed in this thesis were done using a Bruker TI Premiere equipped with a diamond Berkovich indenter, shown in Figure 2-5(a) with a basic schematic in Figure 2-5(b) [89].
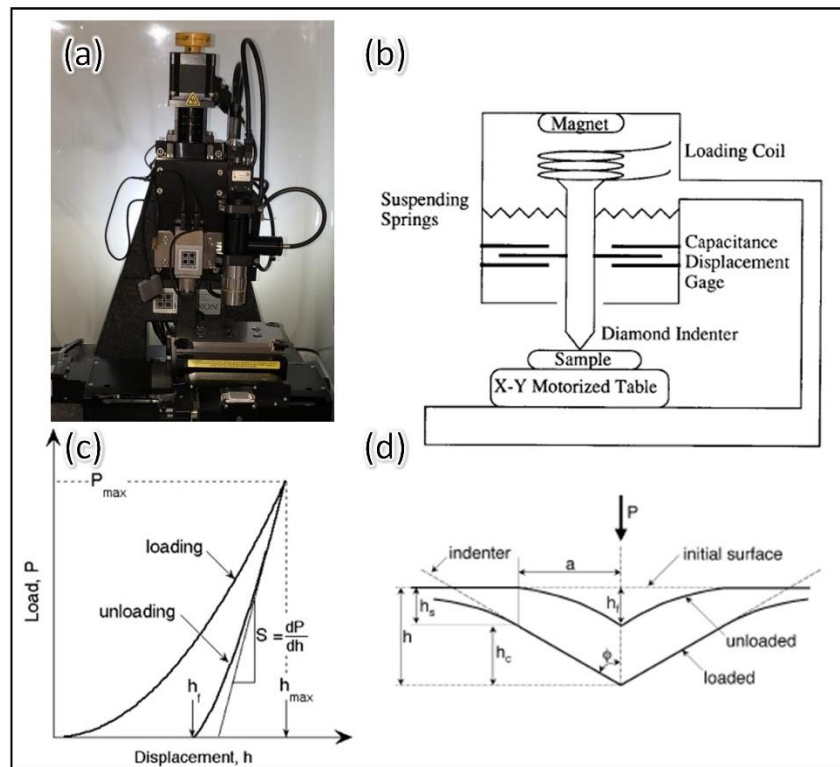
Figure 2-5. (a) Hysitron TI Premiere used for all nanoindentation tests in this study. (b) Schematic depicting the various components within a nanoindentation system. (c) Typical load-displacement curve collected from a nanoindentation test resulting in the (d) deformation zone with a residual indent. [204]

Figure 2-5(c) presents a common load-displacement curve from a nanoindentation test from which the hardness (H) and reduced modulus (E_r) can be calculated using the following method [90]. From the curve in Figure 2-5(c), the maximum load (P_{max}), stiffness (S) and the maximum indentation depth (h_{max}) can be determined. The experimentally measured stiffness is determined from the slope of the upper portion of the unloading curve, and is expressed as:

$$S = \frac{dP}{dh} \tag{2-3}$$

In order to find the geometry of the of the residual contact area, the contact depth (h_c) must be calculated from h_{max} based on the schematic shown in Figure 2-5(d). Equation 2-4 removes the "sink-in" depth and provides h_c:

$$h_c = h_{max} - \xi \frac{P_{max}}{S} \tag{2-4}$$

with ξ being a constant that is dependent on the indenter geometry ($\xi = 0.75$ for this thesis since all tests were conducted with a Berkovich indenter geometry). Having a reliable area function is necessary to proceed further with the hardness calculation and will be briefly reviewed here [205]. Determining the contact area between the indenter tip and the thin film sample is crucial for reliable hardness and modulus measurements and calibrating the area function is a necessary step for operating any nanoindentation equipment. A standard sample (typically Fused Quartz due to its isotropic properties) is indented to different depths in order to establish a relationship between the projected contact area (A_p) and h_c, which is a polynomial:

$$A_P = C_0 h_c^2 + C_1 h_c^1 + C_2 h_c^{1/2} + \cdots \tag{2-5}$$

where C_0 is 24.5 for a Berkovich indenter geometry. One common issue that evolves with extended use of an indenter tip is the geometry becoming blunted, so the area function calibration is crucial for reliable results. Based on Equations (2-4) and (2-5), A_p can be calculated and then can be used to determine both H and E_r:

$$H = \frac{P_{max}}{A_P} \tag{2-6}$$

$$E_r = \frac{\sqrt{\pi}}{2} \frac{S}{\sqrt{A_P}} \tag{2-7}$$

Since the displacement data collected from nanoindentation still includes the deflection of the stiff diamond indenter tip, the film modulus (E) can be extracted using:

$$E = \frac{1 - v_f^2}{\frac{1}{E_r} + \frac{v_i^2 - 1}{E_i}} \tag{2-8}$$

One factor influencing nanoindentation that has been well documented is the indentation size effect (ISE) [206]. A metal's mechanical behavior is dependent on both its extrinsic and intrinsic length scales. Shrinking the dimension associated with plastic deformation leads to a divergence from bulk mechanical behavior. The size effects produce a "smaller is stronger" effect, which is highly relevant to nanoindentation as the hardness increases rapidly at small indentation depths. As characterizing materials on the micro and nanoscale has become more technologically relevant, the influence of size effects is greatly enhanced as materials scientists strive to explain phenomena on these length scales. The ISE has been attributed to strain gradient plasticity and the generation of GNDs leading to the explosion in hardness at small length scales [206]. Because of this, care must be taken to indent deep enough to collect reliable data (typically above 50nm). At the other extreme, it is also crucial to maintain an indentation depth that is below 15% of the film thickness as the substrate can influence the resulting load-displacement curve.

2.4 Transmission electron microscopy

Transmission electron microscopy (TEM) provides the unique capability of collecting a range of information from a single sample, including microstructural imaging, atomic resolution imaging, crystallographic orientation and texture, and chemical distributions. As described by the name, electrons are required to transmit through a sample and as a result samples must be thinner than ~100nm. The wavelength (λ) of the incident radiation used in a microscope determines its resolution, and this can be described by the de Broglie equation, which can be approximated as:

$$\lambda = \frac{1.22}{E^{1/2}} \qquad\qquad (2\text{-}9).$$

Based on Equation 2-9, a TEM with an accelerating voltage of 100 kV would produce electrons with a λ ~ 4pm, leading to an ideal resolution on the order of 10's of pm [207]. However, this is physically impossible due to imperfections related to the electrostatic lenses directing the electrons down the column. A resolution on the order of Angstroms is more realistic, and still enables the study of the atomic structure of materials. A schematic of a TEM is shown in Figure 2-6(a) and an image of the TALOS 200x TEM used in this study is shown in Figure 2-6(b) [207].
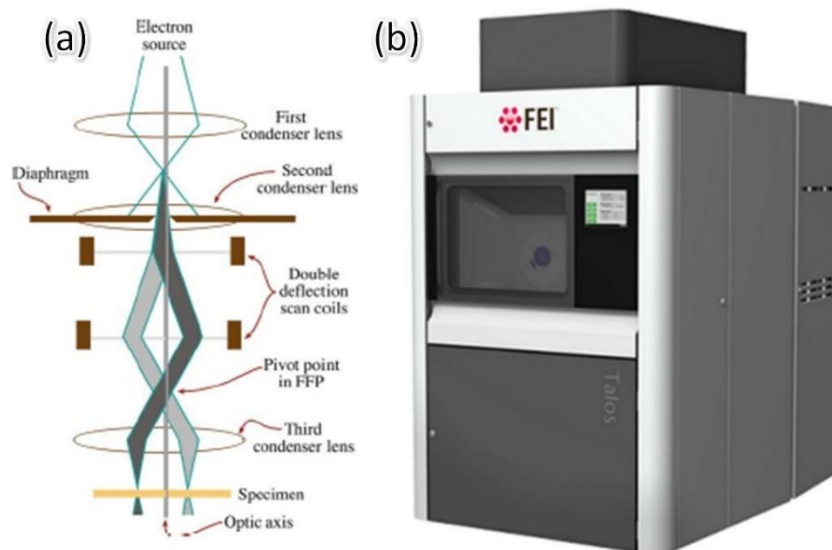
Figure 2-6. (a) Schematic detailing different components and aspects of a typical TEM. (b) Snapshot of a TALOS 200x TEM, used in all the work in this thesis. [207]

After passing through the TEM column, electrons interact with the specimen and various forms of scattering and diffraction occur. This enables the collection of a wide range of information from an individual sample. Different types of detectors and cameras are required to collect this range of information, leading to a very complicated system. Of the multitude of analytical techniques capable of a TEM, this thesis employs a select few which will be reviewed here briefly. Figure 2-7, adapted from [208], provides examples of a few utilized in this thesis.
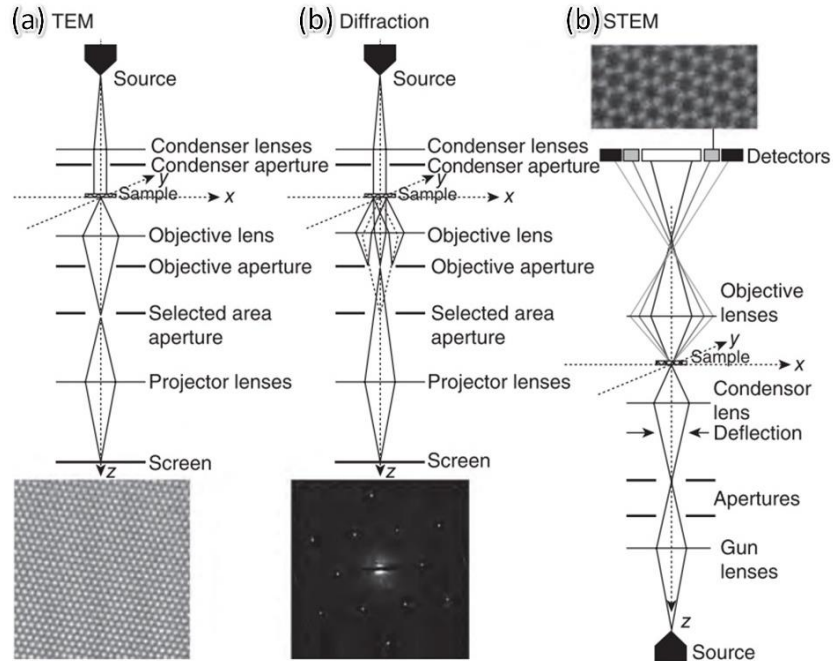
Figure 2-7. Examples of different types of imaging techniques used in a TEM for graphene. (a) TEM, (b) diffraction, and (c) STEM. [208]

Bright field TEM (BF-TEM) is the most common form of imaging in the TEM, and it utilizes the transmitted beam to generate an image of the materials microstructure. Hi-resolution TEM (HRTEM) is a variation of BF-TEM where the user can image the atomic structure or nano-scale defects, such as the lattice shown in Figure 2-7(a). Dark-field TEM (DF-TEM) information is similar to BF-TEM imaging; however, the image is produced from a diffracted beam after tilting to a specific zone axis. This can highlight certain crystallographic orientations or crystalline defects. Selected area diffraction (SAD) takes advantage of the wave properties of an electron and can produce a transmitted diffraction pattern, such as the example in Figure 2-7(b), that provides crystal structure and orientation information. Scanning transmission electron microscopy (STEM), depicted using graphene in Figure 2-7(c), is often used to characterize nanoscale or atomic defects due to the focusing of the electron beam to a fine probe. Additionally, operating the TALOS 200x in STEM mode enables the collection of chemistry information through energy dispersive spectroscopy (EDS). The TALOS 200x a high-angle annular dark field (HAADF) detector and super X electron-dispersive X-ray (EDS or EDX) detector equipped to perform this analysis. Additionally, the TALOS 200x is equipped with a NanoMegas ASTAR system that utilizes precession electron diffraction to characterize crystallographic orientation and texture over a wide

area of a sample [209]. This can produce inverse pole figure maps, grain boundary maps, kernel average misorientation maps, and phase mapping. All of these techniques were combined within this thesis, and examples of each are shown throughout this work.

2.5   *In-situ* micropillar compression

The development of micropillar compression testing in the mid 2000's revealed similar "smaller-is-stronger" size dependent plasticity in samples uninfluenced by strain gradients [210–212]. This mechanical testing method utilizes a truncated Berkovich or conical diamond flat punch tip in a nanoindentation system to compress micropillars prepared using a focused ion beam (FIB). Energetic ions (typically Ga^+) sputter away material from the surface of a bulk sample, generating a pillar that is subsequently compressed. Uchic [211] developed two FIB pillar fabrication methods, (1) the annular method and (2) the ion lathe method, depicted in Figure 2-8. For the annular method, the ion beam is oriented perpendicular to the sample surface, and a cavity is milled using annular milling patterns around the area of interest. This cavity serves to ensure the indenter does not interact with surrounding bulk material, as well as allowing for *in-situ* SEM imaging during compression. To finish this method, the beam is kept at this angle to mill the final pillar shape. A consequence of this process is a small taper angle that influences analysis. The ion lathe method remedies this, as the surface is tilted to slightly off the FIB column during the final polishing step and the ion beam is used similar to a lathe, removing taper [211]. The annular method is more common since it takes significantly less time to fabricate a sample, reducing ion beam exposure time. Electroplating is another technique that is less commonly used to fabricate micropillars. Figure 2-9 shows two single crystal pillars fabricated by Uchic [211] using the ion lathe technique.
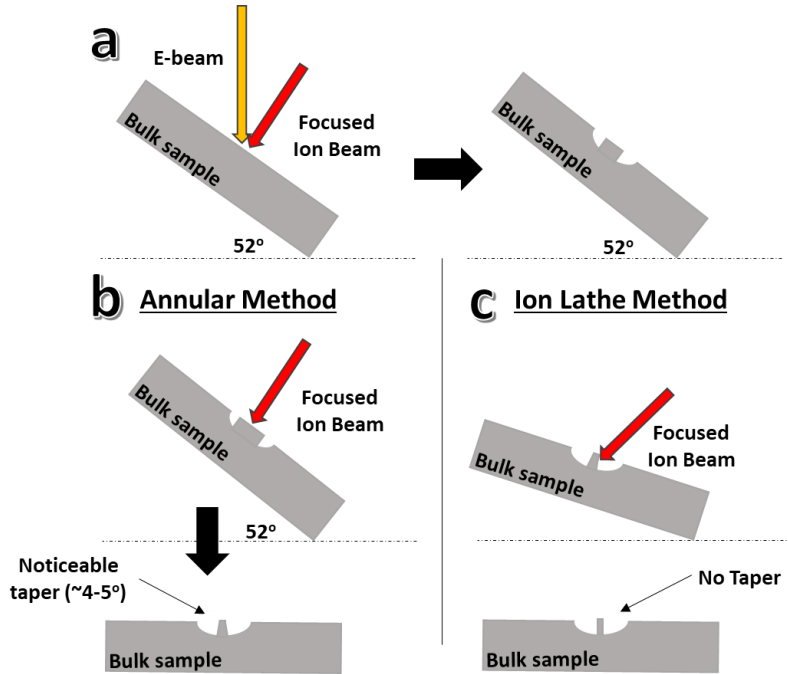
Figure 2-8. Schematic illustrating the FIB process (using a duel beam FIB-SEM) for machining micropillars. (a) the first step of each method that continues in (b)annular method and (c)ion lathe method. A key characteristic of the annular step is the slight taper on the final micropillar in (b). The "lathe" method tilted to 28° from the FIB column serves to eliminate this taper, but takes a significant amount of time, so can be foregone if the taper is minimized during (b).
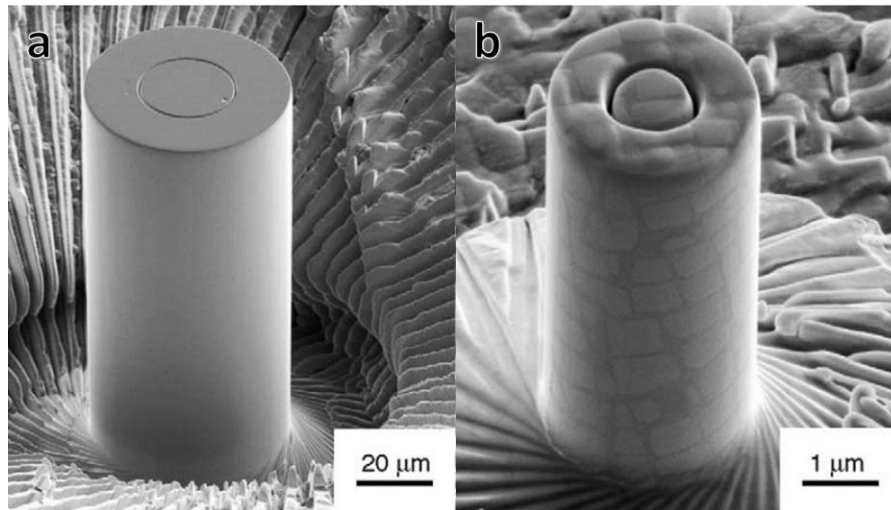
Figure 2-9. (a) SEM image of a 43 µm diameter Ni3Al micropillar prepared by Uchic et al using the FIB ion lathe method, with a gage length of 90 µm. (b) A Ni superalloy micropillar with a diameter of 2.3 µm diameter and a gage length of 4.6 µm. The Ni3Al precipitates are visible on the surface of the pillar. [211]

86

Micropillar compression allows for testing at the length scale of most dislocation activity. In addition, specific orientations can be fabricated from within a bulk sample, or local heterogeneities can be isolated in nanostructured materials. Single crystal micropillars were initially studied as they allowed direct comparison to widely tested bulk single crystals. Uchic [210] identified the "smaller-is-stronger" size effect in Ni micropillars without the influence of strain gradients. In addition, these samples experienced large periods of stochastic plastic flow intermittently followed by elastic loading. These phenomena were demonstrated in a wide range of FCC metals, including Ni [210], Au [212], Al [213] and Cu [214], with the results from microcompression of Au [212] shown in Figure 2-10.
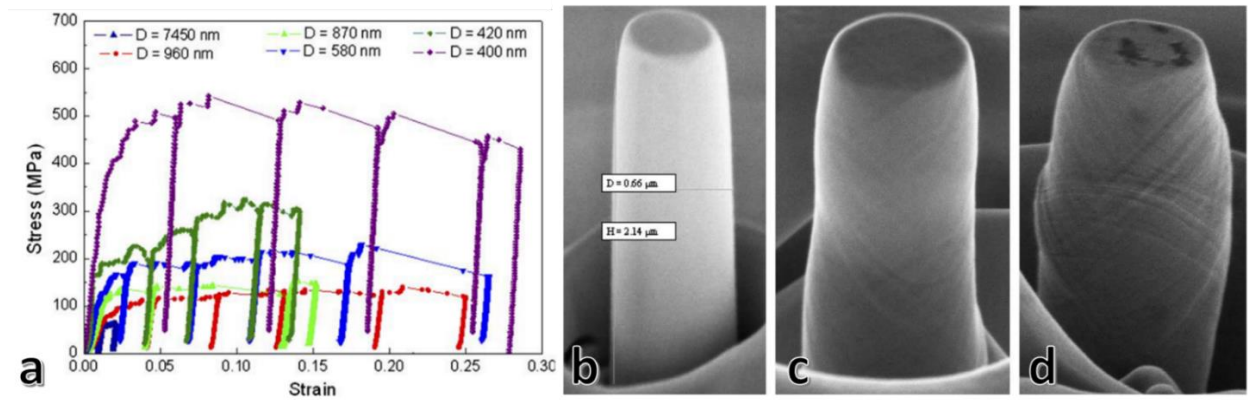
Figure 2-10. (a) Resulting stress-strain curves from micropillar compression testing of Au with pillar size ranging from 7450nm – 400nm illustrating the smaller is stronger trend. (b-d) SEM images of (b) undeformed, (c) deformed, and (d) severely deformed Au micropillar. [212]

New theories that described this unusual compressive behavior include a source limited model explaining the strength size effect, and a dislocation starvation model capturing intermittent plastic flow. Both of these theories suggest that dislocation nucleation drives plasticity in samples at this scale. Parthasarathy [215] suggested that the proximity of the free surface generates single-arm Frank-Read sources, decreasing the source length. A higher stress is required to operate these sources, leading to smaller pillars being stronger. Building upon this, a weakest-link model suggested the strength is controlled by the weakest surface dislocation source [216]. In dislocation starvation, the annihilation (or "mechanical annealing" [217]) of pre-existing dislocations at the free surface effectively creates a dislocation free sample [212,218,219]. Dislocations are not able to multiply in FCC metals due to the lack of cross slip, and instead annihilate at the free surface

[220]. This requires dislocation nucleation to continue plastic flow, which is dependent on the initial dislocation structure. The variability in initial dislocation structure leads to the stochastic nature of plasticity in single crystal micropillars.

Due to the complicated FIB pillar fabrication technique and the limited sample volume, micropillar compression faces many challenges pertaining to interpreting results. Minor alterations to pillar geometry can generate artifacts in the data that misrepresent the true mechanical behavior [221]. For example, pillar taper produces a non-uniform stress field, leading to a stress concentration at the pillar top. Zhang et. al [222] highlight that pillar taper can generate spurious work hardening and the experimental results from nanocrystalline Ni shown in [223] corroborate the numerical simulations. The Ni pillars from this study are nanocrystalline, where no work hardening is expected, however the stress-strain curves show clear work hardening [223]. Taper generates strain gradients, producing a higher density of GND's, which is a possible explanation for the spurious hardening [224].

Outside of geometrical constraints, other factors must be considered. The elastic deflection of the substrate/bulk material below the pillar influences the accuracy of modulus measurements [221]. This issue has been corrected analytically by Greer [212] by subtracting out the Sneddon compliance (Eq. 3) [225], from the inverse of the measured stiffness (Equation 2-10).

$$C_{Sneddon} = \frac{\sqrt{\pi}(1-v^2)}{2E_{polyX}\sqrt{A_P}} \tag{2-10}$$

$$S_{pillar} = \frac{1}{(1/S_{meas})-C_{Sneddon}} \tag{2-11}$$

Further issues with measuring modulus and the yield point hinge on the ability to establish good alignment between the indenter and the pillar. Unloading segments during compression can be done to establish that good alignment is made. If the unloading is linear, it verifies that the unloading is purely elastic, and that the indenter is well aligned. Building upon this, Uchic[221] noted that the base material restricts the pillar aiding in preventing plastic deformation in the bulk. Furthermore, the constraint of the pillar and friction between the platen and the pillar top helps prevent plastic instabilities, such as buckling [222]. Both Zhang using FEM [222] and Uchic using electron backscatter diffraction (EBSD) [221] evaluated the influence of this friction. Although it prevents buckling, as shown in Figures 2-11(a) and 2-11(c), it does impact the uniformity of the internal stress field. Similar to pillar taper, this leads to inaccuracies in flow stress and incorrect

representation of strain hardening behavior [222]. Understanding the friction state within micropillar compression experiments aids in interpreting the resulting stress strain curve.
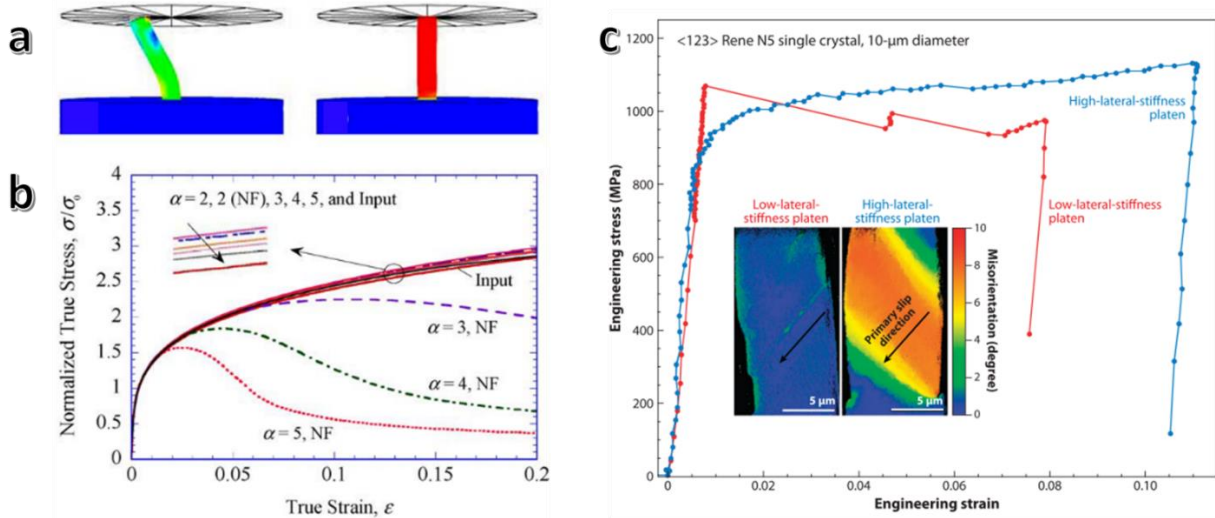
Figure 2-11. (a) Results of numerical model demonstrating buckling in samples without considering friction (left) versus no buckling with friction (right). (b) Resulting stress-strain curves from numerical model that detail the drop-off in stress due to buckling in no-friction (NF) samples with α>2. (c) Experimental results detailing similar trend with differences in resulting stress-strain curves for the low-stiffness/high-stiffness platens. EBSD of the compressed pillars reveal alterations in the stress field. [221,222]
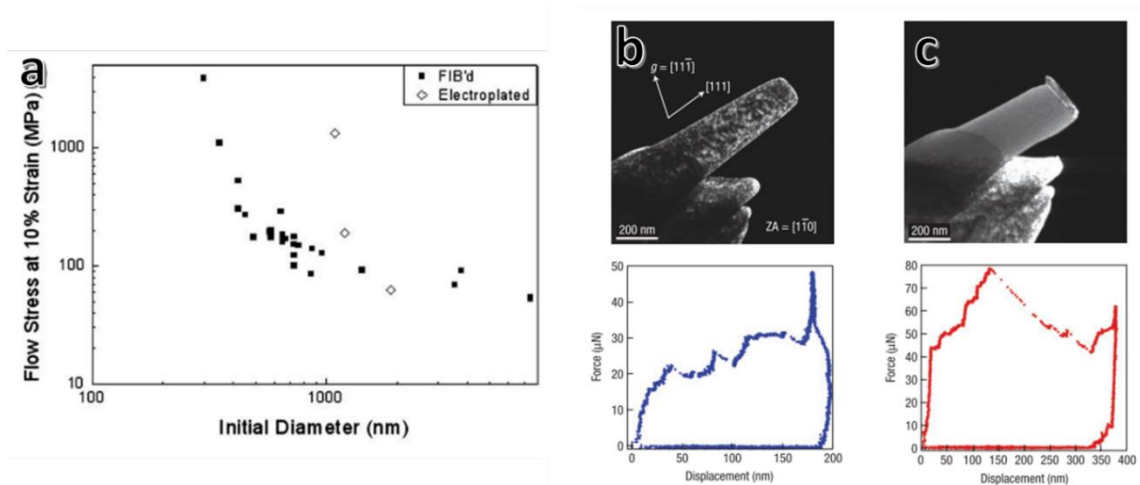
Figure 2-12. (a) Flow stress vs pillar diameter demonstrating comparable stress levels and slopes for the FIB (black squares) and electroplated pillars (white diamonds). (b) DF TEM image of Ni pillar before mechanical treatments (shown in plot below TEM image). Force is applied, demonstrating "mechanical annealing" with a pristine, dislocation free pillar in (c). [217,218]

Figure 2-12(a) shows similar size effects between FIB and electroplated Au samples, demonstrating that Ga$^+$ damage is minimal. In comparison, it was identified that the longer milling times characteristic of the lathe method did in fact influence the mechanical behavior [226]. Further exploring this, Shan, utilized mechanical pre-loading on Ni nanopillars to study the effect of varying initial dislocation density [217]. Shan compared as prepared FIB samples, containing pre-existing dislocations, with the "mechanical annealed" samples, which were relatively dislocation free and found similar strengthening trends [217]. This further establishes that the effect of FIB milling on the resulting mechanical properties is not significant and do not drastically affect the results. Overall, many of these experimental issues have been accounted for and factored into analysis, but it is still important to critically assess these factors test the validity of the results. To extract accurate information from micropillar compression tests, assessing the extent of these constraints is important.

For the work in this thesis, *in-situ* micropillar compression experiments were performed using a Bruker/Hysitron PI 88 nanoindenter inside a FEI Quanta 3D scanning electron microscope to probe the deformability and compressive strength of these films. Pillars and TEM samples of deformed pillars were fabricated using an equipped focused ion beam (FIB) inside an FEI Quanta 3D scanning electron microscope. The pillar height and diameter were ~1600 nm and 800 nm respectively, with the taper minimized below ~2° during pillar fabrication. Pillars were compressed using a Bruker/Hysitron PI 88 nanoindenter to ~20% strain using displacement control, with a strain rate at 5×10^{-3}. Pillars were compressed with numerous partial unloading segments to assess the validity of the alignment during compression. To calculate the true stress and true strain, first, the influence of any elastic deformation of the Si substrate underneath the films and the diamond flat punch was estimated using the formulation by Sneddon [225] where he considered the pressed elastic half-space of a cylinder. The equation for the modified displacement is below:

$$u = u_{mea} - \frac{1-v_{dia}^2}{E_{dia}}\left(\frac{F}{d_{it}}\right) - \frac{1-v_{Si}^2}{E_{Si}}\left(\frac{F}{d_b}\right) \tag{2-12}.$$

In Equation (2-12), v_{dia} and E_{dia} represent the Poisson ratio and the modulus of diamond, 0.07 and 1140Gpa, respectively. F is the measured force with u_{mea} the measured displacement. D_{it}, d_b represent the top and bottom diameter of pillars. Likewise, The E_{Si} and v_{Si} denote the elastic modulus and Poisson ratio of the Si (111) substrates, and are 189 GPa and 0.26, respectively.

Because of the pillar dilation commonly seen in micropillar compression, the deformation is not homogonous meaning the classic model for converting engineering stress to true stress in not applicable, specifically $\sigma_t = \sigma_e(1 - \varepsilon_e)$. As a result, the true stress was calculated using dynamic measurements of the instantaneous diameter of the pillar top to provide an accurate estimation of the updated contact area throughout the experiment. The true strain was calculated using the classical formulation, $\varepsilon_t = \ln(1 + \varepsilon_e)$.

3. MICROSTRUCTURAL & MECHANICAL PROPERTIES OF NANOTWINNED AL-ZR WITH SIGNIFICANT 9R PHASE

The density functional theory (DFT) calculations had been completed by Dr. Dongyue Xie, Dr. Mingyu Gong and Dr. Jian Wang from the University of Nebraska-Lincoln.

This chapter includes content reproduced with permission from "Microstructural evolution of nanotwinned Al-Zr alloy with significant 9R phase" by N.A. Richter, Y.F. Zhang, D.Y. Xie, R. Su, Q. Li, S. Xue, T.J. Niu, J. Wang, H. Wang and X. Zhang, *Materials Research Letters* 9(2) (2020): 91-98 Copyright 2020 Taylor and Francis Group.

And from "Exploring the deformation behavior of nanotwinned Al–Zr alloy via *in situ* compression" by N.A. Richter, M. Gong, Y.F. Zhang, T.J. Niu, B. Yang, J. Wang, H. Wang and X. Zhang, *Journal of Applied Physics* 132 (2022): 065104 Copyright 2022 AIP Publishing.

3.1   Overview

Nanotwinned metals have demonstrated the capacity for concomitant high strength and ductility. However, metals with high stacking fault energies, such as Aluminum (Al), have a low propensity for twin formation. Here, we show the fabrication of supersaturated solid-solution Al-Zr alloys with a high density of growth twins. Incoherent twin boundaries (ITBs) are strong barriers to dislocation motion, while mobile partial dislocations promote plasticity. These deformable nanotwinned Al-Zr alloys reach a flow stress of ~1 GPa, as demonstrated using in-situ micropillar compression tests. Density functional theory calculations uncover the role Zr solute plays in the formation and deformation of the nanotwinned microstructure. This study features a strategy for incorporating ITBs and 9R phase into Al alloys for simultaneous benefits to strength and deformability.

3.2   Introduction

Aluminum alloys are a mainstay for lightweight structural applications. However, like most metallic materials, increasing their strength is typically accompanied by sacrificing ductility [227–229]. Nanocrystalline (NC) metals have high strength due to a lack of dislocation pile-ups in nanograins, but they often have poor ductility manifested by shear banding, as conventional dislocation plasticity mechanisms are difficult to operate in nanograins [45,230–232]. Softening is often observed in nanocrystalline metals below critical grain sizes due to the activation of grain

boundary (GB) sliding and GB diffusion based deformation mechanisms [49,233]. A significant amount of research aimed at mitigating strength-ductility trade-off has led to some profound discoveries and innovations. A classic example is twinning induced plasticity (TWIP) steels, where deformation twins offer simultaneous strength and plasticity [227,234–237]. High entropy alloys (HEAs) are a newer family of metallic materials that have recently incorporated TWIP effects to avoid sacrificing ductility [238,239]. Another avenue for simultaneous enhancement of strength and deformability is through gradient microstructures [240–244]. The combination of fine grains and coarse grains in these structurally graded metals helps to overcome the strength-ductility trade-off.

The influences of twin boundaries on strength and ductility have been extensively investigated in face-centered-cubic (FCC) metals with low stacking fault energy (SFE), predominately Cu (45 mJ m^{-2}) [169,245] and Ag (16 mJ m^{-2}) [170,246]. When deposited using electrodeposition or magnetron sputtering, these metals form abundant Σ3 (111) coherent twin boundaries (CTBs) with nanoscale twin spacing, and CTBs strongly inhibit dislocation transmission [51,172,173,247–252], as demonstrated using *in-situ* nanoindentation experiments and molecular dynamics simulations [156,253–255]. Σ3 {112} Incoherent twin boundaries (ITBs) and Shockley partial dislocations are also important for maintaining ductility and high strengths [156,173,256,257]. Nanotwinned (NT) metals also possess a high strength-to-resistivity ratio [169,172,258] and have remarkable thermal stability [135,136,259,260] compared with their nanocrystalline counterparts as CTBs store much lower energy than high angle GBs, and electron scattering coefficient at CTBs is one order of magnitude lower than high angle GBs [258]. TBs are difficult to form in FCC metals with a high SFE due to the high ratio of the stable SFE to unstable SFE (γ_{sf}/γ_{usf}), which prevents the formation of stacking faults by limiting the distance between leading and trailing partials [187,261]. Thus twins in high SFE metals can rarely form except under extreme conditions, such as severe plastic deformation or at the high stress concentration of crack tips [187,262,263]. Recent discoveries in high SFE metal films, such as Ni (120 mJ m^{-2}) and Al (160 mJ m^{-2}), show the formation of a high density of growth twins [154,171,189,192,193,200,243,264–267]. Xue et al. demonstrated a texture dependence on the formation mechanisms of growth twins in Al [189,190] and Bufford et al. identified a template method for replicating TB structures from a low SFE coherent seed layer into high SFE Al films [154,158]. More recently, alloying sputtered Al films with various transition metal solutes has

demonstrated the capability of forming NT microstructures in Al composed of abundant ITBs [200]. These Al alloys possess extremely high strengths (up to ~2Gpa compressive flow stress [139,183]) while maintaining impressive plasticity due to the presence of a high density of partial dislocations making up the periodic 9R phase [159,177].

This work investigates the deformability of NT Al-Zr alloy films, with the aim of demonstrating simultaneous improvements to strength and deformability. Literature suggests Zr is a slow diffuser in Al and plays a critical role in stabilizing microstructures as a result [268,269]. These observations prompt us to investigate the impact of Zr solutes on mechanical stability of GBs and TBs in NT Al alloys. *In-situ* microcompression tests explore this phenomenon, with a multifaceted look into the role of Zr solute on the microstructure of these alloys using density functional theory calculations and microscopy. This study underscores the role TBs on the strength and work hardening ability of Al alloys.

3.3   Experimental

Magnetron sputtering was used to deposit 2 μm thick Al-xZr (x = 0-10 at%) films with a 40nm Ag seed layer onto HF etched Si (111) substrates. Al (99.999%), Ag (99.999) and Zr (99.995%) targets were used, and the chamber base pressure was below 4×10^{-8} torr before deposition. Out-of-plane θ-2θ X-ray diffraction (XRD) scans were completed using a Panalytical Empyrean X'pert PRO MRD diffractometer operated at 40kV using Cu $K\alpha_1$ X-rays to explore the texture and structure of the films. Transmission electron microscopy (TEM) samples were prepared by mechanical grinding, dimpling, and low-energy ion milling, with care taken to avoid sample heating. The microstructure and composition were examined using an FEI Talos 200X analytical microscope operated at 200 kV with a Fischione high-angle annular dark field (HAADF) detector and super X energy-dispersive X-ray spectroscopy (EDS) detector. Crystallographic orientation mapping and GB misorientation measurements were made using Nanomegas ASTAR™ with a camera length of 205mm, a precession angle of 0.6º, and a step size of 5 nm in the same TEM. The hardness and moduli of these films were measured using a Hysitron TI Premiere nanoindenter under displacement control. 75 indents at different depths were performed on each sample to guarantee data reliability, and the indentation depth was less than 15% of the film thickness to exclude any substrate effects. Micropillar compression was performed to probe the deformability and compressive strength of these films. Pillars and TEM samples of deformed

pillars were fabricated using an equipped focused ion beam (FIB) inside an FEI Quanta 3D scanning electron microscope. The pillar height and diameter were ~800 and 1600nm respectively, with the taper angle minimized to below 2° during pillar fabrication. Pillars were compressed using a Hysitron PI88 nanoindenter to ~20% strain using displacement control, with a strain rate at 5×10^{-3}. Pillars were compressed with numerous partial unloading segments to assess the validity of the alignment during compression. To calculate the true stress and true strain, First, the influence of any elastic deformation of the Si substrate underneath the films and the diamond flat punch was estimated using the formulation by Sneddon [225] where he considered the pressed elastic half-space of a cylinder. The equation for the modified displacement is below:

$$u = u_{mea} - \frac{1-v_{dia}^2}{E_{dia}}\left(\frac{F}{d_{it}}\right) - \frac{1-v_{Si}^2}{E_{Si}}(\frac{F}{d_b}) \tag{3-1}$$

In Equation 3-1, v_{dia} and E_{dia} represent the Poisson ratio and the modulus of diamond, 0.07 and 1140Gpa, respectively. F is the measured force with u_{mea} the measured displacement. D_{it}, d_b represent the top and bottom diameter of pillars. Likewise, The E_{Si} and v_{Si} denote the elastic modulus and Poisson ratio of the Si (111) substrates, and are 189 Gpa and 0.26, respectively. Because of the pillar dilation commonly seen in micropillar compression, the deformation is not homogonous meaning the classic model for converting engineering stress to true stress in not applicable, specifically $\sigma_t = \sigma_e(1 - \varepsilon_e)$. As a result, the true stress was calculated using dynamic measurements of the instantaneous diameter of the pillar top to provide an accurate estimation of the updated contact area throughout the experiment. The true strain was calculated using the classical formulation, $\varepsilon_t = \ln(1 + \varepsilon_e)$.

3.4   Results

The XRD patterns in Figure 3-1(a) reveal the strong (111) texture, with the Al(111) peak intensity decreasing with increasing Zr content. The lack of additional peaks also confirms the formation of a super-saturated solid solution across all compositions. The pole figure scans presented in Figure 3-2 support these findings and further identify the presence of twin boundaries in Al-Zr sputtered films. The bright field (BF) TEM image in Figure 3-1(b) shows Al-4.3Zr is composed of low angle grain boundaries (LAGBs), further characterized in the kernel average misorientation (KAM) and grain boundary (GB) maps shown in Figure 3-4, and the corresponding

selected area diffraction (SAD) pattern demonstrating "single-crystal like" texture. In comparison, the inserted SAD pattern of Al-10Zr in Figure 3-1(c) reveals diffraction ring indicative of high angle grain boundaries (HAGBs). The addition of Zr reduces the average grain size in Al from 98 nm (with primarily low-angle GBs) to 50 nm with dominant high-angle GBs. Figure 2I shows the lattice parameter measured by x-ray diffraction follows Vegard's law with Zr composition, which further confirms the formation of a solid solution [270]. The inverse pole figure (IPF) maps collected from ASTAR in Figure 3-3 show the texture progression from single-crystal like (dominant singular texture oriented grains with low misorientation boundaries separating them) {111} texture in for Al-4.3Zr to randomly oriented nanograins in Al-10Zr. Figure 3-4 reveals the NT Al-10Zr sample is composed of a distribution of high angle and low angle grain boundaries as well as Σ3 twin boundaries. The results from these IPF maps correspond well with the SAD evolution and clearly show the strong grain refinement induced by Zr solutes.
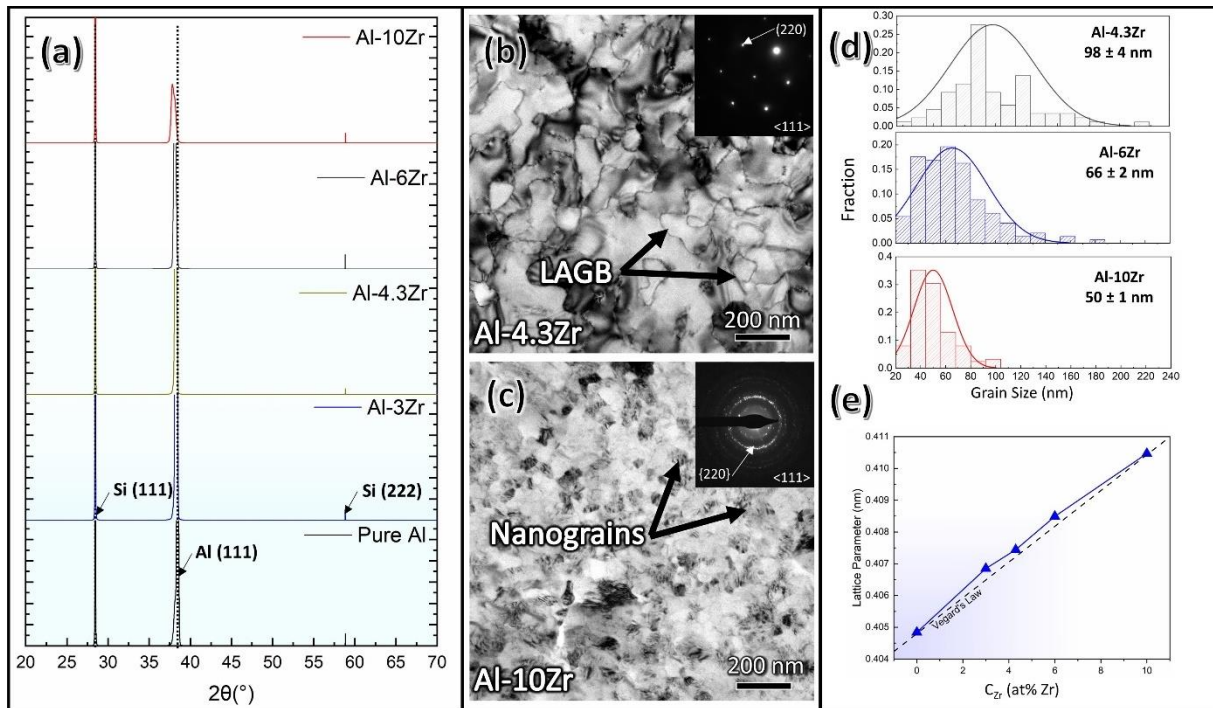
Figure 3-1. (a) XRD scans of the (111) textured NT Al-Zr films deposited on Si (111) substrates. (b) Plan-view BF-TEM micrograph with corresponding selected area diffraction (SAD) insert of an Al-4.3Zr sample reflecting its single crystal-like texture and numerous low angle grain boundaries (LAGB). (c) BF-TEM micrograph with corresponding SAD insert of an Al-10Zr plan-view sample possessing fine polycrystalline nanograins with strong (111) out-of-plane texture. (d) Grain-size statistics for each NT Al-Zr sample demonstrating clear structural refinement with increasing Zr content. I Lattice parameter evolution with Zr content.
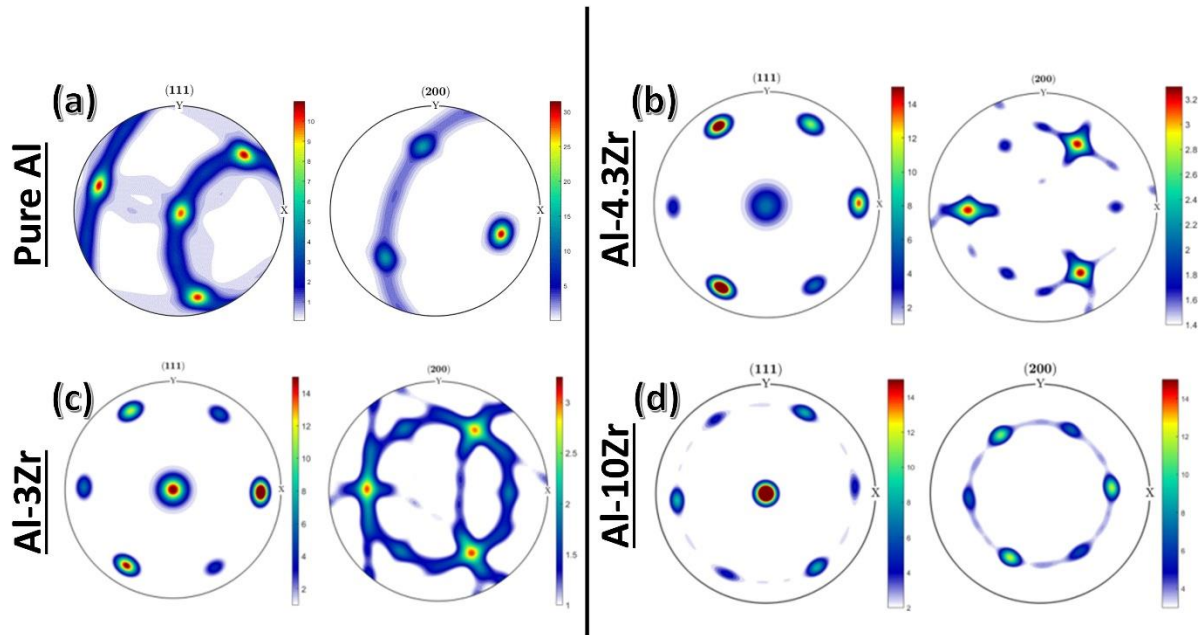
Figure 3-2. X-ray pole figures for Al-Zr alloys identifying the textural evolution with increasing Zr content. All samples are {111} textured. However, it is evident the transition from single-crystal Al to nanotwinned Al-Zr. Al-10Zr also demonstrates some in-plane rotation as indicated by the streaks between the 6 (220) spots on the (111) pole figure.
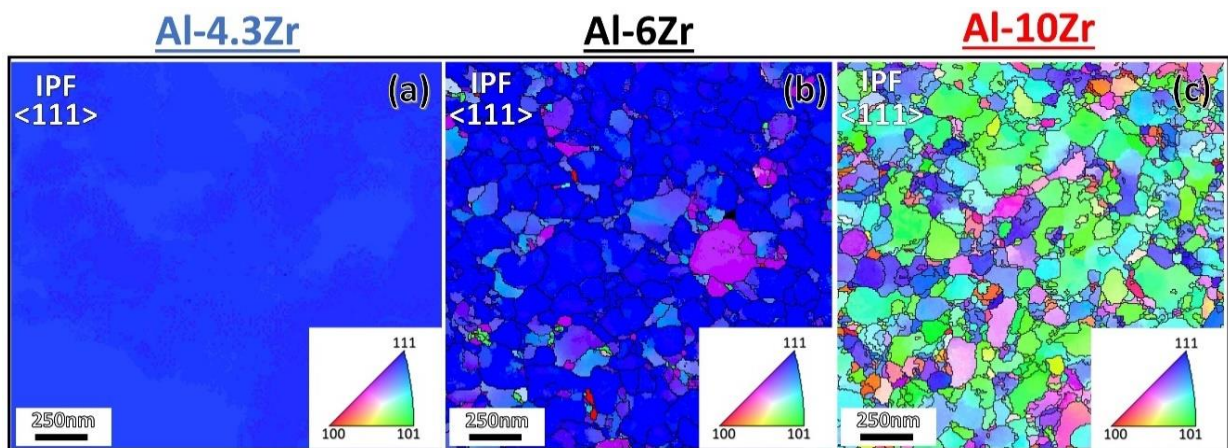
Figure 3-3. (a) ASTAR IPF map demonstrating the single-crystal-like {111} out-of-plane texture in Al-4.3Zr. (b) IPF of (111) textured Al-6Zr. (c) IPF of nanocrystalline Al-10Zr. All images were taken along the <111> zone axis.

Cross-section TEM analysis was also conducted along the <110> zone axis to study the microstructure in further detail. Comparing BF-TEM images for the Al-4.3Zr (Figure 3-5(a)) and Al-10Zr (Figure 3-5(d)) samples, it is obvious the microstructures are both composed of an abundance of vertically oriented columnar boundaries. The inserted SAD patterns in Figures 3-5(a, d) confirm these samples are highly twinned. Additionally, the dark field (DF) TEM images (Figure 3-6) taken with $\bar{g} = [\bar{2}00]$ also show the twin relationship across a columnar ITB, with the matrix (M) and twin (T) variants labelled. The high-resolution TEM (HRTEM) image of Al-4.3Zr in Figure 3-5(c) shows a sharp ITB taken from the location outlined by the box in Fig. 3-5(a). The HRTEM image in Figure 3.5(f) taken from the box location in Fig. 3-5(d) of the Al-10Zr sample shows the formation of diffuse ITBs, or 9R phase. ITBs are composed of a repeating array of 3 Shockley partial dislocations (b_2:b_1:b_3), where b_1 is mobile and reduces the boundary energy by gliding away from the sessile b_2 and b_3 [155,271]. This arrangement produces a "diffuse" ITB, termed 9R phase due to the periodicity of the phase. This 9R phase stabilization leads to a larger volume fraction of 9R phase at higher Zr content, which directly impacts the mechanical properties, to be discussed later.
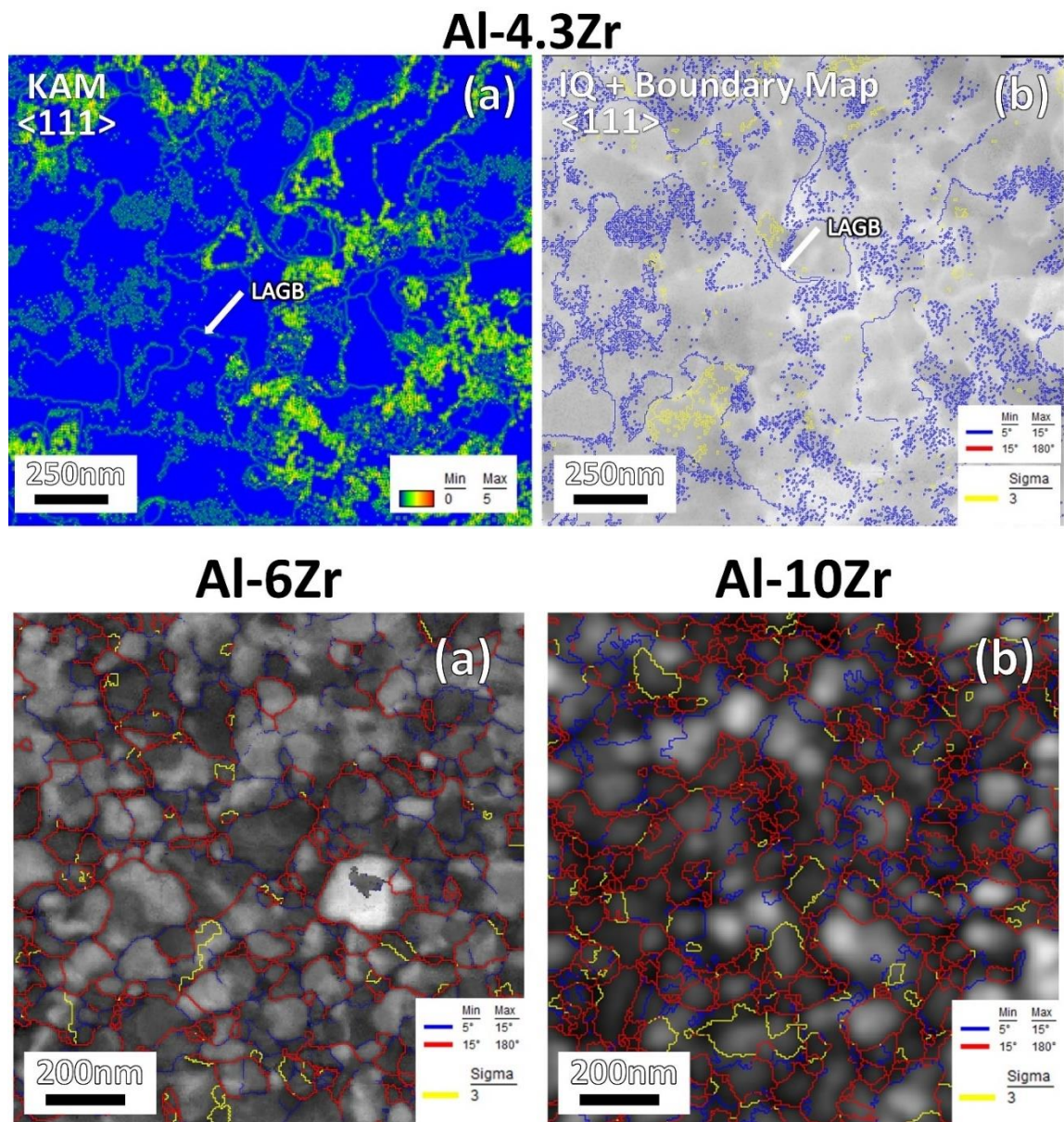
Figure 3-4. Automated crystallographic orientation mapping conducted using a TEM highlighting low angle grain boundaries (LAGB) in NT Al-4.3Zr using (a) kernel average misorientation (KAM) map and (b) image quality (IQ) overlayed with a grain boundary (GB) map. Image quality (IQ) maps overlayed with grain boundary (GB) maps revealing the boundary type information for (a) NT Al-6Zr and (b) NT Al-10Zr.
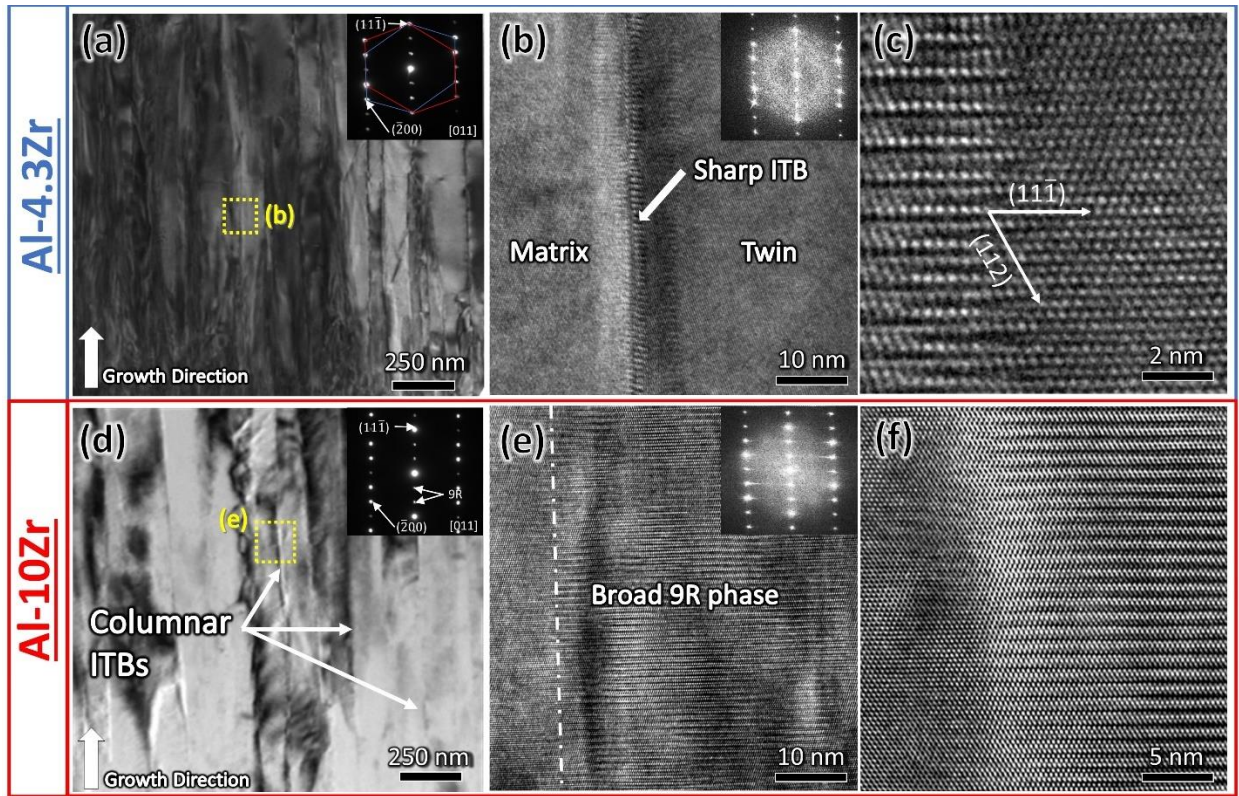
Figure 3-5. (a) Cross-section TEM (XTEM) micrograph and corresponding SAD insert of Al-4.3Zr revealing an abundance of columnar ITBs. 9R spots are also identified in the SAD pattern. (b,c) Hi-resolution TEM (HRTEM) images of a sharp ITB in the Al-4.3Zr film. (d) XTEM micrograph and corresponding SAD insert of Al-10Zr revealing a further refined columnar structure containing ITBs, confirmed by the SAD insert. 9R spots are also identified. (e-f) HRTEM images showing a broad patch of 9R phase spanning 50 nm across an entire column in the Al-10Zr film, representative of the overall microstructure seen in these films.

Figure 3-7(a-c) contains *in-situ* SEM snapshots from micropillar compression tests conducted on Pure Al, Al-4.3Zr and Al-10Zr. Looking at the real-time morphological evolution of the pillars provides insight into the deformability of these alloys under compression. The Pure Al (Figures 3-7(a)) micropillar displays evident shear band formation. In comparison, the Al-4.3Zr micropillar exhibits pillar barreling indicative of significant plasticity. The Al-10Zr pillar is also highly deformable, however the morphology transitions to limited dilation of the pillar top. The true stress-strain curves in Figure 3-7(d) show Al reaches a maximum flow stress of ~150MPa with a highly serrated flow curve, commonly seen due to shear banding. The NT Al-4.3Zr and Al-10Zr samples reach significantly higher flow stress, ~600 MPa and 1.1 GPa, respectively. Interestingly, they maintain significant compressive deformability at these high strengths. Additionally, the work hardening response is noticeably improved from the Al-4.3Zr to the Al-10Zr, highlighted in the work hardening rate plot in Figure 3-7i, which will be discussed in greater detail later.
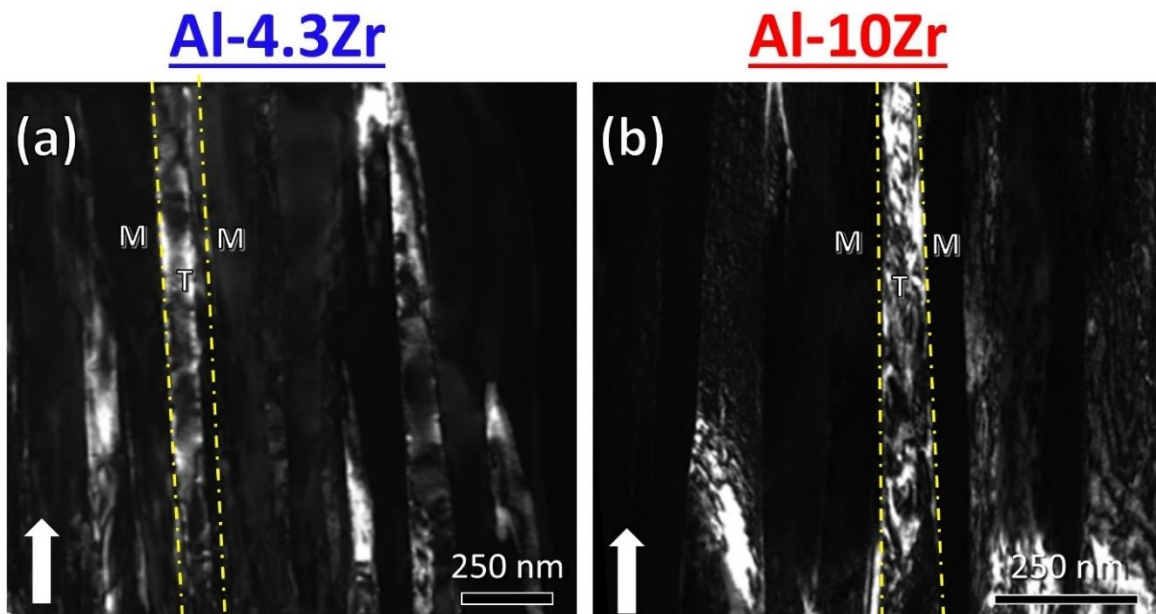
Figure 3-6. Dark field (DF) TEM images reflecting the fine nanotwinned columnar structure in both the (a) Al-4.3Zr and (b) Al-10Zr samples. Both images were taken along the **g** = [200] with the matrix and twin variants labeled across vertical ITBs.
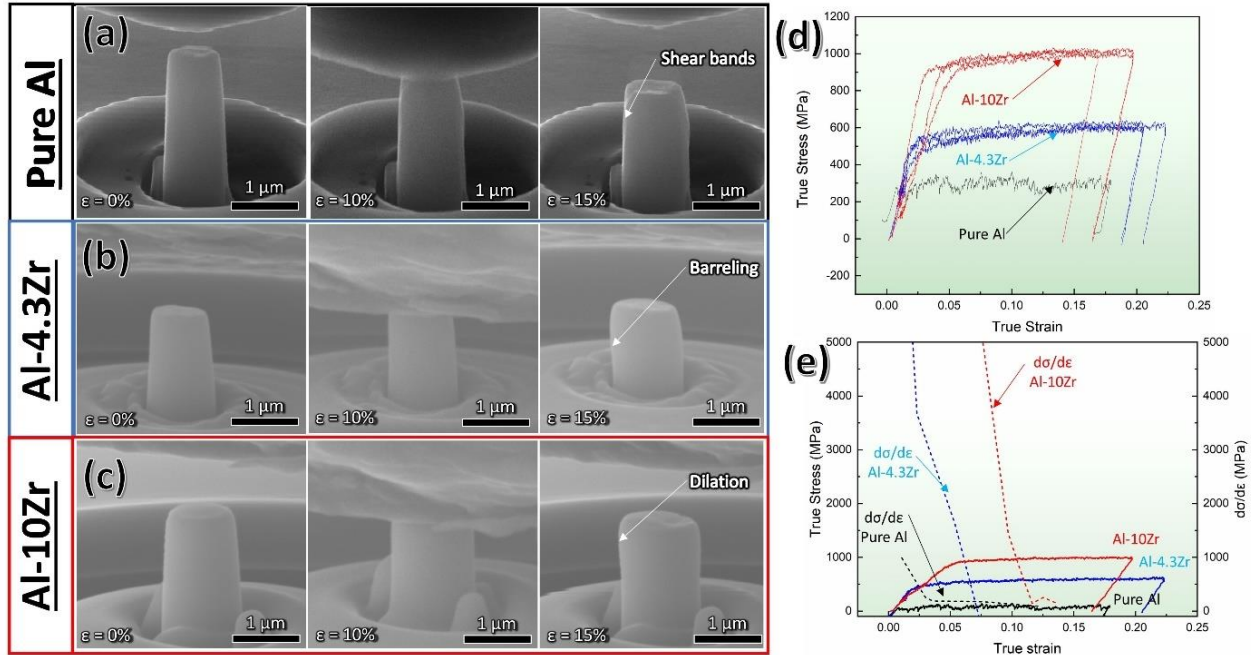
Figure 3-7. *In-situ* snapshots of micropillar compression tests for (a) Pure Al, (b) Al-4.3Zr, and (c) Al-10Zr. These snapshots identify clear shear banding in the Pure Al sample in (a), and more uniform deformation represented by (b) barreling and (c) dilation of the pillar top. (d) True stress-strain curves for the 3 Al-Zr alloys demonstrating increasing flow stress with Zr content. I The Al-10Zr sample has higher work hardening rate than the Al-4.3Zr and Al samples.

Figure 3-8 contains the post-mortem TEM analysis of the deformed Al-4.3Zr micropillar. Figure 3-8(a) shows a BF TEM image overview of the deformed pillar taken along the [011] zone axis. Figure 3-8(b) shows a DF TEM image taken along the $\vec{g} = \frac{1}{3}[\bar{1}\bar{1}1]$, revealing the extent of detwinning occurring throughout the top half of the pillar. The microstructure remains relatively unchanged at the base of the pillar. Figures 3-8(c-e) show the SAD pattern evolution from the pillar top (Figure 3-8(c)) down to the base (Figure 3.8I), corresponding to the regions highlighted by the yellow circles in Figure 3-8(a). The progression of the diffraction patterns shows the same trend depicted in the dark field, with the pillar top experiencing almost complete detwinning and significant grain rotation. The SAD pattern of the pillar base reflects little grain rotation and the twin and 9R superlattice spots remain intact. Figures 3-8(f) and 3-8(g) contain HRTEM images taken from the regions highlighted using the yellow squares in Figure 3-8(a). Figure 3-8(f) taken from the top region of the deformed pillar confirms the extent of detwinning that takes place as the entire region is composed of single-crystal FCC structure with no 9R phase. In comparison,

103

HRTEM image taken from the pillar base in Figure 3-8(g) shows pristine 9R phase that remains intact through deformation.
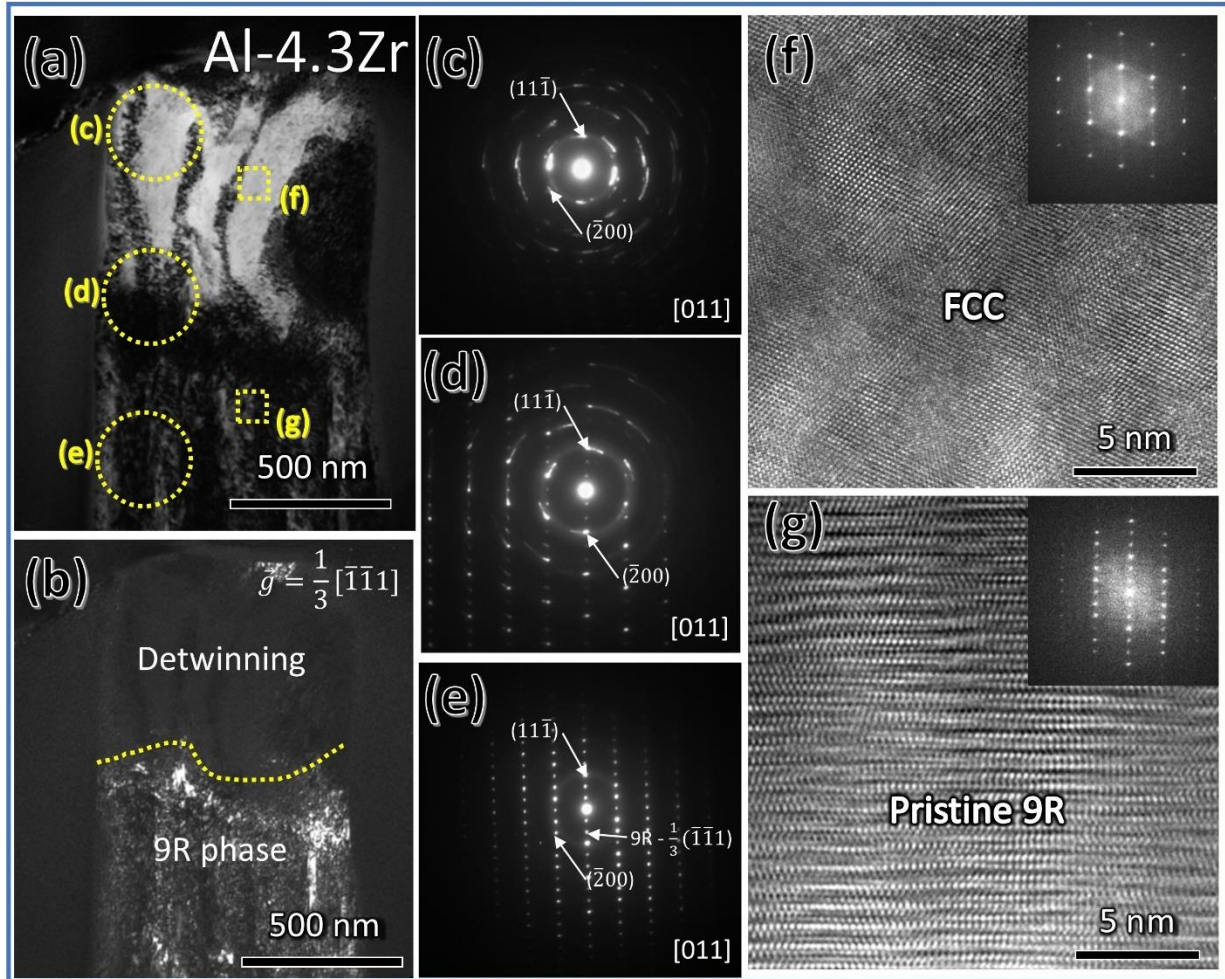
Figure 3-8. (a) Low magnification BF-TEM image showing an overview of the deformed Al-4.3Zr micropillar, with a (b) corresponding DF-TEM image, $\vec{g} = [\bar{1}1\bar{1}]$. (c-e) SAD patterns corresponding to the regions circled in (a). (f, g) HRTEM images taken from the (f) top (severely detwinned) and (g) base region (microstructurally stable) of the deformed pillar.

The BF TEM image for the deformed Al-10Zr pillar in Figure 3-9(a) reveals a difference in post-deformed microstructure with higher Zr content. The columnar ITB structure is continuous throughout the pillar, unlike the Al-4.3Zr sample which experienced extensive detwinning. Figure 3-9(b) shows an EDS map, which exhibits no solute segregation after deformation. Figures 3-9(c-e) show the SAD pattern evolution moving from the pillar top down to the base. Figure 3-9(c) shows clear grain rotation near the pillar top. Both the twin and 9R spots are retained in each

diffraction pattern throughout the pillar. HRTEM images were also collected at four representative locations highlighted using yellow squares in Figure 3-9(a). Figure 3-9(f) taken at the top of the deformed pillar shows 9R phase that is highly deformed due to interactions with dislocations. Figure 3-9(g) reveals minor detwinning and discontinuous 9R phase in the middle of the pillar. The pillar base shown in more detail in Figures 3.9(h-i) contains a significant fraction of 9R phase, similar to the as-deposited Al-10Zr microstructure.
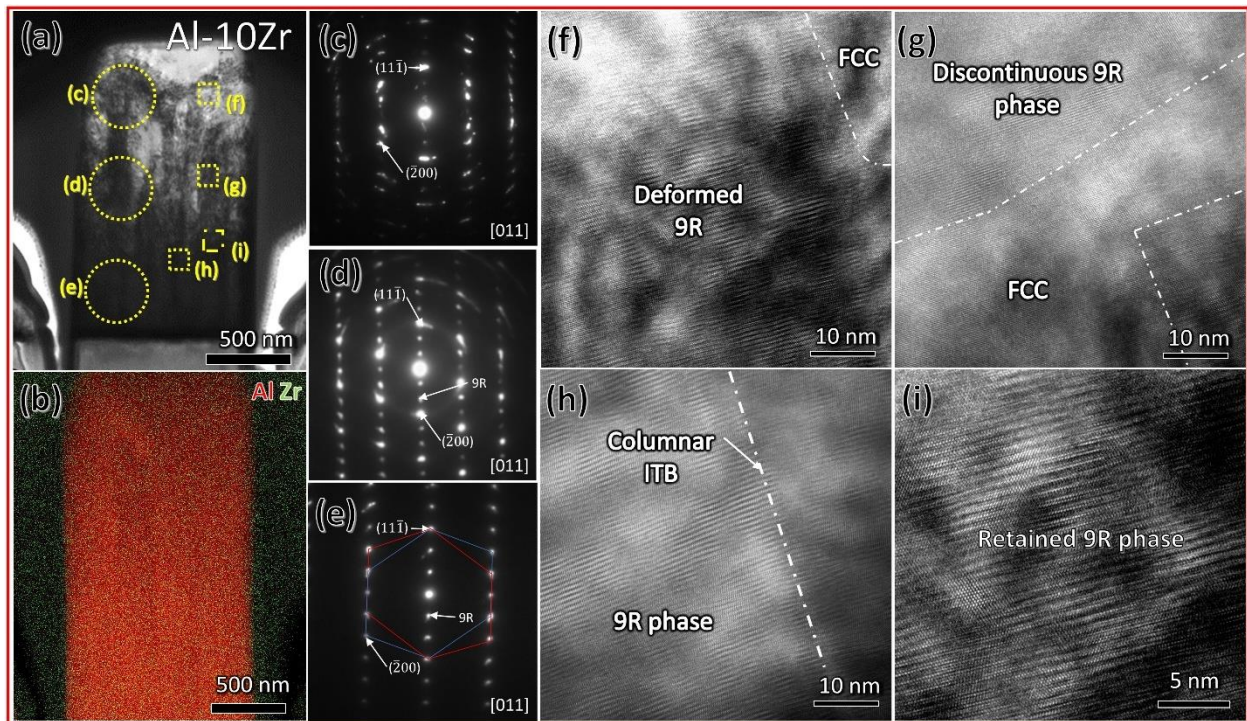
Figure 3-9. (a) Low magnification XTEM image showing an overview of the deformed Al-10Zr micropillar, with a (b) corresponding EDS map. (c-e) SAD patterns corresponding to the regions circled in (a). (f, g) HRTEM images taken from the (f) top and (g) middle portion of the deformed pillar showing distorted 9R phase. (h, i) HRTEM images taken from the pillar base showing a relatively undeformed base.

3.5 Discussion

To understand the difference in deformation response with evolving Zr content, it is first necessary to extract the difference in microstructure in these alloys. As evident in the grain size evolution (Figure 3-1(d)) and XTEM images (Figure 3-5), Zr addition is a significant factor in both grain refinement and alteration of the ITB structure. Density functional theory (DFT) calculations were performed to explain the influence of Zr solute on the formation of ITBs and 9R phase during deposition. A schematic in Figure 3-10(a) illustrates the atomic configurations used in the DFT calculations for determining the migration energies of trimers and heptamers. Magnetron sputtering inherently possesses an extremely high quenching rate [272]. This far-from-equilibrium process promotes an extension of solid solubility limits, a significant factor of the microstructural evolution presented in this study [272,273]. As is evident in the XRD presented in Figure 3-1, these Al-Zr films present no evidence of intermetallic phase formation and are complete solid solutions even at 10at% Zr. Another aspect of this high degree of solubility relates to the defect formation energies. Figure 3-10(b) contains a plot detailing the defect formation energies corresponding to Zr solute residing at either interstitial (octahedral vs tetrahedral) or substitutional sites. The DFT calculations reveal that Zr prefers to reside at substitutional sites in the Al lattice. The slow diffusing Zr solute [274] obstructs Al self-diffusion, providing an increased energy barrier for the correction of any stacking faults or twins formed during deposition. Additionally, the migration energies of surface trimer (Figure 3-10(c)) and heptamer (Figure 3-10(d)) clusters were calculated using DFT. Multiple pathways were calculated for the trimer case, with the red symbols indicating a cluster shifting from a hollow site to residing over an HCP atom, and black showing the reverse movements. Each of the conditions calculated in Figures 3-10(c-d) results in an increase in migration energy for these surface clusters, with the heptamer migration energy increasing by 0.19eV. These calculations suggest that Zr increases the energy barrier for defaulting during film growth. In spite of the high SFE inherent to Al and its alloys, the DFT presented here provides a compelling explanation for how Zr additions aid in stabilizing the unique NT microstructure synthesized in this study.
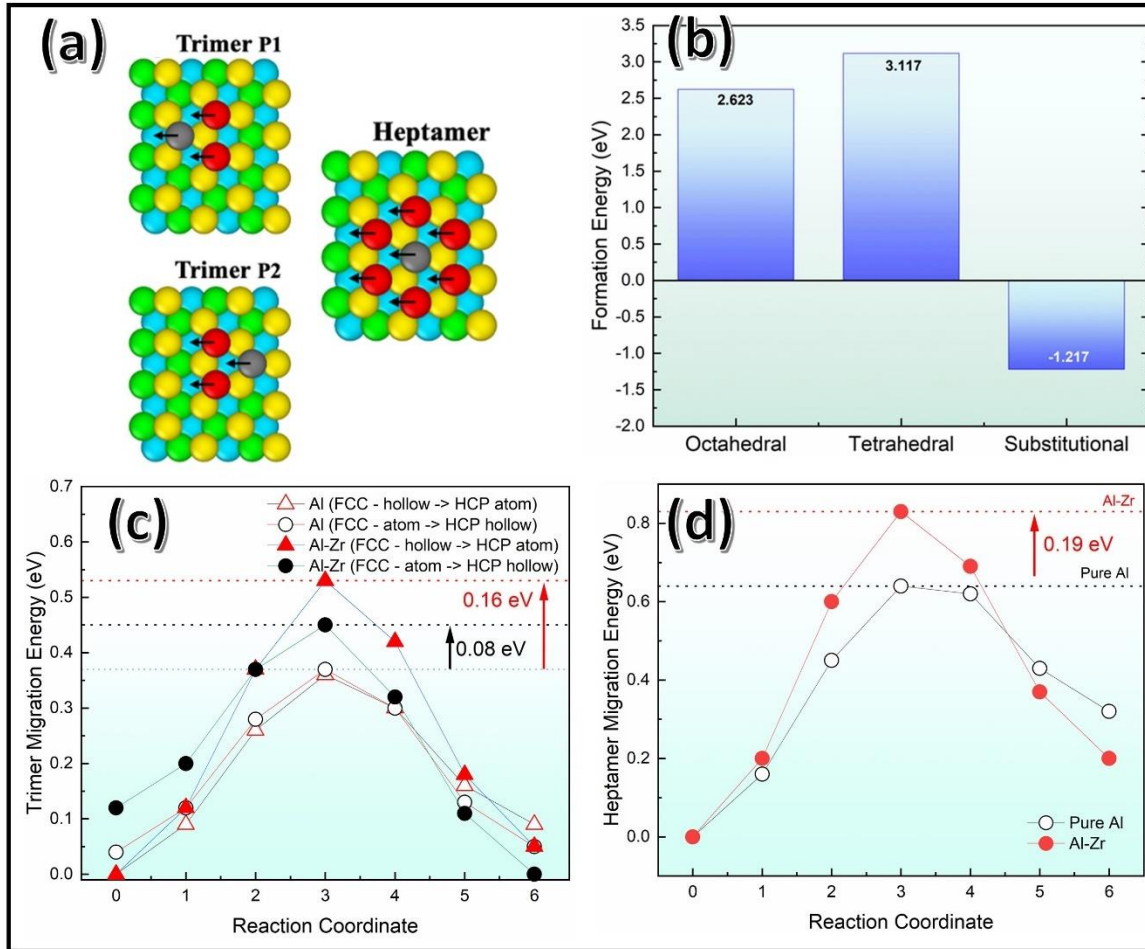
Figure 3-10. (a) Schematics detailing the methodology implemented for these calculations. (b) Formation energies for various Zr defects in Al, demonstrating that Zr prefers to reside at substitutional sites on the Al lattice. (c) Density functional theory (DFT) results for the migration energy of surface trimers during deposition. For the calculations, the red symbols represent path 'Trimer P1' with the atom shifted from a hollow site to over an HCP atom, while the black symbols represent path 'Trimer P2' moving in the opposite direction. (d) DFT results for the migration energy of surface heptamers during deposition.

The high strengths of these NT Al-Zr alloy films arise from several factors that are closely tied to the unique microstructure of the films. These include solid solution strengthening (SSS), ITB induced boundary strengthening, and 9R phase induced strengthening. First, although the equilibrium solid solubility of Zr in Al is minimal, due to the high quenching rate in sputtering, a high concentration of Zr atoms can be trapped in matrix, forming a supersaturated solid solution. The Zr solute atoms induce lattice distortion and the consequent SSS in NT Al-Zr can be estimated by using the Fleischer equation [38],

$$\Delta\sigma_{SS} = 0.0235 * G_{solv} * {\varepsilon_s}^{3/2} c^{1/2} \tag{3-2}$$

where $\Delta\sigma_{ss}$ represents the strength increment, G_{solv} is the shear modulus of Al, c is the solute concentration. E_s is defined as:

$$\varepsilon_s = \left| \frac{\frac{1}{G_{solv}} * \frac{dG}{dc}}{1 + \frac{1}{2}\left|\frac{1}{G_{solv}} * \frac{dG}{dc}\right|} - 3 * \frac{1}{a_{solv}} * \frac{da}{dc} \right| \tag{3-3}$$

where G is the shear modulus of the alloy, a_{solv} and a are the lattice parameter of Al and the alloy respectively. For this calculation, it is assumed that both dG/dc and da/dc are linear with solute concentration. These calculations demonstrate the minor hardening contribution from SSS, with only a $\Delta\sigma_{ss}$ increase of 0.0283 GPa for 10at% Zr, after considering the Tabor (2.7) [39] and Taylor (3.1) factors [40]. This calculation suggests that SSS alone cannot account for the high strength of the NT Al-Zr alloys.

The Hall-Petch plot in Fig. 3-11(c) captures the impact of the TB induced strengthening effects. Since the influence of SSS is minor, the large increase in Hall-Petch slope (k_y) to ~9.29 GPa/nm$^{1/2}$ (comparing with 4.7 GPa/nm$^{1/2}$ NC Al) can be attributed to the presence of both sharp ITBs and expanded 9R phase, similar to thin and thick GBs reported recently in Ni alloys [41]. Ding et al show that a thick GB leads to a high Hall-Petch slope compared with the same alloys with thin GBs. MD simulations prove that the thick GB is more effective to strengthen polycrystalline materials [41]. The ability of ITBs to provide strengthening by blocking dislocations has been clearly supported by both in-situ nanoindentation and MD simulations, demonstrating the ability of ITBs in Al films to resist dislocation pileups and induce substantial work hardening [22]. In addition, MD simulations of compression tests of NT Al-Fe further elucidate the extensive interactions between dislocations and 9R phase [30]. The high fraction of 9R phase in these NT Al-Zr alloys provides an opportunity to isolate 9R's impact on Hall-Petch strengthening. The presence of the 9R phase (Figure 3-5(f)) and the periodic SF structure means that mobile dislocations will be obstructed by 9R phase, or diffuse ITBs, in addition to the narrow (sharp) ITB columnar boundaries. 9R phase effectively block the transmission of mobile dislocations, and adds a new component to the strengthening equation as follows:

$$\sigma = \sigma_0 + \Delta\sigma_{ss} + k_d d^{-1/2} + k_{9R} L^{-1/2} \tag{3-4}$$

where k_{9R} and L represent the 9R strengthening coefficient and spacing between 9R regions, respectively. Since MD simulations have demonstrated the similarity between ITBs and high angle GBs in preventing dislocation emission [42,43], a *k* value of ~4.7 GPa/nm$^{1/2}$ [37] for NC Al (Fig

3-11i) was adopted for k_{ITB}, and d represents the columnar grain size measured in this study, or the spacing between narrow ITBs. L, the spacing between regions of 9R phase, was determined based on a ratio between the average 9R width (d_{9R}) and the volume fraction of 9R phase (f_{9R}), shown in Figure 3-11(a). Figure 3-11(b) illustrates the terms described here and relates them to the microstructure. The equation for L is given by:

$$L = \frac{d_{9R}}{f_{9R}} - d_{9R} \qquad (3\text{-}5)$$

With L determined, Equation 3-5 was used to estimate $k_{9R,}$ which was calculated to be 6.9 Gpa/nm$^{1/2}$. It is reasonable that k_{9R} is greater than k_{ITB} (4.7 Gpa/nm$^{1/2}$) as the diffuse ITB and periodic SF structure provide additional obstacles to dislocation motion, as supported by MD simulations [30]. This simple estimation demonstrates the substantial impact of 9R phase on the mechanical properties of these NT Al alloys.
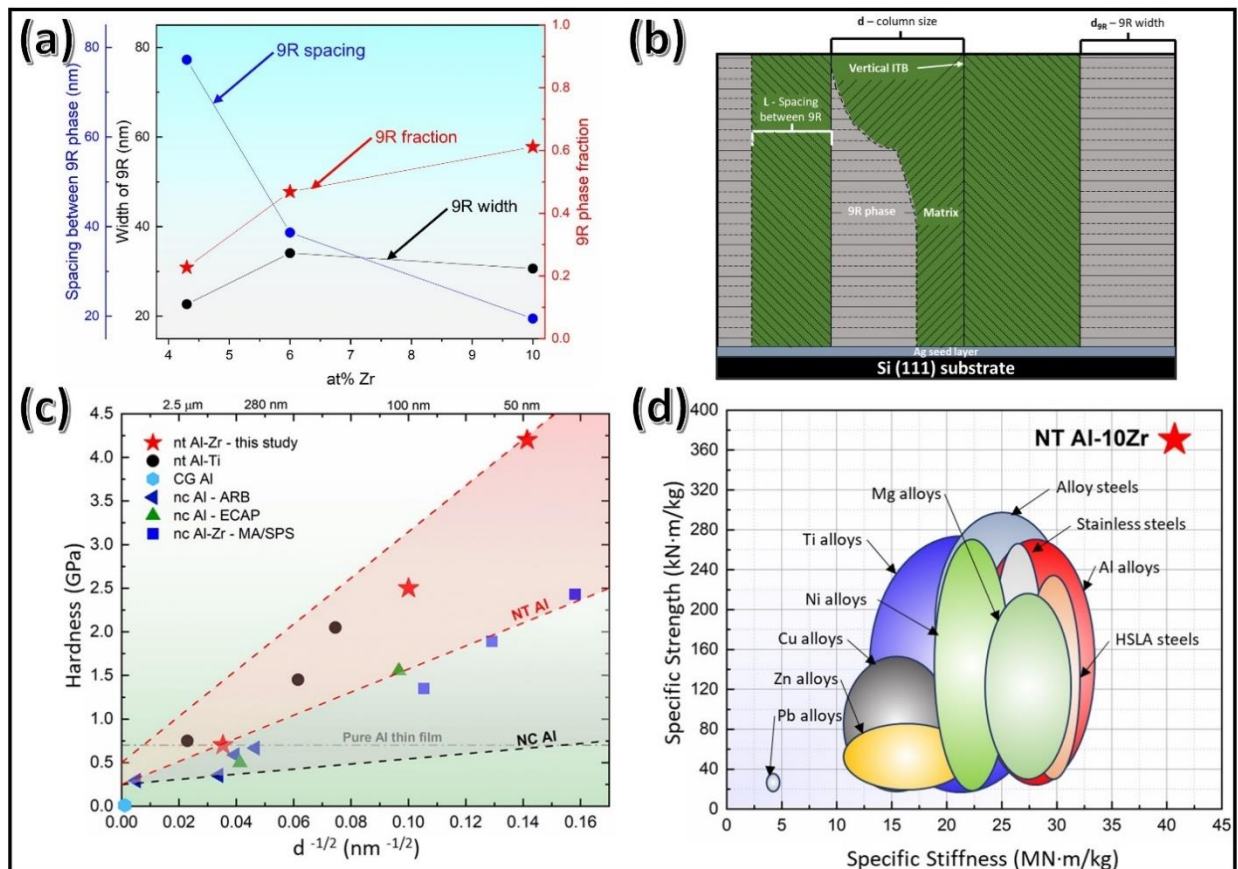
Figure 3-11. (a) Statistics detailing the width of 9R patches (width of diffuse ITBs), spacing between 9R phase patches and 9R phase fraction measured using HRTEM images. (b) Schematic demonstrating the microstructural features seen in the NT Al-Zr films, with key terms used for the statistics in (a) labeled. (c) Hall-Petch plot comparing the results from this study with other NT Al and NC Al samples from literature [195,275–277]. (d) Specific strength – specific stiffness bubble plot demonstrating the high strength and light weight capability of NT Al-Zr alloys.

Zr solute plays a further role on altering the plasticity exhibited by these alloys. The extent of these changes is heavily tied into the relationship between Zr solute content and the fraction 9R phase stabilized in the microstructure as a result. Figure 3-11(a) shows the overall phase fraction of 9R phase (f_{9R}) increases to 60% with 10at% Zr. Figure 3-11(b) illustrates the microstructural characteristics of NT Al-Zr alloys with ITBs and 9R phase. The values shown in Figure 3-11(a) were determined based on extensive HRTEM analysis, measuring the average column size (d) and average 9R width (d_{9R}). The spacing between 9R phase (L), which was used to determine the contribution of 9R to the increasing Hall-Petch slope in the previous study [271], was calculated based on Equation 4. As shown in Figure 3-11(a), the width of 9R increases with Zr content until ~6at% Zr, beyond which it plateaus at ~30nm. L continues to drop since Zr further refines the column size, reducing the matrix width between each patch of 9R phase. Thus, f_{9R} increases with the further addition of Zr solutes in the alloys.

The increase in the work hardening rate determined from micropillar compression testing (Figure 3-11i) can be attributed to several possible sources tied into this microstructure evolution. First, the increase in f_{9R} leads to a larger percentage of the matrix composed of the complex stacking fault array of diffuse ITBs. As a result, dislocations will have an increased rate of interaction with defects, leading to the slight jump in work hardening response. These types of dislocation-9R phase interactions were captured using molecular dynamics simulations carried out in NT Al-Fe by Li et al [159]. Second, the reduction in grain size from 100nm (Al-4.3Zr) down to 50nm (Al-10Zr) has further implications on the work hardening. Decreasing grain size has been shown to play an important role in work hardening. The correlation between work hardening and grain size can be expressed by [22]

$$\frac{d\sigma}{d\varepsilon} \propto \frac{d\rho}{d\varepsilon} = M\left(\frac{k_0}{b}\frac{1}{d} + \frac{k_1}{b}\sqrt{\rho} - f\rho\right) \tag{3-6}$$

where ρ is the dislocation density, M is the Taylor factor, b is the magnitude of the Burgers vector, f is a constant, sensitive to the strain rate and temperature, d is the grain size, and k_0 and k_1 are Hall-Petch constants related to the nature of the grain boundaries. Sun et al. utilized a modified Kocks-Mecking model to explain the increase in work hardening seen in NC FeCrAl alloys [278,279]. The work hardening increase in their UFG FeCrAl alloys was attributed to a higher dislocation storage rate at finer grain sizes, which is reflected in Equation 3-6. This phenomenon provides another supporting argument for the augmentation of work hardening in the NT Al-10Zr with finer grains.

Third, we examine the evolution of the ITB structures induced by mechanical loading and its correlation to the work hardening. The post-mortem TEM of the deformed Al-4.3Zr pillar (Figure 3-8(a, b)) shows the top half of the pillar experienced extensive detwinning (softening). In contrast, the pillar base maintaining the as-deposited microstructure, leading to hardening. The concomitant high strengths and large deformability demonstrated here can thus be linked to the simultaneous strain hardening (explained earlier) and strain softening (detwinning) during microcompression. However, Al-4.3Zr and Al-10Zr possess similar as-deposited microstructures yet a noticeable difference in the work hardening response (Figure 3-7i). Such a difference lies in the extent of detwinning occurred in the two alloys. In contrast, as shown in Figure 3-9, the twin and 9R phase retain even at the top of the deformed pillar in Al-10Zr, which experiences the largest stress state due to pillar taper inherent to the fabrication process [222]. The stress concentration and rotational gradients present at the pillar top have also been attributed to test constraints, rather than induced from taper alone [280]. The resulting reduction in strain softening in the Al-10Zr alloy is because the higher Zr content stabilizes the mobile partial dislocations composing 9R phase and inhibits detwinning, leading to more extensive work hardening. The stabilization of 9R phase by Zr solutes is consistent with DFT calculations showing the increase of migration energy barriers for trimers and heptamers in Al. Despite geometrical constraints (pillar taper) limiting the ability to accurately determine the work hardening exponent, the pillars in this study exhibit similar geometries and a self-comparison on work hardening ability should still be valid [222]. Overall, the extended degree of solid solubility achievable through magnetron sputtering leaves its fingerprint on both the microstructural evolution and the mechanical response of these NT Al alloys. This study highlights the significance of solutes on stabilization of 9R phase and consequent impact on accomplishment of high strength and work hardening ability in NT Al alloys.

3.6   Conclusion

Sputtered Al-Zr alloys with abundant ITBs and 9R phase have high strength (1.1 Gpa flow stress) and highly deformability. The post-mortem TEM analyses of the deformed pillars uncover the importance of the columnar ITBs in the work hardening response of these alloys. DFT calculations explain the role of Zr solutes in formation and stabilization of ITBs in Al. The interplay of ITBs and 9R phase with dislocations induces high strength and significant work

111

hardening ability in Al alloys. This work highlights the mechanical properties of Al alloys and underscore an important method for fabricating high strength Al alloy coatings.

3.7   Acknowledgement

4. ASSESSING STRAIN RATE SENSITIVITY OF NANOTWINNED AL-ZR ALLOYS THROUGH NANOINDENTATION

4.1 Overview

Nanotwinned metals have exhibited many enhanced physical and mechanical properties. Twin boundaries have recently been introduced into sputtered Al alloys in spite of their high stacking fault energy and. These twinned Al alloys possess unique microstructures composed of vertically aligned $\Sigma 3(112)$ incoherent twin boundaries (ITBs) and have demonstrated remarkable mechanical strengths and thermal stability. However, their strain rate sensitivity has not been fully assessed. A modified nanoindentation method has been employed here to accurately determine the strain rate sensitivity of nanotwinned Al-Zr alloys. The hardness of these alloys reaches 4.2 GPa while simultaneously exhibiting an improved strain rate sensitivity. The nanotwinned Al-Zr alloys have shown grain size dependent strain rate sensitivity, consistent with previous literature findings. This work provides insight into a previously unstudied aspect of nanotwinned Al alloys.

4.2 Introduction

The mechanical strength of single phase metallic materials is often largely determined by their grain size (d), and such dependence is often described by the classic Hall-Petch relationship [39,40,281,282]:

$$\sigma_y = \sigma_0 + k_y d^{\frac{-1}{2}} \tag{4-1}$$

Where σ_y is the yield strength, σ_0 is the friction stress and k_y is the Hall-Petch coefficient. Various efforts have been made to pushing material grain sizes into the nanometer regime [233,283], via severe plastic deformation [99,278,284,285], physical vapor deposition [286–290], and inert gas condensation [94,291–293]. These studies have focused on nanocrystalline (NC) materials with grain sizes of less than 100 nm that show remarkable mechanical properties as well as novel grain boundary (GB) mediated deformation mechanisms [294]. Another mechanical property closely linked to GB spacing is strain rate sensitivity (SRS) [295]. SRS is an important

parameter that describes both the deformability and thermally activated deformation (creep) of metallic materials [95,296,297]. Correspondingly, increasing the SRS exponent (m) is typically linked to enhanced ductility [95,295]. The variation in SRS of metallic materials is also heavily dependent on its crystal structure. Body centered cubic (BCC) metals are much more sensitive to changes in temperature and strain rate than face centered cubic (FCC) metals due to their lower activation volumes [102,295,298,299]. FCC metals exhibit increasing SRS with decreasing grain sizes, while BCC metals show the opposite trend [95,102,299]. Chen et al. demonstrated that UFG and NC FCC Cu revealed increasing m with decreasing grain size [297]. Quantifying the relationship between SRS and microstructures is crucial to fully understand the mechanical response NC metallic materials.

Nanotwinned (NT) metals have been extensively investigated due to their simultaneous increase in strengths and ductility [169,172,173,248,300]. Most prior studies on NT metals have focused on systems with low stacking fault energy (SFE) [192,193,301], characteristic of a few FCC metals including Cu (22 mJ/m^2) [302,303], Ag (16 mJ/m^2) [170,304] and several stainless steels (~50 mJ/m^2) [305]. A high SFE provides a significant barrier to twin formation [306]. Recently, magnetron sputtering has been used to stabilize far from equilibrium NT structures in high SFE Al films [189,190,307]. The addition of transition metal solute reduces twin spacing and can further promote the strong {111} texture needed to form vertically aligned Σ3(112) incoherent twin boundaries (ITBs) [159,195,200,264,271,308,309]. Zhang et al. reported a flow strength of ~2 GPa in NT Al-Ni alloys using *in-situ* micropillar compression while maintaining remarkable deformability and thermal stability [139,196]. Molecular dynamics (MD) simulations and *in-situ* mechanical testing identified the mobility of partial dislocations composing 9R phase as a significant factor in accommodating the deformability of NT Al alloys while simultaneously providing a barrier to dislocation motion [159]. Zr solute has proven effective in promoting a high twin density and large volume fraction of 9R phase [271,308]. Additionally, Zr enables prominent thermal stability of nanostructures in NT Al-Co-Zr alloys [307]. Understanding the behavior of Zr solute in Al is also relevant to a range of cast and additively manufactured Al alloys [310–312]. NT metals have also exhibited enhanced SRS due to the activation of Shockley partial dislocations [313,314]. However, the contribution of ITBs on the SRS of NT Al alloys has not been explored to date and remains a gap in current understanding.

In this study, we applied a nanoindentation technique to probe the SRS of NT Al-Zr. We used the modified nanoindentation technique to overcome the difficulty of large measurement uncertainty at low strain rate and were able to arrive at a reliable SRS for specimens. The NT Al alloys exhibit grain size dependent SRS comparable to Al and Al alloys with similar grain sizes. The roles of ITB microstructure and partial dislocations on enhanced SRS in NT Al alloys are discussed.

4.3 Experimental

2 μm Al-Zr alloy films with 50 nm Ag seed layers were magnetron sputtered at room temperature onto HF etched Si(111) substrates. The Ag seed layer serves to promote a strong (111) texture in the Al-Zr alloy films due to the similarity in lattice parameters. 99.999% Al, 99.995% Zr and 99.999% Ag targets were used for deposition at a gas pressure of 3.5 mTorr. The chamber base pressure was evacuated to $5 \times 10\text{-}9$ Torr. A Panalytical Empyrean X'pert PRO MRD diffractometer was used to collect out-of-plane θ-2θ and pole figure X-ray diffraction (XRD) scans. Transmission electron microscopy (TEM) samples were mechanically polished and thinned using low-energy Ar ion milling. TEM imaging was conducted using an FEI Talos 200X analytical microscope operated with an accelerating voltage of 200kV. Energy dispersive x-ray spectroscopy (EDS) was conducted using a Fischione ultra-high-resolution high angle annular dark field (HAADF) detector and super X EDS detector. Hardness and elastic modulus were calculated from nanoindentation measurements performed using a Berkovich tip on a Hysitron TI Premiere nanoindenter under displacement control. The indentation depth was less than 15% of the film thickness to prevent any substrate effects. Figure 1(d) depicts the test setup schematically and Figure 1(e) contains typical plots of the displacement vs time for tests at various strain rates.

A modified nanoindentation methodology was implemented in this study to reliably probe film hardness at low strain rates [95]. Thermal drift provides a significant hurdle to reliable nanoindentation experiments when indenting at low strain rates ($\dot{\varepsilon} < 0.05$ s^{-1}) leading to significant scatter in both hardness and modulus measurements. Conventional nanoindentation calculates the reduced modulus (E_r) and hardness (H) using the following method:

$$h_c = h - \frac{0.75 \cdot P}{S} \tag{4-2}$$

$$A = m_0 h_c^2 + m_1 h_c \tag{4-3}$$

$$E_r = \frac{\sqrt{\pi}}{2} \frac{S}{\sqrt{A}} \qquad (4\text{-}4)$$

$$H = P\big/A \qquad (4\text{-}5),$$

where h_c is the contact depth, P is the normal applied load, S is the stiffness, A is the contact area, and m_0 and m_1 are constants determined through a calibration process using a known material. As thermal drift leads to unreliable determination of the contact area, the modified method utilizes the standard nanoindentation method at high strain rates to measure Er, and then back calculates A and H using Eq. 5 and:

$$A = \frac{\pi}{4} \cdot \frac{S^2}{E_r^2} \qquad (4\text{-}6).$$

A flow chart adapted from [95] has been included as Supplementary Figure 4 to further clarify the procedure. Constant strain rate indents were performed on each sample at 6 different strain rates (0.005 s^{-1}, 0.01 s^{-1}, 0.05 s^{-1}, 0.1 s^{-1}, 0.5 s^{-1} and 1 s^{-1}) with 75 indents performed per test to ensure statistical reliability.

4.4   Results

Structural and textural information for the nanotwinned (NT) Al-Zr alloys were collected using both pole figure and θ-2θ XRD scans. Figure 4-1(a) demonstrates that the pure Al film pole figures possess 3-fold symmetry, characteristic of strong (111) texture. Notably, Zr solute additions induce a shift to 6-fold symmetry in the Al-4.3Zr and Al-10Zr pole figures indicating the formation of a high density of twin boundaries, highlighted in Figures 4-1(b-c). The twin spot intensity is stronger in the Al-10Zr sample than the other samples, indicating that the twin density increases with higher Zr content. In the θ-2θ XRD spectra in Figure 4-2, only peaks from the Si(111) substrates and the Al films were present suggesting no second phase formation. Peaks corresponding to the Ag (222) are present due to the seed layer.
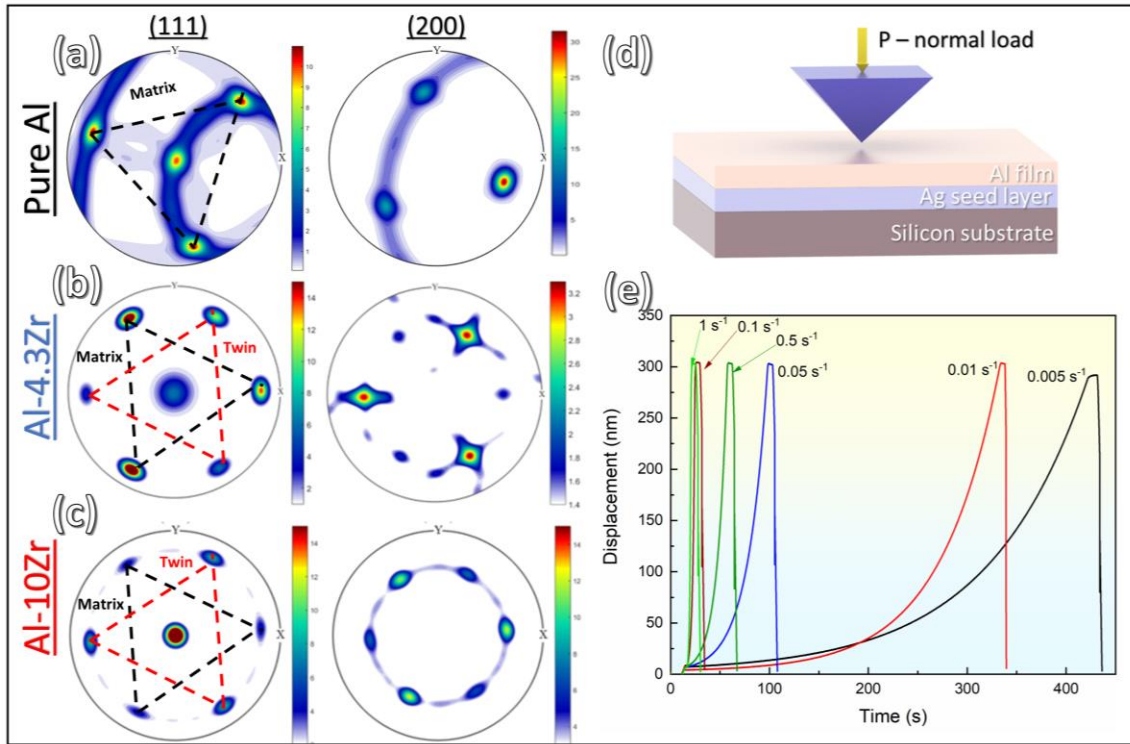
Figure 4-1. Comparison of (111) and (200) x-ray pole figures among (a) pure Al, (b) nanotwinned (NT) Al-4.3Zr and (c) NT Al-10Zr revealing strong (111) texture in all three films. The six-fold symmetry in the Al-Zr alloys indicates twin formation. (d) Schematic detailing the nanoindentation test setup used in this study. (e) Displacement vs time plots for Al-10Zr highlighting the various constant strain rates used during each displacement controlled nanoindentation test on each sample.
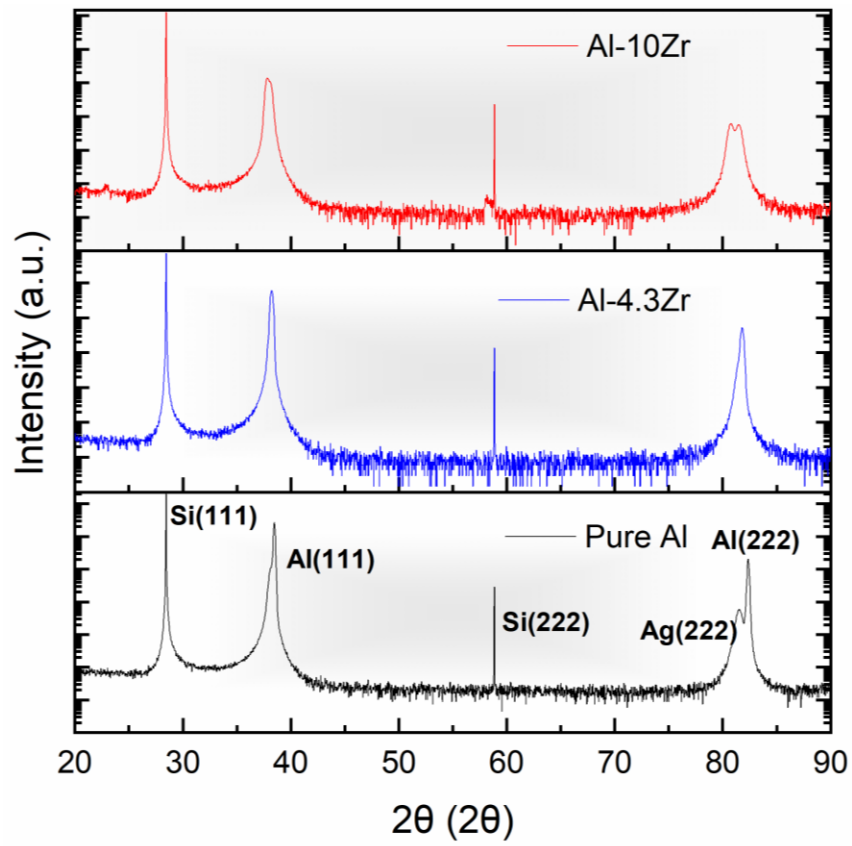
Figure 4-2. X-ray diffraction (XRD) spectra for Pure Al and NT Al-Zr alloys deposited in this study.
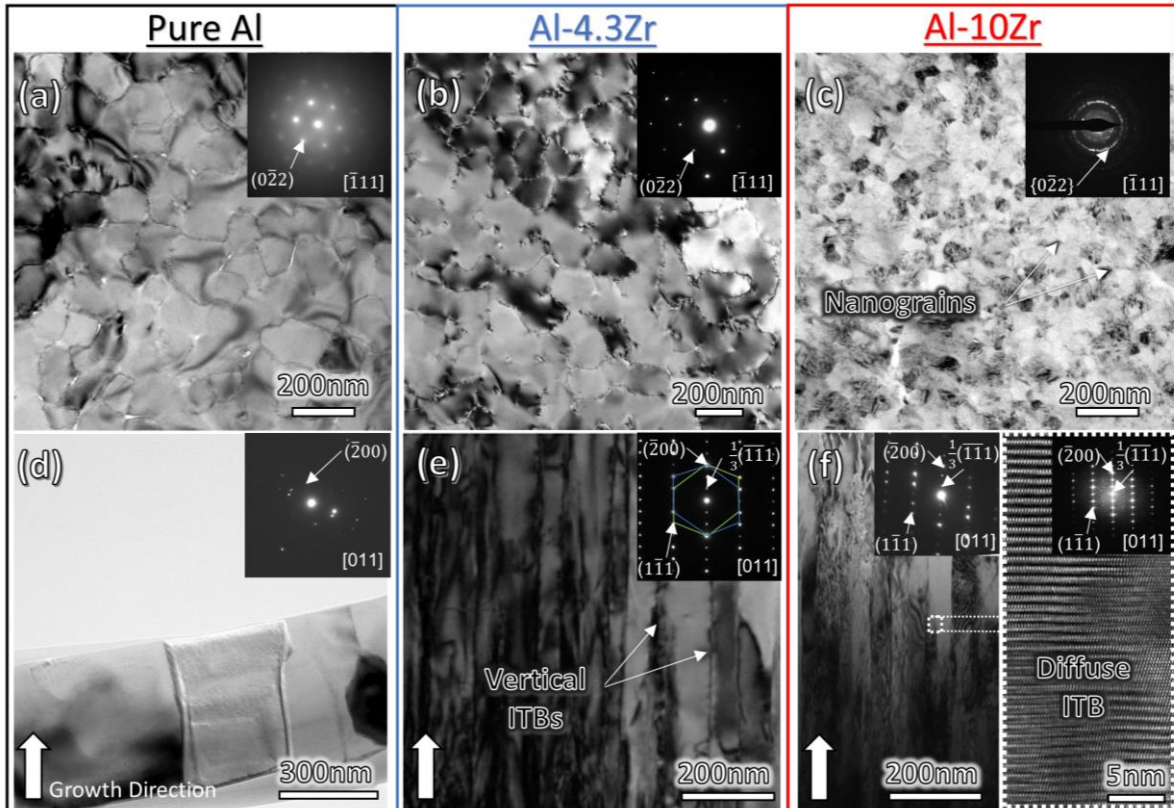
Figure 4-3. (a) Plan-view (PV) transmission electron microscopy (TEM) micrograph of the ultra-fine grained pure Al film with the corresponding inserted selected area diffraction (SAD) pattern revealing single-crystal like (111) out-of-plane texture. (b) PV-TEM micrograph of the NT Al-4.3Zr alloy film revealing fine grains and the corresponding SAD pattern identifying single-crystal like (111) texture. (c) PV-TEM micrograph of the NT Al-10Zr alloy film revealing fine grains and the corresponding SAD pattern showing strong (111) out-of-plane texture. (d) Cross-section TEM (XTEM) micrograph of pure Al with the corresponding SAD pattern. (e) XTEM micrograph of the NT Al-4.3Zr alloy with the corresponding SAD pattern revealing columnar nanotwin boundaries. (f) XTEM micrograph of the NT Al-10Zr alloy with the corresponding SAD pattern revealing columnar nanotwin boundaries and a hi-resolution TEM (HRTEM) inset highlighting the periodic stacking fault array in diffuse ITBs, or 9R phase.
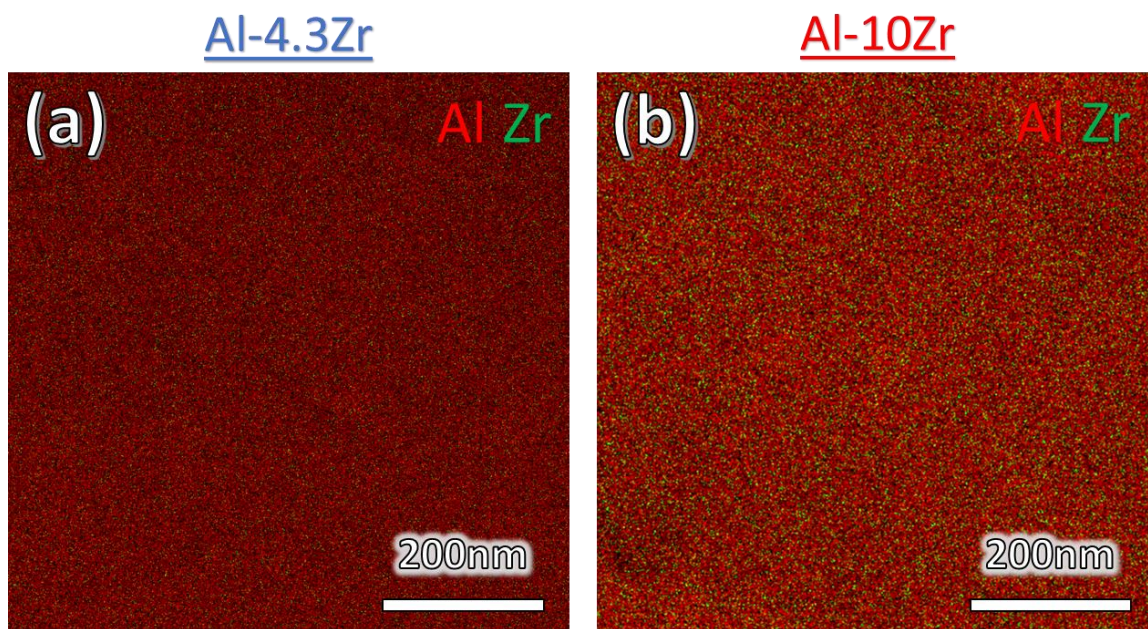
Figure 4-4. EDS scans revealing the complete solid solution of NT Al-Zr alloys and uniform distribution of Zr solute throughout the matrix.

The microstructure of the as-deposited NT Al-Zr alloys was investigated using TEM and both plan-view (PV) and cross-section TEM (XTEM) are presented in Figure 4-3. Figure 4-3(a) contains a bright field (BF) PVTEM image of the pure Al film revealing ultra-fine grains (~250nm). The selected area diffraction (SAD) patterns for Pure Al (Figure 4-3(a)) and NT Al-4.3Zr (Figure 4-3(b)) identifies single crystal-like (111) texture, which is identified by a collection of individual grains all exhibiting strong out-of-plane (111) texture. Notably, the Zr solute additions refine the microstructure down to ~50 nm in the NT Al-10Zr film. Figure 4-3(c) reveals a breakdown of the single crystal-like texture and a nanocrystalline microstructure in the Al-10Zr film, as identified by the (220) diffraction ring in the corresponding SAD pattern. This textural evolution has been explored and discussed in our previous work [271,308]. The grain size distributions are presented in Figure 4-6 with over 100 measurements per sample. Figure 4-4 contains EDS maps collected using TEM which reveals a complete solid solution of Zr solute into the Al matrix. XTEM images are presented in Figure 4-3(d-f) to further assess the microstructural evolution as Zr solute content increases. The Pure Al film (Figure 4-3(d)) is composed of coarse columns (~250nm) with no twin boundaries identified through the corresponding SAD pattern. Figures 4-3(e-f) reveal the NT Al-Zr films are composed of an abundance of vertically oriented $\Sigma 3(112)$ incoherent twin boundaries (ITBs). The twinned diffraction spots in the corresponding SAD patterns in Figures 4-3(e-f) confirms the presence of vertically oriented twin boundaries. In addition, the $\frac{1}{3}(\bar{1}\bar{1}1)$ spots present in the SAD patterns in Figures 4-3(e) and 4-3(f) confirm the presence of stacking faults composing diffuse ITBS, or 9R phase. The HRTEM image inset in Figure 4-3(f) depicts the periodic stacking fault array constructing 9R phase, with the Fast Fourier Transform (FFT) containing both twin spots and the $\frac{1}{3}(\bar{1}\bar{1}1)$ mentioned previously. The hardness was measured using displacement controlled nanoindentation and the resulting hardness values are plotted with Zr content in Figure 4-5(a).
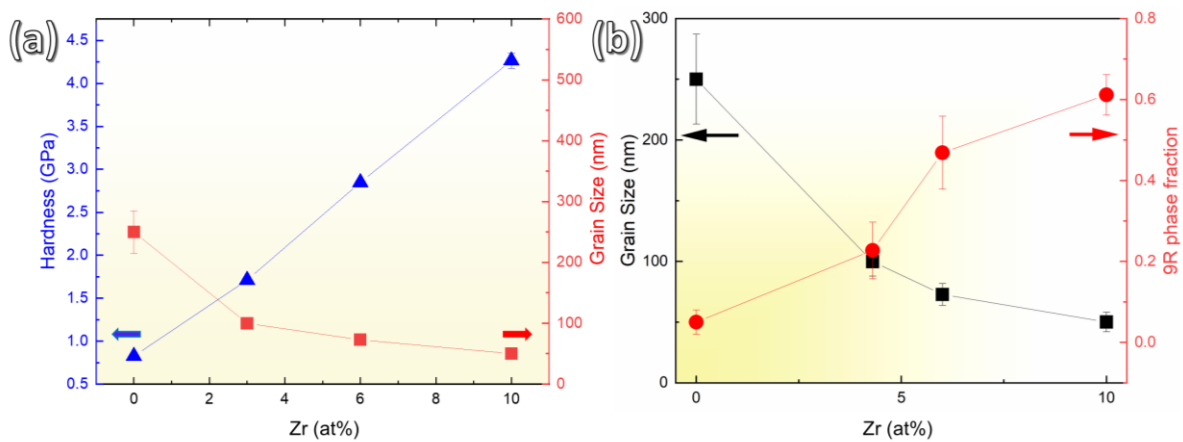
Figure 4-5. (a) Hardness and grain size plotted as a function of Zr solute concentration. (b) Plot detailing the evolution of grain size and 9R phase fraction with concentration of Zr.
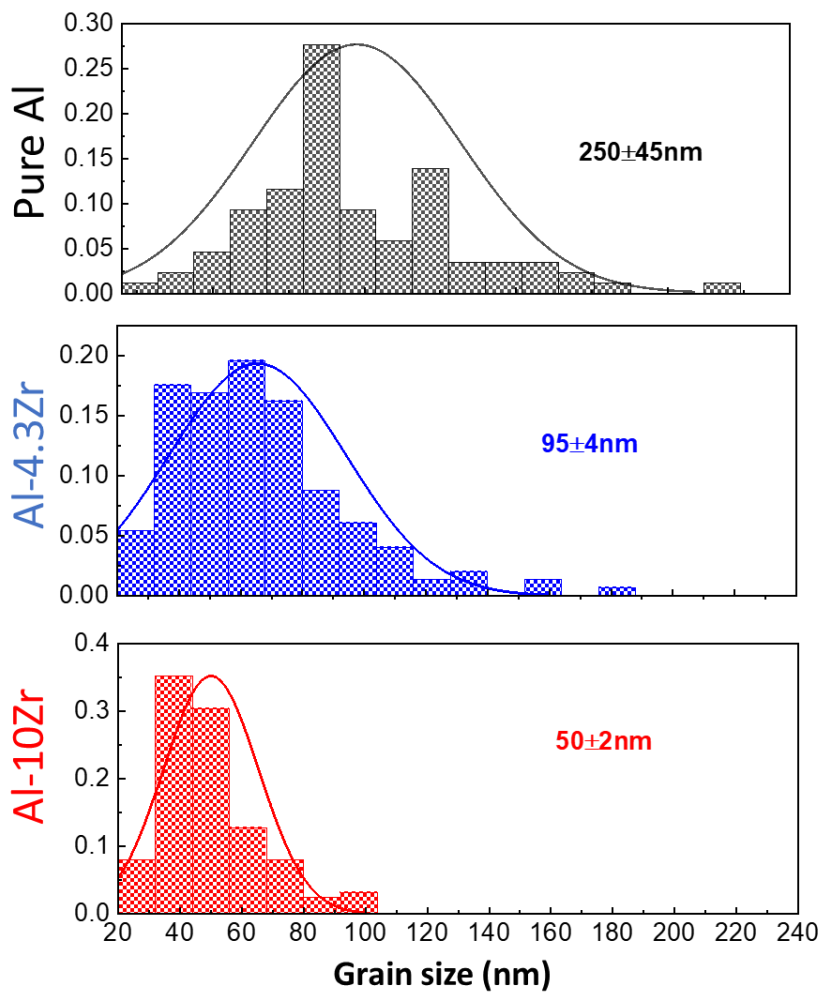
Figure 4-6. Grain size distributions for Pure Al, Al-4.3Zr and Al-10Zr measured from TEM images using the line-intercept method.
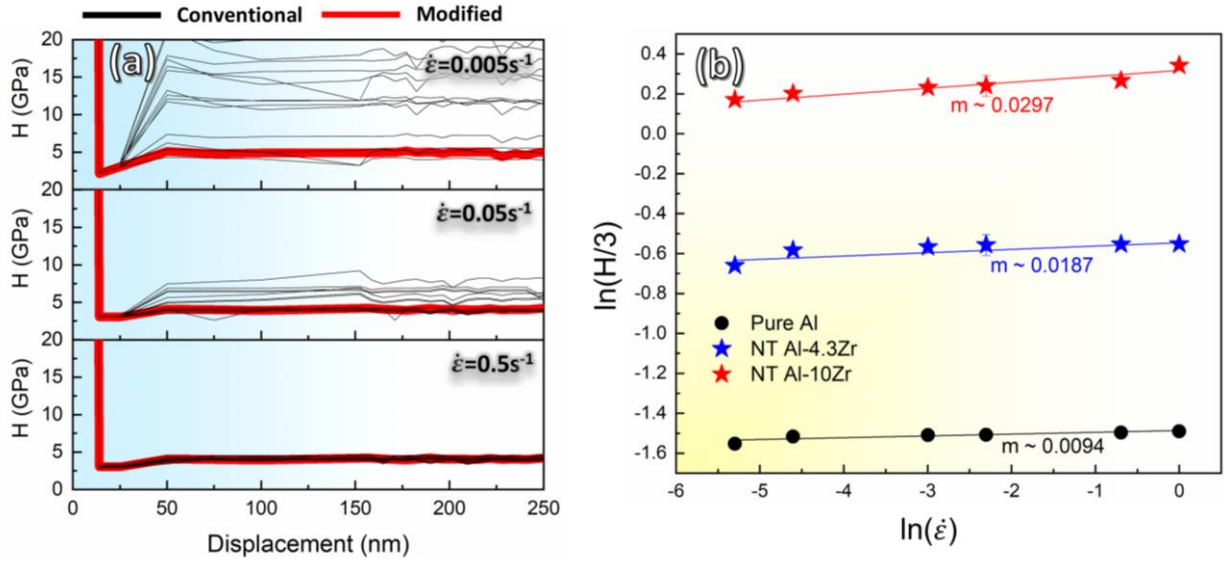
Figure 4-7. (a) Comparisons of hardness vs displacement plots for the NT Al-10Zr specimen by using the conventional and modified nanoindentation method at various strain rates. (b) Comparison of constant strain rate nanoindentation results among Al, and NT Al-4.3Zr and Al-10Zr films revealing an increase in strain rate sensitivity (m) at higher Zr content.

Figure 4-5(b) plots the grain size and 9R phase fraction against the Zr content, revealing significant grain size reduction down to ~50 nm as well as a consistent increase in 9R fraction with increasing Zr content. The 9R phase fraction was determined using HRTEM analysis of ~100 grains per sample and the details of the calculation are provided in [271]. A monotonic increase in hardness is identified with increasing Zr content, with the NT Al-10Zr films reaching a hardness of ~4.2GPa. Constant strain rate nanoindentation was also conducted at the 6 different strain rates presented in Figure 4-1(e). Figure 4-7(a) compares the results from the conventional and modified nanoindentation methods [95] and demonstrates the reliability of the modified method at low strain rates. In contrast, the conventional method introduces unusually high hardness and large variations at low strain rates. As the SRS of a material is a measure of the change in flow stress for various strain rates ($m = \frac{\partial \sigma}{\partial \varepsilon} = \frac{\ln \sigma}{\ln \varepsilon}$), H must be divided by the Taylor factor (~3) in order to estimate the film flow stress. Accordingly, the results from the constant strain rate tests are presented as ln(H/3) vs ln($\dot{\varepsilon}$) in Figure 4-7(b), where the slope gives the strain rate sensitivity (SRS), *m*. The Pure Al films exhibit a *m* of ~0.0094, which corresponds well with previous literature. Notably, increasing

Zr content and twin density leads to a jump in *m* up to 0.0187 and 0.0297 in the NT Al-4.3Zr and Al-10Zr coatings.

4.5   Discussion

The unique NT microstructure presented in this study originates from a few factors. First, the dominant (111) texture promotes twin formation during the nucleation and growth of the sputtered Al-Zr coatings. The Zr solute improves this texture, whereas the pure Al films are polycrystalline in nature and composed of randomly oriented grains. $\Sigma3(112)$ ITBs, shown in Figure 4-3(e-f), form along specific crystallographic planes which are prevalent in (111) textured films. The difference in microstructure between Pure Al and NT Al-Zr is stark as the strong texture alters the grain boundary structure, promoting ITBs in NT Al. Second, the high quench rates experienced during magnetron sputtering trap a higher volume fraction of Zr solute atoms in solution, generating a super saturated solid solution [315]. The Zr solute facilitates significant grain refinement and strong (111) texture as depicted in Figure 4-3(a), leading to an abundance of vertically oriented ITBs. The high SFE of Al and the lack of solute leads to a microstructure of randomly oriented high angle grain boundaries in pure Al. 9R phase is the nomenclature used to describe diffuse ITBs, and an example of this is provided in the HRTEM micrograph in Figure 4-3(f). Based on HRTEM evidence of ITBs in pure Cu and molecular dynamics simulations, ITBs are composed of a periodic array of 3 Shockley partial dislocations with a $b_2:b_1:b_3$ arrangement involving 3 adjacent {111} planes [155–159]. The b_2 and b_3 Shockley partials are relatively immobile mixed dislocations with $1/6\,[\bar{2}11]$ and $1/6[1\bar{2}1]$ Burgers vectors, respectively. The b_1 Shockley partial is a pure edge dislocation with a Burgers vector of $1/6[11\bar{2}]$. b_1 is able to glide due to a smaller Peierls barrier, leading to diffuse ITBs, or 9R phase [155]. MD simulations demonstrate the contribution of Fe solute in stabilizing 9R phase in pure Al [159]. The high SFE of Al prevents 9R formation in pure Al, whereas the Zr solute stabilizes the diffuse ITB structure by pinning the Shockley partials. Figure 4-8(b) reflects the increase in 9R phase identified at higher Zr solute levels. HR-TEM images are presented depicting the progression of 9R phase with strain rate sensitivity in Figure 4-8.
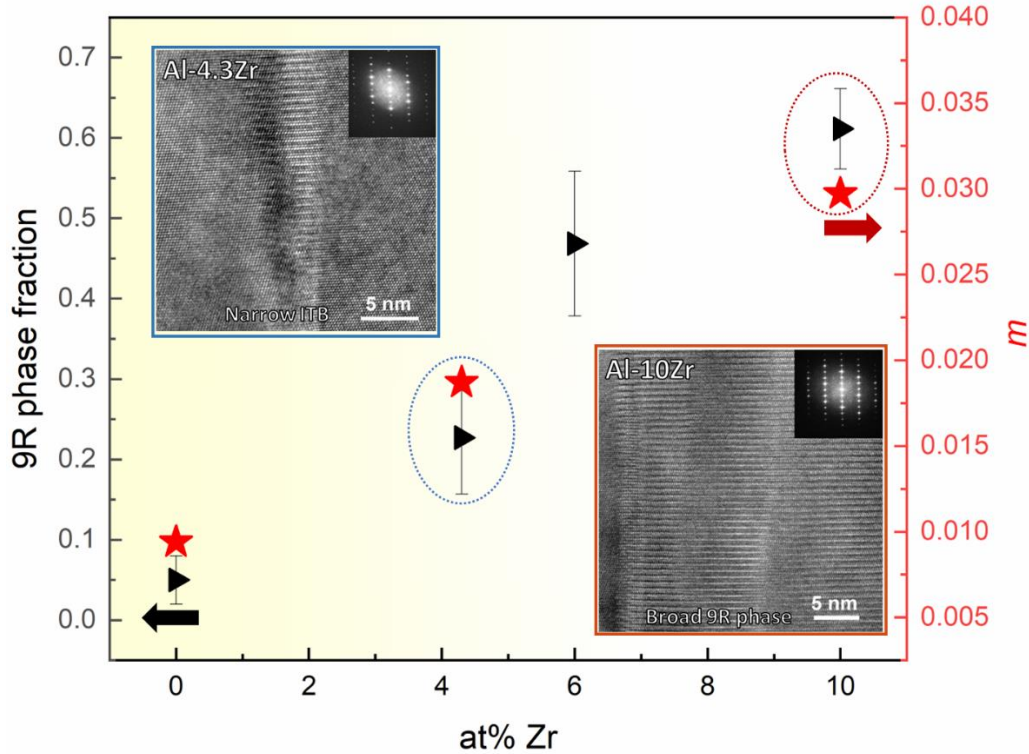
Figure 4-8. Plot relating 9R phase fraction and *m* as a function of at% Zr. Additional HR-TEM insets identify with corresponding data points revealing the difference in 9R phase.

The hardness of NT Al-Zr reaches 4.2GPa as shown in Figure 4-5(a), which is high comparing to classical Al alloys. The strengthening mechanisms contributing to this high hardness include solid solution strengthening and boundary strengthening. Per our previous work, the contribution from solid solution strengthening was calculated based on the Fleischer formulation [271]. Despite the super-saturated solid solution stabilized by the high sputter quench rate, it was found that solid solution strengthening only contributes ~28MPa in the Al-10Zr alloy. This value is far below the measured hardness, and since the XRD spectra presented in Figure 4-2 identifies no second phase formation, boundary strengthening was determined to be the main factor behind the improved mechanical properties. The Hall-Petch coefficient for NT Al-Zr alloys was determined to be ~9.3 GPa·nm$^{1/2}$, which is almost twice that for nanocrystalline Al [271,308]. As MD simulations and *in-situ* nanoindentation experiments demonstrate that ITBs obstruct dislocation motion and transmission similar to conventional grain boundaries [177], the jump in Hall-Petch slope can be attributed to the high density of stacking faults composing 9R phase. Our previous work determined that 9R phase contributes ~6.9 GPa·nm$^{1/2}$ to the Hall-Petch slope,

supporting the significant role stacking faults can play on mechanical properties. This analysis corresponds well with previous MD simulations identifying extensive interactions between dislocations and 9R phase in NT Al-Fe [159]. Su et al. also demonstrated an enhancement of mechanical properties in Co thin films with an abundance of stacking faults [316].

The modified nanoindentation method implemented in this study enabled the probing of the strain rate sensitivity of NT Al-Zr alloys. To minimize data skew at low strain rates due to thermal drift, the modified method from Liu et al. [95] was utilized to analyze the constant strain rate nanoindentation data. The indent area at low strain rates (A) was calculated based on the reduced elastic modulus (Er) measured at high strain rates, mitigating the issue of thermal drift at low strain rates. This enables quick analysis of the already collected data while maintaining consistency across the test methods at different strain rates. Figure 4-7(a) compares the hardness values as a function of indentation depth and underscores the issues with the conventional method at low strain rates. High levels of thermal drift at low strain rates (0.005 s^{-1}) induce artificially high hardness and large skew in the data compared with the high strain rates (0.5 s-1). Figure 4-7(a) highlights the consistency and reliability of the modified method as the data are consistent and reproducible. To assess the performance of these coatings and to further validate the results from this study, we compared the m values collected in this work with prior studies on various FCC metals (Figure 4-9(a)) implementing various test techniques (tensile testing, compression, or rate jump tests) in Figure 5(a) [104,105,231,296,317–321]. It has been well documented that m increases with decreasing grain size in FCC metal systems, and Figure 4-9(b) reflects the same trend [297]. The Pure Al film exhibits a similar rate sensitivity (m = 0.0094) as the ultra-fine grained Al and Cu tested using bulk methods, which further validates the methodology used in this work. Compared with bulk Al and Al alloys, the NT Al-4.3Zr and Al-10Zr alloys have greater m values [319], increasing to 0.0297 in the Al-10Zr alloy. This suggests the presence of ITBs and 9R phase bolster the SRS in NT Al alloys.
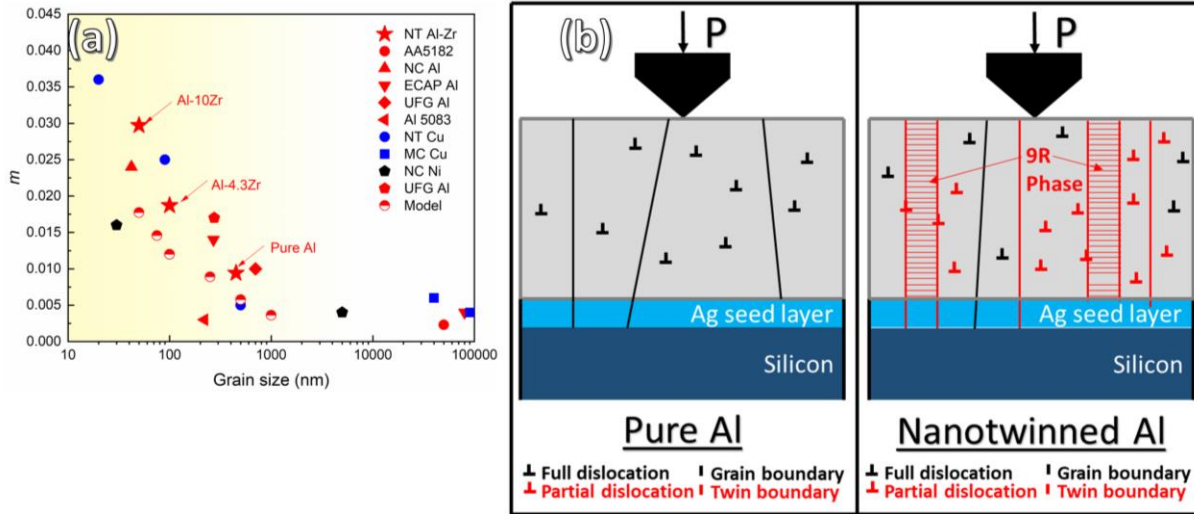
Figure 4-9. (a) Comparison of known values of m for various FCC metals (Al, Ni, Cu) plotted as a function of grain size as tested using various techniques. The results from the nanoindentation technique are consistent with previous findings and highlight the bolstered strain rate sensitivity in NT Al-Zr alloys [22,24,58,66-71]. (b) Schematic comparing the UFG Al film with full dislocations and conventional grain boundaries (GBs) with the nanotwinned Al-Zr alloys composed of a mixture of GBs and ITBs as well as an abundance of partial dislocations (9R phase).

The SRS of NC FCC metals has been shown to be highly dependent on grain size (d) [102,297,298], and is given by [103]:

$$m = \frac{kT}{\xi b} \cdot \frac{1}{\chi(\alpha\mu b\sqrt{\rho}d) + \beta\sqrt{d}} \tag{4-7}$$

where k is Boltzmann's constant, b is the Burgers vector, μ is shear modulus, ξ is distance swept by a glide dislocation, and α, β, and χ are proportional factors. This model suggests that *m* will increase as grain size decreases, in agreement with the results from this study [103,322]. Equation 4-7 provides insight into grain size dependent variation of *m*, however its application to specific cases is difficult as it depends on a number of proportional factors that are yet to be determined [103]. The estimated *m* for NC Al with a grain size of 50 nm is 0.017, which is below that of NT Al-10Zr with a similar grain size. This difference can be attributed to multiple factors that are accounted for within the model itself, including the magnitude of b, the dislocation density (ρ) providing dislocation barriers during deformation, and the activation volume, represented through ξ. The influence of grain size has been isolated as a factor as the plots in Figure 4-9(a) directly compare *m* in NT Al-Zr with various FCC metals composed of similar grain sizes (columnar twin spacing in this study). First, as demonstrated in the HRTEM in Figure 4-3(f) and depicted schematically in Figure 4-9(a), introducing an abundance of ITBs provides a high density

of mobile Shockley partial dislocations that carry plasticity. The b of these partial dislocations is $\frac{1}{6} < 112 >$, which is smaller in magnitude than the full dislocations operating in NC Al at similar grain sizes (60 – 100 nm). As captured in Equation (2), dislocations with a smaller b will increase *m*. Incorporating this into the model increases the predicted *m* from 0.017 to 0.033, which is closer to the experimentally measured *m* of 0.0294. Second, ρ increases slightly due to the presence of partial dislocations composing 9R phase. However, the current model accounts for a moderate pre-existing dislocation density and any slight changes are muted by the inverse square root relationship between ρ and *m.* Finally, ξ is expected to decrease in NT Al alloys since the high-density stacking faults composing 9R phase provide additional barriers to dislocation motion, leading to an increase in *m*.

Previous research exploring the SRS of NT Cu has highlighted the role coherent twin boundaries (CTBs) play on improving mechanical properties [169,173]. Refining twin spacing to ~15 nm bolstered strength to 900 MPa while maintaining significant plasticity [173]. The concomitant high strength and ductility are attributed to an abundance of pre-existing mobile partial dislocations forming steps on the CTBs, the density of which increases at finer twin thicknesses [173]. Similarly, Lu et al. investigated the influence of these nanoscale twins on rate sensitivity, and found that increasing twin density improved *m* [104]. The increased *m* values were attributed to extensive dislocation interactions with CTBs and an increased dislocation generation from the steps along CTBs. *In-situ* nanoindentation tests of CTBs in Cu revealed Shockley partial dislocations can propagate along CTBs promoting extensive dislocation activity within twins [253,323]. As the 9R phase identified in NT Al-Zr are composed of arrays of mobile Shockley partial dislocations, it is likely responsible for the improved SRS of NT Al-Zr [155,271]. Although the high strength and deformability of NT Al alloys has extensively documented through *in-situ* micropillar compression [138,139,183,307,308], no attempts to characterize the SRS of this unique microstructure composed of vertically aligned ITBs. Figure 4-9(b) contrasts the pure Al and NT Al-Zr microstructures. Plasticity in the pure Al films is dominated by full dislocation motion since the grain size is on the order of a few hundred nanometers, and the SRS follows previous literature and model predictions. In comparison, Figure 4-9(b) depicts the increase in partial dislocations in NT Al alloys accompanying the increased twin density, and the mobility of these partials drives the boost in SRS. Accompanying the boost in plasticity, the abundance of 9R phase and Shockley partials captured in the HRTEM in Figure 4-3(f) provides a source for improving *m.* As mentioned

previously, the decrease in b provides another source for the rate sensitivity increase in NT Al-Zr. Ultimately, the microstructural complexity of NT Al-Zr is crucial in maintaining high strength and plasticity [159,308], and its influence on SRS is evidenced through this study.

4.6   Conclusion

The application of a constant strain rate nanoindentation methodology enabled the probing of strain rate sensitivity of nanotwinned Al-Zr sputtered films. Increasing Zr content leads to significant grain refinement down to 50 nm, and the promotion of incoherent twin boundaries and 9R phase led to a corresponding jump in hardness up to 4.2 GPa. Similarly, increasing the Zr content also boosts strain rate sensitivity in nanotwinned Al-Zr alloys, which has been linked to the increase in partial dislocation density and mobility. This study represents a major finding and fills a previously unexplored gap in literature and identifies the role incoherent twin boundaries play in improving the rate sensitivity, and ultimately the deformability and fracture resistance, of NT Al-Zr alloys

4.7   Acknowledgements

5. SOLUTE SYNERGY INDUCED THERMAL STABILITY IN HIGH STRENGTH NANOTWINNED AL-CO-ZR ALLOYS

Density Functional Theory (DFT) calculations were performed by Dr. Mingyu Gong and Dr. Jian Wang from the University of Nebraska-Lincoln.

This chapter includes content reproduced with permission from "Solute synergy induced thermal stability of high-strength nanotwinned Al-Co-Zr alloys" by N.A. Richter, Y.F. Zhang, M. Gong, T.J. Niu, B. Yang, S. Xue, J. Wang, H. Wang, and X. Zhang, *Materials Science and Engineering: A* (2022): 144477 Copyright (2022) Elsevier Ltd.

5.1 Overview

Reducing the grain size into the nanoscale regime in metallic materials provides high mechanical strengths, however at the cost of degrading thermal stability, as grain refinement has led to the high driving force for grain coarsening. In this study, we present a solute synergy strategy that stabilizes the microstructures of high strength nanotwinned (NT) Al-Co-Zr alloys. Zr solute additions promote microstructural and mechanical stability up to 400 °C. *In-situ* microcompression tests demonstrate concomitant high strengths and deformability up to 400 °C in these ternary NT alloys. Density functional theory calculations provide insight into the interplay between Co and Zr solute and how they pin and stabilize incoherent twin boundaries. This work provides a strategy for enhancing both strength and thermal stability of nanocrystalline materials when combining synergistic solute pairs.

5.2 Introduction

Aluminum (Al) alloys have been extensively investigated due to their impressive strength-to-weight ratio combined with high conductivity and corrosion resistance. Precipitate strengthening is famously used to strengthen commercial Al 7075 alloys, however even these alloys only reach a tensile strength of ~700 MPa [324] and experience grain coarsening beyond just ~200 °C [109,325,326]. Prior studies show that Al alloys are often limited by low mechanical strength compared with their steel counterparts, and especially poor microstructural and mechanical stability at temperatures above 200 °C [327]. More recently, other strategies have been explored to further raise the strengthening limit of Al alloys by restricting grain size down to the

nanocrystalline (NC) regime. Severe plastic deformation (SPD) processes utilize high levels of dislocation activity to segment and refine the microstructures of metallic materials into nanoscale [101,328]. High pressure torsion (HPT) of an Al-Zn alloy resulted in a tensile strength of ~800 Mpa with a grain size below 100nm [329], and Liddicoat et. al reported that HPT of Al7075 reaches approximately twice the strength of the commercial T6 heat treated alloy [330]. Surface mechanical grinding treatments (SMGT) have also been used to fabricate Ni alloys with thick grain boundaries (GBs), that promote both high strength and thermal stability [58,59]. Additionally, far from equilibrium deposition techniques (magnetron sputtering, etc.) have been used to fabricate NC metals. $CoCrFeNiAl_{0.3}$ high entropy alloy (HEA) coatings fabricated using magnetron sputtering are capable of reaching a hardness of 11.4 Gpa, 4 times its cast counterpart [114]. Sputtered Pt thin films were shown to have high hardness (7.4 Gpa) and a stable structure under nanoindentation and tensile loading, however experienced extensive grain coarsening and rapid crack propagation under fatigue loading [331]. Despite these successes, NC metals fabricated by both SPD and deposition techniques are still severely limited by poor thermal stability.

Typically, the thermal stability of nanostructured metals is hindered by the inherent instability driven by the excess boundary energy from the large volume fraction of GBs. This drawback often leaves nanostructured metals incapable of broad implementation at high temperature environments and makes fabrication difficult due to the typically necessary thermal step during processing [129,332]. Electrodeposited Ni samples with a grain size of 10 nm experienced microstructural instabilities at annealing temperatures as low as 80 °C [333]. Similarly, sputtered NC Cu with grain sizes of ~50 nm was shown to coarsen at ~100 °C using *in-situ* heating in a transmission electron microscope [287], and NC Cu samples were also reported to coarsen during nanoindentation at ambient temperatures due to the excess energy associated with grain boundaries [334]. Alloying can lead to an alteration in energy landscape by increasing the energetic barrier (Zener pinning) to grain growth [335–337] or by decreasing the energy benefit from coarsening by lowering the boundary energy [124,126,338]. Classically, both solute and precipitation can be used to inhibit GB motion through Zener pinning and have been implemented in various NC metals [125,339–341]. Using atom probe tomography, mechanically alloyed NC Fe-Zr alloys were shown to form Fe-Zr-O nanoclusters that pin and stabilize the nanograined structure [342]. Additionally, Weismüller demonstrated thermodynamically that preferentially segregated solutes to GBs can lower the GB free energy by tailoring the enthalpy of mixing in the

bulk state to be low relative to the enthalpy of segregation to the GBs [124,130]. Further thermodynamic model development, specifically accounting for phase separation [130,332,337,343] and experimental exploration [127,337,344] of NC systems has further supported the efficacy of this approach. Investigation of Cu-Ta alloys revealed that both of these mechanisms can operate at different temperature regimes, with oxide particles found to pin boundaries at elevated temperatures in these alloys [345,346]. Phase separation can lead to the breakdown of each of these mechanisms leading to severe coarsening [130,347], and further work needs to be done to mitigate these adverse effects.

Nanotwinned (NT) metals have been heavily investigated since they simultaneously possess high strengths and ductility. Low stacking fault energy (SFE) metals (Cu, Ag, stainless steel) were initially explored due to the high propensity for forming growth twins in both electrodeposited and sputtered films [169,170,172,245,252,262]. NT metals also possess a high strength-to-resistivity ratio and remarkable thermal stability compared with NC counterparts due to the lower boundary energy of Σ3 coherent twin boundaries (CTBs) compared with conventional GBs [135,136,169,258,260,348]. More recently, it has been demonstrated that the addition of transition metal solutes (Fe, Ni, Zr, etc.) into Al films during magnetron sputtering can result in a supersaturated solid solution with a high density of incoherent twin boundaries (ITBs) [159,195–197,271,308]. Density functional theory (DFT) calculations reveal that these solutes serve to lower the SFE and raise the energy barrier for detwinning [200]. This effect works in conjunction with the large quench rate induced by magnetron sputtering to stabilize the NT Al microstructure, capable of reaching a hardness exceeding 5 Gpa [139,196,264,271,289,309]. However, these binary alloys still suffer from limited thermal stability, with NT Al-Fe coarsening at 280 °C [199].

This study builds upon an alternative strategy relying on the synergistic interactions of solute additions to stabilize twin boundary in NT Al alloys at elevated temperatures [138,139]. As documented previously, Co solute is an effective grain refiner and promotes an abundance of ITBs in sputtered films despite forming brittle intermetallics in cast Al alloys [197]. Also the binary NT Al-Co alloys have limited thermal stability as shown in the current study. Hence we explored the addition of a third element (Zr) into the NT Al-Co alloys as a means to further stabilize ITBs and nanoscale grain sizes during annealing, thus leading to the retention of ultra-high strength of NT Al alloys after high temperature annealing.

5.3   Experimental

An AJA ATC-2200-UHV magnetron sputtering system with a base pressure of 8×10^{-9} Torr and an Ar gas pressure of ~3.5mTorr was used to deposit Al (99.999%), Co (99.99%) and Zr (99.95%) onto Si (111) wafers etched using hydrofluoric acid. The composition of the deposited films was controlled by using a built-in quartz crystal rate monitor to record the deposition rate of each target. The resulting film thickness is ~2 μm and some films were then annealed under vacuum in the AJA system at temperatures ranging from 150 to 450 °C for 1.5 hours. After annealing, the samples were cooled to room temperature in the chamber at a cooling rate of ~15 °C $\min^{-1}$

A Panalytical Empyrean X′pert PRO MRD diffractometer operated at 40kV using Cu Kα1 X-rays was used to perform X-ray diffraction (XRD) θ–2θ and pole figure scans to evaluate the overall texture and structure. Transmission electron microscopy (TEM) samples were prepared by mechanical grinding, dimpling, and low-energy ion milling, with care taken to avoid sample heating. The microstructure and composition were examined using an FEI Talos 200X analytical microscope operated at 200 kV with a Fischione high-angle annular dark field (HAADF) detector and super X energy-dispersive X-ray spectroscopy (EDS) detector. The compositions of the deposited alloys are given as follows in atomic percent: 95.19 ± 1.95 at% Al and 4.81 ± 0.65 at% Co (referred to as NT Al-5Co) and 93.87 ± 1.96 at% Al, 4.47 ± 0.6 at% Co, and 1.65 ± 0.21 at% Zr (referred to as NT Al-5Co-2Zr). Grain sizes were measured using the line intercept method on cross-section TEM images to ensure statistical significance and reduce any possibilities of skewed data due to bias. Hardness and elastic modulus measurements were conducted using a Bruker TI Premier nanoindenter at different indentation depths under displacement control mode. 75 indents were made per sample and the indentation depth was kept below 15% of the film thickness (300nm) to prevent incorporating substrate effects.

In-situ micropillar compression experiments performed using a Bruker/Hysitron PI 88 nanoindenter inside a FEI Quanta 3D scanning electron microscope to probe the deformability and compressive strength of these films. Pillars and TEM samples of deformed pillars were fabricated using an equipped focused ion beam (FIB) inside an FEI Quanta 3D scanning electron microscope. The pillar height and diameter were ~800 nm and 1600 nm respectively, with the taper minimized below ~2° during pillar fabrication. Pillars were compressed using a Bruker/Hysitron PI 88 nanoindenter to ~20% strain using displacement control, with a strain rate at 5×10^{-3}. Pillars were

compressed with numerous partial unloading segments to assess the validity of the alignment during compression.

DFT calculations were conducted using the Vienna ab-initio simulation package (VASP). The calculations are based on the projector augmented wave (PAW) method, generalized gradient approximation (GGA) approach, and Perdew-Burke-Ernzerhof (PBE) exchange correlation density functional. For the pseudopotentials in this calculation, the electron configuration of Al, Co and Zr are $[Ne]3s^2 3p^1$, $[Ar]3d^7 4s^2$, and $[Kr]4d^2 5s^2$, respectively. The kinetic energy cut-off for the plane wave expansion was set to 500 eV. The self-consistent iteration and atomic realization stopped with the criteria of 10^{-6} eV and 0.01 eV $Å^{-1}$ respectively.

5.4   Results

5.4.1   As-deposited microstructure characterization

Al-Co and Al-Co-Zr alloys were investigated to assess the role of Zr solute on the structure and stability of NT Al-Co alloys. Figure 5-1(a) contains XRD patterns for each deposited Al-5Co-xZr alloy (x = 0, 2, 5, 8 at%), identifying strong (111) texture in each sample, with the exception of the amorphous Al-5Co-8Zr. The drop in intensity in the Al-5Co-5Zr and Al-5Co-8Zr films were due to amorphization, and as a result were omitted from the thermal stability portion of this study. These results also indicate the formation of a single solid-solution phase with only the Al(111) and Si substrate peaks present. Figure 5-1(b-c) shows the XRD pole figures for the Al-5Co and Al-5Co-2Zr alloys, depicting strong (111) texture. The addition of Zr further improves texture, leading to the progression from the {111} ring contour (Al-5Co) to the six-fold symmetry (Al-5Co-2Zr), indicating an increase in twin density.
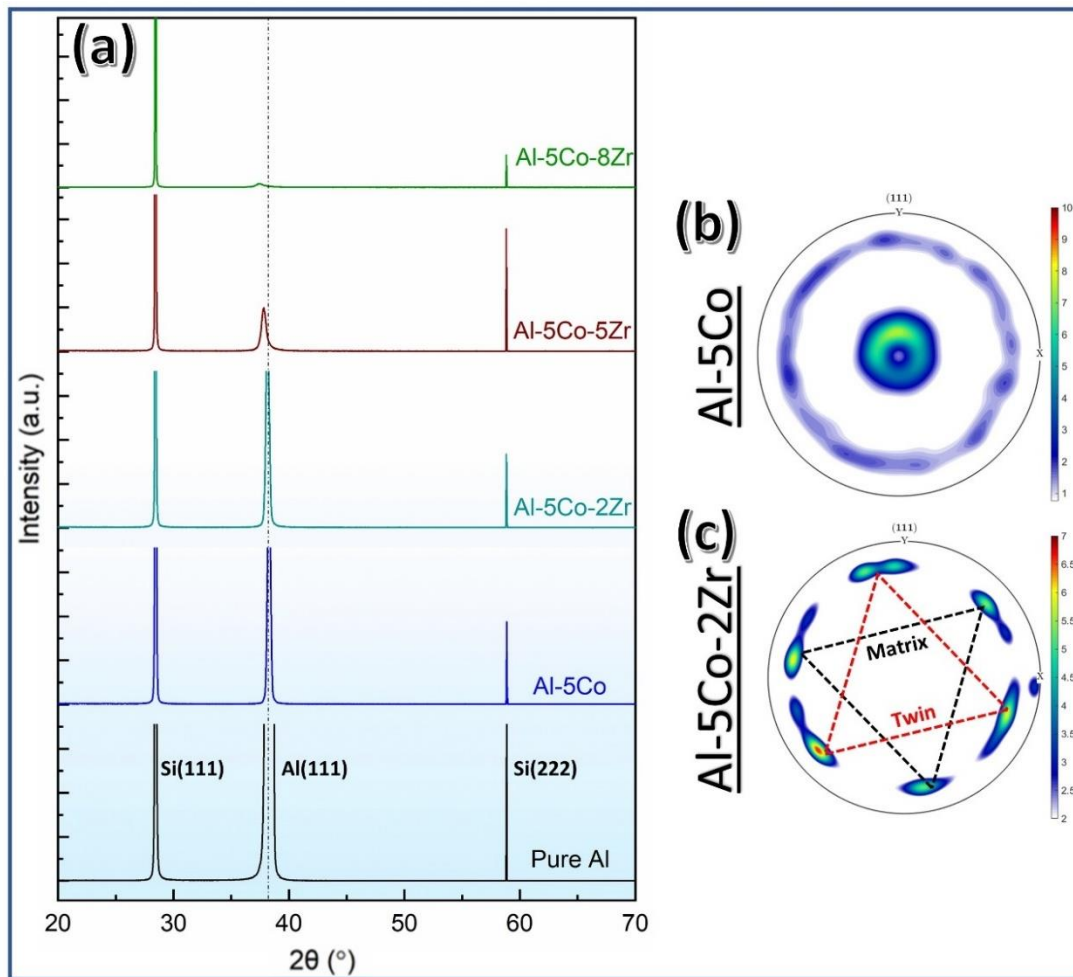
Figure 5-1. (a) As-deposited x-ray diffraction (XRD) profiles for each deposited sample. (b) {111} pole figure for the NT Al-5Co binary alloy showing strong (111) texture. (c) {111} pole figure for the NT Al-5Co-2Zr ternary alloy showing strong (111) texture and distinct twin and matrix spots.
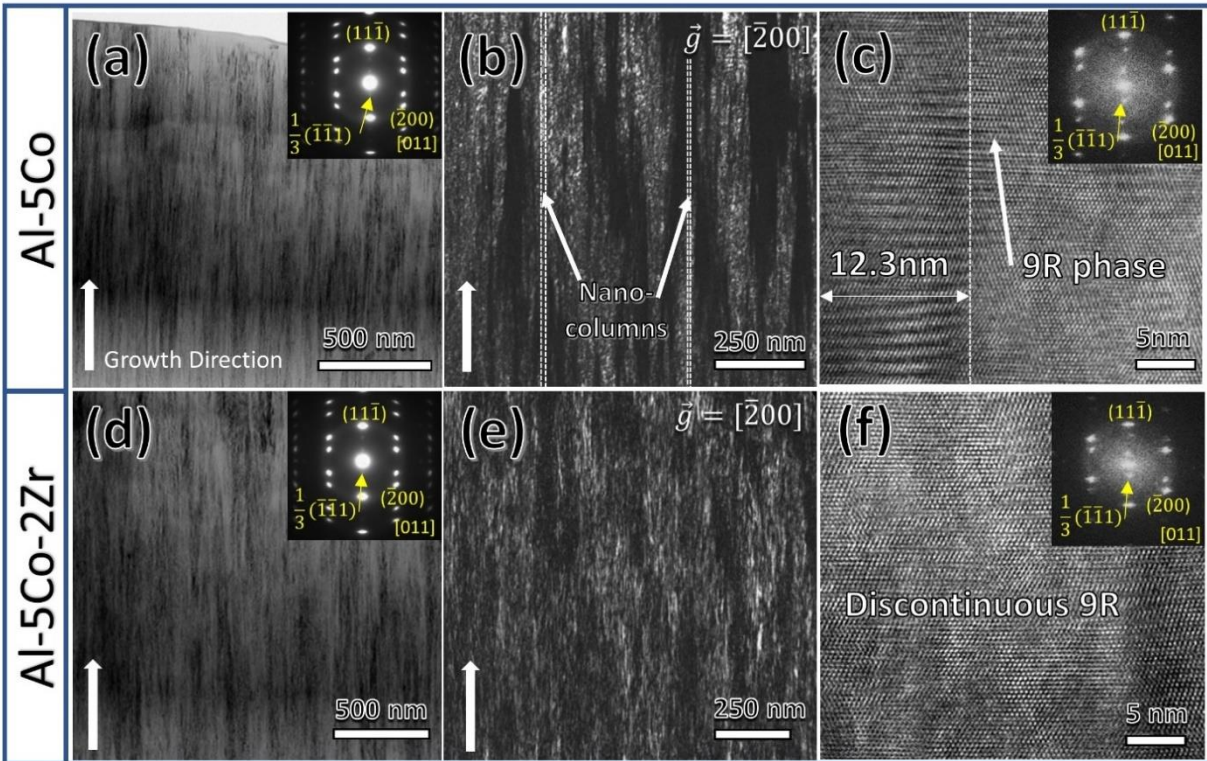
Figure 5-2. As-deposited microstructure characterized using cross-section TEM (XTEM). (a) Bright field (BF) TEM micrograph with corresponding selected area diffraction (SAD) pattern of Al-5Co revealing a fine nanotwinned structure. (b) Dark field (DF) TEM micrograph taken along the $\vec{g} = [\bar{2}00]$ of Al-5Co further characterizing the nanotwinned structure. (c) High-resolution TEM (HRTEM) image showing fine nanocolumns and diffuse ITBs, or 9R phase, in Al-5Co. (d) BF-TEM micrograph with corresponding SAD pattern of Al-5Co-2Zr showing the nanotwinned structure. I DF-TEM micrograph taken along the $\vec{g} = [\bar{2}00]$ of Al-5Co-2Zr further characterizing the nanotwinned structure. (f) HRTEM image showing fine nanocolumns and discontinuous 9R phase in Al-5Co-2Zr.

Microstructural characterization was conducted on these NT Al-Co-Zr alloys using TEM. The bright-field (BF) and dark-field (DF) TEM micrographs in Figure 5-2(a-b) reveal a fine nanocolumnar structure in the binary Al-5Co alloy, with an average grain size of 11.5 ± 1.6 nm. The inserted selected area diffraction (SAD) pattern confirms strong {111} texture along the growth direction. High-resolution TEM (HRTEM) identifies the presence of ITBs in Figure 5-2i, as well as an abundance of 9R phase dispersed among the nanocolumns. The symmetry of the SAD pattern in Figure 5-2(a) and fast Fourier transform (FFT) in Figure 5-2(c) confirm the presence of twin boundaries in the films and the $\frac{1}{3}(\bar{1}\bar{1}1)$ spot in each of these patterns confirms the presence of 9R phase. This phase forms due to the separation of mobile partial dislocations composing incoherent twin boundaries (ITBs). The Al-5Co-2Zr microstructure is similar to the binary alloy, as shown in Figure 5-2(d, e), with the column size slightly further reduced to 8.9 ± 2.1 nm. Figure 5-2(f) contains a representative HRTEM image finding the twinned structure to be composed of sub-column boundaries and discontinuous 9R phase patches. EDS scans were conducted for both alloys and Co and Zr distributions are shown in Figure 5-3(a-d), confirming the formation of a complete solid solution without phase segregation.
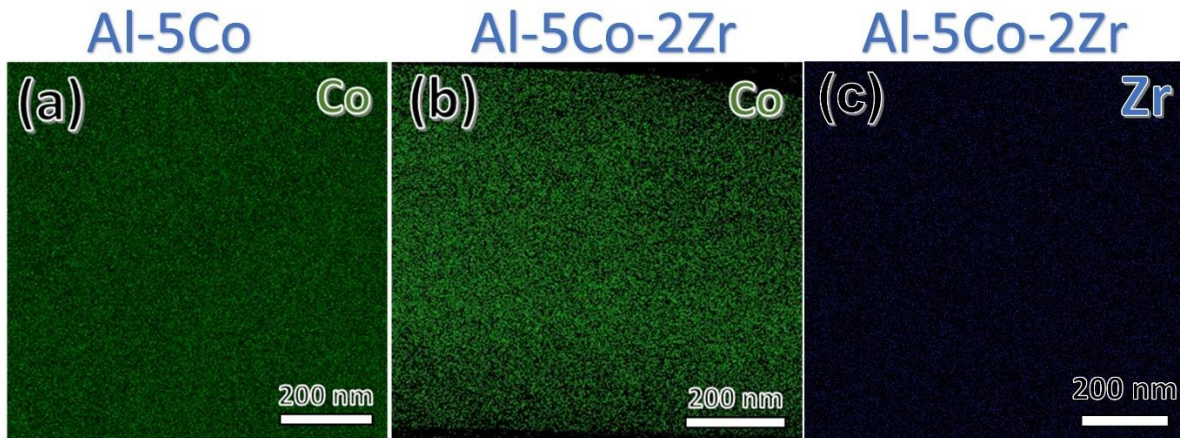
Figure 5-3. Co EDS maps of (a) Al-5Co and (b) Al-5Co-2Zr showing complete solid solutions in the as-deposited state. Zr EDS map of (c) Al-5Co-2Zr revealing uniform distribution of Zr throughout the alloy.

5.4.2 Microstructural thermal stability

NT Al-Co-Zr alloys were annealed at temperatures ranging from 150 to 450 °C for 1.5 hours to assess their thermal stability. The XRD patterns in Figure 5-4(a-b) detail the structural and textural evolution of each NT alloy at various annealing temperatures. Peaks corresponding to the Al_9Co_2 intermetallic and other Al textured peaks are present after annealing at 250 °C in the binary alloy. In contrast, the formation of the Al_9Co_2 and Al_3Zr intermetallics was suppressed in the ternary Al-5Co-2Zr alloy until 450 °C. To quantify the structural thermal stability, systematic post annealing TEM analysis was conducted. Figure 5-5 compares the annealed plan-view microstructural evolution of the NT Al-5Co and Al-5Co-2Zr alloys. It is clear both the as-deposited alloys are composed of nanograins and are strongly {111} textured based on the corresponding SAD pattern in Figures 5-5(a, d). Upon annealing at 250 °C, the nanograins in the NT Al-5Co alloy begin to coarsen and partially recrystallize. Figures 5-5(c-d) reveal complete recrystallization occurs at and above 350 °C, with the grain size evolving from ~10 nm in the as-deposited films to above 80 nm after annealing at 450 °C. The SAD pattern evolution in Figure 5-5(a-d) depicts both the texture breakdown as well as the precipitation of an Al_9Co_2 intermetallic starting at 250 °C in the binary alloy. The SAD pattern in Figure 3(d) illustrates the complete loss of {111} texture resulting in a coarser grained polycrystalline structure. In comparison, the grain size in the Al-5Co-2Zr alloy remains below 15 nm after annealing for 1.5 hours at 350 °C, and the corresponding SAD patterns in Figure 3(e-g) still reflect a strong {111} texture and suppressed phase separation up to 350 °C. Figure 3(h) depicts complete recrystallization and the precipitation of the Al_9Co_2 and Al_3Zr intermetallic phases at 450 °C.
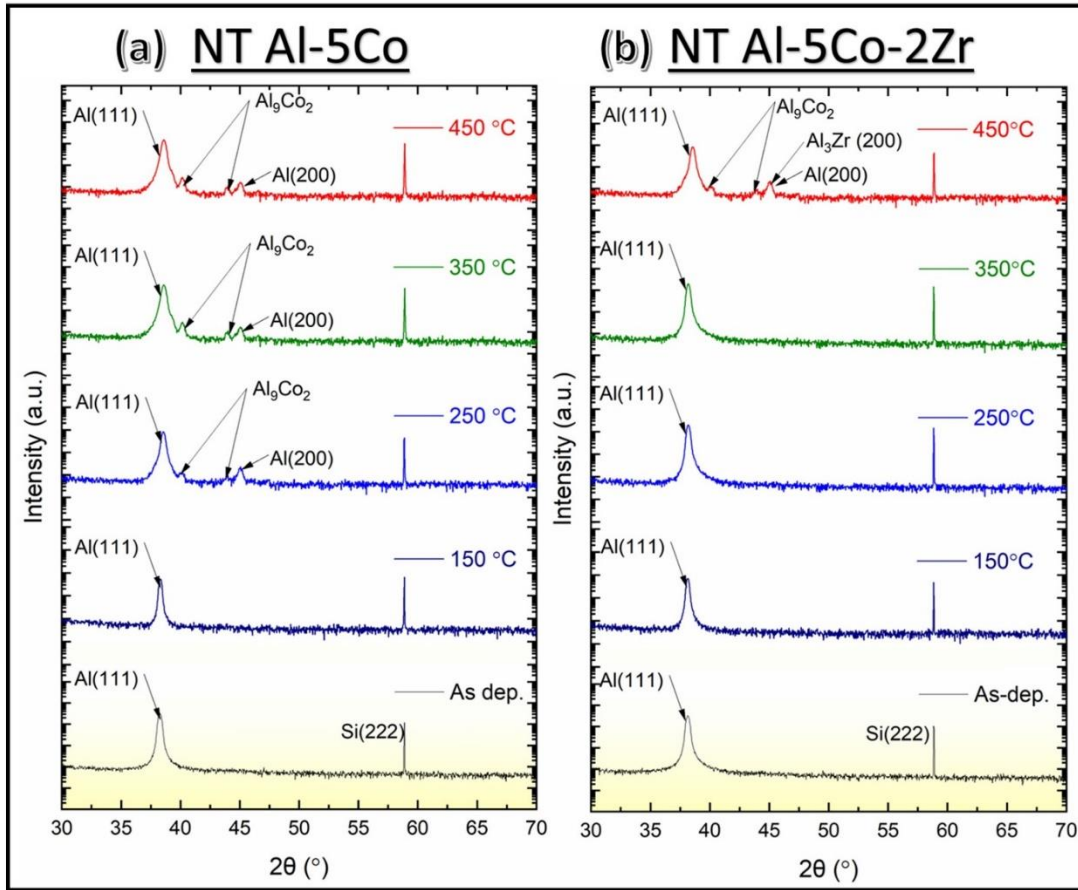
Figure 5-4. XRD patterns detailing the structure and texture evolution in both the (a) binary Al-5Co and (b) ternary Al-5Co-2Zr alloys with increasing annealing temperature.
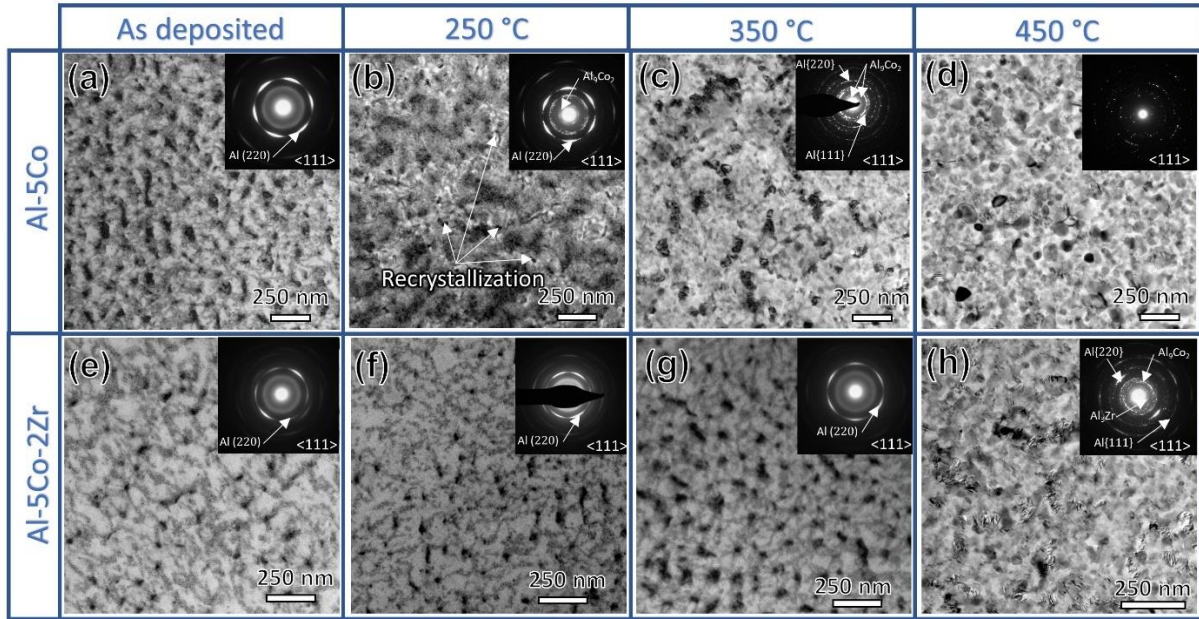
Figure 5-5. Plan-view (PV) BFTEM micrographs revealing the microstructural evolution of (a-d) Al-5Co and (e-h) Al-5Co-2Zr upon vacuum annealing at the corresponding temperatures for 1.5 h.

The degree of this phase separation at various annealing temperatures is further clarified in TEM-EDS Co and Zr elemental maps in Figure 5-6 for both alloys. The Al-5Co alloy exhibits Co rich contours around the coarsened grain boundaries at 250 °C (Figure 5-6(b)) and complete phase separation is pronounced after annealing at 350 and 450 °C (Figure 5-6(c-d). The ternary alloy suppresses this phase separation completely until 450 °C, which is illustrated by the uniform Zr distribution in the EDS maps in Figure 5-6(e-h) up to 350 °C. Co EDS maps in Figure 5-7(e-h) show the Co distributions in the Al-5Co-2Zr alloy at varying temperature.
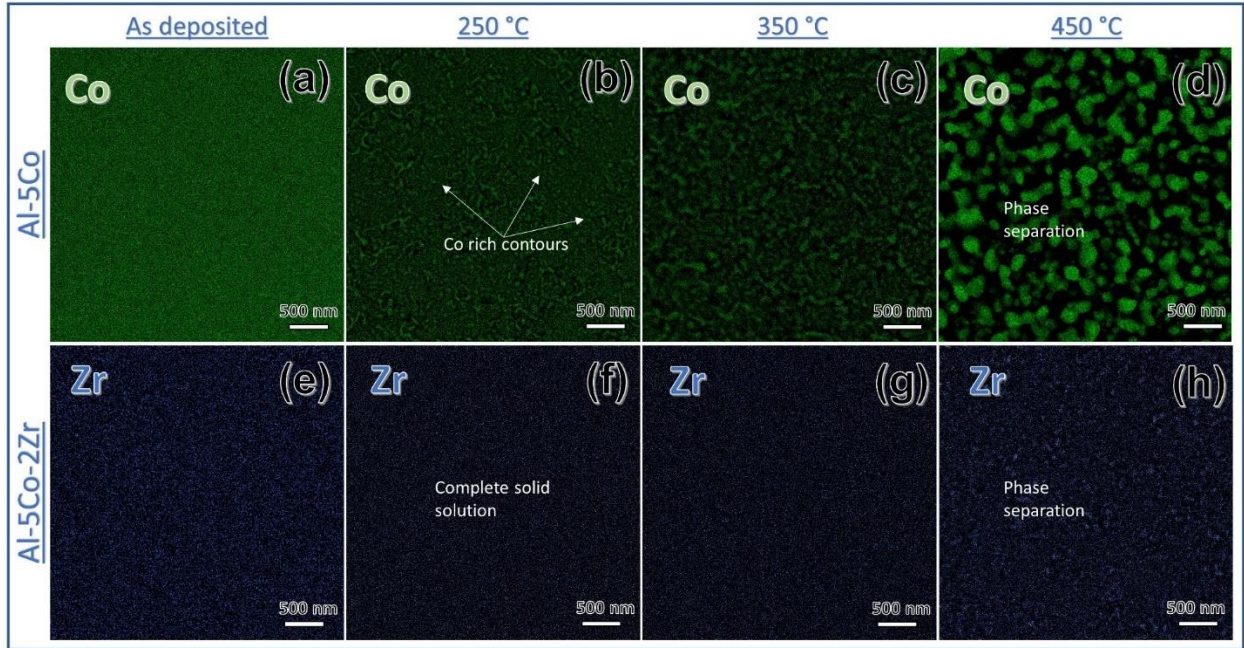
Figure 5-6. Co and Zr EDS map of plan-view TEM specimens revealing the chemical distribution in (a-d) Al-5Co, (e-h) Al-5Co-2Zr upon annealing at the corresponding temperatures.
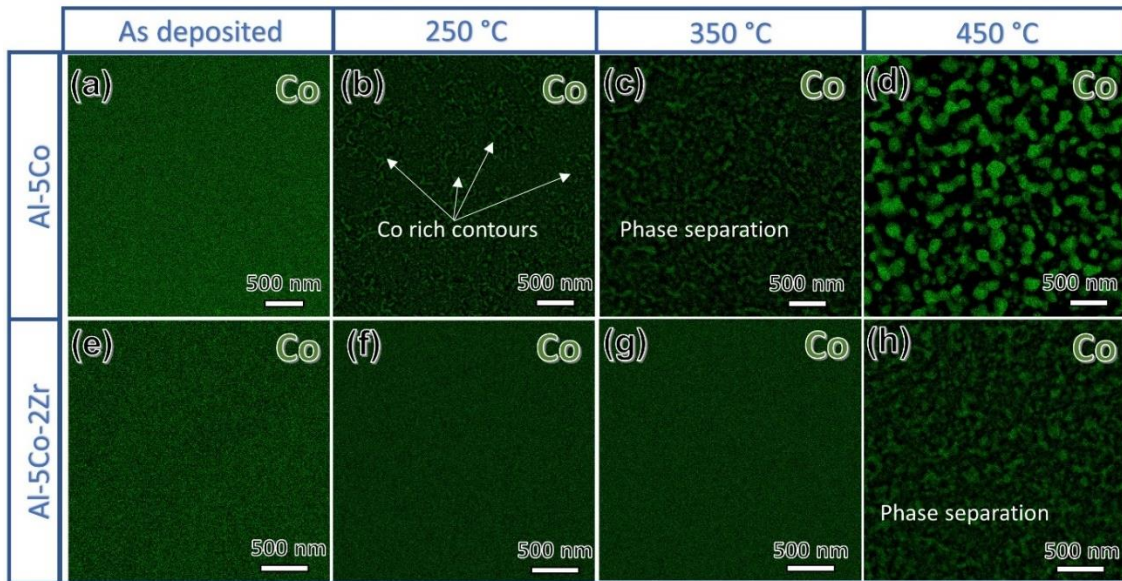
Figure 5-7. EDS maps depicting the progression of Co solute distribution in NT Al-5Co-2Zr alloys after annealing for 1.5 hours corresponding to each labeled temperature, (a) As-deposited, (b) 250 °C, (c) 350 °C and (d) 450 °C.

The microstructures of specific annealed samples were further explored after annealing using XTEM. After annealing the Al-5Co alloy at 250 °C, BF and DF TEM micrographs in Figure 5-8(a-b) show the maintenance of a columnar structure, albeit slightly coarsened. The corresponding SAD pattern shows minor{111} texture, similar to the PVTEM SAD pattern in Figure 5-5(b). The Co EDS map in Figure 5(c) shows Co segregation to the columnar boundaries, forming the aforementioned Co contours depicted in Figure 5-6(b). The Al-5Co-2Zr alloy annealed at 450 °C was also investigated to assess the stability of the columnar ITB structure. Both the BF and DF TEM micrographs in Figure 5-8(d-e) reflect completely recrystallized grains and the removal of columnar ITBs and nanocolumns. The Co EDS map in Figure 5-8(f) also shows complete phase separation and recrystallization.
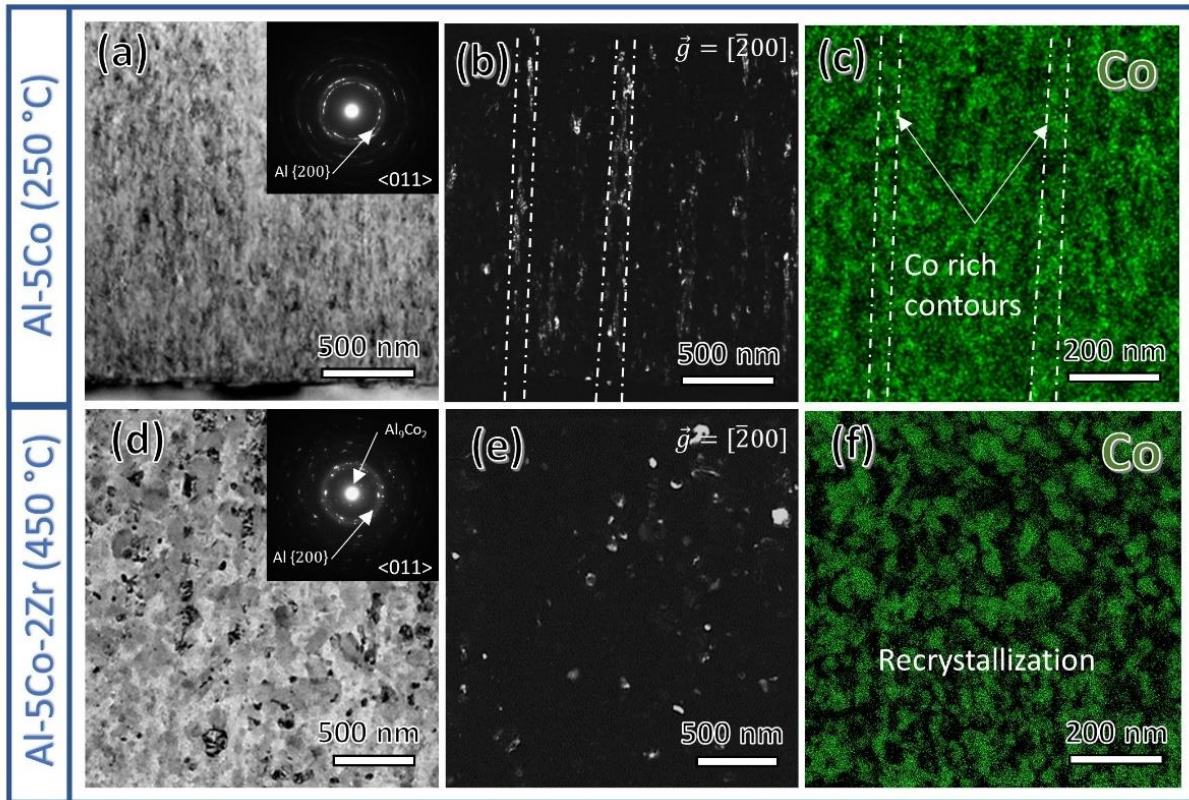
Figure 5-8. (a) BF-TEM with corresponding SAD insert, (b) DF-TEM and (c) Co EDS map images of Al-5Co annealed at 250 °C. (d) BF-TEM with corresponding SAD insert, I DF-TEM and (f) Co EDS map of Al-5Co-2Zr annealed at 450 °C
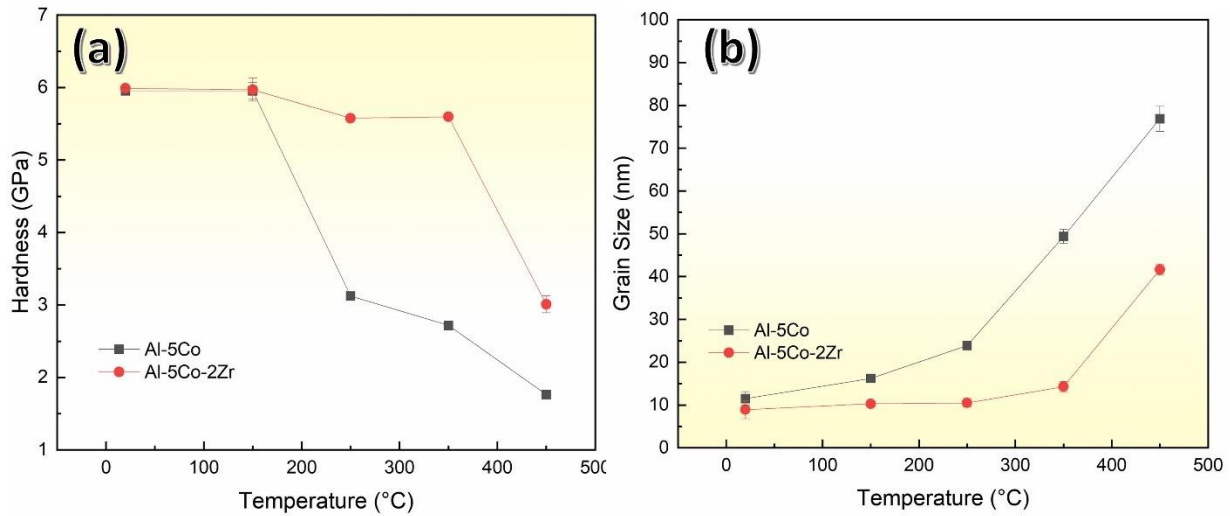
Figure 5-9. (a) Hardness evolution with annealing temperature comparing the NT Al-5Co and Al-5Co-2Zr alloys. (b) Grain size evolution with annealing temperature comparing the NT Al-5Co and Al-5Co-2Zr alloys. Each annealing experiment was conducted for 1.5 hours.

The hardness of the as-deposited alloys was compared with literature in the Hall-Petch plot in Figure 5-9(a). The as-deposited Al-5Co and Al-5Co-2Zr have nearly identical microstructures and reach a hardness of ~5.9 GPa, while Al-2Co achieves a hardness of 4.1 GPa. These Al-Co alloys far outperform most NC Al alloys, as well as NT Al-Zr and Al-Ti binary alloys [195,271,277,296,349]. The progression of the hardness with annealing temperature plotted in Figure 5-9(b) shows the binary Al-5Co alloy softens from 5.9 to 3 GPa after annealing at 250 °C, and further drops to 1.7 GPa after 450 °C annealing. Remarkably, the Al-5Co-2Zr alloy maintains an ultra-high hardness above ~5.7 GPa even after annealing at 350 °C, and softens upon recrystallization at 450 °C. In comparison, the various NC and commercial Al alloys presented from literature typically soften at temperatures ranging from 100-200 °C. This hardness evolution exemplifies the significant thermal stability of the NT Al-Co alloy with Zr additions.

144
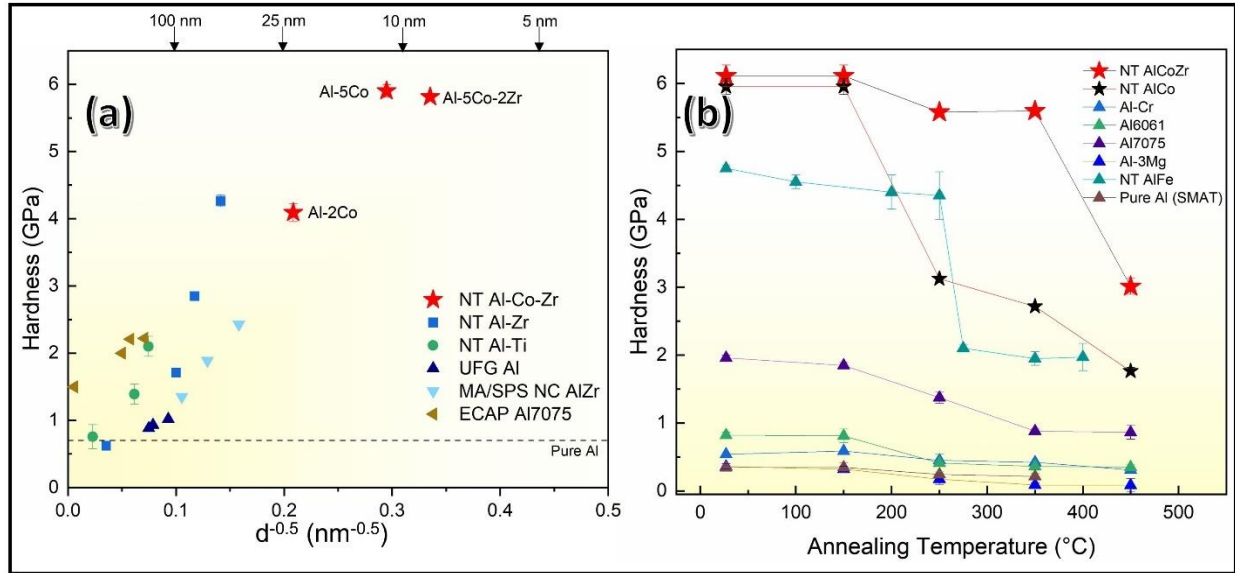
Figure 5-10. (a) Hall-Petch plot comparing the as-deposited NT Al-Co-Zr alloys with literature [195,271,277,296,349]. (b) Hardness evolution with annealing temperature for various nanocrystalline Al alloys [18,113,138,349–352].

5.4.3 *In-situ* micropillar compression

Room temperature *in-situ* micropillar compression tests were conducted to examine the plastic deformability of the annealed NT Al alloys. Figure 5-11(a) shows the true stress-true strain curves for both the as-deposited (AD) and annealed (at 250 °C) NT Al-5Co alloy. The yield and flow stress of the AD NT Al-5Co reaches 1.1 ± 0.2 GPa and 1.16 ± 0.18 GPa, respectively, while the annealed binary sample softens to 378 ± 44 MPa and 515 ± 60 MPa, respectively. Each flow stress value was measured at 10% strain to maintain consistency. Both alloys remain highly deformable, with obvious dilation of the pillar top seen in both cases (Figure 5-11(b-i)). Figure 5-11(d) compares the true stress-true strain curves for the AD and annealed (450 °C) Al-5Co-2Zr alloy. The yield and flow stress of the AD NT Al-5Co-2Zr reaches 1.18 ± 0.3 Gpa and 1.19 ± 0.21 Gpa, respectively, while the annealed ternary sample softens to 397 ± 28 MPa and 506 ± 40 MPa, respectively. Each flow stress value was measured at 10% strain to maintain consistency. The samples annealed at 450 °C (0.77 T_m) exhibit softening to 500 MPa. *In-situ* SEM snapshots in Figure 5-11(k-r) show the dilation of the pillar top in both the NT AD and the 450 °C annealed specimen. Corresponding *in-situ* videos are included in the Supplementary section of this work. No samples were tested beyond 250 °C in the binary case as they would simply exhibit more softening as the microstructure coarsened based on the hardness and microstructure evolution.

145

Similarly, no compression tests were conducted on the 250 and 350 °C annealed NT Al-5Co-2Zr since they are almost microstructurally identical to the as-deposited case. The curves presented here represent the points where the results deviate due to annealing.
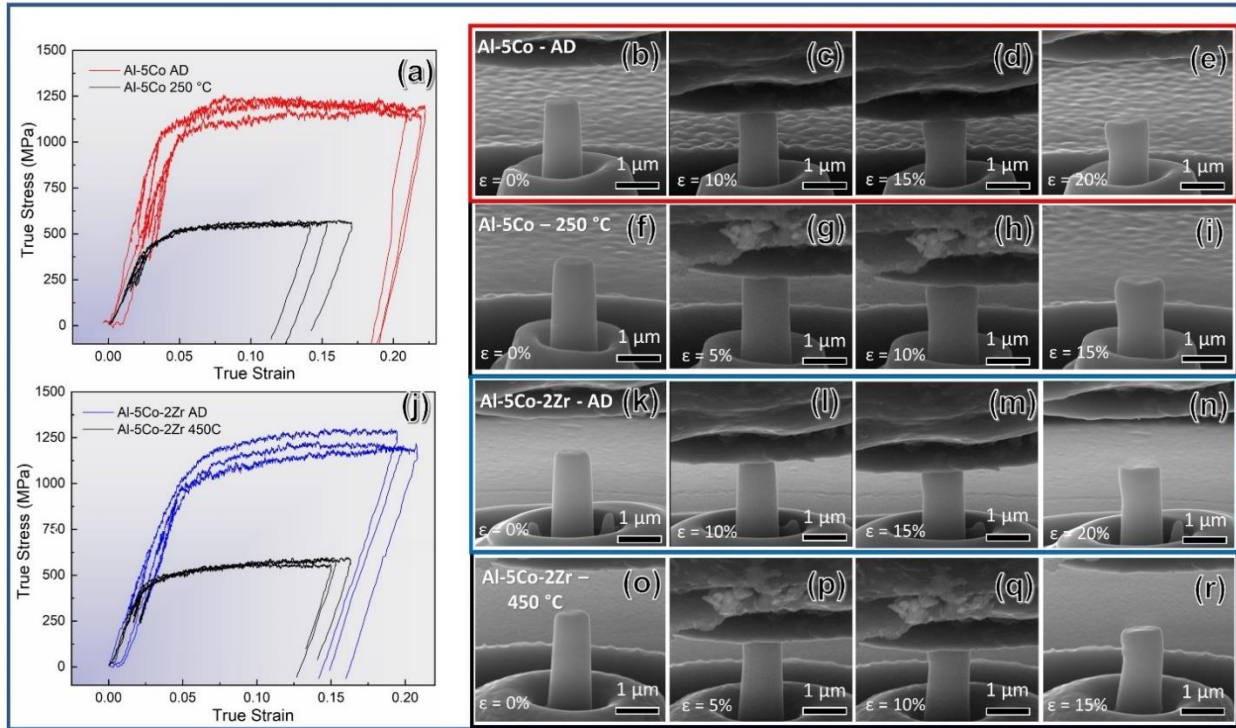
Figure 5-11. Micropillar compression test results for the as-deposited and annealed Al-5Co and Al-5Co-2Zr with the 'nanotwinned' microstructures. (a) Resulting true stress-strain curves for the as-deposited (AD) and 250 °C annealed Al-5Co micropillars showing significant stress reduction upon annealing. *In-situ* SEM snapshots of the (b-e) AD and (f-i) 250 °C annealed Al-5Co micropillars compressed at different strain levels showing dilation of the pillar top. (j) The true stress-strain curves for the AD and 450 °C annealed Al-5Co-2Zr micropillars showing significant stress reduction upon annealing. In-situ snapshots of the (k-n) AD and (o-r) 450 °C annealed Al-5Co-2Zr micropillars at various strain levels. Corresponding *in-situ* video files are presented in the supplementary information of this work.

5.5   Discussion

5.5.1   Strengthening mechanisms and deformability

Increasing the strength of an alloy typically leads to a significant drop in plastic deformability, as depicted in the classical "banana curve" for steels [18,350]. Figure 5-10 demonstrates that both the as-deposited Al-5Co and Al-5Co-2Zr alloys possess high hardness (5.9 GPa) compared with most Al alloys, while the micropillar compression stress-strain curves shown in Figure 5-11 reflect that they maintain prominent plasticity. The strength of these alloys is

derived from multiple factors, namely an increased level of solid solubility enabled by magnetron sputtering, the formation of extremely fine columnar grains on the order of tens of nm, and an abundance of ITBs and 9R phase. Our previous studies suggest the influence of solid solution strengthening is relatively minor in these sputtered NT Al alloys, with 10at% Zr only generating a 28.3 MPa increase in hardness, with similar findings in binary NT Al-Co alloys [197,271]. These findings suggest the strength increase seen here is driven by the columnar grain size and by ITBs. The Hall-Petch plot in Figure 5-10(a) demonstrates the hardness improvement with decreasing grain size. Another significant feature is the variation in Hall-Petch slope between NT Al alloys compared with NC Al alloys from literature [195,271,277,296,349]. A combination of the NT Al-Co-Zr and previous NT Al data depicts a Hall-Petch slope of 9.3 GPa•nm$^{1/2}$, which nearly doubles that of the NC Al and Al alloy value of 4.7 GPa•nm$^{1/2}$. This significant variation in Hall-Petch slope is related to boundary type. In these NT Al-Co-Zr alloys, most of the columnar boundaries are Σ3 ITBs and 9R phase, which have been shown to be a stronger barrier to the propagation and penetration of dislocations than conventional GBs [177,192,193,252,255].

The difference in boundary type also impacts the deformability of these NT alloys exhibited during microcompression (Figure 5-11). It is evident from Figure 5-1 that these alloys are composed of predominately vertical ITBs. The HRTEM images in Figure 5-1 reveal significant 9R phase (diffuse ITBs) dispersed throughout the microstructure. This structure has been well documented in various systems [71,159,258] and is composed of a repeating array of partial dislocations, as revealed by Wang et al using molecular dynamics simulations [155]. These partial dislocations have been identified to be mobile, and are directly related to detwinning processes in NT metals [156,173,323]. The mobility of these ITBs, and consequently the 9R phase, plays a significant role in maintaining plasticity in the NT Al-Co-Zr alloys presented here, and is recognized by the dilation of the pillar top in Figure 5-11. The interaction of dislocations with the vertical ITBs leads to work hardening [177] while the simultaneous detwinning phenomenon promotes softening and significant plasticity [159]. The microstructural stability reported here of the NT Al-Co-Zr alloy suggests that these alloys would exhibit similar mechanical responses at elevated temperatures until complete recrystallization at 450 °C (0.78T$_m$).

5.5.2 The role of Zr solute on microstructural stability of NT Al alloys

The influence of even a small percentage of Zr added into the binary NT Al-Co alloys is striking as the microstructure and mechanical properties remain stable up to 450 °C. This observation is manifested through the microstructural and chemical stability shown in the pre-annealing and post-annealing TEM analyses in Figures 5-(5-7). These samples were annealed under high vacuum, so the impact of oxidation was negligible in this study. The hardness evolution as a function of annealing temperature is compared with various Al alloys from literature in Figure 5-10(b) [199,325,353–356]. As illustrated schematically in Figure 5-12(a), the binary Al-Co alloys experience recrystallization and precipitation of the Al_9Co_2 intermetallic phase at 250 °C, whereas the presence of Zr solute suppresses this process until 450 °C in Al-5Co-2Zr alloy (Figure 5-12(b)), and stabilizes uniform solid solution and fine columnar grains up to 350 °C.
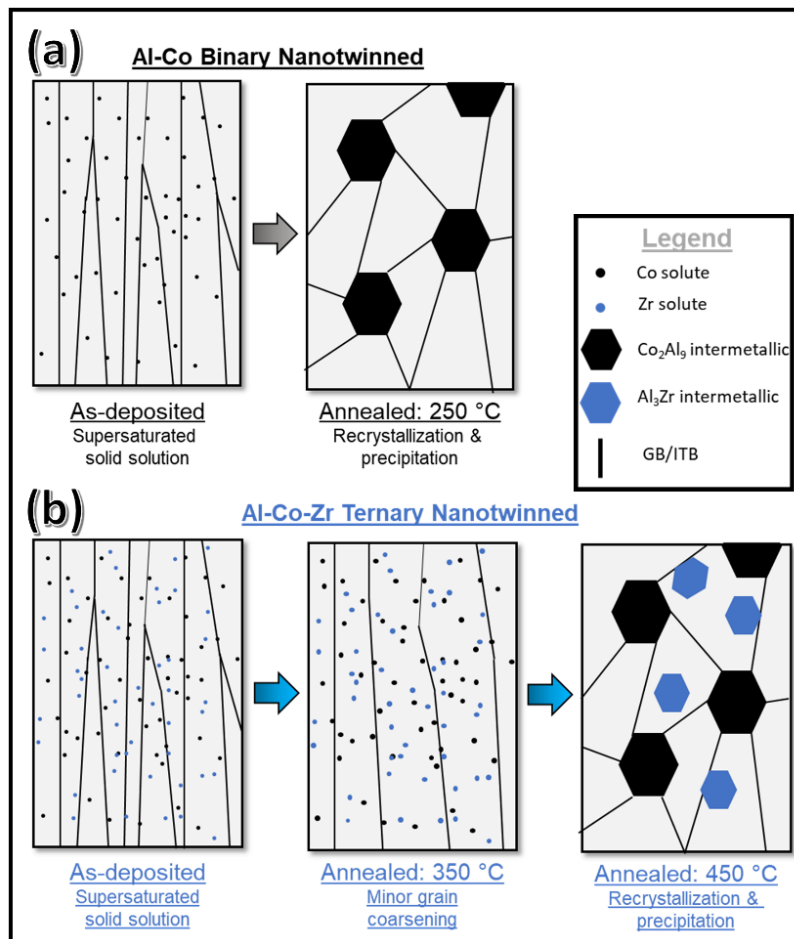
Figure 5-12. Schematics illustrating the microstructural evolution characteristics with annealing temperature for the binary (a) Al-5Co and ternary (b) Al-5Co-2Zr with the resulting phases not shown to scale.

148

These trends correspond well with the hardness evolution with annealing temperature. When compared with other NC and UFG Al alloys in Figure 5-10(b), it is evident that the thermal stability of NT Al alloys far outperforms their NC counterparts, with NT Al-Co even outperforming NT binary Al-Fe alloys [199]. Two factors drive the improved thermal stability, the lower boundary energy of TBs in these NT Al-Co-Zr alloys and the addition of Zr solute. This distinction is necessary, as it is often reported that NT metals have improved thermal stability compared to the significant softening seen in NC Al alloys. Additionally, the NT Al-Co-Zr alloy far outperforms the binary NT Al-Co and Al-Fe alloys composed of similar microstructures. First, it has been well established that NT metals (i.e. Cu, Ag etc.) have improved thermal stability due to the low TB energy compared with typical GBs [135,136,260]. Specifically looking at Al, Uesugi et al. demonstrated that typical tilt boundaries in Al have boundary energies of 400 mJ/m^2, while Σ3 TBs have boundary energies of 120 mJ/m^2 [357]. This study supports the increased stability of the NT microstructure, however further investigation of solute interactions is necessary to understand the bolstered thermal stability of Al-Co-Zr alloy.

Zr solute facilitates significant improvements to the thermal stability of the columnar NT microstructure in Al-Co. Recrystallization and grain coarsening processes are driven by accelerated diffusion of atoms through the matrix at elevated temperatures [358–360]. The presence of solute atoms in the lattice can alter the kinetics of this diffusion restricting the potential for recrystallization. As shown in Figure 5-5 and Figure 5-9(b), the grain size coarsens to approximately 75 nm in the binary Al-Co alloy at 450 °C, while the grain size of the ternary Al-Co-Zr remains 40 nm, not significantly larger than the as-deposited alloy. It has been well established that the diffusivity of Zr in Al (D_{Zr}) is low leading to a slow diffusing solute [361]. Bulk Al alloys have recently taken advantage of this behavior and reported unique "core-shell" Al$_3$(Sc, Zr) L1$_2$ precipitates that retard grain coarsening at significant fractions of the melting temperature (0.74T$_m$) [355,362]. This trend can also be applied to these NT Al-Co-Zr alloys as the large activation energy and large pre-exponential factors indicate Zr will diffuse slowly through Al [363]. At 400 °C, the diffusivity of Co in Al, D_{Co}, is reported to be 1.76×10^{-15} m^{2}s^{-1}, whereas D_{Zr} in Al is five orders of magnitude lower, 1.2×10^{-20} m^{2}s^{-1} [274,364]. Since Zr prefers to occupy substitutional sites in Al [271] and is uniformly distributed throughout the matrix, the slow diffusivity of Zr is highly important to the thermal stability of microstructures in NT Al-Co-Zr reported in this study. As a result, the Zr solute directly influences the mobility of both Co and Al

atoms, resulting in the prevention of both recrystallization and phase separation, which both depend on diffusion.
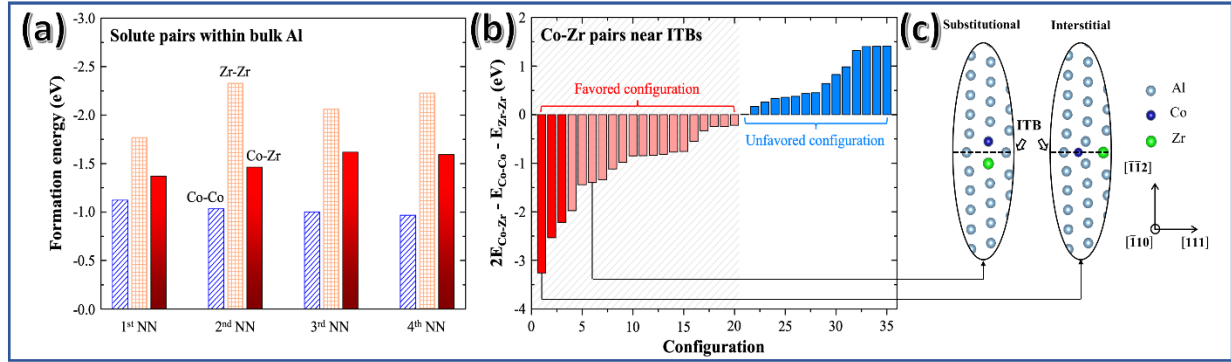
Figure 5-13. (a) Formation energy of solute pairs (two solutes could be each other's 1st, 2nd, 3rd and 4th nearest neighbor (NN)) within bulk Al. (b) The comparable formation energies, i.e. $2E_{Co-Zr} - E_{Co-Co} - E_{Zr-Zr}$, of Co-Zr pairs with 35 possible configurations near ITBs. (c) Two typical low energy configurations: 1) both Co and Zr solutes are substitutional atoms (on the left); 2) Both Co and Zr solute are interstitial solute atoms (on the right).

5.5.3   Synergy between Co and Zr solutes

A common pitfall associated with fabricating nanocrystalline metals is their inherent thermal instability [233,325,365]. As a result, research focused on nanocrystalline materials has largely been centered around remedying this deficiency [134,366,367]. A review presented recently by Schuh and Lu discusses the common strategies employed to address the limited thermal stability of nanocrystalline metals [125]. First, alloying elements can be added that preferentially segregate and function to either pin GBs or lower GB energy limiting the capacity for grain coarsening [126,127,338,368]. This principle provides a relatively straightforward approach to stabilizing nanograins against rapid coarsening as the solutes thermodynamically prefer to segregate and arrest GB migration [131,132,369–372]. Expanding this strategy employs more complex thermodynamics to select solute that prevents second-phase formation but prefers segregation to GBs to enable GB pinning [127,128,343,347]. Darling et al. identified an Fe-Zr alloy capable of withstanding annealing at $0.92\,T_m$ due to the GB energy reduction enabled through Zr solute additions [373].

A second strategy relies on GB engineering to fabricate materials composed of low energy GBs based off their crystallography [129,134,374]. $\Sigma3(111)$ twin boundaries are highly coherent

and symmetrical GBs that have intrinsically low energy [193,375]. Anderoglu et al. reported almost no change in NT spacing in sputtered Cu foils after annealing at 0.8 T_m [136]. Zhang et al and Bufford et al observed similar findings in stainless steel and Ag thin films, respectively [135,260]. Tailoring film texture and resulting GB crystallography can be a highly effective means for imparting improved thermal stability [344,374]. As will be further discussed, both of these strategies are active in promoting the thermal stability reported in this study.

Similar to the aforementioned stabilization strategy, the energetic landscape for diffusion can be altered through selection of alloying elements. This directly leads to the notable thermal stability reported in this study. Density functional theory (DFT) calculations were conducted to compare the energy associated with the formation of Co-Zr, Co-Co and Zr-Zr pairs in an Al lattice. Figure 5-13(a) contains the solute pair formation energy. The first, second and third nearest neighbors (NN) for Co-Co pairs have respective energies (E_{Co-Co}) of -1.15 eV, -1.03 eV and -1.00 eV, comparing to Co-Zr pairs with energies (E_{Co-Zr}) of -1.38eV, -1.46eV and -1.75eV, respectively. This comparison indicates that Co-Zr solute pairs are more stable and preferable over Co-Co pairs. This aspect is important as the slow diffusing Zr solute will slow down the diffusion of Co solute, preventing phase separation and Co segregation seen at 250 °C in the binary NT Al-Co alloys. Figure 5-13(b) details the energy difference between solute pairs ($2E_{Co-Zr} - E_{Co-Co} - E_{Zr-Zr}$, of Co-Zr pair) corresponding to 35 different configurations for Co-Zr pairs forming around ITBs, with the selected configurations in Figure 5-13(c) depicting examples of both substitutional and interstitial sites. 20 of the 35 configurations analyzed were favorable, with the substitutional Co-Zr pair having the lowest energy configuration. These DFT calculations highlight the synergistic interplay that Co-Zr solute pairs can play in pinning ITBs, and GBs demonstrated in this study.

The capability of solute pairings to Improve thermal stability into nanocrystalline Al alloy systems has been previously explored. Notably, the work by Balbus et al utilized Ni and Ce solute to stabilize nanograins in an Al-Ni-Ce alloy up to 0.7 T_m [376]. This strategy effectively stabilized sub-10 nm grains and aided in significantly reducing shear localization through the formation of Ni-Ce rich grain boundaries. The joint segregation provided a simultaneous microstructure stabilization with a means to obstruct dislocation and shear band propagation [376]. Another study explored the thermal stability of NT Al-Fe-Ti alloys that exhibited similar microstructures to this study [138]. They identified that Ti additions enabled microstructural stability up to 0.72 T_m, far outperforming its binary counterparts [138,199]. Similarly, the DFT analysis presented here

coupled with the EDS analyses performed in this study highlight the role Co-Zr solute pairs play in raising the energy barriers for migration of ITBs through solute segregation. These solutes exhibit a relationship in how they function to promote thermal stability in otherwise unstable microstructures. The Co solute promotes fine grains, which is evident as the binary Al-Co alloy has a similar as-deposited grain size as the ternary Al-Co-Zr. The Zr solute is a slow diffuser and prefers to reside and pin Co solute to the ITBs, preventing both phase separation into Co rich regions and grain coarsening through Zener pinning. The synergistic behavior of these solutes highlights an effective strategy for increasing thermal stability through careful selection of solutes.

5.6   Conclusion

Extensive microscopy studies and in situ micromechanical testing of supersaturated Al-Co-Zr alloys in this study have shown these alloys have high mechanical strength, plastic deformability and thermal stability. Co solute in sputtered Al films refines the microstructure to the nanoscale and Zr solute helps to further enhance (111) texture and promote twinning . Zr solute, a slow diffuser in Al, synergistically works with Co to pin ITBs from migration when exposed to high temperatures, leading to substantial thermal stabilization up to 450 °C ($0.78\ T_m$). DFT calculations show the Co-Zr solute pairs are very stable and prevent the Co solute segregations, thus stabilize the microstructures of ITBs and 9R phase. This study underscores the importance solute pairs play on the mechanical and thermal stability of Al alloys and provides a possible route for the discovery of high strength, thermally stable alloys with fine grains.

5.7   Acknowledgements

6. TEXTURE DEPENDENCE OF TWIN FORMATION IN AL-3ZR SPUTTERED FILMS

6.1 Overview

Twin formation is challenging in Al and its alloys due to an inherently high stacking fault energy. Recent developments have identified twin formation mechanisms in sputtered Al alloy coatings composed of finely spaced nanocolumns bounded by incoherent twin boundaries leading to significantly improved mechanical properties and thermal stability. The influence of film texture on twin formation in Al sputtered alloys and the subsequent mechanical response is less well understood. Here, epitaxially grown Al coatings on various oriented Si substates demonstrate the difference in twin structure caused by film texture. (111) and (112) epitaxial Al-3Zr films are composed of the finest grains (~70 and 100 nm, respectively) and highest twin densities, although the twin character is identified to be different based on film orientation. Correspondingly, these coatings also possess the highest hardness, and can be attributed to the hardening imparted by higher twin densities compounded with the refined microstructure. Detailed texture analysis via transmission electron microscopy uncovers the changing film structure and provides insight into the change in mechanical properties.

6.2 Introduction

Nanotwinned (NT) metals have garnered significant attention recently due their many advantageous properties [159,181,196,248,264,266,377–380]. Twin boundaries (TBs) are $\Sigma 3$ coincident site lattice (CSL) boundaries characterized through mirror symmetry and low inherent grain boundary energy [169,381–383]. These highly coherent planar defects impart many desirable properties, including concomitant high strength and ductility [159,196,271,308], improved wear properties [309] and strain rate sensitivity [104,384,385], improved thermal stability [139,193,386] and high electrical conductivity [169,172,173,258]. The slip discontinuity across TBs inhibits dislocation transmission, providing effective barriers to dislocation motion and generating high flow strengths. Molecular dynamics (MD) simulations [179,180] and *in-situ* nanoindentation experiments [157,323] demonstrate the efficacy of TBs as barriers to dislocation motion. Dislocations require a high resolved shear stress in order to dissociate at the twin interface and

153

recombine in the adjacent grain [179,180]. Wang et al. identified detwinning mechanisms through *in-situ* nanoindentation in NT Cu, highlighting the plasticity carrying capability of TBs [156]. *In-situ* nanoindentation experiments in Al also reveal the improved work hardening provided by incoherent twin boundaries (ITBs) [177]. TBs have also been identified in ceramic materials and aid in improving fracture toughness by inhibiting crack propagation [387,388].

Twins can be introduced into metals via annealing (annealing twins), as plasticity carriers (deformation twins) or during crystal growth (growth twins). Σ3 TBs in FCC metals are categorized by their habit plane, with coherent twin boundaries (CTBs) residing on {111} planes and incoherent twin boundaries (ITBs) lying on {112} planes 1. CTBs possess extremely low boundary energies and are highly stable. Metals with a low stacking fault energy (SFE), such as Ag (16 mJ/m^2) [389], Au (32 mJ/m^2) [390] or Cu (45 mJ/m^2) [304,389], have a higher propensity for twin formation. Even under equilibrium conditions, twins are common among these metals. General planar fault energy (GPFE) curves modeling <112> slip of Shockley partials lying on {111} planes provides more insight to the twinnability of FCC metals [261]. Lower ratios between the unstable SFE (γ_{USFE}) and the stable SFE (γ_{SFE}) indicate a higher propensity for stable twin formation. During physical vapor deposition of low SFE metals, the free energy difference between twinned nuclei and defect free nuclei is negligible, leading to a higher density of stabilized stacking faults and twins in the resulting films [135,189,262]. Bufford et al. documented a high density of nanometer spaced Σ3{111} CTBs orthogonal to the growth direction bounded by both columnar high angle boundaries and Σ3{112} ITBs in (111) textured magnetron sputtered Ag [170]. This unique nanostructure exhibited high hardness and the CTBs remained stable at elevated temperatures while the high angle columnar boundaries coarsened dramatically [135]. In comparison, NT Cu fabricated by electrodeposition is composed of an ultrafine polycrystalline aggregate containing nanometer spaced CTBs [169,173,258]. FCC metals with a high SFE, such as Ni (120 mJ/m^2) [391] and Al (140 mJ/m^2) [392], have a much larger energy penalty for twin formation. Far-from-equilibrium processing techniques, specifically electrodeposition and magnetron sputtering, have been utilized to introduce a high density of growth twins into high SFE metals [159,171,196,393,394]. Li et al. reported a unique nanoscale network of Σ3{111} CTBs and Σ3{112} ITBs in highly textured electrodeposited Ni, leading to improved corrosion resistance and mechanical properties [171].

Understanding the thermodynamic aspects governing nucleation and growth of TBs is crucial to synthesizing NT materials. The reduction in interfacial energy provided by Σ3 TBs is a major driving force for twin formation [181,264]. A thermodynamic vapor nucleation model developed by Zhang et al. [262] and expanded upon in the work by Xue et al. [189] determines the critical radius difference between defect free and twinned nuclei. Lower SFEs (γ_t) and increased deposition flux (J) both promote twin formation as the twinned nuclei critical radius approaches the defect free nuclei critical radius. A reduced twin spacing is documented at higher deposition rates in both magnetron sputtered [172] and electrodeposited [169,173] of NT Cu. Additionally, applying larger substrate biases during magnetron sputtering provides increased ion bombardment energy and higher levels of residual stress, driving partial dislocation motion and finer twin spacings in NT Cu [395]. In contrast, higher substrate temperatures provides the necessary energy for atoms to diffuse into their correct FCC stacking site, increasing twin thickness [396]. Film texture has been also documented to influence twin formation as different surface energies are associated with twin variants in differently oriented crystals [190,290]. This thermodynamic model further indicates that increasing J alone is insufficient to introduce growth twins into high SFE metals [189]. A template method was developed as an alternative means to replicate twin structures from a low SFE "template" layer into a high SFE film [154]. Yu et al. documented that (1) a low SFE seed layer and (2) a coherent interface between layers enabling epitaxial growth and twin replication were needed to execute this methodology [301]. Ag/Al [154] and Cu/Ni [397] template/film pairs demonstrate this phenomenon as a high density of ITBs and CTBs were replicated from Ag and Cu into Al and Ni, respectively.

As twin nucleation and growth are kinetic processes, altering deposition conditions directly impacts twin formation. Competitive grain growth and grain coarsening wipe out twin variants from high SFE metals during physical vapor deposition [189]. Kinetically interrupting film growth processes through the introduction of coherent interfaces stabilizes twinned variants in high SFE Al layers in Al/Mg [191] and Al/Ti multilayers [192,193]. Recently, magnetron sputtering of highly {111} textured Al-X alloys with transition metal solutes (X = Fe, Ni, Co, Ti, Zr) has been identified as a means to synthesize high strength NT Al alloys composed of an abundance of vertically oriented Σ3{112} ITBs [159,195–198]. Extensive networks of diffuse ITBs, or "9R phase", are stabilized within these microstructures, providing additional sources for both dislocation motion obstruction and plasticity [159,308]. Using density functional theory

calculations, Gong et al. demonstrated how various transition metal solutes alter the SFE of Al and promote grain refinement [200]. These sputtered alloys form super-saturated solid solutions, and the solutes kinetically pin the partial dislocations composing ITBs and prevent fault correction during film growth. Solute selection is key as certain transition metal solutes promote twin formation (Fe, Ni, Zr, etc.) while others do not (Cr, Mo) [289].

In this study, the dependence of film texture on twin density and resulting mechanical properties was studied in NT Al-3Zr sputtered films. This expands upon the previous work by Xue et al. [190] identifying texture dependent twin formation mechanisms in pure Al and injects the influence of solute into the formation of these twin structures. Extensive transmission electron microscopy (TEM) experiments detail the resulting microstructures, highlighting the difference in twin structure in differently textured Al films. Nanoindentation hardness measurements also provide insight into the change in deformation mechanisms as the film texture changes. Additionally, the aforementioned thermodynamic model describing twin formation in physical vapor deposition is expanded upon to help explain the difference in twin density as a function of texture. This work provides insight into twin formation mechanisms and direction on fabricating twinned structures in high SFE metals.

6.3   Experimental

Pure Al and Al with 3at%Zr (Al-3Zr) coatings 1µm in thickness were deposited using magnetron sputtering at room temperature. A 50nm Ag seed layer was deposited to promote epitaxial growth on different textured Si substrates ((100), (110), (111), (112) and amorphous SiO_2). Al (99.999%), Ag (99.999%) and Zr (99.995%) targets were used, and the sputter chamber was evacuated to ~8 x 10^{-8} torr prior to deposition. A Panalytical Empyrean X'pert PRO MRD diffractometer operated at 40 kV using Cu Kα1 x-rays was used to perform out-of-plane θ-2θ x-ray diffraction (XRD) scans and to collect pole figure measurements. Transmission electron microscopy (TEM) samples were prepared from the as-deposited films using mechanical grinding, dimpling and low energy Ar ion milling. Any sample heating was avoiding during sample preparation processes to ensure reliable microstructural analysis. A Thermo Fisher Talos 200X analytical microscope operated at 200 kV was used to assess film microstructure. This microscopy is equipped with a Fischione high-angle annular dark field (HAADF) detector and a super X energy-dispersive x-ray spectroscopy (EDS)detector enabling chemical analysis. Crystallographic

156

orientation mapping and GB misorientation measurements were performed using the TALOS 200X using a Nanomegas ASTAR^{TM} system with a camera length of 205 mm, a precession angle of 0.6°, and a step size of 8 nm. A Hysitron TI Premiere nanoindentation system was used to probe the hardness and moduli of the as-deposited films. The indent depth was maintained below 15% to avoid incorporating substrate effects, and 50 indents were conducted per sample to ensure statistical reliability.

6.4   Results

Out-of-plane θ-2θ and pole figure XRD measurements were collected to assess the overall Al-3Zr film structure and texture on differently oriented Si substrates. Figure 6-1(a) reveals the change in Al-3Zr film texture when deposited on differently oriented Si substrates with Ag seed layers. Si(100) and amorphous SiO2 (referred to as (100) Al-3Zr and (SiO$_2$) Al-3Zr hereafter, respectively) substrates form polycrystalline randomly oriented films based on the resulting XRD spectra. In comparison, films deposited on Si(110), Si(111) and Si(112) (referred to as (110) Al-3Zr, (111) Al-3Zr and (112) Al-3Zr hereafter, respectively) all resulted in highly textured Al-3Zr coatings with similar corresponding textures. Each of these spectra contains peaks associated to these strong textures, with some minor peak splitting identified in higher order peaks due to the Ag seed layer. Since the (112) oriented films contain crystallographic orientations with 2θ values beyond the range of our diffractometer, an out-of-plane sample rotation of χ=19.47° to the Al(111) peaks was necessary to confirm the strong (112) texture. Additionally, no second phase peaks were identified in any of the spectra in Figure 6-1(a), suggesting super saturated solid solutions form regardless of substrate. Figure 6-1(b-f) contains the resulting (111) pole figure scans for each coating, further confirming the texture trends identified previously. Notably, the pole figure for the (111) Al-3Zr in Figure 6-1(c) possesses 6-fold symmetry indicating a high density of growth twins within the microstructure. This symmetry is also seen in the pole figures for (112) Al-Zr in Figure 6-1(d). There is a 15° rotation in the diffraction spots in the (112) Al-3Zr alloy indicative of the rotation in the crystallographic planes when compared with (111) Al-3Zr.

157
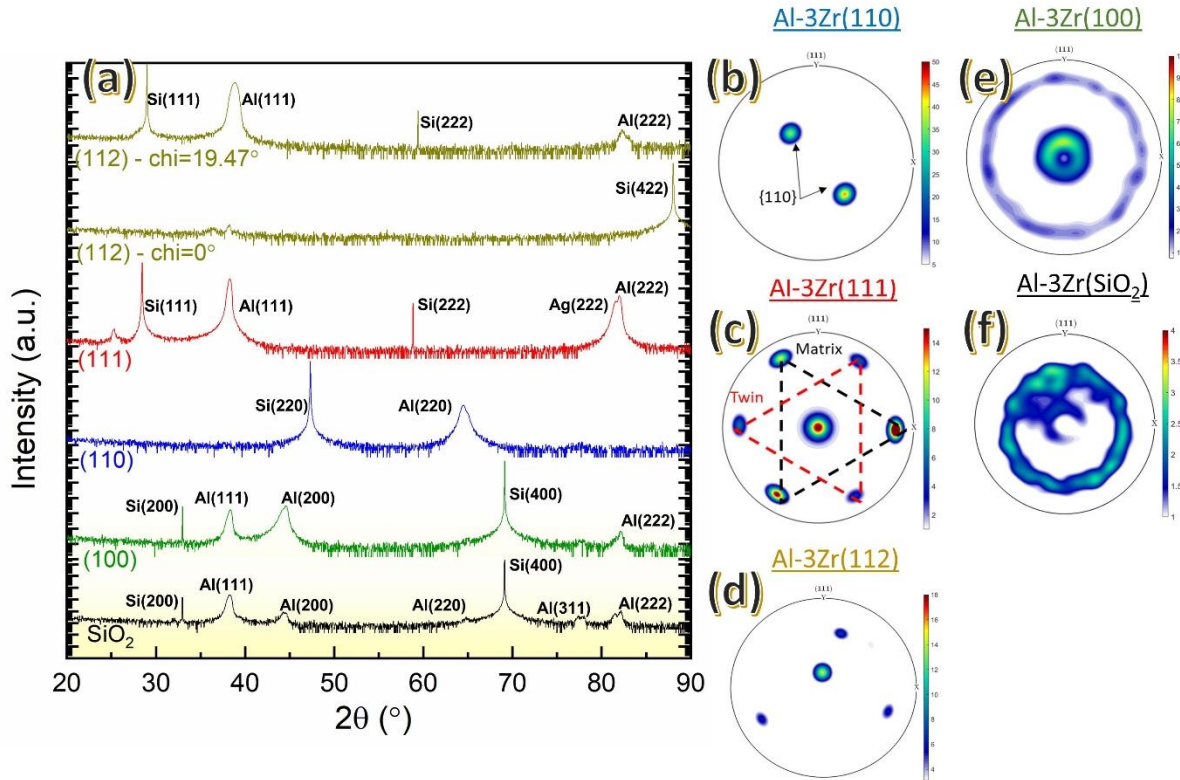
Figure 6-1. (a) XRD spectra for Al-3Zr alloys deposited on various Si substrates. (b-f) XRD pole figure collected along the (111) pole for Al-3Zr alloys deposited on (b) Si(110), (c) Si(111), (d) Si(112), (e) Si(100) and (f) amorphous SiO$_2$ substrates

The hardness was measured using nanoindentation for both pure Al and Al-3Zr deposited on each studied Si substrate and the results are presented in Figure 6-2(a). Very little variation is seen in pure Al, with (111) Al reaching a hardness of ~0.9 GPa, whereas the rest of the films only reach an average hardness of ~0.8 GPa. In comparison, the Al-3Zr all reach a higher hardness than their pure Al counterpart, with the (111) Al-3Zr and (112) Al-3Zr reaching ~1.5GPa, almost double that of pure Al. (110 Al-3Zr achieves a high hardness of ~1.3GPa while (100) Al-3Zr and (SiO$_2$) Al-3Zr only reach a hardness of 1 GPa. The average grain size was measured using the line intercept method from plan-view TEM micrographs and is plotted as a function of substrate texture in Figure 6-2(b). The pure Al grain size from the study by Xue et al. [190] was used as a reference and the grain sizes reach 160, 400 and 340 nm when deposited on Si(110), Si(111) and Si(112), respectively. In comparison, (110) Al-3Zr, (111) Al-3Zr and (112) Al-3Zr all experience a reduction in grain size, reaching 124, 77, and 101 nm, respectively. (100) Al-3Zr and (SiO$_2$) Al-3Zr both exhibit a grain size over 140 nm.

158
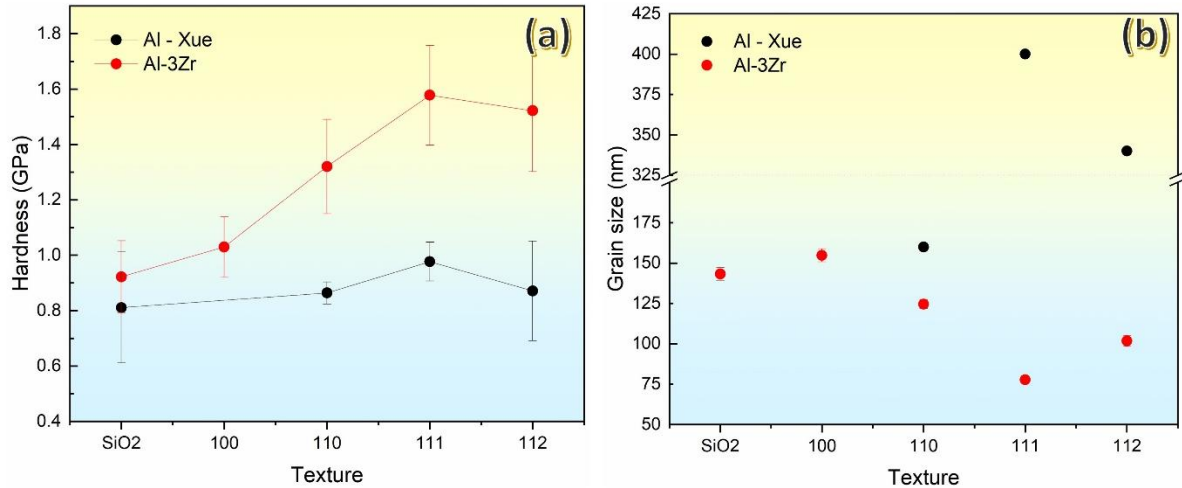
Figure 6-2. (a) Hardness and (b) grain size plotted against substrate texture.

The microstructure of each Al-3Zr coating was thoroughly assessed using TEM to compare grain structure and twin propensities as well as fully assess the film textures. Figure 6-3 contains plan-view (PV) TEM images collected from the (100) Al-3Zr and (SiO$_2$) Al-3Zr coatings revealing both to be composed of ultrafine grains (~145nm). The corresponding SAD patterns in Figure 6-3(a) and 6-3(c) reveal the grains are randomly oriented in both samples. This is further confirmed from the IPF maps presented in Figures 6-3(b) and 6-3(d) where no clear dominant texture is identified with a mixture of grain orientations. The (110) Al-3Zr, (111) Al-3Zr and (112) Al-3Zr films were similarly characterized and the resulting TEM data is shown in Figure 6-4. Each film exhibits single crystal like texture based on the corresponding SAD patterns inserted in Figures 6-4(a, c, e). The inserted SAD patterns correspond to (110), (111) and (112) FCC single crystals and the IPF maps in Figures 6-4(b, d, f) reinforces the extremely strong texture as each map is almost monochromatic. Individual domains (composed of the same out of plane texture) can be discerned in the BF-TEM images in Figures 6-4(a, c, e) and the (110) Al-3Zr, (111) Al-3Zr and (112) Al-3Zr films possess grain sizes of 124, 77 and 101 nm, respectively.

159
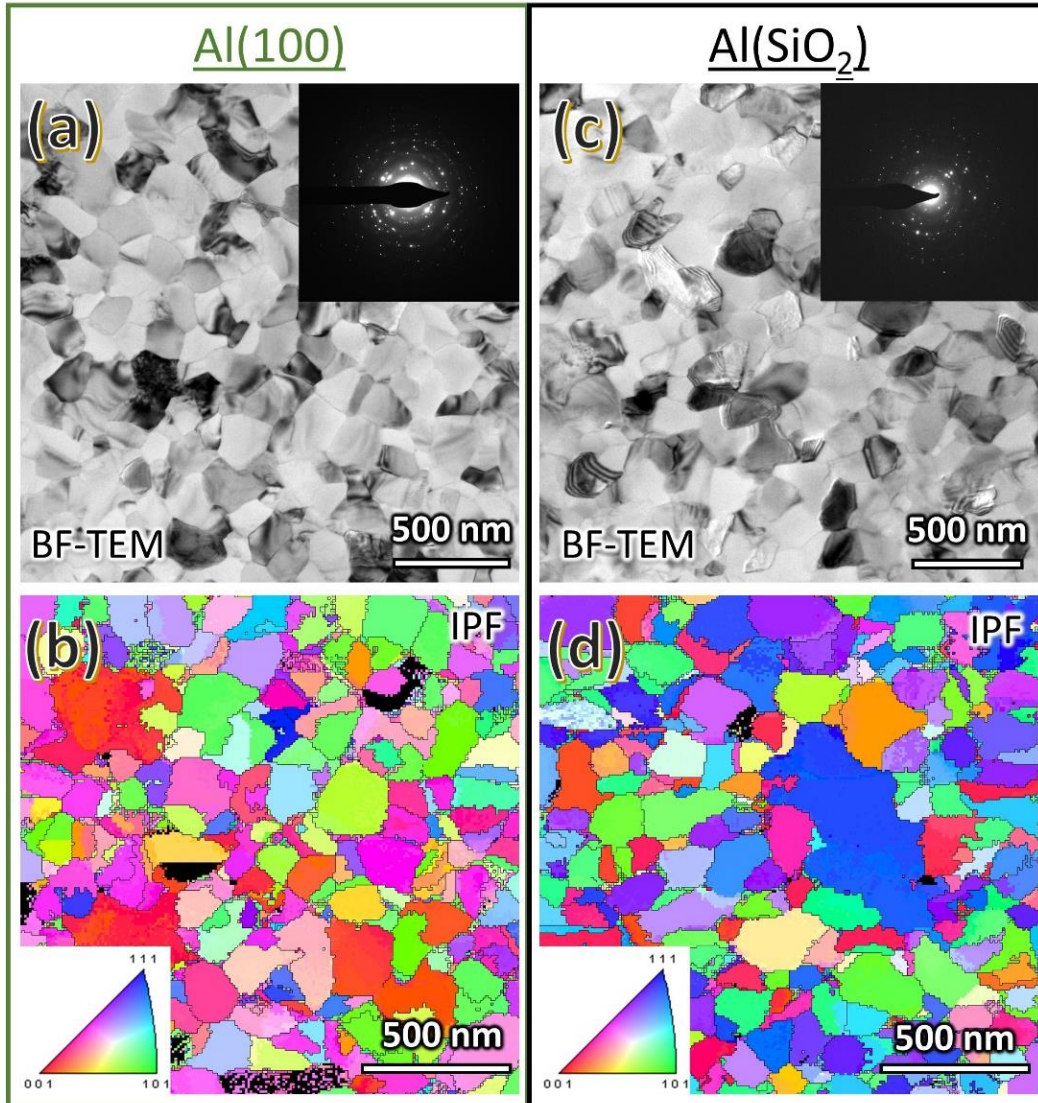
Figure 6-3. (a) BF-TEM micrograph revealing the polycrystalline microstructure in Al-3Zr deposited on Si(100) with corresponding SAD pattern. (b) IPF map further confirming the polycrystalline microstructure composed of ultrafine grains in Al-3Zr deposited on Si(100). (c) BF-TEM micrograph revealing the polycrystalline microstructure in Al-3Zr deposited on amorphous SiO_2 with corresponding SAD pattern. (d) IPF map further confirming the polycrystalline microstructure composed of ultrafine grains in Al-3Zr deposited on amorphous SiO_2.
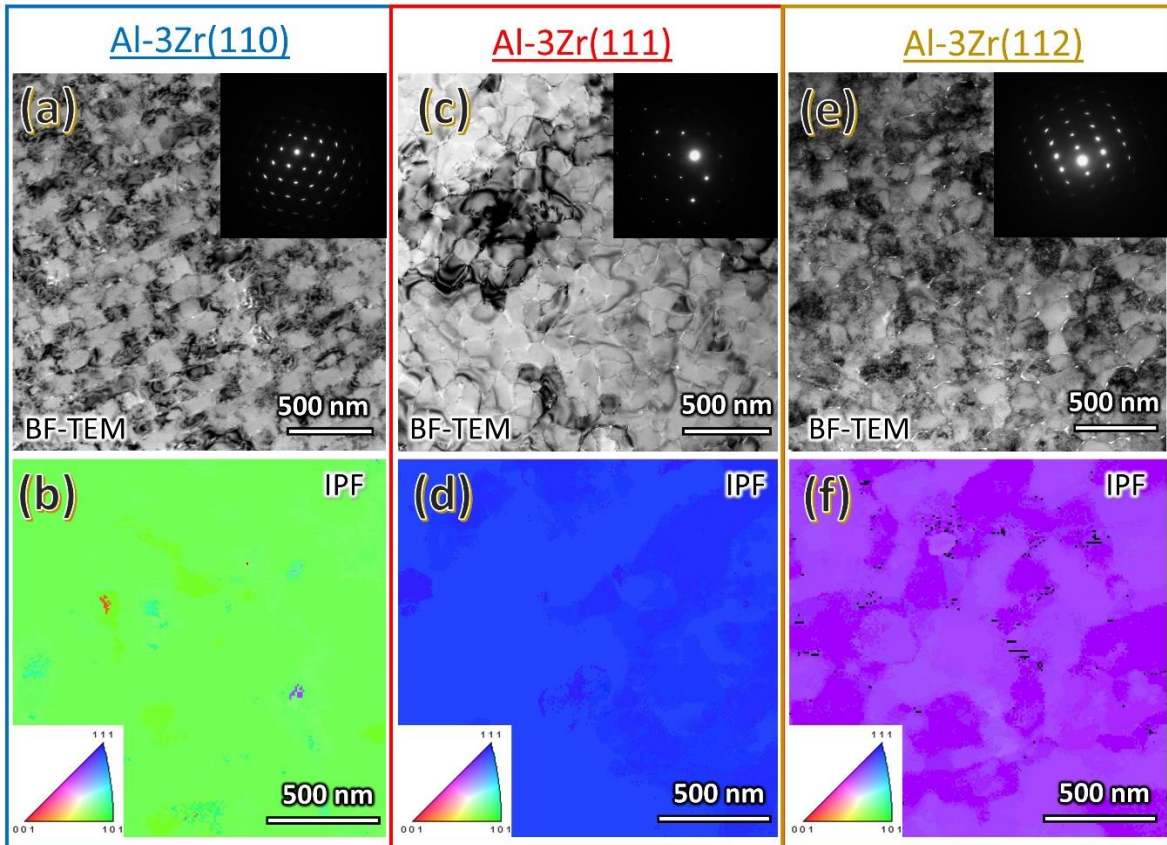
Figure 6-4. (a) BF-TEM micrograph with corresponding SAD pattern inset and (b) IPF map revealing highly textured (110) Al-3Zr deposited on Si(110). (c) BF-TEM micrograph with corresponding SAD pattern inset and (d) IPF map revealing highly textured (111) Al-3Zr deposited on Si(111). (e) BF-TEM micrograph with corresponding SAD pattern inset and (f) IPF map revealing highly textured (112) Al-3Zr deposited on Si(112).

Cross-section TEM (XTEM) samples were also prepared along the <110> zone axis in order to fully assess the twin structures within each film. Figure 6-5(a) contains a BF-TEM micrograph revealing randomly oriented columnar grains with high angle grain boundaries (HAGB) labeled. This result corresponds well with the PV TEM data presented in Figure 6-3 and due to structural similarities, the (100) Al-3Zr data in Figure 6-5 is representative for the (SiO_2) Al-3Zr sample. Multiple SAD patters are shown in Figure 6-5(a_1, a_2), and the corresponding regions of interest are labeled in Figure 6-5(a). These patterns confirm the zone axis to be [011] of the single crystal Si(100) substrate and reveal the columnar grains to be randomly oriented. This is further confirmed in both the DF-TEM micrograph and IPF + boundary map in Figures 6-5(b) and 6-5(c), respectively. Additionally, the IPF + boundary map demonstrates the nature of the columnar boundaries to be HAGB, all with a misorientation over 15°. Figure 6-5(d) contains a BF-TEM micrograph collected at a higher magnification revealing the termination of 2 CTBs within the first 50nm of the film growth process. Figure 6-5(e) provides a HRTEM image of one CTB terminated at a columnar HAGB. Additionally, Figure 6-5(f) reveals the other CTB shown in Figure 6-5(d) is terminated by an ITB within a grain interior. Fast Fourier transforms (FFTs) are provided in Figures 6-5(f_1, f_2) and confirm the twinned structure shown in Figure 6-5(f). These instances of twin formation in the (100) Al-3Zr coating were very sparse indicating a low propensity for twin formation.
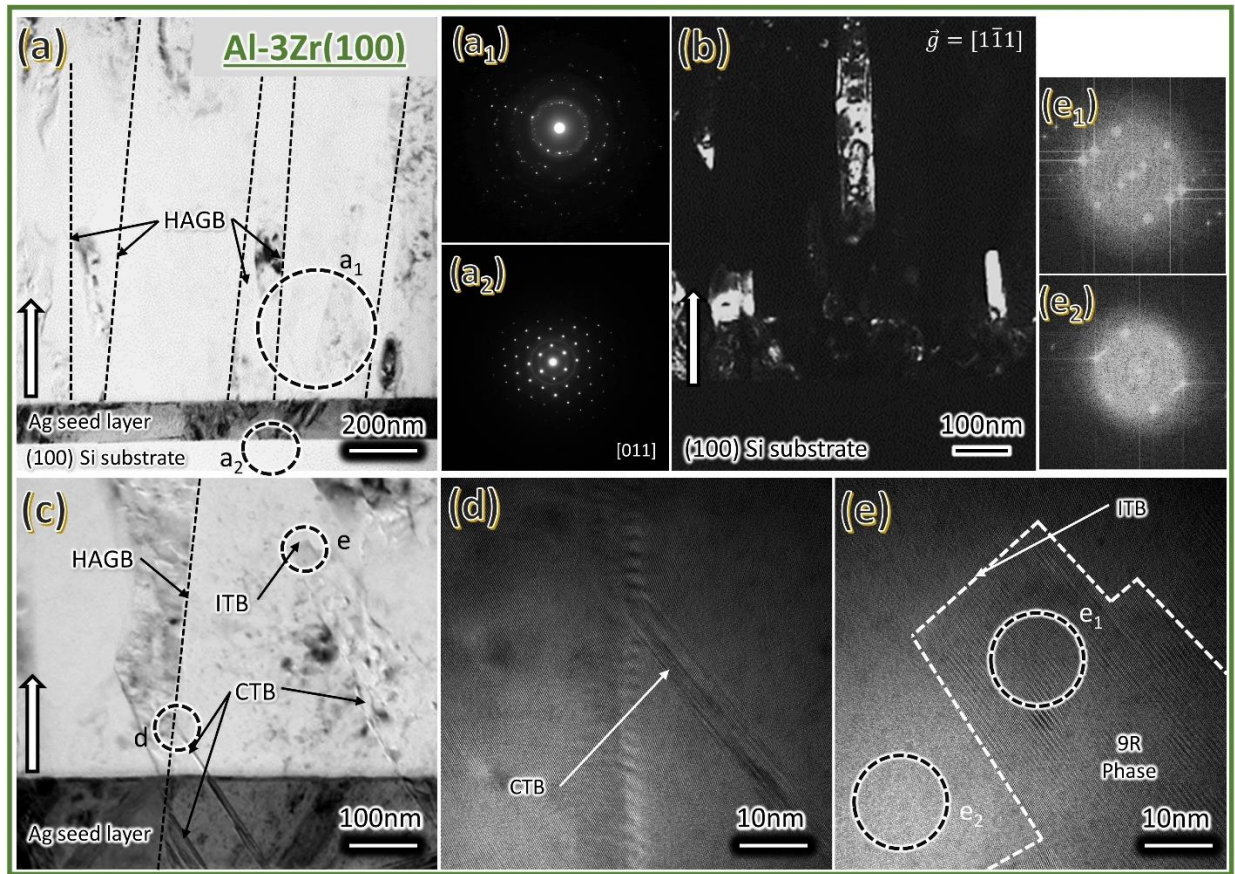
Figure 6-5. (a) BF-TEM micrograph identifying multiply columnar HAGB in Al-3Zr deposited on a Ag seed layer and Si(100) substrate. This image is taken along the [011] zone axis of the Si(100) substrate. (a_1) SAD pattern corresponding to the label in (a) revealing randomly oriented columnar grains in the Al-3Zr film. (a_2) SAD pattern taken from the labeled region in (a) confirming the [011] zone axis of the Si(100) substrate. (b) DF-TEM micrograph collected with $\vec{g} = [1\bar{1}1]$ identifying multiple ultrafine columnar grains. (c) IPF + boundary map collected using ASTAR revealing randomly oriented columnar grains. (d) BF-TEM micrograph identifying a CTB replicated from the Ag seed layer terminated at a HAGB. (e) HRTEM image from the labeled region in (d) identifying the termination of the CTB at a columnar boundary. (f) HRTEM image identifying the termination of a CTB at an ITB with corresponding FFTs from (f_1) and (f_2) regions

Figure 6-6(a) contains a BF-TEM image of the (110) Al-3Zr film with the corresponding SAD pattern provided in Figure 6-6(b) revealing single crystal-like texture. The images were collected along the [011] zone axis in order to assess the twin structure. Multiple threading dislocations and columnar domain boundaries were identified throughout the film, labeled in Figure 6-6(a). Figure 6-6(c) contains a DF-TEM image collected with a $\vec{g} = [200]$ identifying a columnar grain with a width of ~150nm, corresponding well with the measured grain size (124nm). The HRTEM images presented in Figures 6-6(d-g) fully characterize and represent the twin structures found throughout the (110) Al-3Zr coating. Inclined CTBs were identified and one is

presented in Figure 6-6(d) which is terminated at a grain boundary within the film. Additionally, as characterized in Figure 6-6(f), these twins are thick (~15-20nm) and the CTBs bound patches of 9R phase stabilized in the as-deposited microstructure. Figure 6-6(g) presents an example of a CTB replicated from the Ag seed layer into the high SFE Al layer, in addition to the replicated 9R phase.
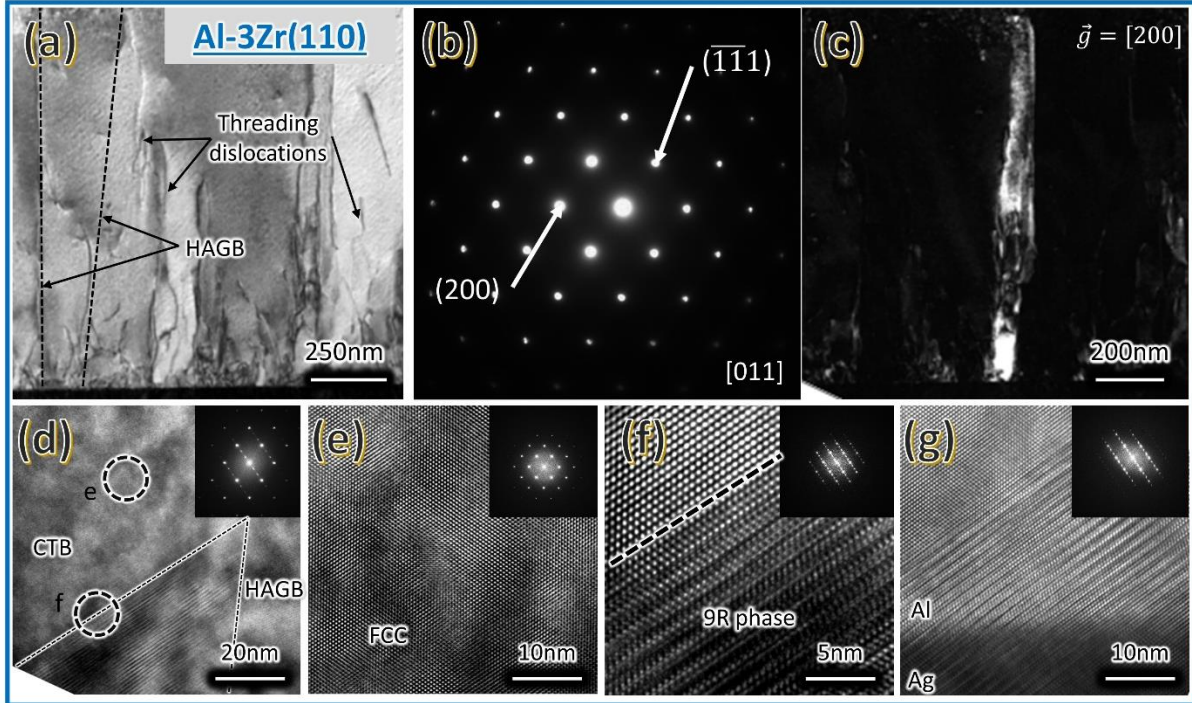
Figure 6-6. (a) Low magnification BF-TEM micrograph of the (110) Al-3Zr sample revealing multiple columnar boundaries and threading dislocations. (b) SAD diffraction pattern corresponding to the image in (a) revealing single crystal like texture collected along the [011] zone axis. (c) DF-TEM micrograph identifying a columnar grain collected with $\vec{g} = [200]$. (d) Medium magnification BF-TEM image identifying a thick twin boundary bounded by a CTB being terminated at a columnar HAGB. (e) HRTEM image confirming the FCC structure along the [011] zone axis corresponding to the labeled region in (d). (f) HRTEM image identifying a thick twin with a CTB bounding 9R phase corresponding to the labeled region in (d). (g) HRTEM of a CTB and 9R phase replicating from the Ag seed layer into the Al-3Zr film.

Figure 6-7(a) contains a BF-TEM micrograph of the (111) Al-3Zr taken along the [011] zone axis revealing an abundance of columnar boundaries ~70nm in size. The corresponding SAD pattern in Figure 6-7(b) reveals the twinned nature of the columnar grains and confirms the nanostructure to be composed of a high density of vertical ITBs. The DF-TEM micrograph in Figure 6-7(c) further confirms this twin relationship with matrix and twin variants labeled corresponding to the labels on the SAD pattern in Figure 6-7(b). Additionally, the IPF + boundary

map in Figure 6-7(d) shows the high density of ITBs along with the films strong texture. Figure 6-7(e) shows a HRTEM image of the interface between the (111) Al-3Zr film and the Ag seed layer revealing a high density of stacking faults in the Ag layer promoting the formation of an ITB and 9R phase in the Al-3Zr film. Additionally, an HRTEM image and FFT inset in Figure 6-7(f) further identify the 9R phase structure that fills a large volume fraction of the film microstructure. The twin spots and superlattice spots in both the SAD in Figure 6-7(b) and the FFT in Figure 6-7(f) provide further proof of ITB and 9R phase formation. Figure 6-8(a) contains a BF-TEM image collected along the [111] zone axis identifying multiple threading dislocations. No twins were identified due to the zone axis and further work is needed to assess the twin structure along the [011] zone axis.
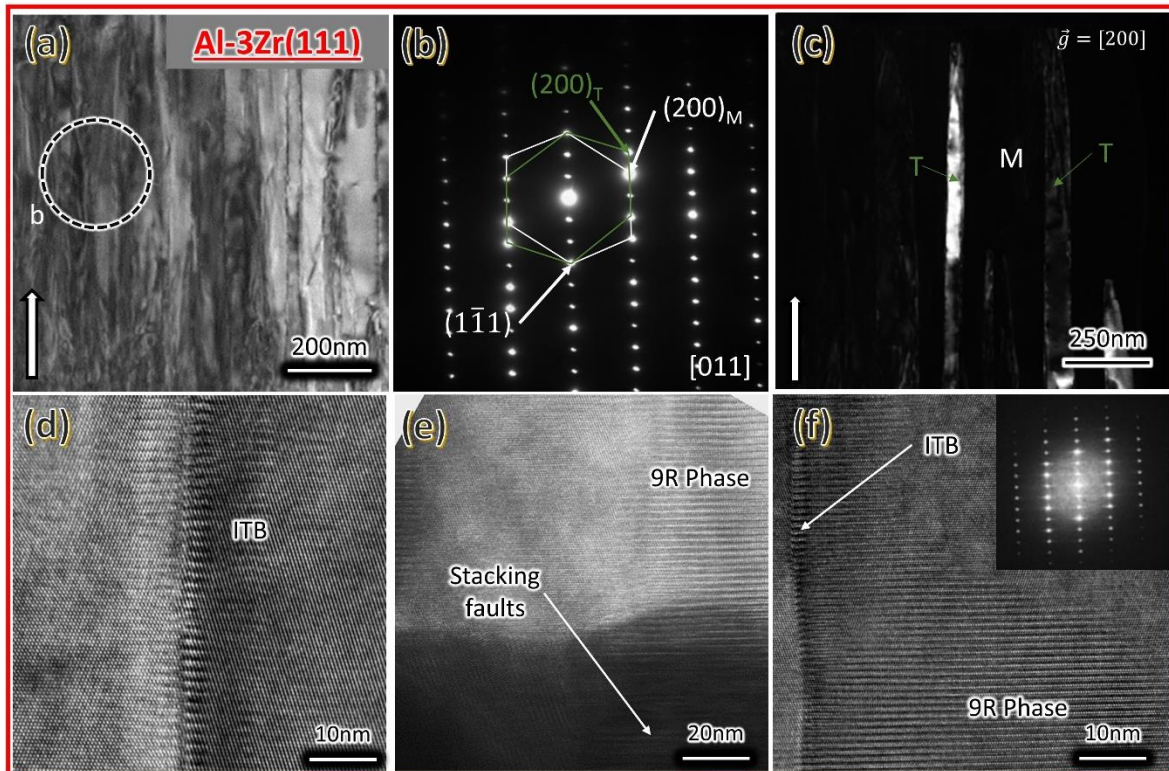
Figure 6-7. (a) BF-TEM micrograph identifying a high density of columnar ITBs in Al-3Zr deposited on Si(111). (b) SAD pattern corresponding to the region labeled in (a) identifying the columnar boundaries as twins with intermediate diffraction spots corresponding to 9R phase formation. (c) DF-TEM image taken with a $\vec{g} = [200]$ with matrix and twin variants labeled. (d) IPF map collected using ASTAR revealing single crystal like texture and columnar ITBs. (e) HRTEM image revealing the nucleation of an ITB and 9R phase in Al-3Zr from a high density of stacking faults in the low SFE Ag seed layer. (f) HRTEM image of a columnar ITB and broad 9R phase formed in Al-3Zr deposited on Si(111) with a corresponding FFT insert.
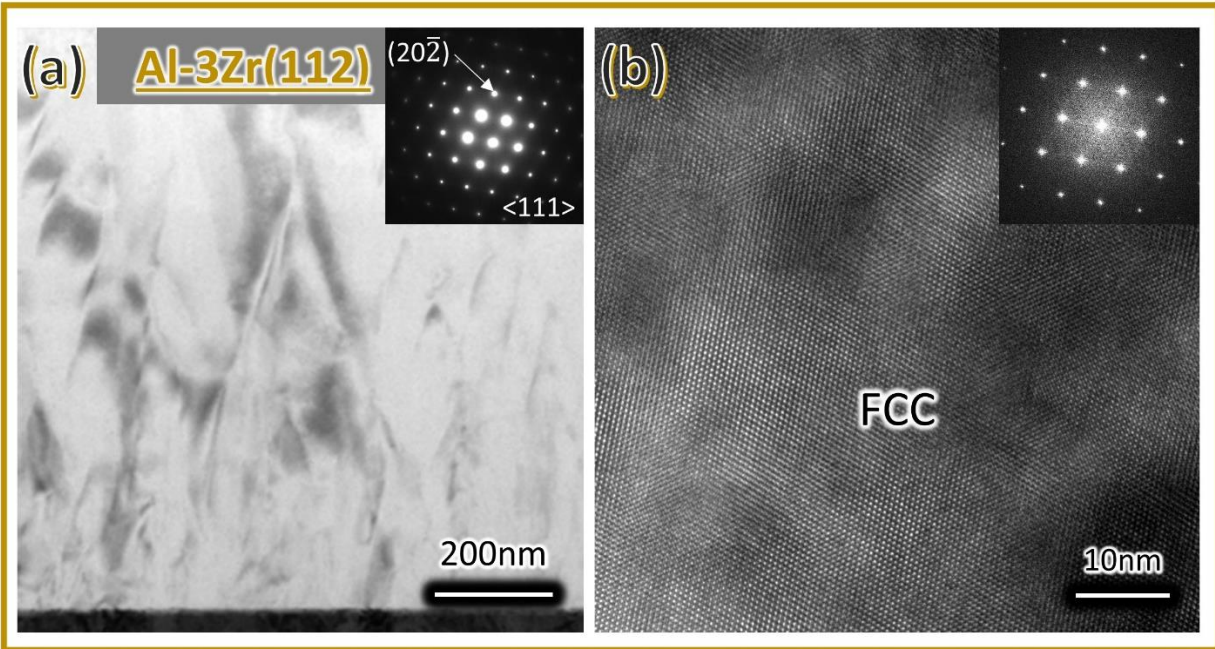
Figure 6-8. (a) BF-TEM image collected along the [111] zone axis for Al-3Zr on Si(112) with corresponding (b) HRTEM image identifying the clean FCC microstructure. Image collection along the [011] zone axis is needed to adequately image the twin structure.

6.5   Discussion

Stabilizing twins in Al typically requires extreme conditions, and multiple factors have been deemed important to promote twinning. One factor essential for growth twin formation in high SFE Al is an extremely fast quench rate. Rapid quenching, characteristic of magnetron sputtering (upwards of 10^{12} Ks^{-1}), pushes the system far from equilibrium and enables the stabilization of typically unstable structures [398]. This has been demonstrated extensively with the fabrication of nanotwinned metals [170,173,255,301,393], however the difference in twin propensity in this work is tied to the crystallography of the Al-3Zr films as each coating was deposited under the same conditions. As established by Xue et al. [189,190] in sputtered pure Al, film texture is important for twin propensity. Additionally, they reported that twin nucleation can originate from (1) the formation of a twinned nucleus or (2) from the impingement of two growing grains possessing a twinned relationship. Based on Figure 6-1(a) and the PV TEM data in Figures 6-3 and 6-4, certain substrates are able to promote highly textured, nearly single crystal Al-3Zr ((110), (111) and (112) Al-3Zr) whereas (100) and (SiO$_2$) Al-3Zr both formed randomly textured polycrystalline films. Due to a diminished texture, the (100) and (SiO$_2$) Al-3Zr films present

166

minimal twin stabilization (Figure 6-5), with the few nucleated twins becoming annihilated within the first 80 nm of the film growth process due to the large energy penalty (Figure 6-5(d-f)). By increasing the randomness of grain orientation during nucleation, the twin propensity is minimized twofold. First, a (111) oriented nucleus containing a twin is less likely to be formed. Subsequently, the few twin variants that do form are suppressed due to competitive growth processes and the energy penalty for twin formation in Al. As a result, these twins are terminated within the film at both high angle grain boundaries and by an ITB to minimize the excess energy resulting from the high SFE. Second, the probability of two variants possessing a twin relationship nucleating close enough to impinge upon each other during film growth is significantly reduced. The resulting (100) and (SiO$_2$) Al-3Zr films possess very few twins, and the Zr solute serves to reduce the randomly oriented grain sizes, however this solute does not provide enough of an energy barrier to prevent detwinning processes in randomly textured films.

The films exhibiting strong texture all contain a higher twin density than the randomly textured Al-3Zr coatings. Xue et al. [190] demonstrated this previously in pure Al, asserting that (112) oriented Al produced coatings with the highest twin density, and this study strove to incorporate the influence of solute on these twin formation mechanisms. As is apparent in Figure 6-2(b), the grain size is reduced dramatically with the introduction of just 3at% Zr, however the strong film texture is unaffected. In the highly textured (110) Al-3Zr, multiple inclined twins are identified throughout the film extending beyond a few hundred nm's. A majority of these twins terminate at columnar grain boundaries and often nucleate either within the Ag seed layer or at another columnar grain boundary. Due to the refined grain size and that a majority of these CTBs nucleate in the early stages of film growth, a majority of twins terminate at columnar boundaries before reaching the film surface. Additionally, the twin structure resembles the microstructure reported in (110) oriented Ag by Bufford et al [170]. One contrast between (110) Al and (110) Al-3Zr films reported in this study is the thickness of the resulting twins. As presented in Figures 6-6(f-g), the inclined CTBs bound regions of 9R phase, which was previously unidentified in (110) Al which typically contained sharp CTBs. This twin evolution is a result of solute additions and is similarly found in (111) Al-3Zr which contain an abundance of finely spaced columnar ITBs with large patches of 9R phase stabilized in the resulting film directly resulting from the introduction of solute. This has been discussed at length in multiple studies [159,195–198,271,308], however the role of Zr will be briefly discussed here. First, Zr acts as a grain refiner promoting a higher

nucleation rate during the initial stages of film growth. Because of the strong (111) texture, the probability of forming twin variants is greatly enhanced and the grain refinement further increases the density of these twinned variants. Additionally, as uncovered from density functional theory (DFT) calculations in [271,308], Zr further acts to increase the energy barrier for partial dislocation migration, preventing the correction of stacking faults in the as deposited coating, resulting in expansive patches of 9R phase, such as the case in Figure 6-7(f). As a result, the film is able to grow to 1µm thickness without significant detwinning. In comparison, the Zr solute is able to stabilize an increased twin density and promote a refined grain size in the (112) Al-3Zr coatings.

A thermodynamic model describing vapor nucleation has provided insight into the formation of growth twins and is given by:

$$r^*_{perfect} = \frac{\gamma}{\left(\frac{kT}{\Omega}\ln\left[\frac{J\sqrt{2\pi mkT}}{P_S}\right]\right)} \tag{6-1}$$

$$r^*_{twin} = \frac{\gamma}{\left(\frac{kT}{\Omega}\ln\left[\frac{J\sqrt{2\pi mkT}}{P_S}\right]-\frac{\gamma_t}{h}\right)} \tag{6-2},$$

where r^* represents the critical nucleus radius, γ is the surface energy, k is Boltzmann's constant, T is the temperature, Ω is the atomic volume, J is the deposition flux, m is the atomic mass of the sputtered material, and P_s is the vapor pressure above the solid. [262]. Based on Equation 6-1, Bufford et al. predicted twins would be rare in Al even at high deposition rates [170]. Similar to the (100) Al-3Zr and (SiO$_2$) Al-3Zr cases, Xue et al. established that the formation of inclined twins requires a smaller energy than horizontal twins as in Equation 6-2 and determined a maximum twin density at film thicknesses of ~80nm. This coincides well with the randomly textured coatings in this study as the few identified twins terminate around 80nm into the film. Further, Equation 6-2 also dictates that a reduced twin boundary energy (γ_t) will reduce r^*_{twin} and increase twin propensity. DFT simulations from [271,308] establish that increased Zr solute will slightly reduce the SFE of the Al alloys (125.7 down to 107.8 mJm^{-2}), providing a smaller energy barrier for twin formation. This works in conjunction with reduced grain sizes to further increase the twin density in Al-3Zr compared to a pure Al reference. Additionally, the reduced grain sizes helps promote thicker twins and broader patches of 9R phase in the resulting films.

The hardness of each coating is intimately linked with the film texture as each clearly demonstrates a difference in microstructure. Increased twin boundary density and reduced grain sizes both work to obstruct dislocation motion and improve film hardness. As a result, (111) Al-3Zr exhibits the highest hardness as it is composed of the finest grains and the highest twin density.

The columnar ITBs and abundant 9R phase obstruct dislocation glide and boost the hardness to ~1.5GPa. Similarly, (112) Al-3Zr reaches a hardness of ~1.45 GPa as the Zr solute restricts the grain size down to ~100nm. The high density and combination of CTBs and ITBs are the means for improving the film hardness. The (110) Al-3Zr films reach a hardness of ~1.2 GPa due to the introduction of inclined CTBs and stacking faults composing 9R phase as well as reduced grain size. However, the inclined twins do not obstruct dislocation slip as significantly as the vertical ITBs in (111) Al-3Zr, resulting in slightly lower hardness. In contrast, the (100) Al-3Zr and (SiO_2) Al-3Zr are composed of ultrafine grains and almost no twin boundaries, leading to only a marginal hardness increase compared with its pure Al counterparts. Overall, controlling the twin morphology through film texture provides a straightforward means to tailor mechanical properties, and also has implications in future additive manufacturing endeavors related to Al.

6.6   Conclusions and future work

This study identified the combined influence of film texture and solute additions on twin formation in Al sputtered alloys. The largest twin density was recognized in (111) Al-3Zr and (112) Al-3Zr with a notable difference in twin morphology dependent on crystallography. (110) Al-3Zr also contained twins albeit at a significantly lower density. These (111) and (112) textured coatings also possess the highest hardness (~1.5GPa), and the refined microstructure and increased twin densities play a major role. Intensive TEM experiments identified the changing film structure and provided insight into the change in mechanical properties and was combined with a thermodynamic and crystallographic assessment of twin formation in nanotwinned Al-3Zr alloys. This work clearly demonstrates the role Zr solute during film growth and how the resulting microstructures can tailor the mechanical response. Further work is needed to expand upon the thermodynamic and crystallographic rationale behind the twin formation mechanisms. Additional microscopy investigation is needed to fully assess the twin densities in the (112) oriented films and to better correlate the twin structure's relationship with the film's mechanical properties.

6.7   Acknowledgements

7. SUMMARY

This thesis probes the microstructural, mechanical and thermal properties of nanotwinned Al-Zr sputtered films using a suite of electron microscopy and micromechanical techniques. The fundamentals of twin formation, strengthening and stability were studied in depth. The major findings can be summarized as follows:

(1) Zr solute promotes significant grain refinement and boost in twin density by increasing the energy barrier for surface diffusion. This microstructural evolution promotes high hardness (4.2 GPa) and flow stress (1.1 GPa) while maintaining significant deformability. The abundance of incoherent twin boundaries and 9R phase stabilized by Zr helps maintain high levels of deformability while increasing strength.

(2) Nanotwinned Al-Zr alloys exhibit a significantly improved strain rate sensitivity over their Al and Al alloy counterparts due to boost in partial dislocation density (9R phase) and decrease in activation volume. A unique constant strain rate nanoindentation methodology was employed to probe this phenomenon

(3) Co and Zr solute help refine the microstructure down to below 10nm while promoting a high density of incoherent twin boundaries. *In-situ* micropillar compression testing uncovers the high flow stress (1.5 GPa) capable of these nanotwinned Al-Co-Zr alloys. These solutes exhibit a synergistic relationship pinning the microstructure and imparting thermal stability up to ~0.78 T_m.

(4) Al film texture was determined to play a significant role in twin density and formation. (100), (110) and SiO_2 substrates all promote a low twin density, larger grain size and low hardness (~.9 GPa). (111) and (112) textured Al films grown epitaxially on Si contain refined structures (below 100nm) and a large twin density

There remains a few questions that still can be addressed to fully assess the mechanical response and twin formation mechanisms of nanotwinned Al alloys:

(1) Mechanical response of Al-Co-Zr alloys at high temperatures

(2) *In-situ* TEM nanoindentation probing the mechanical response of ITBs with different solute

(3) Altering substrate conditions during magnetron sputtering, including substrate bias and temperature

(4) Tensile response of the unique nanotwinned microstructure presented in this thesis

(5) Fabrication of bulk Al alloys containing a significant fraction of twin boundaries

REFERENCES

[1]   J. Blinkhorn, M. Grove, The structure of the Middle Stone Age of eastern Africa, Quat. Sci. Rev. 195 (2018) 1–20. https://doi.org/10.1016/j.quascirev.2018.07.011.

[2]   E. Fidan, D. Sari, M. Türkteki, An Overview of the Western Anatolian Early Bronze Age, Eur. J. Archaeol. 18 (2015) 60–89. https://doi.org/10.1179/1461957114y.0000000070.

[3]   F. d'Errico, C.S. Henshilwood, Additional evidence for bone technology in the southern African Middle Stone Age, J. Hum. Evol. 52 (2007) 142–163. https://doi.org/10.1016/j.jhevol.2006.08.003.

[4]   S.C. Murray, Eastern Mediterranean Bronze Age Trade in Archaeological Perspective: A Review of Interpretative and Empirical Developments, Springer US, 2022. https://doi.org/10.1007/s10814-022-09177-5.

[5]   A.C.T.M. Van Zwieten, J.H. Bulloch, Some considerations on the toughness properties of ferritic stainless steels-A brief review, Int. J. Press. Vessel. Pip. 56 (1993) 1–31. https://doi.org/10.1016/0308-0161(93)90114-9.

[6]   Y. Tomita, Development of fracture toughness of ultrahigh strength, medium carbon, low alloy steels for aerospace applications, Int. Mater. Rev. 45 (2000) 27–37. https://doi.org/10.1179/095066000771048791.

[7]   W.F. Smith, Structure and properties of engineering alloys, 2nd ed., McGraw-Hill, United States of America, 1993.

[8]   A.R. Hind, S.K. Bhargava, S.C. Grocott, The surface chemistry of Bayer process solids: A review, Colloids Surfaces A Physicochem. Eng. Asp. 146 (1999) 359–374. https://doi.org/10.1016/S0927-7757(98)00798-5.

[9]   W.E. Haupin, Electrochemistry of the hall-heroult process for aluminum smelting, J. Chem. Educ. 60 (1983) 279–282. https://doi.org/10.1021/ed060p279.

[10]   B. Zhou, B. Liu, S. Zhang, The advancement of 7xxx series aluminum alloys for aircraft structures: A review, Metals (Basel). 11 (2021). https://doi.org/10.3390/met11050718.

[11]   C. Berlanga-Labari, M. V. Biezma-Moraleda, P.J. Rivero, Corrosion of cast aluminum alloys: A review, Metals (Basel). 10 (2020) 1–30. https://doi.org/10.3390/met10101384.

[12] H. Chen, C. Zhang, D. Jia, D. Wellmann, W. Liu, Corrosion behaviors of selective laser melted aluminum alloys: A review, Metals (Basel). 10 (2020). https://doi.org/10.3390/met10010102.

[13] P. Moghimian, T. Poirié, M. Habibnejad-Korayem, J.A. Zavala, J. Kroeger, F. Marion, F. Larouche, Metal powders in additive manufacturing: A review on reusability and recyclability of common titanium, nickel and aluminum alloys, Addit. Manuf. 43 (2021). https://doi.org/10.1016/j.addma.2021.102017.

[14] M.L. Montero Sistiaga, R. Mertens, B. Vrancken, X. Wang, B. Van Hooreweder, J.P. Kruth, J. Van Humbeeck, Changing the alloy composition of Al7075 for better processability by selective laser melting, J. Mater. Process. Technol. 238 (2016) 437–445. https://doi.org/10.1016/j.jmatprotec.2016.08.003.

[15] A. Morozova, A. Mogucheva, D. Bukin, O. Lukianova, N. Korotkova, N. Belov, R. Kaibyshev, Effect of Si and Zr on the microstructure and properties of Al-Fe-Si-Zr alloys, Metals (Basel). 7 (2017) 1–12. https://doi.org/10.3390/met7110495.

[16] H. Okamoto, Al-Zn (Aluminum-Zinc), J. Phase Equilibria. 16 (1995) 125–126.

[17] Y. Zhong, M. Yang, Z.K. Liu, Contribution of first-principles energetics to Al-Mg thermodynamic modeling, Calphad Comput. Coupling Phase Diagrams Thermochem. 29 (2005) 303–311. https://doi.org/10.1016/j.calphad.2005.08.004.

[18] J.G. Kim, S.M. Baek, H.H. Lee, K.G. Chin, S. Lee, H.S. Kim, Suppressed deformation instability in the twinning-induced plasticity steel-cored three-layer steel sheet, Acta Mater. 147 (2018) 304–312. https://doi.org/10.1016/j.actamat.2018.01.042.

[19] A.D. Rollett, U.F. Kocks, A Review of the Stages of Work Hardening, Solid State Phenom. 35–36 (1993) 1–18. https://doi.org/10.4028/www.scientific.net/ssp.35-36.1.

[20] J.S. Koehler, The nature of work-hardening, Phys. Rev. 86 (1952) 52–59. https://doi.org/10.1103/PhysRev.86.52.

[21] T.H. Courtney, Mechanical Behavior of Materials, 2nd ed., Waveland Press, Inc., 2009.

[22] U.F. Kocks, H. Mecking, Physics and phenomenology of strain hardening: The FCC case, Prog. Mater. Sci. 48 (2003) 171–273. https://doi.org/10.1016/S0079-6425(02)00003-8.

[23] H. Mughrabi, Elektronenmikroskopische Untersuchung der Versetzungsanordnung verformter Kupfereinkristalle im belasteten Zustand: II. Die Versetzungsanordnung im Bereich II, Philos. Mag. 23 (1971) 897–929. https://doi.org/10.1080/14786437108216995.

[24] E. Göttler, Versetzungsstruktur und Verfestigung von [100]-Kupfereinkristallen I. Versetzungsanordnung und Zellstruktur zugverformter Kristalle, Philos. Mag. 28 (1973) 1057–1076. https://doi.org/10.1080/14786437308220968.

[25] V. V. Bulatov, L.L. Hsiung, M. Tang, A. Arsenlis, M.C. Bartelt, W. Cai, J.N. Florando, M. Hiratani, M. Rhee, G. Hommes, T.G. Pierce, T.D. De La Rubia, Dislocation multi-junctions and strain hardening, Nature. 440 (2006) 1174–1178. https://doi.org/10.1038/nature04658.

[26] X. Liu, S. Jiang, J. Lu, J. Wei, D. Wei, F. He, The dual effect of grain size on the strain hardening behaviors of Ni-Co-Cr-Fe high entropy alloys, J. Mater. Sci. Technol. 131 (2022) 177–184. https://doi.org/10.1016/j.jmst.2022.06.001.

[27] T.L. Johnston, C.E. Feltner, Grain size effects in the strain hardening of polycrystals, Metall. Mater. Trans. 1 (1970) 1161–1167. https://doi.org/10.1007/BF02900226.

[28] T. Richeton, J. Weiss, F. Louchet, Dislocation avalanches: Role of temperature, grain size and strain hardening, Acta Mater. 53 (2005) 4463–4471. https://doi.org/10.1016/j.actamat.2005.06.007.

[29] I. Safi, Recent aspects concerning DC reactive magnetron sputtering of thin films: a review, Surf. Coatings Technol. 127 (2000) 203–218. https://doi.org/10.1016/S0257-8972(00)00566-1.

[30] U.F. Kocks, M.G. Stout, A.D. Rollett, The Influence of Texture on Strain Hardening, Pergamon Press plc, 1989. https://doi.org/10.1016/b978-0-08-034804-9.50008-5.

[31] D. Kumar, G. Shankar, K.G. Prashanth, S. Suwas, Texture dependent strain hardening in additively manufactured stainless steel 316L, Mater. Sci. Eng. A. 820 (2021) 141483. https://doi.org/10.1016/j.msea.2021.141483.

[32] A.B. Lopes, F. Barlat, J.J. Gracio, J.F. Ferreira Duarte, E.F. Rauch, Effect of texture and microstructure on strain hardening anisotropy for aluminum deformed in uniaxial tension and simple shear, Int. J. Plast. 19 (2003) 1–22. https://doi.org/10.1016/S0749-6419(01)00016-X.

[33] F. Barlat, J.M. Ferreira Duarte, J.J. Gracio, A.B. Lopes, E.F. Rauch, Plastic flow for non-monotonic loading conditions of an aluminum alloy sheet sample, Int. J. Plast. 19 (2003) 1215–1244. https://doi.org/10.1016/S0749-6419(02)00020-7.

[34] T.S. Byun, N. Hashimoto, K. Farrell, Temperature dependence of strain hardening and plastic instability behaviors in austenitic stainless steels, Acta Mater. 52 (2004) 3889–3899. https://doi.org/10.1016/j.actamat.2004.05.003.

[35] H. Mecking, U.F. Kocks, Kinetics of flow and strain-hardening, Acta Metall. 29 (1981) 1865–1875. https://doi.org/10.1016/0001-6160(81)90112-7.

[36] P.S. Bhat, V. Chang, M. Li, Effect of elevated temperature on strain-hardening engineered cementitious composites, Constr. Build. Mater. 69 (2014) 370–380. https://doi.org/10.1016/j.conbuildmat.2014.07.052.

[37] C.B. Finfrock, M.M. Thrun, D. Bhattacharya, T.J. Ballard, A.J. Clarke, K.D. Clarke, Strain Rate Dependent Ductility and Strain Hardening in Q&P Steels, Metall. Mater. Trans. A Phys. Metall. Mater. Sci. 52 (2021) 928–942. https://doi.org/10.1007/s11661-020-06127-y.

[38] S.S. Ezz, Y.Q. Sun, P.B. Hirsch, Strain rate dependence of the flow stress and work hardening of γ', Mater. Sci. Eng. A. 192–193 (1995) 45–52. https://doi.org/10.1016/0921-5093(94)03202-5.

[39] E.O. Hall, The deformation and ageing of mild steel: III Discussion and Results, Proc. Phys. Soc. Sect. B. 64 (1951) 747–753. https://doi.org/10.1088/0370-1301/64/9/303.

[40] N.J. Petch, The cleavage strength of polycrystals, J. Iron Steel Inst. 174 (1953) 25–28.

[41] Z.C. Cordero, B.E. Knight, C.A. Schuh, Six decades of the Hall–Petch effect – a survey of grain-size strengthening studies on pure metals, Int. Mater. Rev. 61 (2016) 495–512. https://doi.org/10.1080/09506608.2016.1191808.

[42] Y.Z. Tian, Y.P. Ren, S. Gao, R.X. Zheng, J.H. Wang, H.C. Pan, Z.F. Zhang, N. Tsuji, G.W. Qin, Two-stage Hall-Petch relationship in Cu with recrystallized structure, J. Mater. Sci. Technol. 48 (2020) 31–35. https://doi.org/10.1016/j.jmst.2019.12.023.

[43] A.H. Chokshi, A. Rosen, J. Karch, H. Gleiter, On the Validity of the Hall-Petch relationship in nanocrystalline materials, Scr. Metall. 23 (1989) 1679–1684.

[44] G.E. Fougere, J.R. Weertman, R.W. Siegel, S. Kim, Grain-size dependent hardening and softening of nanocrystalline Cu and Pd, Scr. Metall. Mater. 26 (1992) 1879–1883. https://doi.org/10.1016/0956-716X(92)90052-G.

[45] J.R. Trelewicz, C.A. Schuh, The Hall-Petch breakdown in nanocrystalline metals: A crossover to glass-like deformation, Acta Mater. 55 (2007) 5948–5958. https://doi.org/10.1016/j.actamat.2007.07.020.

[46] F.A. Mohamed, Interpretation of nanoscale softening in terms of dislocation-accommodated boundary sliding, Metall. Mater. Trans. A Phys. Metall. Mater. Sci. 38 (2007) 340–347. https://doi.org/10.1007/s11661-006-9057-6.

[47] J. Shiotze, F.D. Di Tolla, K.W. Jacobsen, Softening of nanocrystalline metals at very small grain sizes, Lett. to Nat. 391 (1998) 561–563.

[48] X.L. Wu, Y.T. Zhu, Inverse grain-size effect on twinning in nanocrystalline Ni, Phys. Rev. Lett. 101 (2008) 1–4. https://doi.org/10.1103/PhysRevLett.101.025503.

[49] C.E. Carlton, P.J. Ferreira, What is behind the inverse Hall-Petch behavior in nanocrystalline materials?, Acta Mater. 976 (2007) 19–24. https://doi.org/10.1016/j.actamat.2007.02.021.

[50] S.S. Quek, Z.H. Chooi, Z. Wu, Y.W. Zhang, D.J. Srolovitz, The inverse hall-petch relation in nanocrystalline metals: A discrete dislocation dynamics analysis, J. Mech. Phys. Solids. 88 (2016) 252–266. https://doi.org/10.1016/j.jmps.2015.12.012.

[51] X. Ke, J. Ye, Z. Pan, J. Geng, M.F. Besser, D. Qu, A. Caro, J. Marian, R.T. Ott, Y.M. Wang, F. Sansoz, Ideal maximum strengths and defect-induced softening in nanocrystalline-nanotwinned metals, Nat. Mater. 18 (2019) 1207–1214. https://doi.org/10.1038/s41563-019-0484-3.

[52] F.H. Duan, Y. Naunheim, C.A. Schuh, Y. Li, Breakdown of the Hall-Petch relationship in extremely fine nanograined body-centered cubic Mo alloys, Acta Mater. 213 (2021) 116950. https://doi.org/10.1016/j.actamat.2021.116950.

[53] V. Randle, Grain boundary engineering : an overview after 25 years Grain boundary engineering : an overview after 25 years, Mater. Sci. Technol. 26 (2010) 253–261. https://doi.org/10.1179/026708309X12601952777747.

[54] T. Watanabe, Grain boundary engineering : historical perspective and future prospects, J. Mater. Sci. 46 (2010) 4095–4115. https://doi.org/10.1007/s10853-011-5393-z.

[55] D.L. Olmsted, S.M. Foiles, E.A. Holm, Survey of computed grain boundary properties in face-centered cubic metals : I . Grain boundary energy, Acta Mater. 57 (2009) 3694–3703. https://doi.org/10.1016/j.actamat.2009.04.007.

[56] L. Tan, Microstructure tailoring for property improvements by grain boundary engineering, J. Nucl. Mater. 374 (2008) 270–280. https://doi.org/10.1016/j.jnucmat.2007.08.015.

[57] P.R. Cantwell, M. Tang, S.J. Dillon, J. Luo, G.S. Rohrer, M.P. Harmer, Grain boundary complexions, Acta Mater. 62 (2014) 1–48. https://doi.org/10.1016/j.actamat.2013.07.037.

[58] J. Ding, D. Neffati, Q. Li, R. Su, J. Li, S. Xue, Z. Shang, Y. Zhang, H. Wang, Y. Kulkarni, X. Zhang, Y. Kulkarnib, X. Zhang, Thick grain boundary induced strengthening in nanocrystalline Ni alloy, Nanoscale. 11 (2019) 23449–23458. https://doi.org/10.1039/c9nr06843k.

[59] J. Ding, Z. Shang, Y.F. Zhang, R. Su, J. Li, H. Wang, X. Zhang, Tailoring the thermal stability of nanocrystalline Ni alloy by thick grain boundaries, Scr. Mater. 182 (2020) 21–26. https://doi.org/10.1016/j.scriptamat.2020.02.032.

[60] R. Su, D. Neffati, J. Cho, Z. Shang, Y. Zhang, J. Ding, Q. Li, S. Xue, H. Wang, Y. Kulkarni, X. Zhang, High-strength nanocrystalline intermetallics with room temperature deformability enabled by nanometer thick grain boundaries, Sci. Adv. 7 (2021) eabc8288. https://doi.org/10.1126/SCIADV.ABC8288.

[61] L.A. Gypen, A. Deruyttere, The combination of atomic size and elastic modulus misfit interactions in solid solution hardening, Scr. Metall. 15 (1981) 815–820.

[62] S. Qiu, X.-C.C. Zhang, J. Zhou, S. Cao, H. Yu, Q.-M.M. Hu, Z. Sun, Influence of lattice distortion on stacking fault energies of CoCrFeNi and Al-CoCrFeNi high entropy alloys, J. Alloys Compd. 846 (2020) 156321. https://doi.org/10.1016/j.jallcom.2020.156321.

[63] F. Wang, G.H. Balbus, S. Xu, Y. Su, J. Shin, P.F. Rottmann, K.E. Knipling, J.C. Stinville, L.H. Mills, O.N. Senkov, I.J. Beyerlein, T.M. Pollock, D.S. Gianola, Multiplicity of dislocation pathways in a refractory multiprincipal element alloy, Science. 370 (2020) 95–101. https://doi.org/10.1126/science.aba3722.

[64] L. Li, Q. Fang, J. Li, B. Liu, Y. Liu, P.K. Liaw, Lattice-distortion dependent yield strength in high entropy alloys, Mater. Sci. Eng. A. 784 (2020) 139323. https://doi.org/10.1016/j.msea.2020.139323.

[65] D. Gaertner, K. Abrahams, J. Kottke, V.A. Esin, I. Steinbach, G. Wilde, S. V. Divinski, Concentration-dependent atomic mobilities in FCC CoCrFeMnNi high-entropy alloys, Acta Mater. 166 (2019) 357–370. https://doi.org/10.1016/j.actamat.2018.12.033.

[66] Z. Wang, Q. Fang, J. Li, B. Liu, Y. Liu, Effect of lattice distortion on solid solution strengthening of BCC high-entropy alloys, J. Mater. Sci. Technol. 34 (2018) 349–354. https://doi.org/10.1016/j.jmst.2017.07.013.

[67] C. Varvenne, A. Luque, W.A. Curtin, Theory of strengthening in fcc high entropy alloys, Acta Mater. 118 (2016) 164–176. https://doi.org/10.1016/j.actamat.2016.07.040.

[68] Y. Zhang, Y.J. Zhou, J.P. Lin, G.L. Chen, P.K. Liaw, Solid-solution phase formation rules for multi-component alloys, Adv. Eng. Mater. 10 (2008) 534–538. https://doi.org/10.1002/adem.200700240.

[69] A. Roy, P. Sreeramagiri, T. Babuska, B. Krick, P.K. Ray, G. Balasubramanian, Lattice distortion as an estimator of solid solution strengthening in high-entropy alloys, Mater. Charact. 172 (2021) 110877. https://doi.org/10.1016/j.matchar.2021.110877.

[70] F. Abdeljawad, P. Lu, N. Argibay, B.G. Clark, B.L. Boyce, S.M. Foiles, Grain boundary segregation in immiscible nanocrystalline alloys, Acta Mater. 126 (2017) 528–539. https://doi.org/10.1016/j.actamat.2016.12.036.

[71] H. Abdolvand, K. Louca, C. Mareau, M. Majkut, J. Wright, On the nucleation of deformation twins at the early stages of plasticity, Acta Mater. 196 (2020) 733–746. https://doi.org/10.1016/j.actamat.2020.07.010.

[72] H. Aboulfadl, J. Deges, P. Choi, D. Raabe, Dynamic strain aging studied at the atomic scale, Acta Mater. 86 (2015) 34–42. https://doi.org/10.1016/j.actamat.2014.12.028.

[73] T.J. Rupert, J.C. Trenkle, C.A. Schuh, Enhanced solid solution effects on the strength of nanocrystalline alloys, Acta Mater. 59 (2011) 1619–1631. https://doi.org/10.1016/j.actamat.2010.11.026.

[74] R. Labusch, A Statistical Theory of Solid Solution Hardening, Phys. Status Solidi. 41 (1970) 659–669.

[75] T. Uesugi, K. Higashi, First-principles studies on lattice constants and local lattice distortions in solid solution aluminum alloys, Comput. Mater. Sci. 67 (2013) 1–10. https://doi.org/10.1016/j.commatsci.2012.08.037.

[76] L. Liu, R. Wang, X. Wu, L. Gan, Q. Wei, Temperature effects on the generalized planar fault energies and twinnabilities of Al , Ni and Cu : First principles calculations q, Comput. Mater. Sci. 88 (2014) 124–130. https://doi.org/10.1016/j.commatsci.2014.03.005.

[77] M. Muzyk, Z. Pakiela, K.J. Kurzydlowski, Ab initio calculations of the generalized stacking fault energy in aluminium alloys, Scr. Mater. 64 (2011) 916–918. https://doi.org/10.1016/j.scriptamat.2011.01.034.

[78] D. Zhao, O.M. Løvvik, K. Marthinsen, Y. Li, Impurity effect of Mg on the generalized planar fault energy of Al, J. Mater. Sci. 51 (2016) 6552–6568. https://doi.org/10.1007/s10853-016-9834-6.

[79] C. Booth-Morrison, D.C. Dunand, D.N. Seidman, Coarsening resistance at 400 °c of precipitation-strengthened Al-Zr-Sc-Er alloys, Acta Mater. 59 (2011) 7029–7042. https://doi.org/10.1016/j.actamat.2011.07.057.

[80] S.J. Andersen, C.D. Marioara, J. Friis, S. Wenner, R. Holmestad, Precipitates in aluminium alloys, Adv. Phys. X. 3 (2018) 790–814. https://doi.org/10.1080/23746149.2018.1479984.

[81] W.D. Callister, D.G. Rethwisch, Materials Science and Engineering: An introduction, 8th ed., Wiley, 2000. https://doi.org/10.1016/0261-3069(91)90101-9.

[82] C.S. Kaira, T.J. Stannard, V. De Andrade, F. De Carlo, N. Chawla, Exploring novel deformation mechanisms in aluminum–copper alloys using in situ 4D nanomechanical testing, Acta Mater. 176 (2019) 242–249. https://doi.org/10.1016/j.actamat.2019.07.016.

[83] J.F. Nie, Precipitation and hardening in magnesium alloys, Metall. Mater. Trans. A Phys. Metall. Mater. Sci. 43 (2012) 3891–3939. https://doi.org/10.1007/s11661-012-1217-2.

[84] C. Sigli, F. De Geuser, A. Deschamps, J. Lépinoux, M. Perez, Recent advances in the metallurgy of aluminum alloys. Part II: Age hardening, Comptes Rendus Phys. 19 (2018) 688–709. https://doi.org/10.1016/j.crhy.2018.10.012.

[85] W.A. Soffa, D.E. Laughlin, High-strength age hardening copper-titanium alloys: Redivivus, Prog. Mater. Sci. 49 (2004) 347–366. https://doi.org/10.1016/S0079-6425(03)00029-X.

[86] G.E. Dieter, Mechanical Metallurgy, 2nd ed., McGraw-Hill, New York, 1961.

[87] R.J. Clifton, High strain rate behawior of metals, Appl. Mech. Rev. 43 (1990) S9–S22. https://doi.org/10.1115/1.3120862.

[88] R. Schwaiger, B. Moser, M. Dao, N. Chollacoop, S. Suresh, Some critical experiments on the strain-rate sensitivity of nanocrystalline nickel, Acta Mater. 51 (2003) 5159–5172. https://doi.org/10.1016/S1359-6454(03)00365-3.

[89] W.D. Nix, Mechanical properties of thin films, Metall. Trans. A. 20 (1989) 2217–2245. https://doi.org/10.1146/annurev.ms.20.080190.002135.

[90] W.C. Oliver, G.M. Pharr, An improved technique for determining hardness and elastic modulus using load and displacement sensing indentation experiments, J. Mater. Res. 7 (1992) 1564–1583.

[91] A.C. Fischer-Cripps, A simple phenomenological approach to nanoindentation creep, Mater. Sci. Eng. A. 385 (2004) 74–82. https://doi.org/10.1016/j.msea.2004.04.070.

[92] C.L. Wang, Y.H. Lai, J.C. Huang, T.G. Nieh, Creep of nanocrystalline nickel: A direct comparison between uniaxial and nanoindentation creep, Scr. Mater. 62 (2010) 175–178. https://doi.org/10.1016/j.scriptamat.2009.10.021.

[93] B.N. Lucas, W.C. Oliver, Indentation power-law creep of high-purity indium, Metall. Mater. Trans. A Phys. Metall. Mater. Sci. 30 (1999) 601–610. https://doi.org/10.1007/s11661-999-0051-7.

[94] S.K. Ganapathi, M. Aindow, H.L. Fraser, D.A. Rigney, A comparative study of the nanocrystalline material produced by sliding wear and inert gas condensation, Mater. Res. Soc. Symp. Proc. 206 (1991) 593–598.

[95] Y. Liu, J. Hay, H. Wang, X. Zhang, A new method for reliable determination of strain-rate sensitivity of low-dimensional metallic materials by using nanoindentation, Scr. Mater. 77 (2014) 5–8. https://doi.org/10.1016/j.scriptamat.2013.12.022.

[96] V. Maier-Kiener, K. Durst, Advanced Nanoindentation Testing for Studying Strain-Rate Sensitivity and Activation Volume, Jom. 69 (2017) 2246–2255. https://doi.org/10.1007/s11837-017-2536-y.

[97] J. Cho, J. Li, H. Wang, Q. Li, Z. Fan, A.K. Mukherjee, W. Rheinheimer, H. Wang, X. Zhang, Study of deformation mechanisms in flash-sintered yttria-stabilized zirconia by in-situ micromechanical testing at elevated temperatures, Mater. Res. Lett. 7 (2019) 194–202. https://doi.org/10.1080/21663831.2019.1575924.

[98] S.L. Yan, H. Yang, H.W. Li, X. Yao, Variation of strain rate sensitivity of an aluminum alloy in a wide strain rate range: Mechanism analysis and modeling, J. Alloys Compd. 688 (2016) 776–786. https://doi.org/10.1016/j.jallcom.2016.07.077.

[99] J. Ding, S. Xue, Z. Shang, J. Li, Y. Zhang, R. Su, T. Niu, H. Wang, X. Zhang, Characterization of precipitation in gradient Inconel 718 superalloy, Mater. Sci. Eng. A. 804 (2021) 140718. https://doi.org/10.1016/j.msea.2020.140718.

[100] H. Kim, H. Ha, J. Lee, S. Son, H.S. Kim, H. Sung, J.B. Seol, J.G. Kim, Outstanding mechanical properties of ultrafine-grained Al7075 alloys by high-pressure torsion, Mater. Sci. Eng. A. 810 (2021). https://doi.org/10.1016/j.msea.2021.141020.

[101] P. Wang, Y. Xiang, X. Wang, Z. Liu, S. Qu, Z. Zhuang, New insight for mechanical properties of metals processed by severe plastic deformation, Int. J. Plast. 123 (2019) 22–37. https://doi.org/10.1016/J.IJPLAS.2019.05.005.

[102] Q. Wei, S. Cheng, K.T. Ramesh, E. Ma, Effect of nanocrystalline and ultrafine grain sizes on the strain rate sensitivity and activation volume: Fcc versus bcc metals, Mater. Sci. Eng. A. 381 (2004) 71–79. https://doi.org/10.1016/j.msea.2004.03.064.

[103] Q. Wei, Strain rate effects in the ultrafine grain and nanocrystalline regimes-influence on some constitutive responses, J. Mater. Sci. 42 (2007) 1709–1727. https://doi.org/10.1007/s10853-006-0700-9.

[104] L. Lu, R. Schwaiger, Z.W. Shan, M. Dao, K. Lu, S. Suresh, Nano-sized twins induce high rate sensitivity of flow stress in pure copper, Acta Mater. 53 (2005) 2169–2179. https://doi.org/10.1016/j.actamat.2005.01.031.

[105] J. May, H.W. Höppel, M. Göken, Strain rate sensitivity of ultrafine-grained aluminium processed by severe plastic deformation, Scr. Mater. 53 (2005) 189–194. https://doi.org/10.1016/j.scriptamat.2005.03.043.

[106] Q. Wei, T. Jiao, S.N. Mathaudhu, E. Ma, K.T. Hartwig, K.T. Ramesh, Microstructure and mechanical properties of tantalum after equal channel angular extrusion (ECAE), Mater. Sci. Eng. A. 358 (2003) 266–272. https://doi.org/10.1016/S0921-5093(03)00305-8.

[107] K. Zhang, J.R. Weertman, J.A. Eastman, Rapid stress-driven grain coarsening in nanocrystalline Cu at ambient and cryogenic temperatures, Appl. Phys. Lett. 87 (2005) 1–4. https://doi.org/10.1063/1.2008377.

[108] V. Maier, K. Durst, J. Mueller, B. Backes, H.W. Höppel, M. Göken, Nanoindentation strain-rate jump tests for determining the local strain-rate sensitivity in nanocrystalline Ni and ultrafine-grained Al, J. Mater. Res. 26 (2011) 1421–1430. https://doi.org/10.1557/jmr.2011.156.

[109] Z. Horita, T. Fujinami, M. Nemoto, T.G. Langdon, Equal-channel angular pressing of commercial aluminum alloys: Grain refinement, thermal stability and tensile properties, Metall. Mater. Trans. A Phys. Metall. Mater. Sci. 31 (2000) 691–701.

[110] F. Czerwinski, Thermal stability of aluminum alloys, Materials (Basel). 13 (2020) 1–49. https://doi.org/10.3390/ma13153441.

[111] P. Zheng, Y. Li, J. Zhang, J. Shen, T. Nagasaka, T. Muroga, H. Abe, On the thermal stability of a 9Cr-ODS steel aged at 700 °C up to 10000 h - Mechanical properties and microstructure, Mater. Sci. Eng. A. 783 (2020) 139292. https://doi.org/10.1016/j.msea.2020.139292.

[112] Y. Du, W. Huo, J. Xu, W. Zhang, Mechanical Behavior and Strengthening Mechanisms in Precipitation-Strengthened Aluminum Alloy with Gradient Structure Induced by Sliding Friction Treatment, Metall. Mater. Trans. A Phys. Metall. Mater. Sci. (2020) 1–15. https://doi.org/10.1007/s11661-020-06038-y.

[113] H.W. Chang, P.M. Kelly, Y.N. Shi, M.X. Zhang, Thermal stability of nanocrystallized surface produced by surface mechanical attrition treatment in aluminum alloys, Surf. Coatings Technol. 206 (2012) 3970–3980. https://doi.org/10.1016/j.surfcoat.2012.03.069.

[114] W. Liao, S. Lan, L. Gao, H. Zhang, S. Xu, J. Song, X. Wang, Y. Lu, Nanocrystalline high-entropy alloy (CoCrFeNiAl0.3) thin-film coating by magnetron sputtering, Thin Solid Films. 638 (2017) 383–388.

[115] T.T. Sasaki, T. Mukai, K. Hono, A high-strength bulk nanocrystalline Al-Fe alloy processed by mechanical alloying and spark plasma sintering, Scr. Mater. 57 (2007) 189–192. https://doi.org/10.1016/j.scriptamat.2007.04.010.

[116] B. Srinivasarao, K. Oh-ishi, T. Ohkubo, K. Hono, Bimodally grained high-strength Fe fabricated by mechanical alloying and spark plasma sintering, Acta Mater. 57 (2009) 3277–3286. https://doi.org/10.1016/j.actamat.2009.03.034.

[117] J. Ye, L. Ajdelsztajn, J.M. Schoenung, Bulk Nanocrystalline Aluminum 5083 Alloy Fabricated by a Novel Technique : Cryomilling and Spark Plasma Sintering, Metall. Mater. Trans. (2005).

[118] M. Ames, J. Markmann, R. Karos, A. Michels, A. Tschöpe, R. Birringer, Unraveling the nature of room temperature grain growth in nanocrystalline materials, Acta Mater. 56 (2008) 4255–4266. https://doi.org/10.1016/j.actamat.2008.04.051.

[119] S. Brandstetter, K. Zhang, A. Escuadro, J.R. Weertman, H. Van Swygenhoven, Grain coarsening during compression of bulk nanocrystalline nickel and copper, Scr. Mater. 58 (2008) 61–64. https://doi.org/10.1016/j.scriptamat.2007.08.042.

[120] K.T. Kashyap, T. Chandrashekar, Effects and mechanisms of grain refinement in aluminium alloys, Bull. Mater. Sci. 24 (2001) 345–353. https://doi.org/10.1007/BF02708630.

[121] I. Maxwell, A. Hellawell, The constitution of the system Al-Ti-B with reference to Aluminum-Base alloys, Met. Trans. 3 (1972) 1487–1493. https://doi.org/10.1007/bf02643037.

[122] H. Jiang, Y. Song, L. Zhang, J. He, S. Li, J. Zhao, Efficient grain refinement of Al alloys induced by in-situ nanoparticles, J. Mater. Sci. Technol. 124 (2022) 14–25. https://doi.org/10.1016/j.jmst.2021.12.077.

[123] L. Li, M. Saber, W. Xu, Y. Zhu, C.C. Koch, R.O. Scattergood, High-temperature grain size stabilization of nanocrystalline Fe-Cr alloys with Hf additions, Mater. Sci. Eng. A. 613 (2014) 289–295. https://doi.org/10.1016/j.msea.2014.06.099.

[124] J. Weissmüller, Alloy effects in nanostructures, Nanostructured Mater. 3 (1993) 261–272. https://doi.org/10.1016/0965-9773(93)90088-S.

[125] C.A. Schuh, K. Lu, Stability of nanocrystalline metals: The role of grain-boundary chemistry and structure, MRS Bull. 46 (2021) 225–235. https://doi.org/10.1557/S43577-021-00055-X/FIGURES/8.

[126] A.E. Perrin, C.A. Schuh, Stabilized Nanocrystalline Alloys: The Intersection of Grain Boundary Segregation with Processing Science, Annu. Rev. Mater. Res. 51 (2021) 241–268. https://doi.org/10.1146/ANNUREV-MATSCI-080819-121823.

[127] X. Zhou, A. Gupta, G.J. Tucker, G.B. Thompson, Manipulation of solute partitioning mechanisms for nanocrystalline stability, Acta Mater. 208 (2021) 116662. https://doi.org/10.1016/j.actamat.2021.116662.

[128] W. Xing, A.R. Kalidindi, D. Amram, C.A. Schuh, Solute interaction effects on grain boundary segregation in ternary alloys, Acta Mater. 161 (2018) 285–294. https://doi.org/10.1016/j.actamat.2018.09.005.

[129] S.N. Mathaudhu, B.L. Boyce, Thermal Stability: The Next Frontier for Nanocrystalline Materials, Jom. 67 (2015) 2785–2787. https://doi.org/10.1007/s11837-015-1708-x.

[130] H.A. Murdoch, C.A. Schuh, Stability of binary nanocrystalline alloys against grain growth and phase separation, Acta Mater. 61 (2013) 2121–2132. https://doi.org/10.1016/j.actamat.2012.12.033.

[131] K.A. Darling, B.K. VanLeeuwen, J.E. Semones, C.C. Koch, R.O. Scattergood, L.J. Kecskes, S.N. Mathaudhu, Stabilized nanocrystalline iron-based alloys: Guiding efforts in alloy selection, Mater. Sci. Eng. A. 528 (2011) 4365–4371. https://doi.org/10.1016/J.MSEA.2011.02.080.

[132] J.R. Trelewicz, C.A. Schuh, Grain boundary segregation and thermodynamically stable binary nanocrystalline alloys, Phys. Rev. B - Condens. Matter Mater. Phys. 79 (2009) 094112. https://doi.org/10.1103/PHYSREVB.79.094112/FIGURES/10/MEDIUM.

[133] H.A. Murdoch, C.A. Schuh, Estimation of grain boundary segregation enthalpy and its role in stable nanocrystalline alloy design, J. Mater. Res. 28 (2013) 2154–2163. https://doi.org/10.1557/jmr.2013.211.

[134] C.M. Barr, S.M. Foiles, M. Alkayyali, Y. Mahmood, P.M. Price, D.P. Adams, B.L. Boyce, F. Abdeljawad, K. Hattar, The role of grain boundary character in solute segregation and thermal stability of nanocrystalline Pt–Au, Nanoscale. (2021). https://doi.org/10.1039/d0nr07180c.

[135] D. Bufford, H. Wang, X. Zhang, Thermal stability of twins and strengthening mechanisms in differently oriented epitaxial nanotwinned Ag films, J. Mater. Res. 28 (2013) 1729–1739. https://doi.org/10.1557/jmr.2013.50.

[136] O. Anderoglu, A. Misra, H. Wang, X. Zhang, Thermal stability of sputtered Cu films with nanoscale growth twins, J. Appl. Phys. 103 (2008). https://doi.org/10.1063/1.2913322.

[137] Z. Yang, J. Banhart, Natural and artificial ageing in aluminium alloys – the role of excess vacancies, Acta Mater. 215 (2021) 117014. https://doi.org/10.1016/J.ACTAMAT.2021.117014.

[138] Q. Li, D. Xie, Z. Shang, X. Sun, J. Cho, Y. Zhang, S. Xue, H. Wang, J. Wang, X. Zhang, Coupled solute effects enable anomalous high-temperature strength and stability in nanotwinned Al alloys, Acta Mater. 200 (2020) 378–388. https://doi.org/10.1016/j.actamat.2020.08.059.

[139] Y.F. Zhang, R. Su, D.Y. Xie, T.J. Niu, S. Xue, Q. Li, Z. Shang, J. Ding, N.A. Richter, J. Wang, H. Wang, X. Zhang, Design of super-strong and thermally stable nanotwinned Al alloys: Via solute synergy, Nanoscale. 12 (2020) 20491–20505. https://doi.org/10.1039/d0nr05707j.

[140] S. Dais, R. Messer, A. Seeger, Nuclear-Magnetic-Resonance Study of Self-Diffusion in Aluminium, Mater. Sci. Forum. 15–18 (1987) 419–424. https://doi.org/10.4028/www.scientific.net/msf.15-18.419.

[141] C. Moreau, A. Allouche, E.J. Knystautas, Measurements of the diffusion rate of lithium in aluminum at low temperature by elastic recoil detection analysis, J. Appl. Phys. 58 (1985) 4582–4586. https://doi.org/10.1063/1.336250.

[142] S. Fujikawa, K. Hirano, Y. Fukushima, Diffusion of Silicon in Aluminum, Metall. Trans. A. 9A (1978) 1811–1815.

[143] S. Fujikawa, K. Hirano, Diffusion of 28Mg in Aluminum, Mater. Sci. Eng. 27 (1977) 25–33.

[144] M. Mantina, S.L. Shang, Y. Wang, L.Q. Chen, Z.K. Liu, 3d transition metal impurities in aluminum: A first-principles study, Phys. Rev. B - Condens. Matter Mater. Phys. 80 (2009) 1–7. https://doi.org/10.1103/PhysRevB.80.184111.

[145] T. Oğurtani, Kinetics of diffusion in the Nb-Al system, Metall. Trans. 3 (1972) 425–429. https://doi.org/10.1007/BF02642046.

[146] R.P. Agarwala, S.P. Murarka, M.S. Anand, Diffusion of chromium in aluminium, Acta Metall. 12 (1964) 871–874. https://doi.org/10.1016/0001-6160(64)90145-2.

[147] G.M. Hood, R.J. Schultz, The diffusion of manganese in Alumnum, Philos. Mag. A J. Theor. Exp. Appl. Phys. 23 (1971) 1479–1489.

[148] K. ichi Hirano, R.P. Agarwala, M. Cohen, Diffusion of iron, nickel and cobalt in aluminum, Acta Metall. 10 (1962) 857–863. https://doi.org/10.1016/0001-6160(62)90100-1.

[149] D. Simonovic, M.H.F. Sluiter, Impurity diffusion activation energies in Al from first principles, Phys. Rev. B - Condens. Matter Mater. Phys. 79 (2009) 1–12. https://doi.org/10.1103/PhysRevB.79.054304.

[150] N.L. Peterson, S.J. Rothman, Impurity Diffusion in Aluminum, Phys. Rev. B. 871 (1970).

[151] C. Watanabe, T. Kondo, R. Monzen, Coarsening of Al3Sc precipitates in an Al-0.28 wt pct Sc alloy, Metall. Mater. Trans. A Phys. Metall. Mater. Sci. 35 A (2004) 3003–3008. https://doi.org/10.1007/s11661-004-0247-9.

[152] S.P. Murarka, R.P. Agarwala, Diffusion of rare elements in Al, Tech. Rep. 368; Bhabha At. Res. Cent. (Indian At. Energy Commision). (1968).

[153] E. Ma, Y.M. Wang, Q.H. Lu, M.L. Sui, L. Lu, K. Lu, Strain hardening and large tensile elongation in ultrahigh-strength nano-twinned copper, Appl. Phys. Lett. 85 (2004) 4932–4934. https://doi.org/10.1063/1.1814431.

[154] D. Bufford, Y. Liu, Y. Zhu, Z. Bi, Q.X. Jia, H. Wang, X. Zhang, Formation mechanisms of high-density growth twins in aluminum with high stacking-fault energy, Mater. Res. Lett. 1 (2013) 51–60. https://doi.org/10.1080/21663831.2012.761654.

[155] J. Wang, O. Anderoglu, J.P. Hirth, A. Misra, X. Zhang, Dislocation structures of σ3 {112} twin boundaries in face centered cubic metals, Appl. Phys. Lett. 95 (2009) 93–96. https://doi.org/10.1063/1.3176979.

[156] J. Wang, N. Li, O. Anderoglu, X. Zhang, A. Misra, J.Y. Huang, J.P. Hirth, Detwinning mechanisms for growth twins in face-centered cubic metals, Acta Mater. 58 (2010) 2262–2270. https://doi.org/10.1016/j.actamat.2009.12.013.

[157] N. Li, J. Wang, X. Zhang, A. Misra, In-situ TEM study of dislocation-twin boundaries interaction in nanotwinned Cu films, Jom. 63 (2011). https://doi.org/10.1007/s11837-011-0160-9.

[158] D. Bufford, Z. Bi, Q.X. Jia, H. Wang, X. Zhang, Nanotwins and stacking faults in high-strength epitaxial Ag/Al multilayer films, Appl. Phys. Lett. 101 (2012). https://doi.org/10.1063/1.4768000.

[159] Q. Li, S. Xue, J. Wang, S. Shao, A.H. Kwong, A. Giwa, Z. Fan, Y. Liu, Z. Qi, J. Ding, H.H. Wang, J.R. Greer, H.H. Wang, X. Zhang, High-Strength Nanotwinned Al Alloys with 9R Phase, Adv. Mater. 30 (2018) 1–9. https://doi.org/10.1002/adma.201704629.

[160] A. Liversidge, CV.--The crystalline structure of gold and platinum nuggets and gold ingots, J. Chem. Soc. Trans. 71 (1897) 1125–1131.

[161] H. Gleiter, The formation of annealing twins, Acta Metall. 17 (1969).

[162] H.C.H. Carpenter, S. Tamura, The Formation of Twinned Metallic Crystals, Proc. R. Soc. London. Ser. A. Math. Phys. Character. 113 (1926) 161–182.

[163] S. Mahajan, C.S. Pande, M.A. Imam, B.B. Rath, Formation of annealing twins in FCC crystals, Acta Mater. 45 (1997) 2633–2638.

[164] M.A. Meyers, L.E. Murr, A model for the formation of annealing twins in FCC metals and alloys, Acta Metall. 26 (1978) 951–962.

[165] B.B. Rath, M.A. Imam, C.S. Pande, Nucleation and Growth of Twin Interfaces in FCC Metals and Alloys, Mater. Phys. Mech. 1 (2000) 61–66. http://www.ipme.ru/e-journals/MPM/no_2100/rath/rath.pdf.

[166] M. Schneider, E.P. George, T.J. Manescau, T. Záležák, J. Hunfeld, A. Dlouhý, G. Eggeler, G. Laplanche, Analysis of strengthening due to grain boundaries and annealing twin boundaries in the CrCoNi medium-entropy alloy, Int. J. Plast. 124 (2020) 155–169. https://doi.org/10.1016/j.ijplas.2019.08.009.

[167] J.R. Cahoon, Q. Li, N.L. Richards, Microstructural and processing factors influencing the formation of annealing twins, Mater. Sci. Eng. A. 526 (2009) 56–61. https://doi.org/10.1016/j.msea.2009.07.021.

[168] A. Hunter, R.F. Zhang, I.J. Beyerlein, T.C. Germann, M. Koslowski, Dependence of equilibrium stacking fault width in fcc metals on the γ-surface, Model. Simul. Mater. Sci. Eng. 21 (2013). https://doi.org/10.1088/0965-0393/21/2/025015.

[169] L. Lu, Y. Shen, X. Chen, L. Qian, K. Lu, Ultrahigh Strength and High Electrical Conductivity in Copper, Science (80-.). 304 (2004) 422–426. https://doi.org/10.1126/science.1092905.

[170] D. Bufford, H. Wang, X. Zhang, High strength, epitaxial nanotwinned Ag films, Acta Mater. 59 (2011) 93–101. https://doi.org/10.1016/j.actamat.2010.09.011.

[171] Q. Li, S. Xue, P. Price, X. Sun, J. Ding, Z. Shang, Z. Fan, H. Wang, Y. Zhang, Y. Chen, H. Wang, K. Hattar, X. Zhang, Hierarchical nanotwins in single-crystal-like nickel with high strength and corrosion resistance produced via a hybrid technique, Nanoscale. 12 (2020) 1356. https://doi.org/10.1039/c9nr07472d.

[172] O. Anderoglu, A. Misra, H. Wang, F. Ronning, M.F. Hundley, X. Zhang, Epitaxial nanotwinned Cu films with high strength and high conductivity, Appl. Phys. Lett. 93 (2008) 5–8. https://doi.org/10.1063/1.2969409.

[173] L. Lu, X. Chen, X. Huang, K. Lu, Revealing the maximum strength in nanotwinned copper, Science (80-.). 323 (2009) 607–610. https://doi.org/10.1126/science.1167641.

[174] P.J. Imrich, C. Kirchlechner, D. Kiener, G. Dehm, Internal and external stresses: In situ TEM compression of Cu bicrystals containing a twin boundary, Scr. Mater. 100 (2015) 94–97. https://doi.org/10.1016/j.scriptamat.2014.12.023.

[175] G. Cheng, S. Yin, C. Li, T.H. Chang, G. Richter, H. Gao, Y. Zhu, In-situ TEM study of dislocation interaction with twin boundary and retraction in twinned metallic nanowires, Acta Mater. 196 (2020) 304–312. https://doi.org/10.1016/j.actamat.2020.06.055.

[176] L. Liu, J. Wang, S.K. Gong, S.X. Mao, High Resolution Transmission Electron Microscope Observation of Zero-Strain Deformation Twinning Mechanisms in Ag, Phys. Rev. Lett. 106 (2011). https://doi.org/10.1103/PhysRevLett.106.175504.

[177] D. Bufford, Y. Liu, J. Wang, H. Wang, X. Zhang, In situ nanoindentation study on plasticity and work hardening in aluminium with incoherent twin boundaries, Nat. Commun. 5 (2014) 1–8. https://doi.org/10.1038/ncomms5864.

[178] X. Zhang, A. Misra, H. Wang, M. Nastasi, J.D. Embury, T.E. Mitchell, R.G. Hoagland, J.P. Hirth, Nanoscale-twinning-induced strengthening in austenitic stainless steel thin films, Appl. Phys. Lett. 84 (2004) 1096–1098. https://doi.org/10.1063/1.1647690.

[179] Z.H. Jin, P. Gumbsch, E. Ma, K. Albe, K. Lu, H. Hahn, H. Gleiter, The interaction mechanism of screw dislocations with coherent twin boundaries in different face-centred cubic metals, Scr. Mater. 54 (2006) 1163–1168. https://doi.org/10.1016/j.scriptamat.2005.11.072.

[180] Z.H. Jin, P. Gumbsch, K. Albe, E. Ma, K. Lu, H. Gleiter, H. Hahn, Interactions between non-screw lattice dislocations and coherent twin boundaries in face-centered cubic metals, Acta Mater. 56 (2008) 1126–1135. https://doi.org/10.1016/j.actamat.2007.11.020.

[181] I.J. Beyerlein, X. Zhang, A. Misra, Growth Twins and Deformation Twins in Metals, Annu. Rev. Mater. Res. 44 (2014) 329–363. https://doi.org/10.1146/annurev-matsci-070813-113304.

[182] Z. You, X. Li, L. Gui, Q. Lu, T. Zhu, H. Gao, L. Lu, Plastic anisotropy and associated deformation mechanisms in nanotwinned metals, Acta Mater. 61 (2013) 217–227. https://doi.org/10.1016/j.actamat.2012.09.052.

[183] Q. Li, S. Xue, Y. Zhang, X. Sun, H. Wang, X. Zhang, Plastic anisotropy and tension-compression asymmetry in nanotwinned Al-Fe alloys: An in-situ micromechanical investigation, Int. J. Plast. 132 (2020) 102760. https://doi.org/10.1016/j.ijplas.2020.102760.

[184] Z. You, X. Li, L. Gui, Q. Lu, T. Zhu, H. Gao, L. Lu, Plastic anisotropy and associated deformation mechanisms in nanotwinned metals, Acta Mater. 61 (2013) 217–227. https://doi.org/10.1016/j.actamat.2012.09.052.

[185] Y. Chen, X. Zhang, J. Wang, Radiation Enhanced Absorption of Frank Loops by Nanovoids in Cu, JOM. 68 (2016) 235–241. https://doi.org/10.1007/s11837-015-1689-9.

[186] Y. Chen, K.Y. Yu, Y. Liu, S. Shao, H. Wang, M.A. Kirk, J. Wang, X. Zhang, Damage-tolerant nanotwinned metals with nanovoids under radiation environments, Nat. Commun. 6 (2015). https://doi.org/10.1038/ncomms8036.

[187] S. Xue, Z. Fan, O.B. Lawal, R. Thevamaran, Q. Li, Y. Liu, K.Y. Yu, J. Wang, E.L. Thomas, H. Wang, X. Zhang, High-velocity projectile impact induced 9R phase in ultrafine-grained aluminium, Nat. Commun. 8 (2017) 1–9. https://doi.org/10.1038/s41467-017-01729-4.

[188] Y.T. Zhu, X.Z. Liao, S.G. Srinivasan, Y.H. Zhao, M.I. Baskes, F. Zhou, E.J. Lavernia, Nucleation and growth of deformation twins in nanocrystalline aluminum, Appl. Phys. Lett. 85 (2004) 5049–5051. https://doi.org/10.1063/1.1823042.

[189] S. Xue, Z. Fan, Y. Chen, J. Li, H. Wang, X. Zhang, The formation mechanisms of growth twins in polycrystalline Al with high stacking fault energy, Acta Mater. 101 (2015) 62–70. https://doi.org/10.1016/j.actamat.2015.08.046.

[190] S. Xue, W. Kuo, Q. Li, Z. Fan, J. Ding, R. Su, H. Wang, X. Zhang, Texture-directed twin formation propensity in Al with high stacking fault energy, Acta Mater. 144 (2018) 226–234. https://doi.org/10.1016/j.actamat.2017.10.053.

[191] S.C. Xue, Y.F. Zhang, Q. Li, J. Ding, H. Wang, X. Zhang, Tailoring the formation of twins in Al by introducing epitaxial layer interfaces, Scr. Mater. 192 (2021) 1–6. https://doi.org/10.1016/j.scriptamat.2020.09.043.

[192] Y.F. Zhang, Q. Li, M. Gong, S. Xue, J. Ding, J. Li, J. Cho, T. Niu, R. Su, N.A. Richter, H. Wang, J. Wang, X. Zhang, Deformation behavior and phase transformation of nanotwinned Al/Ti multilayers, Appl. Surf. Sci. 527 (2020) 146776. https://doi.org/10.1016/j.apsusc.2020.146776.

[193] Y.F. Zhang, R. Su, T.J. Niu, N.A. Richter, S. Xue, Q. Li, J. Ding, B. Yang, H. Wang, X. Zhang, Thermal stability and deformability of annealed nanotwinned Al/Ti multilayers, Scr. Mater. 186 (2020) 219–224. https://doi.org/10.1016/j.scriptamat.2020.04.015.

[194] Y.F. Zhang, S. Xue, Q. Li, J. Li, J. Ding, T.J. Niu, R. Su, H. Wang, X. Zhang, Size dependent strengthening in high strength nanotwinned Al/Ti multilayers, Acta Mater. 175 (2019) 466–476. https://doi.org/10.1016/j.actamat.2019.06.028.

[195] Y.F. Zhang, S. Xue, Q. Li, C. Fan, R. Su, J. Ding, H. Wang, H. Wang, X. Zhang, Microstructure and mechanical behavior of nanotwinned AlTi alloys with 9R phase, Scr. Mater. 148 (2018) 5–9. https://doi.org/10.1016/j.scriptamat.2018.01.010.

[196] Y.F. Zhang, Q. Li, S.C. Xue, J. Ding, D.Y. Xie, J. Li, T. Niu, H. Wang, H. Wang, J. Wang, X. Zhang, Ultra-strong nanotwinned Al–Ni solid solution alloys with significant plasticity, Nanoscale. 10 (2018) 22025–22034. https://doi.org/10.1039/c8nr05139a.

[197] S. Xue, Q. Li, D.Y. Xie, Y.F. Zhang, H. Wang, H. Wang, J. Wang, X. Zhang, High strength, deformable nanotwinned Al–Co alloys, Mater. Res. Lett. 7 (2019) 33–39. https://doi.org/10.1080/21663831.2018.1552211.

[198] S. Xue, Q. Li, Z. Fan, H.H. Wang, Y. Zhang, J. Ding, H.H. Wang, X. Zhang, Strengthening mechanisms and deformability of nanotwinned AlMg alloys, J. Mater. Res. 33 (2018) 3739–3749. https://doi.org/10.1557/jmr.2018.372.

[199] Q. Li, J. Cho, S. Xue, X. Sun, Y. Zhang, Z. Shang, H. Wang, X. Zhang, High temperature thermal and mechanical stability of high-strength nanotwinned Al alloys, Acta Mater. 165 (2019) 142–152. https://doi.org/10.1016/J.ACTAMAT.2018.11.011.

[200] M. Gong, W. Wu, D. Xie, N.A. Richter, Q. Li, Y. Zhang, S. Xue, X. Zhang, J. Wang, Mingyu Gong, Wenqian Wu, Dongyue Xie, N. A. Richter, Qiang Li, Yifan Zhang, Sichuang Xue, Xinghang Zhang, Jian Wang, First-principles calculations for understanding microstructures and mechanical properties of co-sputtered Al alloys, Nanoscale. 13 (2021) 14987–15001. https://doi.org/10.1039/D1NR03333F.

[201] C. Bonafos, L. Khomenkhova, F. Gourbilleau, E. Talbot, A. Slaoui, M. Carrada, S. Schamm-Chardon, P. Dimitrakis, P. Normand, Nano-composite MOx materials for NVMs, Elsevier, 2022. https://doi.org/10.1016/B978-0-12-814629-3.00007-6.

[202] A.A. Bunaciu, E. gabriela Udriştioiu, H.Y. Aboul-Enein, X-Ray Diffraction: Instrumentation and Applications, Crit. Rev. Anal. Chem. 45 (2015) 289–299. https://doi.org/10.1080/10408347.2014.949616.

[203] C. Hammond, The Basics of Crystallograhy and Diffraction, 3rd ed., Oxford University Press, 2009.

[204] G.M. Pharr, W.C. Oliver, Measurement of Thin Film Mechanical Properties Using Nanoindentation, MRS Bull. 17 (1992) 28–33. https://doi.org/10.1557/S0883769400041634.

[205] K. Herrmann, N.M. Jennett, W. Wegener, J. Meneve, K. Hasche, R. Seemann, Progress in determination of the area function of indenters used for nanoindentation, Thin Solid Films. 377–378 (2000) 394–400. https://doi.org/10.1016/S0040-6090(00)01367-5.

[206] G.M. Pharr, E.G. Herbert, Y. Gao, The Indentation Size Effect: A Critical Examination of Experimental Observations and Mechanistic Interpretations, Annu. Rev. Mater. Res. 40 (2010) 271–292. https://doi.org/10.1146/annurev-matsci-070909-104456.

[207] D.B. Williams, C.B. Carter, Transmission Electron Microscopy, 2nd ed., Springer, New York, 2009.

[208] J.C. Meyer, Transmission electron microscopy (TEM) of graphene, Graphene Prop. Prep. Characterisation Devices. (2014) 101–123. https://doi.org/10.1533/9780857099334.2.101.

[209] E.F. Rauch, J. Portillo, S. Nicolopoulos, D. Bultreys, S. Rouvimov, P. Moeck, Automated nanocrystal orientation and phase mapping in the transmission electron microscope on the basis of precession electron diffraction, Zeitschrift Fur Krist. 225 (2010) 103–109. https://doi.org/10.1524/zkri.2010.1205.

[210] M.D. Uchic, D.M. Dimiduk, J.N. Florando, W.D. Nix, Sample Dimensions Influence Strength and Crystal Plasticity, Science (80-.). 305 (2004) 986–990. https://doi.org/10.1126/science.1098993.

[211] M.D. Uchic, D.M. Dimiduk, A methodology to investigate size scale effects in crystalline plasticity using uniaxial compression testing, Mater. Sci. Eng. A. 400–401 (2005) 268–278. https://doi.org/10.1016/j.msea.2005.03.082.

[212] J.R. Greer, W.C. Oliver, W.D. Nix, Size dependence of mechanical properties of gold at the micron scale in the absence of strain gradients, Acta Mater. 53 (2005) 1821–1830. https://doi.org/10.1016/j.actamat.2004.12.031.

[213] K.S. Ng, A.H.W. Ngan, Stochastic nature of plasticity of aluminum micro-pillars, Acta Mater. 56 (2008) 1712–1720. https://doi.org/10.1016/j.actamat.2007.12.016.

[214] D. Kiener, W. Grosinger, G. Dehm, R. Pippan, A further step towards an understanding of size-dependent crystal plasticity: In situ tension experiments of miniaturized single-crystal copper samples, Acta Mater. 56 (2008) 580–592. https://doi.org/10.1016/j.actamat.2007.10.015.

[215] T.A. Parthasarathy, S.I. Rao, D.M. Dimiduk, M.D. Uchic, D.R. Trinkle, Contribution to size effect of yield strength from the stochastics of dislocation source lengths in finite samples, Scr. Mater. 56 (2007) 313–316. https://doi.org/10.1016/j.scriptamat.2006.09.016.

[216] D.M. Norfleet, D.M. Dimiduk, S.J. Polasik, M.D. Uchic, M.J. Mills, Dislocation structures and their relationship to strength in deformed nickel microcrystals, Acta Mater. 56 (2008) 2988–3001. https://doi.org/10.1016/j.actamat.2008.02.046.

[217] Z.W. Shan, R.K. Mishra, S.A. Syed Asif, O.L. Warren, A.M. Minor, Mechanical annealing and source-limited deformation in submicrometre- diameter Nicrystals, Nat. Mater. 7 (2008) 115–119. https://doi.org/10.1038/nmat2085.

[218] J.R. Greer, W.D. Nix, Nanoscale gold pillars strengthened through dislocation starvation, Phys. Rev. B - Condens. Matter Mater. Phys. 73 (2006) 1–6. https://doi.org/10.1103/PhysRevB.73.245410.

[219] W.D. Nix, J.R. Greer, G. Feng, E.T. Lilleodden, Deformation at the nanometer and micrometer length scales: Effects of strain gradients and dislocation starvation, Thin Solid Films. 515 (2007) 3152–3157. https://doi.org/10.1016/j.tsf.2006.01.030.

[220] C.R. Weinberger, W. Cai, Surface-controlled dislocation multiplication in metal micropillars, Proc. Natl. Acad. Sci. 105 (2008) 14304–14307. https://doi.org/10.1073/pnas.0806118105.

[221] M.D. Uchic, P.A. Shade, D.M. Dimiduk, Plasticity of Micrometer-Scale Single Crystals in Compression, Annu. Rev. Mater. Res. 39 (2009) 361–386. https://doi.org/10.1146/annurev-matsci-082908-145422.

[222] H. Zhang, B.E. Schuster, Q. Wei, K.T. Ramesh, The design of accurate micro-compression experiments, Scr. Mater. 54 (2006) 181–186. https://doi.org/10.1016/j.scriptamat.2005.06.043.

[223] G. Mohanty, J.M. Wheeler, R. Raghavan, J. Wehrs, M. Hasegawa, S. Mischler, L. Philippe, J. Michler, Elevated temperature, strain rate jump microcompression of nanocrystalline nickel, Philos. Mag. 95 (2015) 1878–1895. https://doi.org/10.1080/14786435.2014.951709.

[224] B. Kondori, A. Needleman, A.A. Benzerga, Discrete dislocation simulations of compression of tapered micropillars, J. Mech. Phys. Solids. 101 (2017) 223–234. https://doi.org/10.1016/j.jmps.2017.01.015.

[225] I.N. Sneddon, The relation between load an penetration in the axisymmetric boussinesq problem for punch of arbitrary profile, Int. J. Eng. Sci. 3 (1965) 47–57. https://doi.org/10.1016/0020-7225(65)90019-4.

[226] J. Hu, E.T. Lilleodden, The influence of focused-ion beam preparation technique on microcompression investigations: Lathe vs. annular milling, Scr. Mater. 77 (2014) 49–51. https://doi.org/10.1016/j.scriptamat.2014.01.016.

[227] Y. Wei, Y. Li, L. Zhu, Y. Liu, X. Lei, G. Wang, Y. Wu, Z. Mi, J. Liu, H. Wang, H. Gao, Evading the strength-ductility trade-off dilemma in steel through gradient hierarchical nanotwins, Nat. Commun. 5 (2014). https://doi.org/10.1038/ncomms4580.

[228] Z. Li, K.G. Pradeep, Y. Deng, D. Raabe, C.C. Tasan, K. Gokuldoss Pradeep, Y. Deng, D. Raabe, C. Cem Tasan, Metastable high-entropy dual-phase alloys overcome the strength-ductility trade-off, Nature. 534 (2016) 227–230. https://doi.org/10.1038/nature17981.

[229] E. Ma, X. Wu, Tailoring heterogeneities in high-entropy alloys to promote strength–ductility synergy, Nat. Commun. 10 (2019) 1–10. https://doi.org/10.1038/s41467-019-13311-1.

[230] A.A. Karimpoor, U. Erb, K.T. Aust, G. Palumbo, High strength nanocrystalline cobalt with high tensile ductility, Scr. Mater. 49 (2003) 651–656. https://doi.org/10.1016/S1359-6462(03)00397-X.

[231] F. Dalla Torre, H. Van Swygenhoven, M. Victoria, Nanocrystalline electrodeposited Ni: Microstructure and tensile properties, Acta Mater. 50 (2002) 3957–3970. https://doi.org/10.1016/S1359-6454(02)00198-2.

[232] H. Conrad, D. Yang, Effect of an electric field on the plastic deformation kinetics of electrodeposited Cu at low and intermediate temperatures, Acta Mater. 50 (2002) 2851–2866. https://doi.org/10.1016/S1359-6454(02)00109-X.

[233] K.S. Kumar, H. Van Swygenhoven, S. Suresh, Mechanical behavior of nanocrystalline metals and alloys, Acta Mater. 51 (2003) 5743–5774. https://doi.org/10.1016/j.actamat.2003.08.032.

[234] X. Lu, J. Zhao, Z. Wang, B. Gan, J. Zhao, G. Kang, X. Zhang, Crystal plasticity finite element analysis of gradient nanostructured TWIP steel, Int. J. Plast. 130 (2020) 102703. https://doi.org/10.1016/J.IJPLAS.2020.102703.

[235] Y. Shen, J. Liu, H. Xu, H. Liu, Micro-segregation Study of Directional Solidified Fe–Mn–C–Al TWIP Steels, Metall. Mater. Trans. B 2020 516. 51 (2020) 2963–2975. https://doi.org/10.1007/S11663-020-01982-X.

[236] B.C. De Cooman, Y. Estrin, S.K. Kim, Twinning-induced plasticity (TWIP) steels, Acta Mater. 142 (2018) 283–362. https://doi.org/10.1016/J.ACTAMAT.2017.06.046.

[237] R.A. Hadfield, Hadfield's Manganese Steel, Science (80-.). 12 (1888) 284–286.

[238] Z. Yang, D. Yan, W. Lu, Z. Li, A TWIP-TRIP quinary high-entropy alloy: Tuning phase stability and microstructure for enhanced mechanical properties, Mater. Sci. Eng. A. 801 (2021) 140441. https://doi.org/10.1016/j.msea.2020.140441.

[239] X. Feng, J. Zhang, K. Wu, X. Liang, G. Liu, J. Sun, Ultrastrong Al0.1CoCrFeNi high-entropy alloys at small scales: Effects of stacking faults: Vs. nanotwins, Nanoscale. 10 (2018) 13329–13334. https://doi.org/10.1039/c8nr03573c.

[240] Z. Fan, J. Li, Y. Yang, J. Wang, Q. Li, S. Xue, H. Wang, J. Lou, X. Zhang, "Ductile" Fracture of Metallic Glass Nanolaminates, Adv. Mater. Interfaces. 4 (2017) 1–9. https://doi.org/10.1002/admi.201700510.

[241] C. Fan, D. Xie, J. Li, Z. Shang, Y. Chen, S. Xue, J. Wang, M. Li, E.-A. Anter, H. Wang, X. Zhang, 9R phase enabled superior radiation stability of nanotwinned Cu alloys via in situ radiation at elevated temperature, Acta Mater. 167 (2019) 248–256. https://doi.org/10.1016/j.actamat.2019.01.037.

[242] J. Lemaitre, A continuous damage mechanics model for ductile fracture, J. Eng. Mater. Technol. Trans. ASME. 107 (1985) 83–89. https://doi.org/10.1115/1.3225775.

[243] M.A. Meyers, L.E. Murr, A Model for the Formation of Annealing Twins in F.C.C. Metals and Alloys, Acta Metall. 26 (1978) 951–962.

[244] E. Ma, T. Zhu, Towards strength–ductility synergy through the design of heterogeneous nanostructures in metals, Mater. Today. 20 (2017) 323–331. https://doi.org/10.1016/j.mattod.2017.02.003.

[245] X. Zhang, H. Wang, X.H. Chen, L. Lu, K. Lu, R.G. Hoagland, A. Misra, High-strength sputter-deposited Cu foils with preferred orientation of nanoscale growth twins, Appl. Phys. Lett. 88 (2006) 2004–2007. https://doi.org/10.1063/1.2198482.

[246] T. Niu, J. Li, Y. Zhang, J. Cho, J. Ding, R. Su, S. Xue, C. Fan, Z. Shang, D. Chen, Y. Wang, H. Wang, X. Zhang, In-situ Studies on the Mechanical Properties of He Ion Irradiated Nanotwinned Ag, J. Nucl. Mater. (2020) 152392. https://doi.org/10.1016/j.jnucmat.2020.152392.

[247] Q. Zhu, L. Kong, H. Lu, Q. Huang, Y. Chen, Y. Liu, W. Yang, Z. Zhang, F. Sansoz, H. Zhou, J. Wang, Revealing extreme twin-boundary shear deformability in metallic nanocrystals, Sci. Adv. 7 (2021) 1–9.

[248] Q. Fang, F. Sansoz, Columnar grain-driven plasticity and cracking in nanotwinned FCC metals, Acta Mater. 212 (2021) 116925. https://doi.org/10.1016/j.actamat.2021.116925.

[249] J. Li, D.Y. Xie, S. Xue, C. Fan, Y. Chen, H. Wang, J. Wang, X. Zhang, Superior twin stability and radiation resistance of nanotwinned Ag solid solution alloy, Acta Mater. 151 (2018) 395–405. https://doi.org/10.1016/j.actamat.2018.03.052.

[250] F. Sansoz, K. Lu, T. Zhu, A. Misra, Strengthening and plasticity in nanotwinned metals, MRS Bull. 41 (2016) 292–297. https://doi.org/10.1557/mrs.2016.60.

[251] T.A. Furnish, A.M. Hodge, On the mechanical performance and deformation of nanotwinned Ag, APL Mater. 2 (2014) 046112. https://doi.org/10.1063/1.4873215.

[252] Y. Morris Wang, F. Sansoz, T. Lagrange, R.T. Ott, J. Marian, T.W. Barbee, A. V. Hamza, Defective twin boundaries in nanotwinned metals, Nat. Mater. 12 (2013) 697–702. https://doi.org/10.1038/nmat3646.

[253] N. Li, J. Wang, A. Misra, X. Zhang, J.Y. Huang, J.P. Hirth, Twinning dislocation multiplication at a coherent twin boundary, Acta Mater. 59 (2011) 5989–5996. https://doi.org/10.1016/j.actamat.2011.06.007.

[254] T. Zhu, H. Gao, Plastic deformation mechanism in nanotwinned metals: An insight from molecular dynamics and mechanistic modeling, Scr. Mater. 66 (2012) 843–848. https://doi.org/10.1016/j.scriptamat.2012.01.031.

[255] Y. Liu, J. Jian, Y. Chen, H. Wang, X. Zhang, Plasticity and ultra-low stress induced twin boundary migration in nanotwinned Cu by in situ nanoindentation studies, Appl. Phys. Lett. 104 (2014) 231910. https://doi.org/10.1063/1.4882242.

[256] Z.X. Wu, Y.W. Zhang, D.J. Srolovitz, Dislocation-twin interaction mechanisms for ultrahigh strength and ductility in nanotwinned metals, Acta Mater. 57 (2009) 4508–4518. https://doi.org/10.1016/j.actamat.2009.06.015.

[257] X. Li, Y. Wei, L. Lu, K. Lu, H. Gao, Dislocation nucleation governed softening and maximum strength in nano-twinned metals, Nature. 464 (2010) 877–880. https://doi.org/10.1038/nature08929.

[258] O. Anderoglu, A. Misra, F. Ronning, H. Wang, X. Zhang, Significant enhancement of the strength-to-resistivity ratio by nanotwins in epitaxial Cu films, J. Appl. Phys. 106 (2009) 1–9. https://doi.org/10.1063/1.3176483.

[259] X. Zhang, A. Misra, Superior thermal stability of coherent twin boundaries in nanotwinned metals, Scr. Mater. 66 (2012) 860–865. https://doi.org/10.1016/j.scriptamat.2012.01.026.

[260] X. Zhang, A. Misra, H. Wang, J.G. Swadener, A.L. Lima, M.F. Hundley, R.G. Hoagland, Thermal stability of sputter-deposited 330 austenitic stainless-steel thin films with nanoscale growth twins, Appl. Phys. Lett. 87 (2005) 1–3. https://doi.org/10.1063/1.2135871.

[261] H. Van Swygenhoven, P.M. Derlet, A.G. Frøseth, Stacking fault energies and slip in nanocrystalline metals, Nat. Mater. 3 (2004) 399–403. https://doi.org/10.1038/nmat1136.

[262] X. Zhang, A. Misra, H. Wang, T.D. Shen, M. Nastasi, T.E. Mitchell, J.P. Hirth, R.G. Hoagland, J.D. Embury, Enhanced hardening in Cu/330 stainless steel multilayers by nanoscale twinning, Acta Mater. 52 (2004) 995–1002. https://doi.org/10.1016/j.actamat.2003.10.033.

[263] J. Wang, H. Huang, Shockley partial dislocations to twin: Another formation mechanism and generic driving force, Appl. Phys. Lett. 85 (2004) 5983–5985. https://doi.org/10.1063/1.1835549.

[264] Q. Li, S. Xue, C. Fan, N.A. Richter, Y. Zhang, Y. Chen, H. Wang, X. Zhang, Epitaxial nanotwinned metals and alloys: synthesis-twin structure–property relations, CrystEngComm. 23 (2021) 6637–6649. https://doi.org/10.1039/d1ce00787d.

[265] Y. Qi, R.K. Mishra, Ab initio study of the effect of solute atoms on the stacking fault energy in aluminum, Phys. Rev. B - Condens. Matter Mater. Phys. 75 (2007). https://doi.org/10.1103/PhysRevB.75.224105.

[266] H.Z.Z. Zhao, Z.S.S. You, N.R.R. Tao, L. Lu, Anisotropic strengthening of nanotwin bundles in heterogeneous nanostructured Cu: Effect of deformation compatibility, Acta Mater. 210 (2021) 116830. https://doi.org/10.1016/j.actamat.2021.116830.

[267] S. Mahajan, Critique of mechanisms of formation of deformation, annealing and growth twins: Face-centered cubic metals and alloys, Scr. Mater. 68 (2013) 95–99. https://doi.org/10.1016/j.scriptamat.2012.09.011.

[268] N.Y. Tabachkova, A.V. Mikhaylovskaya, W. Mufalo, V.K. Portnoy, A.G. Mochugovskiy, V.S. Levchenko, Precipitation behavior of L1 2 Al 3 Zr phase in Al-Mg-Zr alloy, Mater. Charact. 139 (2018) 30–37. https://doi.org/10.1016/j.matchar.2018.02.030.

[269] K.E. Knipling, R.A. Karnesky, C.P. Lee, D.C. Dunand, D.N. Seidman, Precipitation evolution in Al-0.1Sc, Al-0.1Zr and Al-0.1Sc-0.1Zr (at.%) alloys during isochronal aging, Acta Mater. 58 (2010) 5184–5195. https://doi.org/10.1016/j.actamat.2010.05.054.

[270] L. Vegard, The constitution of the mixed crystals and the space filling of the atoms, Zeitschrift Für Phys. 5 (1921) 17–26. https://doi.org/10.1002/pssb.19660180251.

[271] N.A. Richter, Y.F. Zhang, D.Y. Xie, R. Su, Q. Li, S. Xue, T. Niu, J. Wang, H. Wang, X. Zhang, Y.F. Zhang, D.Y. Xie, R. Su, Q. Li, S. Xue, Microstructural evolution of nanotwinned Al-Zr alloy with significant 9R phase, Mater. Res. Lett. 9 (2020) 91–98. https://doi.org/10.1080/21663831.2020.1840451.

[272] H. Yoshioka, Q. Yan, K. Asami, K. Hashimoto, Pitting potential and structure of sputter-deposited Al-Ti alloys, Mater. Sci. Eng. A. 134 (1991) 1054–1057. https://doi.org/10.1016/0921-5093(91)90923-B.

[273] F. Hehmann, F. Sommer, B. Predel, Extension of solid solubility in magnesium by rapid solidification, Mater. Sci. Eng. A. 125 (1990) 249–265. https://doi.org/10.1016/0921-5093(90)90175-3.

[274] G. Rummel, T. Zumkley, M. Eggersmann, K. Freitag, H. Mehrer, Diffusion of Implanted 3d-Transition Elements in Aluminum Part I: Temperature Dependence, Int. J. Mater. Res. 85 (1995).

[275] R.W. Hayes, R. Rodriguez, E.J. Lavernia, The mechanical behavior of a cryomilled Al–10Ti–2Cu alloy, Acta Mater. 49 (2001) 4055–4068. https://doi.org/10.1016/S1359-6454(01)00278-6.

[276] N. Tsuji, Y. Ito, Y. Saito, Y. Minamino, Strength and ductility of ultrafine grained aluminum and iron produced by ARB and annealing, Scr. Mater. 47 (2002) 893–899. https://doi.org/10.1016/S1359-6462(02)00282-8.

[277] B. Srinivasarao, C. Suryanarayana, K. Oh-ishi, K. Hono, Microstructure and mechanical properties of Al-Zr nanocomposite materials, Mater. Sci. Eng. A. 518 (2009) 100–107. https://doi.org/10.1016/j.msea.2009.04.032.

[278] T. Sun, Z. Shang, J. Cho, J. Ding, T. Niu, Y. Zhang, B. Yang, D. Xie, J. Wang, H. Wang, X. Zhang, Ultra-fine-grained and gradient FeCrAl alloys with outstanding work hardening capability, Acta Mater. 215 (2021) 117049. https://doi.org/10.1016/J.ACTAMAT.2021.117049.

[279] O. Bouaziz, Y. Estrin, Y. Bréchet, J.D. Embury, Critical grain size for dislocation storage and consequences for strain hardening of nanocrystalline materials, Scr. Mater. 63 (2010) 477–479. https://doi.org/10.1016/J.SCRIPTAMAT.2010.05.006.

[280] R. Maaß, M.D. Uchic, In-situ characterization of the dislocation-structure evolution in Ni micro-pillars, Acta Mater. 60 (2012) 1027–1037. https://doi.org/10.1016/j.actamat.2011.11.007.

[281] N. Hansen, Hall-petch relation and boundary strengthening, Scr. Mater. 51 (2004) 801–806. https://doi.org/10.1016/j.scriptamat.2004.06.002.

[282] B. Yang, Z. Shang, J. Ding, J. Lopez, W. Jarosinski, T. Sun, N. Richter, Y. Zhang, H. Wang, X. Zhang, Investigation of strengthening mechanisms in an additively manufactured Haynes 230 alloy, Acta Mater. 222 (2022) 117404. https://doi.org/10.1016/J.ACTAMAT.2021.117404.

[283] H. Gleiter, Nanostructured materials: basic concepts and microstructure, Acta Mater. 48 (2000) 1–29. https://doi.org/10.1016/S1359-6454(99)00285-2.

[284] A. V. Sergueeva, C. Song, R.Z. Valiev, A.K. Mukherjee, Structure and properties of amorphous and nanocrystalline NiTi prepared by severe plastic deformation and annealing, Mater. Sci. Eng. A. 339 (2003) 159–165. https://doi.org/10.1016/S0921-5093(02)00122-3.

[285] X.Z. Liao, Y.H. Zhao, S.G. Srinivasan, Y.T. Zhu, R.Z. Valiev, D. V. Gunderov, Deformation twinning in nanocrystalline copper at room temperature and low strain rate, Appl. Phys. Lett. 84 (2004) 592–594. https://doi.org/10.1063/1.1644051.

[286] E.M. Pinto, A.S. Ramos, M.T. Vieira, C.M.A. Brett, A corrosion study of nanocrystalline copper thin films, Corros. Sci. 52 (2010) 3891–3895. https://doi.org/10.1016/j.corsci.2010.08.001.

[287] S. Simoes, R. Calinas, M.T.F. Vieira, M.T.F. Vieira, P.J. Ferreira, In situ TEM study of grain growth in nanocrystalline copper thin films, Nanotechnology. 21 (2010). https://doi.org/10.1088/0957-4484/21/14/145701.

[288] P.L. Gai, R. Mitra, J.R. Weertman, Structural variations in nanocrystalline nickel films, Pure Appl. Chem. 74 (2002) 1519–1526. https://doi.org/10.1351/pac200274091519.

[289] Q. Li, Z. Shang, X. Sun, C. Fan, R. Su, N.A. Richter, Z. Fan, Y. Zhang, S. Xue, H. Wang, X. Zhang, High-strength and tunable plasticity in sputtered Al–Cr alloys with multistage phase transformations, Int. J. Plast. 137 (2021) 102915. https://doi.org/10.1016/j.ijplas.2020.102915.

[290] T. Niu, Y. Zhang, Z. He, T. Sun, N.A. Richter, H. Wang, X. Zhang, Texture development in Cu-Ag-Fe triphase immiscible nanocomposites with superior thermal stability, Acta Mater. 244 (2023) 118545. https://doi.org/10.1016/j.actamat.2022.118545.

[291] G.W. Nieman, J.R. Weertman, R.W. Siegel, Microhardness of nanocrystalline palladium and copper produced by inert-gas condensation, Scr. Metall. 23 (1989) 2013–2018. https://doi.org/10.1016/0036-9748(89)90223-8.

[292] X.J. Wu, L.G. Du, H.F. Zhang, J.F. Liu, Y.S. Zhou, Z.Q. Li, L.Y. Xiong, Y.L. Bai, Synthesis and tensile property of nanocrystalline metal copper, Nanostructured Mater. 12 (1999) 221–224. https://doi.org/10.1016/S0965-9773(99)00103-8.

[293] J. Wang, S. Wu, S. Fu, S. Liu, M. Yan, Q. Lai, S. Lan, H. Hahn, T. Feng, Ultrahigh hardness with exceptional thermal stability of a nanocrystalline CoCrFeNiMn high-entropy alloy prepared by inert gas condensation, Scr. Mater. 187 (2020) 335–339. https://doi.org/10.1016/j.scriptamat.2020.06.042.

[294] R. Hull, J.M. Gibson, L.E. Brus, D.J. Norris, M.G. Bawendi, A. Zunger, A. Zunger, K.B. Whaley, A.J. Williamson, F.A. Reboredo, G. Galli, B. Gilbert, F. Huang, P.H. Borse, N. Deshmukh, S.K. Kulkarni, M.F. Thorpe, Grain Boundary – Mediated Plasticity in Nanocrystalline Nickel, 305 (2004) 654–658.

[295] R. Liang, A.S. Khan, A critical review of experimental results and constitutive models for BCC and FCC metals over a wide range of strain rates and temperatures, Int. J. Plast. 15 (1999) 963–980. https://doi.org/10.1016/S0749-6419(99)00021-2.

[296] R.W. Hayes, D. Witkin, F. Zhou, E.J. Lavernia, Deformation and activation volumes of cryomilled ultrafine-grained aluminum, Acta Mater. 52 (2004) 4259–4271. https://doi.org/10.1016/j.actamat.2004.05.042.

[297] J. Chen, L. Lu, K. Lu, Hardness and strain rate sensitivity of nanocrystalline Cu, Scr. Mater. 54 (2006) 1913–1918. https://doi.org/10.1016/j.scriptamat.2006.02.022.

[298] Y. Wei, A.F. Bower, H. Gao, Enhanced strain-rate sensitivity in fcc nanocrystals due to grain-boundary diffusion and sliding, Acta Mater. 56 (2008) 1741–1752. https://doi.org/10.1016/j.actamat.2007.12.028.

[299] G.A. Malygin, Analysis of the strain-rate sensitivity of flow stresses in nanocrystalline FCC and BCC metals, Phys. Solid State. 49 (2007) 2266–2273. https://doi.org/10.1134/S1063783407120098.

[300] X. Zhang, O. Anderoglu, A. Misra, H. Wang, Influence of deposition rate on the formation of growth twins in sputter-deposited 330 austenitic stainless steel films, Appl. Phys. Lett. 90 (2007) 2007–2009. https://doi.org/10.1063/1.2720708.

[301] K.Y. Yu, D. Bufford, Y. Chen, Y. Liu, H. Wang, X. Zhang, Basic criteria for formation of growth twins in high stacking fault energy metals, Appl. Phys. Lett. 103 (2013). https://doi.org/10.1063/1.4826917.

[302] J. Xiao, C. Deng, Mitigating the Hall-Petch breakdown in nanotwinned Cu by amorphous intergranular films, Scr. Mater. 194 (2021) 113682. https://doi.org/10.1016/j.scriptamat.2020.113682.

[303] W.M. Stobbs, C.H. Sworn, The weak beam technique as applied to the determination of the stacking-fault energy of copper, Philos. Mag. 24 (1971) 1365–1381. https://doi.org/10.1080/14786437108217418.

[304] A. Howie, P.R. Swann, Direct measurements of stacking-fault energies from observations of dislocation nodes, Philos. Mag. 6 (1961) 1215–1226. https://doi.org/10.1080/14786436108243372.

[305] L. Vitos, J.O. Nilsson, B. Johansson, Alloying effects on the stacking fault energy in austenitic stainless steels from first-principles theory, Acta Mater. 54 (2006) 3821–3826. https://doi.org/10.1016/j.actamat.2006.04.013.

[306] A.G. Frøseth, P.M. Derlet, H. Van Swygenhoven, Twinning in nanocrystalline fcc metals, Adv. Eng. Mater. 7 (2005) 16–20. https://doi.org/10.1002/adem.200400163.

[307] N.A. Richter, Y.F. Zhang, M. Gong, T. Niu, B. Yang, S. Xue, J. Wang, H. Wang, X. Zhang, Solute synergy induced thermal stability of high-strength nanotwinned Al-Co-Zr alloys, Mater. Sci. Eng. A. 862 (2023) 144477. https://doi.org/10.1016/j.msea.2022.144477.

[308] N.A. Richter, M. Gong, Y.F. Zhang, T. Niu, B. Yang, J. Wang, H. Wang, X. Zhang, Exploring the deformation behavior of nanotwinned Al-Zr alloy via in situ compression, J. Appl. Phys. 132 (2022) 065104. https://doi.org/10.1063/5.0098497.

[309] Y. Zhang, T. Niu, N.A. Richter, T. Sun, N. Li, H. Wang, X. Zhang, Tribological behaviors of nanotwinned Al alloys, Appl. Surf. Sci. 600 (2022) 154108. https://doi.org/10.1016/j.apsusc.2022.154108.

[310] D. Bayoumy, D. Schliephake, S. Dietrich, X.H. Wu, Y.M. Zhu, A.J. Huang, Intensive processing optimization for achieving strong and ductile Al-Mn-Mg-Sc-Zr alloy produced by selective laser melting, Mater. Des. 198 (2021) 109317. https://doi.org/10.1016/j.matdes.2020.109317.

[311] Z. Wang, X. Lin, N. Kang, J. Chen, Y. Tang, H. Tan, X. Yu, H. Yang, W. Huang, Directed energy deposition additive manufacturing of a Sc/Zr-modified Al–Mg alloy: Effect of thermal history on microstructural evolution and mechanical properties, Mater. Sci. Eng. A. 802 (2021) 140606. https://doi.org/10.1016/j.msea.2020.140606.

[312] R. Ma, C. Peng, Z. Cai, R. Wang, Z. Zhou, X. Li, X. Cao, Manipulating the microstructure and tensile properties of selective laser melted Al–Mg-Sc-Zr alloy through heat treatment, J. Alloys Compd. 831 (2020) 154773. https://doi.org/10.1016/j.jallcom.2020.154773.

[313] M. Dao, L. Lu, Y.F. Shen, S. Suresh, Strength, strain-rate sensitivity and ductility of copper with nanoscale twins, Acta Mater. 54 (2006) 5421–5432. https://doi.org/10.1016/j.actamat.2006.06.062.

[314] I.C. Choi, Y.J. Kim, Y.M. Wang, U. Ramamurty, J. Il Jang, Nanoindentation behavior of nanotwinned Cu: Influence of indenter angle on hardness, strain rate sensitivity and activation volume, Acta Mater. 61 (2013) 7313–7323. https://doi.org/10.1016/J.ACTAMAT.2013.08.037.

[315] J.P. Chu, Y.W. Lai, T.N. Lin, S.F. Wang, Deposition and characterization of TiNi-base thin films by sputtering, Mater. Sci. Eng. A. 277 (2000) 11–17. https://doi.org/10.1016/s0921-5093(99)00560-2.

[316] R. Su, D. Neffati, S. Xue, Q. Li, Z. Fan, Y. Liu, H. Wang, Y. Kulkarni, X. Zhang, Deformation mechanisms in FCC Co dominated by high-density stacking faults, Mater. Sci. Eng. A. 736 (2018) 12–21. https://doi.org/10.1016/j.msea.2018.08.057.

[317] P.S. Follansbee, U.F. Kocks, A constitutive description of the deformation of copper based on the use of the mechanical threshold stress as an internal state variable, Acta Metall. 36 (1988) 81–93. https://doi.org/10.1016/0001-6160(88)90030-2.

[318] R.C. Picu, G. Vincze, F. Ozturk, J.J. Gracio, F. Barlat, A.M. Maniatty, Strain rate sensitivity of the commercial aluminum alloy AA5182-O, Mater. Sci. Eng. A. 390 (2005) 334–343. https://doi.org/10.1016/j.msea.2004.08.029.

[319] S. Varam, K. V. Rajulapati, K. Bhanu Sankara Rao, Strain rate sensitivity studies on bulk nanocrystalline aluminium by nanoindentation, J. Alloys Compd. 585 (2014) 795–799. https://doi.org/10.1016/j.jallcom.2013.09.116.

[320] E. Izadi, J. Rajagopalan, Texture dependent strain rate sensitivity of ultrafine-grained aluminum films, Scr. Mater. 114 (2016) 65–69. https://doi.org/10.1016/j.scriptamat.2015.12.003.

[321] H. Miyamoto, K. Ota, T. Mimaki, Viscous nature of deformation of ultra-fine grain aluminum processed by equal-channel angular pressing, Scr. Mater. 54 (2006) 1721–1725. https://doi.org/10.1016/j.scriptamat.2006.02.016.

[322] J.E. Bailey, P.B. Hirsch, The dislocation distribution, flow stress, and stored energy in cold-worked polycrystalline silver, Philos. Mag. 5 (1960) 485–497. https://doi.org/10.1080/14786436008238300.

[323] N. Li, J. Wang, J.Y. Huang, A. Misra, X. Zhang, Influence of slip transmission on the migration of incoherent twin boundaries in epitaxial nanotwinned Cu, Scr. Mater. 64 (2011) 149–152. https://doi.org/10.1016/j.scriptamat.2010.09.031.

[324] S.F. Chen, D.Y. Li, S.H. Zhang, H.N. Han, H.W. Lee, M.G. Lee, Modelling continuous dynamic recrystallization of aluminum alloys based on the polycrystal plasticity approach, Int. J. Plast. 131 (2020) 102710. https://doi.org/10.1016/J.IJPLAS.2020.102710.

[325] Y.H. Zhao, X.Z. Liao, Z. Jin, R.Z. Valiev, Y.T. Zhu, Microstructures and mechanical properties of ultrafine grained 7075 Al alloy processed by ECAP and their evolutions during annealing, Acta Mater. 52 (2004) 4589–4599. https://doi.org/10.1016/j.actamat.2004.06.017.

[326] J. Shin, T. Kim, D.E. Kim, D. Kim, K. Kim, Castability and mechanical properties of new 7xxx aluminum alloys for automotive chassis/body applications, J. Alloys Compd. 698 (2017) 577–590. https://doi.org/10.1016/j.jallcom.2016.12.269.

[327] Y.L. Li, C.P. Kohar, R.K. Mishra, K. Inal, A new crystal plasticity constitutive model for simulating precipitation-hardenable aluminum alloys, Int. J. Plast. 132 (2020) 102759. https://doi.org/10.1016/J.IJPLAS.2020.102759.

[328] J. Li, A.K. Soh, Modeling of the plastic deformation of nanostructured materials with grain size gradient, Int. J. Plast. 39 (2012) 88–102. https://doi.org/10.1016/J.IJPLAS.2012.06.004.

[329] R.K. Islamgaliev, N.F. Yunusova, I.N. Sabirov, A. V. Sergueeva, R.Z. Valiev, Deformation behavior of nanostructured aluminum alloy processed by severe plastic deformation, Mater. Sci. Eng. A. 319–321 (2001) 877–881. https://doi.org/10.1016/S0921-5093(01)01052-8.

[330] P. V. Liddicoat, X.-Z.Z. Liao, Y. Zhao, Y. Zhu, M.Y. Murashkin, E.J. Lavernia, R.Z. Valiev, S.P. Ringer, Nanostructural hierarchy increases the strength of aluminium alloys, Nat. Commun. 1 (2010) 1–7. https://doi.org/10.1038/ncomms1062.

[331] R.A. Meirom, D.H. Alsem, A.L. Romasco, T. Clark, R.G. Polcawich, J.S. Pulskamp, M. Dubey, R.O. Ritchie, C.L. Muhlstein, Fatigue-induced grain coarsening in nanocrystalline platinum films, Acta Mater. 59 (2011) 1141–1149. https://doi.org/10.1016/j.actamat.2010.10.047.

[332] T. Chookajorn, H.A. Murdoch, C.A. Schuh, Design of Stable Nanocrystalline Alloys, Science (80-.). 337 (2012) 951–955. https://doi.org/10.1126/SCIENCE.1224737/SUPPL_FILE/CHOOKAJORN.SM.PDF.

[333] U. Klement, U. Erb, A.M. El-Sherik, K.T. Aust, Thermal stability of nanocrystalline Ni, Mater. Sci. Eng. A. 203 (1995) 177–186. https://doi.org/10.1016/0921-5093(95)09864-X.

[334] K. Zhang, J.R. Weertman, J.A. Eastman, Rapid stress-driven grain coarsening in nanocrystalline Cu at ambient and cryogenic temperatures, Appl. Phys. Lett. 87 (2005) 061921. https://doi.org/10.1063/1.2008377.

[335] Z. Chen, F. Liu, H.F. Wang, W. Yang, G.C. Yang, Y.H. Zhou, A thermokinetic description for grain growth in nanocrystalline materials, Acta Mater. 57 (2009) 1466–1475. https://doi.org/10.1016/J.ACTAMAT.2008.11.025.

[336] Z. Chen, F. Liu, X. Yang, C. Shen, Y. Fan, Analysis of controlled-mechanism of grain growth in undercooled Fe–Cu alloy, J. Alloys Compd. 509 (2011) 7109–7115. https://doi.org/10.1016/J.JALLCOM.2011.04.014.

[337] A. Devaraj, W. Wang, R. Vemuri, L. Kovarik, X. Jiang, M. Bowden, J.R. Trelewicz, S. Mathaudhu, A. Rohatgi, Grain boundary segregation and intermetallic precipitation in coarsening resistant nanocrystalline aluminum alloys, Acta Mater. 165 (2019) 698–708. https://doi.org/10.1016/J.ACTAMAT.2018.09.038.

[338] K. Reiner, R. Kirchheim, Grain coarsening inhibited by solute segregation, Acta Mater. 50 (2002) 413–419. https://doi.org/10.1016/S1359-6454(01)00338-X.

[339] C.C. Koch, Structural nanocrystalline materials: An overview, J. Mater. Sci. 42 (2007) 1403–1414. https://doi.org/10.1007/S10853-006-0609-3/FIGURES/5.

[340] K.A. Darling, M. Rajagopalan, M. Komarasamy, M.A. Bhatia, B.C. Hornbuckle, R.S. Mishra, K.N. Solanki, Extreme creep resistance in a microstructurally stable nanocrystalline alloy, Nat. 2016 5377620. 537 (2016) 378–381. https://doi.org/10.1038/nature19313.

[341] T. Frolov, K.A. Darling, L.J. Kecskes, Y. Mishin, Stabilization and strengthening of nanocrystalline copper by alloying with tantalum, Acta Mater. 60 (2012) 2158–2168. https://doi.org/10.1016/j.actamat.2012.01.011.

[342] Y.Z. Chen, K. Wang, G.B. Shan, A. V. Ceguerra, L.K. Huang, H. Dong, L.F. Cao, S.P. Ringer, F. Liu, Grain size stabilization of mechanically alloyed nanocrystalline Fe-Zr alloys by forming highly dispersed coherent Fe-Zr-O nanoclusters, Acta Mater. 158 (2018) 340–353. https://doi.org/10.1016/J.ACTAMAT.2018.07.070.

[343] M. Wagih, C.A. Schuh, Thermodynamics and design of nanocrystalline alloys using grain boundary segregation spectra, Acta Mater. 217 (2021) 117177. https://doi.org/10.1016/J.ACTAMAT.2021.117177.

[344] G.H. Balbus, J. Kappacher, D.J. Sprouster, F. Wang, J. Shin, Y.M. Eggeler, T.J. Rupert, J.R. Trelewicz, D. Kiener, V. Maier-Kiener, D.S. Gianola, Disordered interfaces enable high temperature thermal stability and strength in a nanocrystalline aluminum alloy, Acta Mater. 215 (2021) 116973. https://doi.org/10.1016/j.actamat.2021.116973.

[345] B.C. Hornbuckle, T. Rojhirunsakool, M. Rajagopalan, T. Alam, G.P. Purja Pun, R. Banerjee, K.N. Solanki, Y. Mishin, L.J. Kecskes, K.A. Darling, Effect of Ta Solute Concentration on the Microstructural Evolution in Immiscible Cu-Ta Alloys, JOM. 67 (2015) 2802–2809. https://doi.org/10.1007/S11837-015-1643-X/FIGURES/4.

[346] K.A. Darling, A.J. Roberts, Y. Mishin, S.N. Mathaudhu, L.J. Kecskes, Grain size stabilization of nanocrystalline copper at high temperatures by alloying with tantalum, J. Alloys Compd. 573 (2013) 142–150. https://doi.org/10.1016/j.jallcom.2013.03.177.

[347] A. Bachmaier, M. Pfaff, M. Stolpe, H. Aboulfadl, C. Motz, Phase separation of a supersaturated nanocrystalline Cu–Co alloy and its influence on thermal stability, Acta Mater. 96 (2015) 269–283. https://doi.org/10.1016/J.ACTAMAT.2015.05.053.

[348] L. Sun, D. Li, L. Zhu, H. Ruan, J. Lu, Size-dependent formation and thermal stability of high-order twins in hierarchical nanotwinned metals, Int. J. Plast. 128 (2020) 102685. https://doi.org/10.1016/j.ijplas.2020.102685.

[349] M.H. Shaeri, M.T. Salehi, S.H. Seyyedein, M.R. Abutalebi, J.K. Park, Microstructure and mechanical properties of Al-7075 alloy processed by equal channel angular pressing combined with aging treatment, Mater. Des. 57 (2014) 250–257. https://doi.org/10.1016/J.MATDES.2014.01.008.

[350] O. Bouaziz, S. Allain, C.P. Scott, P. Cugy, D. Barbier, High manganese austenitic twinning induced plasticity steels: A review of the microstructure properties relationships, Curr. Opin. Solid State Mater. Sci. 15 (2011) 141–168. https://doi.org/10.1016/J.COSSMS.2011.04.002.

[351] A.P. Babu, A. Huang, N. Birbilis, On the heat treatment and mechanical properties of a high solute Al–Zn–Mg alloy processed through laser powder bed fusion process, Mater. Sci. Eng. A. 807 (2021). https://doi.org/10.1016/j.msea.2021.140857.

[352] H. Asgharzadeh, A. Simchi, H.S. Kim, Microstructure and mechanical properties of oxide-dispersion strengthened al6063 alloy with ultra-fine grain structure, in: Metall. Mater. Trans. A Phys. Metall. Mater. Sci., Springer, 2011: pp. 816–824. https://doi.org/10.1007/s11661-010-0510-1.

[353] Y. Liu, B. Jin, J. Lu, Mechanical properties and thermal stability of nanocrystallized pure aluminum produced by surface mechanical attrition treatment, Mater. Sci. Eng. A. 636 (2015) 446–451. https://doi.org/10.1016/j.msea.2015.03.068.

[354] P.G. Partridge, M.C. McConnell, The effect of microstructure and composition on the properties of vapour quenched AlCr alloys-II. Tensile properties, Acta Metall. 35 (1987) 1981–1993. https://doi.org/10.1016/0001-6160(87)90027-7.

[355] H. Hasegawa, S. Komura, A. Utsunomiya, Z. Horita, M. Furukawa, M. Nemoto, T.G. Langdon, Thermal stability of ultrafine-grained aluminum in the presence of Mg and Zr additions, Mater. Sci. Eng. A. 265 (1999) 188–196. https://doi.org/10.1016/s0921-5093(98)01136-8.

[356] K.T. Park, H.J. Kwon, W.J. Kim, Y.S. Kim, Microstructural characteristics and thermal stability of ultrafine grained 6061 Al alloy fabricated by accumulative roll bonding process, Mater. Sci. Eng. A. 316 (2001) 145–152. https://doi.org/10.1016/S0921-5093(01)01261-8.

[357] T. Uesugi, K. Higashi, First-principles calculation of grain boundary energy and grain boundary excess free volume in aluminum: Role of grain boundary elastic energy, J. Mater. Sci. 46 (2011) 4199–4205. https://doi.org/10.1007/S10853-011-5305-2/FIGURES/6.

[358] P.W. Voorhees, Ostwald Ripening of Two-Phase Mixtures, Annu. Rev. Mater. Sci. 22 (1992) 197–215.

[359] W. Ostwald, Über die vermeintliche Isomerie des roten und gelben Quecksilberoxyds und die Oberflächenspannung fester Körper, Zeitschrift Für Phys. Chemie. 34U (1900) 495–503. https://doi.org/10.1515/zpch-1900-3431.

[360] R.D. Doherty, D.A. Hughes, F.J. Humphreys, J.J. Jonas, D. Juul Jensen, M.E. Kassner, W.E. King, T.R. McNelley, H.J. McQueen, A.D. Rollett, Current issues in recrystallization: a review, Mater. Sci. Eng. A. 238 (1997) 219–274. https://doi.org/10.1016/S0921-5093(97)00424-3.

[361] A.R. Farkoosh, D.N. Seidman, D.C. Dunand, Microstructure and Mechanical Properties of a Precipitation-Hardened Al–Mn–Zr–Er Alloy, Miner. Met. Mater. Ser. 6 (2021) 239–244. https://doi.org/10.1007/978-3-030-65396-5_35.

[362] C. Booth-Morrison, D.C. Dunand, D.N. Seidman, Coarsening resistance at 400 °C of precipitation-strengthened Al–Zr–Sc–Er alloys, Acta Mater. 59 (2011) 7029–7042. https://doi.org/10.1016/J.ACTAMAT.2011.07.057.

[363] K.E. Knipling, D.C. Dunand, D.N. Seidman, Criteria for developing castable, creep-resistant aluminum-based alloys - A review, Int. J. Mater. Res. 97 (2006) 246–265. https://doi.org/10.1515/ijmr-2006-0042.

[364] T. Marumo, S. Fujikawa, K. Hirano, Diffusion of Zirconium in Aluminum, J. Japanese Inst. Light Met. 23 (1973).

[365] W.L. Li, N.R. Tao, Z. Han, K. Lu, Comparisons of dry sliding tribological behaviors between coarse-grained and nanocrystalline copper, Wear. 274–275 (2012) 306–312. https://doi.org/10.1016/J.WEAR.2011.09.010.

[366] W. Ye, M. Misra, · Pradeep Menezes, · Leslie, T. Mushongera, Influence of Grain Boundary Character on Dopants Segregation in Nanocrystalline Aluminum, Met. Mater. Int. 2022. (2022) 1–9. https://doi.org/10.1007/S12540-022-01203-X.

[367] A. Pariyar, L.S. Toth, S. V. Kailas, L. Peltier, Imparting high-temperature grain stability to an Al-Mg alloy, Scr. Mater. 190 (2021) 141–146. https://doi.org/10.1016/j.scriptamat.2020.08.035.

[368] A. Suhane, D. Scheiber, M. Popov, V.I. Razumovskiy, L. Romaner, M. Militzer, Solute drag assessment of grain boundary migration in Au, Acta Mater. 224 (2022) 117473. https://doi.org/10.1016/J.ACTAMAT.2021.117473.

[369] C.C. Koch, R.O. Scattergood, K.A. Darling, J.E. Semones, Stabilization of nanocrystalline grain sizes by solute additions, J. Mater. Sci. 43 (2008) 7264–7272. https://doi.org/10.1007/S10853-008-2870-0/FIGURES/6.

[370] M. Saber, C.C. Koch, R.O. Scattergood, Thermodynamic Grain Size Stabilization Models: An Overview, Mater. Res. Lett. 3 (2015) 65–75. https://doi.org/10.1080/21663831.2014.997894.

[371] B.K. VanLeeuwen, K.A. Darling, C.C. Koch, R.O. Scattergood, B.G. Butler, Thermal stability of nanocrystalline Pd81Zr19, Acta Mater. 58 (2010) 4292–4297. https://doi.org/10.1016/J.ACTAMAT.2010.04.023.

[372] M. Saber, H. Kotan, C.C. Koch, R.O. Scattergood, Thermodynamic stabilization of nanocrystalline binary alloys, J. Appl. Phys. 113 (2013) 063515. https://doi.org/10.1063/1.4791704.

[373] K.A. Darling, R.N. Chan, P.Z. Wong, J.E. Semones, R.O. Scattergood, C.C. Koch, Grain-size stabilization in nanocrystalline FeZr alloys, Scr. Mater. 59 (2008) 530–533. https://doi.org/10.1016/J.SCRIPTAMAT.2008.04.045.

[374] S. Gollapudi, N. Rai, R. Kushwaha, R.K. Sabat, Crystallographic texture influences on the thermal stability of nanocrystalline materials, J. Mater. Sci. 56 (2021) 11154–11163. https://doi.org/10.1007/s10853-021-05983-2.

[375] K. Lu, L. Lu, S. Suresh, Strengthening materials by engineering coherent internal boundaries at the nanoscale, Science (80-.). 324 (2009) 349–352. https://doi.org/10.1126/science.1159610.

[376] G.H. Balbus, F. Wang, D.S. Gianola, Suppression of shear localization in nanocrystalline Al–Ni–Ce via segregation engineering, Acta Mater. 188 (2020) 63–78. https://doi.org/10.1016/j.actamat.2020.01.041.

[377] F. Duan, Y. Lin, J. Pan, L. Zhao, Q. Guo, D. Zhang, Y. Li, Ultrastrong nanotwinned pure nickel with extremely fine twin thickness, Sci. Adv. 7 (2021). https://doi.org/10.1126/SCIADV.ABG5113.

[378] X. Liu, L. Sun, L. Zhu, J. Liu, K. Lu, J. Lu, High-order hierarchical nanotwins with superior strength and ductility, Acta Mater. 149 (2018) 397–406. https://doi.org/10.1016/J.ACTAMAT.2018.01.047.

[379] O. Anderoglu, A. Misra, J. Wang, R.G. Hoagland, J.P. Hirth, X. Zhang, Plastic flow stability of nanotwinned Cu foils, Int. J. Plast. 26 (2010) 875–886. https://doi.org/10.1016/j.ijplas.2009.11.003.

[380] D. Jang, C. Cai, J.R. Greer, Influence of homogeneous interfaces on the strength of 500 nm diameter Cu nanopillars, Nano Lett. 11 (2011) 1743–1746. https://doi.org/10.1021/nl2003076.

[381] Y.T. Zhu, X.L. Wu, X.Z. Liao, J. Narayan, L.J. Kecske, S.N. Mathaudhu, Dislocation – twin interactions in nanocrystalline fcc metals, Acta Mater. 59 (2011) 812–821. https://doi.org/10.1016/j.actamat.2010.10.028.

[382] H. Jiang, T.J. Klemmer, J.A. Barnard, W.D. Doyle, E.A. Payzant, Epitaxial Growth of Cu (111) films on Si (110) by Magnetron Sputtering: Orientation and Twin Growth, Thin Solid Films. 315 (1998) 13–16.

[383] K. Han, J.P. Hirth, J.D. Embury, Modeling the formation of twins and stacking faults in the Ag-Cu system, Acta Mater. 49 (2001) 1537–1540. https://doi.org/10.1016/S1359-6454(01)00057-X.

[384] Y.F. Shen, L. Lu, M. Dao, S. Suresh, Strain rate sensitivity of Cu with nanoscale twins, Scr. Mater. 55 (2006) 319–322. https://doi.org/10.1016/j.scriptamat.2006.04.046.

[385] N.A. Richter, X. Sheng, B. Yang, B.T. Stegman, H. Wang, X. Zhang, Assessing Strain Rate Sensitivity of Nanotwinned Al-Zr Alloys Through Nanoindentation, Crystals. 13 (2023) 276. https://doi.org/10.2139/ssrn.4305685.

[386] N.A. Richter, Y.F. Zhang, M. Gong, T. Niu, B. Yang, S. Xue, J. Wang, H. Wang, X. Zhang, Solute synergy induced thermal stability of high-strength nanotwinned Al-Co-Zr alloys, Mater. Sci. Eng. A. 862 (2023) 144477. https://doi.org/10.1016/j.msea.2022.144477.

[387] K. Ye, Z. Wang, Twins enhanced mechanical properties of boron carbide, Ceram. Int. 48 (2022) 14499–14506. https://doi.org/10.1016/j.ceramint.2022.01.343.

[388] B.M. Moshtaghioun, D. Gomez-Garcia, A. Dominguez-Rodriguez, R.I. Todd, Grain size dependence of hardness and fracture toughness in pure near fully-dense boron carbide ceramics, J. Eur. Ceram. Soc. 36 (2016) 1829–1834. https://doi.org/10.1016/j.jeurceramsoc.2016.01.017.

[389] R. Meyer, L.J. Lewis, Stacking-fault energies for Ag, Cu, and Ni from empirical tight-binding potentials, Phys. Rev. B - Condens. Matter Mater. Phys. 66 (2002) 521061–521064. https://doi.org/10.1103/PhysRevB.66.052106.

[390] C. Wang, H. Wang, T. Huang, X. Xue, F. Qiu, Q. Jiang, Generalized-stacking-fault energy and twin-boundary energy of hexagonal close-packed Au: A first-principles calculation, Sci. Rep. 5 (2015) 1–11. https://doi.org/10.1038/srep10213.

[391] M. Chandran, S.K. Sondhi, First-principle calculation of stacking fault energies in Ni and Ni-Co alloy, J. Appl. Phys. 109 (2011). https://doi.org/10.1063/1.3585786.

[392] T.C. Schulthess, P.E.A. Turchi, A. Gonis, Systematic study of stacking fault energies of random Al-based alloys, Acta Mater. 46 (1998) 2215–2221. https://doi.org/10.1016/S1359-6454(97)00432-1.

[393] R. Berlia, J. Rajagopalan, High strength and ductility in a heterostructured nanotwinned Ni film, Scr. Mater. 213 (2022) 114594. https://doi.org/10.1016/J.SCRIPTAMAT.2022.114594.

[394] G.M. Valentino, P.P. Shetty, A. Chauhan, J.A. Krogstad, T.P. Weihs, K.J. Hemker, Nanotwin formation in Ni–Mo–W alloys deposited by dc magnetron sputtering, Scr. Mater. 186 (2020) 247–252. https://doi.org/10.1016/j.scriptamat.2020.05.031.

[395] Z.H. Yang, P.C. Wu, T.H. Chuang, Effects of substrate bias on the sputtering of high density (111)-nanotwinned Cu films on SiC chips, Sci. Rep. 12 (2022) 1–10. https://doi.org/10.1038/s41598-022-19825-x.

[396] L. Velasco, A.M. Hodge, The mobility of growth twins synthesized by sputtering: Tailoring the twin thickness, Acta Mater. 109 (2016) 142–150. https://doi.org/10.1016/j.actamat.2016.02.042.

[397] Y. Liu, D. Bufford, S. Rios, H. Wang, J. Chen, J.Y. Zhang, X. Zhang, A formation mechanism for ultra-thin nanotwins in highly textured Cu/Ni multilayers, J. Appl. Phys. 111 (2012). https://doi.org/10.1063/1.3702461.

[398] T.W. Barbee, B.E. Jacobson, D.L. Keith, Microstructure of amorphous 304 stainless steel-carbon alloys synthesized by magnetron sputter deposition, 63 (1979) 143–150.